Carnegie Mellon University
MELLON COLLEGE OF SCIENCE

THESIS

SUBMITTED IN PARTIAL FULFILLMENT OF THE REQUIREMENTS
FOR THE DEGREE OF

DOCTOR OF PHILOSOPHY IN THE FIELD OF PHYSICS

TITLE: "Cosmological Simulation studies of the Intrinsic alignment of galaxies."

PRESENTED BY: Ananth Tennetti

ACCEPTED BY THE DEPARTMENT OF PHYSICS

RACHEL MANDELBAUM 1/9/17

RACHEL MANDELBAUM, CHAIR PROFESSOR DATE

STEPHEN GAROFF 1/9/17

STEPHEN GAROFF, DEPT HEAD DATE

APPROVED BY THE COLLEGE COUNCIL

REBECCA DOERGE 1/9/17

REBECCA DEORGE, DEAN DATE

Cosmological Simulation studies of the Intrinsic alignment of galaxies.

by

Ananth Tenneti

Submitted in partial fulfillment of the
requirements for the degree of
Doctor of Philosophy
at
Carnegie Mellon University
Department of Physics
Pittsburgh, Pennsylvania

Advised by Professor Rachel Mandelbaum
Advised by Professor Tiziana Di Matteo

December 31, 2016

Abstract

Weak lensing refers to a statistical study of the small distortions of the images of galaxy shapes due to the gravitational deflection of light by the foreground structures. Weak lensing has emerged as a powerful probe to constrain cosmological paramters to subpercent errors in future cosmological surveys. However, the intrinsic alignment of galaxies with the large-scale density field is a significant astrophysical contaminant in weak lensing measurements that can bias cosmological constraints and also a useful probe of galaxy formation and evolution. Recent large volume hydrodynamic simulations that include galaxy formation have become an important tool to study intrinsic alignments which are difficult to model analytically and the presence of baryonic component allows us to directly measure galaxy shapes and alignments. This thesis presents a study of the intrinsic alignment of galaxies in the MassiveBlack-II (MBII) hydrodynamic simulation. We first analyze the shapes and alignments of the stellar component of the galaxies in MBII and their dependence on subhalo mass and environment. This is followed by an analyis of two-point statistics quantifying intrinsic alignmnents and their scaling with mass, luminosity and color. We then compare the galaxy shapes and alignments in the hydrodynamic simulation with the shapes of dark matter subhalos in a dark matter-only simulation performed with the same resolution and initial conditions. Finally, we analyze the intrinsic alignments of disks and elliptical galaxies which are morphologically classified based on a dynamical bulge disk decomposition in MBII and Illustris, a hydrodynamic simulation implemented with moving mesh code and different baryonic feedback models. We also carry out a parameter space study by modifying the free paramters in the MBII feedback models and study their impact on intrinsic alignments using small volume simulations.

Acknowledgments

I would like to first thank my advisors, Rachel Mandelbaum and Tiziana Di Matteo for guiding me through the projects of my thesis and providing every possible help and advise. I thank Nick Gnedin for giving me the opportunity to visit Fermilab and advising me on the final project of my thesis. Among my collaborators, I especially thank Yu Feng for his help throughout the course of my thesis as well as Alina Kiessling and Nishikanta Khandai. I also want to thank Sukhdeep, Siamak, Francois, Yen-Chi and other collaborators. Finally, I would like to thank my committee members, Rupert Croft and Andrew Zentner for their comments and feedback on the thesis. Special thanks to Manfred Paulini, members of my research group, everyone in the department, friends and family for their support.

Contents

1 Introduction **1**

1.1 Weak Lensing . . . 3

1.2 Intrinsic Alignments . . . 6

1.2.1 Modeling of Intrinsic Alignments . . . 7

1.3 Cosmological Simulations . . . 8

1.3.1 Gravity . . . 9

1.3.2 Hydrodynamics . . . 9

1.3.3 Smoothed Particle Hydrodynamics (SPH) . . . 10

1.3.4 Feedback Models . . . 11

1.3.5 Radiative Cooling . . . 12

1.3.6 Star formation and Supernova Feedback . . . 12

1.3.7 Wind Feedback . . . 13

1.3.8 AGN Feedback . . . 14

1.4 Thesis Overview . . . 14

1.4.1 Motivation . . . 14

1.4.2 Thesis plan . . . 15

2 Galaxy shapes and alignments **16**

2.1 Methods . . . 18

2.1.1 MassiveBlack-II Simulation . . . 18

2.1.2 Determination of 3D and 2D shapes . . . 21

2.1.3 Convergence tests on axis ratios . . . 22

2.2 Shapes of dark matter and stellar matter of subgroups . . . 24

2.2.1 3D axis ratio distributuions . . . 24

2.2.2 Redshift evolution and mass dependence of 3D axis ratios . . . 24

2.3 Misalignments between stellar matter and dark matter shapes of subhalos 29

2.3.1 Definition of misalignment angle . . . 29

2.3.2 Mass and redshift dependence of misalignments . . . 30

2.4 Shape distributions and misalignments for central vs. satellite galaxies 31

2.5 Conclusions . . . 34

3 Analysis of Two-point Statistics **37**
3.1 Methods 39
3.1.1 MassiveBlack-II Simulation 39
3.1.2 Shapes of galaxies and dark matter halos 40
3.1.3 Misalignment angle 42
3.2 Two-point correlation functions 42
3.2.1 Position angle statistics 42
3.2.2 Projected shape correlation functions 43
3.2.3 Formalism: Linear Alignment Model 45
3.3 The impact of using different inertia tensor definitions 46
3.3.1 Axis ratio distributions 46
3.3.2 Misalignment angle distributions 48
3.3.3 Two-point correlation functions 49
3.3.4 Shapes determined using luminosity weighting 51
3.4 Color dependence of intrinsic alignments 53
3.4.1 Division into blue and red galaxies 53
3.4.2 Axis ratio distributions 54
3.4.3 Misalignment angles and two-point correlation functions . . . 55
3.5 Mass and redshift dependence of two-point correlation functions . . . 55
3.5.1 Mass dependence 56
3.5.2 Redshift evolution 58
3.6 Two point correlation functions: centrals and satellites 59
3.6.1 Alignments of central and satellite galaxies 59
3.6.2 w_{g+} and $w_{\delta+}$ for centrals and satellites 61
3.7 Modeling, Comparisons and Predictions 62
3.7.1 Fitting models to MB-II correlation functions 63
3.7.2 Comparison with luminous galaxy intrinsic alignments 67
3.7.3 Predictions for future weak lensing surveys 68
3.8 Conclusions 70

4 Galaxy shapes and alignments in Dark matter-only simulations **75**
4.1 Introduction 75
4.2 Methods 77
4.2.1 Simulations 77
4.2.2 Shapes of dark matter subhalos 80
4.2.3 Misalignment angle 81
4.2.4 Two-point statistics 81
4.3 Results 83
4.3.1 Mass function 83
4.3.2 Matter correlation function and power spectrum 84
4.3.3 Matching subhalos in MBII and DMO 85
4.4 Shapes and misalignment angles 87

4.4.1 Radial dependence of shapes 88
4.4.2 Misalignment angles 90
4.4.3 Radial dependence of misalignment angles 93
4.5 Intrinsic alignment two-point correlation functions 94
4.6 Conclusions 96

5 Intrinsic alignments of disk and elliptical galaxies 99
5.1 Introduction 99
5.2 Simulations 101
5.2.1 MassiveBlack-II Simulation 101
5.2.2 Illustris Simulation 102
5.2.3 Galaxy and halo catalogs 102
5.3 Methods 102
5.3.1 Galaxy shapes 103
5.3.2 Misalignment angle 104
5.3.3 Two-point statistics 105
5.3.4 Bulge-to-disk decomposition 105
5.4 Galaxy shapes and alignments in Illustris and MBII 106
5.4.1 Galaxy stellar mass function 106
5.4.2 Shapes and misalignment angles 106
5.4.3 Two-point statistics 108
5.5 Morphological Classification in Illustris and MBII 111
5.5.1 Fraction of disk galaxies 111
5.5.2 Shapes and misalignment angles of disks and elliptical galaxies 114
5.5.3 Two-point intrinsic alignment statistics of disks and elliptical galaxies 117
5.6 Conclusions 120

6 Impact of Baryonic Physics 122
6.1 Introduction 122
6.2 Simulations and Feedback Models 123
6.2.1 Star formation and Stellar and AGN Feedback 124
6.2.2 Wind Feedback 125
6.2.3 AGN Feedback 125
6.2.4 Parameters Space Study 126
6.3 Methods 126
6.3.1 Calculation of shapes 126
6.3.2 Two-point statistics 127
6.4 Intrinsic alignments in a smaller volume box including DC mode in the fiducial model 128
6.4.1 Distribution of Shapes and Misalignment angles 129
6.5 Baryonic effects : parameter variation in the fiducial model 132

6.6 Conclusions 136

7 Conclusion and Future Work **138**
7.1 Conclusions 138
7.2 Future Work 139

APPENDICES **141**

A **141**
A.1 Functional forms for dark matter and stellar matter shapes 141
A.2 Functional forms for probability distributions of 3D and 2D misalignment angles 142
A.3 Functional forms for mean misalignment angles in 3D and 2D 144

B **147**
B.1 Fitting Results 147

List of Tables

2.1 Mean 3D misalignments in subgroups at redshifts $z = 1.0, 0.3$, and 0.06 in the mass bins $M1, M2$ and $M3$. 30
2.2 Mean 2D misalignments in subgroups at redshifts $z = 1.0, 0.3$, and 0.06 in mass bins $M1, M2$ and $M3$ 30
2.3 Mean 3D misalignments in central and satellite subgroups at redshifts $z = 1.0, 0.3$, and 0.06 in subhalo mass bins $M1, M2$ and $M3$. 33
2.4 Mean 3D misalignments in central and satellite subgroups at redshifts $z = 1.0, 0.3$, and 0.06 in parent halo mass bins $M1, M2$ and $M3$. . . . 33

3.1 Results of fitting different parameters (luminosity bin samples only) to find their mass and luminosity evolution (Eq. 3.20 and 3.19). Different columns are the parameters that go into Eq. (3.20) and (3.19) while different rows are for different intrinsic alignments model parameters, with A_I being the NLA amplitude, P_A and P_I are power law fits (Eq. 3.18) to w_{g+} and P_A^δ and P_I^δ are power law fits to $w_{\delta+}$. 66
3.2 Results of fitting different parameters (for mass and luminosity threshold samples only) to find their mass and luminosity evolution (Eq. 3.20 and 3.19). Different columns are the parameters that go into Eq. (3.20) and (3.19) while different rows are for different intrinsic alignments model parameters, with A_I being the NLA amplitude, P_A and P_I are power law fits (Eq. 3.18) to w_{g+} and P_A^δ and P_I^δ are power law fits to $w_{\delta+}$. 71

4.1 Simulation parameters: box size ($\mathrm{L_{box}}$), force softening length (ϵ), number of particles (N_{part}), mass of dark matter particle (m_{DM}) and mass of gas particle (m_{gas}) 77

5.1 Mean axis ratios, $\langle q \rangle$ and $\langle s \rangle$, for galaxies in Illustris and MBII. . . . 107
5.2 Mean 3D misalignment angles, $\langle \theta \rangle$ (degrees), between the major axis of galaxies and their host dark matter subhalos in Illustris and MBII. 108
5.3 Mean axis ratios, $\langle q \rangle$ and $\langle s \rangle$, of disks and elliptical galaxies in Illustris and MBII. 116
5.4 Mean misalignment angles in 3D, $\langle \theta \rangle$ (degrees), of disks and elliptical galaxies in Illustris and MBII. 116

6.1 Mean 3D shapes b/a and c/a of the stellar component of the fiducial MBII-100 simulation and three MBII-25 simulations with different DC modes of 0 and $\pm 1\sigma$ 129
6.2 Mean 3D misalignment angles, $\langle\theta\rangle$ (degrees), between the major axis of galaxies and their host dark matter subhalos in the MBII simulation of $100h^{-1}Mpc$ size box and simulations of $25h^{-1}Mpc$ box with DC-modes : 0, $\pm 1\sigma$ 129
6.3 Mean of b/a, c/a, and θ of the stellar shape of galaxies for simulations with varying star formation feedback. 134

A.1 Parameters, γ and a_i for mean axis ratios, $\langle q\rangle$ and $\langle s\rangle$ in mass range, $10^{10.0} - 10^{14.0} h^{-1}M_\odot$ 142
A.2 Parameters for probability distributions of 3D misalignment angles at redshifts $z = 1.0, 0.3$, and 0.06 for subhalos in the mass bins $M1$: $10^{10.0}$–$10^{11.5}h^{-1}M_\odot$, $M2$: $10^{11.5}$–$10^{13.0}h^{-1}M_\odot$ and $M3$: $> 10^{13.0}h^{-1}M_\odot$. 144
A.3 Parameters for probability distributions of 2D misalignment angles at redshifts $z = 1.0, 0.3$, and 0.06 for subhalos in the mass bins $M1$: $10^{10.0}$–$10^{11.5}h^{-1}M_\odot$, $M2$: $10^{11.5}$–$10^{13.0}h^{-1}M_\odot$ and $M3$: $> 10^{13.0}h^{-1}M_\odot$. 144
A.4 Parameters for mean misalignment angles in 3D at redshifts $z = 1.0, 0.3$ and 0.06 for subhalos in the mass range, $10^{10.0} - 10^{14.0}$ $h^{-1}M_\odot$. 146
A.5 Parameters for mean misalignment angles in 2D at redshifts $z = 1.0, 0.3$ and 0.06 for subhalos in the mass range, $10^{10.0} - 10^{14.0}$ $h^{-1}M_\odot$. 146

B.1 Model fits to samples defined by a luminosity threshold, including all galaxies above some lower luminosity limit such that a given comoving abundance is achieved. A_I is the NLA model amplitude, P_A and P_I are the power law parameters. The power-law is fit separately to w_{g+} and $w_{\delta+}$, with superscript δ indicating the fits to $w_{\delta+}$. $\langle L/L_0\rangle$ gives average luminosity for the sample, normalized by pivot luminosity L_0, corresponding to r-band magnitude $M_{r,0} = -22$. 149
B.2 Model fits to samples defined by mass threshold subhalo mass.$\langle M/h^{-1}M_\odot\rangle$ is the average subhalo mass with in the sample. See Table B.1 for description of different parameters. 150
B.3 Model fits to central galaxy intrinsic alignment correlation functions.$\langle M/h^{-1}M_\odot\rangle$ is the average subhalo mass with in the sample. See Table B.1 for description of different parameters. 151
B.4 Model fits to satellite galaxy intrinsic alignment correlation functions.$\langle M/h^{-1}M_\odot\rangle$ is the average subhalo mass with in the sample. See Table B.1 for description of different parameters. 152
B.5 Model fits to intrinsic alignments measurements for samples defined in luminosity bins. See Table B.1 for description of different parameters. 153

List of Figures

1.1 An illustration of Gravitational Lensing 4

2.1 *Top:* Snapshot of the MBII simulation in a slice of thickness $2h^{-1}$Mpc at redshift $z = 0.06$. The bluish-white colored region represents the density of the dark matter distribution and the red lines show the direction of the major axis of ellipse for the projected shape defined by the stellar component. *Bottom Left:* Dark matter (shown in gray) and stellar matter (shown in red) distribution in the most massive group at $z = 0.06$ of mass $7.2 \times 10^{14} h^{-1} M_{\odot}$. The blue and red ellipses show the projected shapes of dark matter and stellar matter of subhalos respectively. *Bottom Middle:* Dark matter and stellar matter distribution in a group of mass $3.8 \times 10^{12} h^{-1} M_{\odot}$. *Bottom Right:* Dark matter and stellar matter distribution in a group of mass $1.1 \times 10^{12} h^{-1} M_{\odot}$. . . . 19

2.2 Dark matter and stellar mass function for FOF groups (halos) at $z = 0.06, 1.0$, compared with the SO-based prediction from [159] generated with $\Delta = 0.75$. 20

2.3 Normalized histograms of axis ratios at $z = 0.06$ showing a comparison between shapes determined by using all particles in the subhalo with those obtained using a random subsample of 50, 300, 500 and 1000 particles in the subhalo. *Left:* q (b/a); *Right:* s (c/a). 23

2.4 Distribution of the number of dark matter and star particles in subgroups at $z = 0.06$, where the colorbar indicates the number density of subhalos. 23

2.5 3d axis ratio distributions of dark matter and stellar matter in subhalos at $z = 0.06$, for masses of subhaloes in the range $10^{10.0} - 10^{14.0} h^{-1} M_{\odot}$. 25

2.6 Comparison of axis ratios, q (b/a) (left panel) and s (c/a) (right panel) between dark matter subgroups and groups at $z = 0.3$ in different mass bins. 26

2.7 Axis ratios q (b/a) (left panel) and s (c/a) (right panel) for stellar matter of subhalos at $z = 0.3$ in mass bins ($M1, M2$ and $M3$) and at $z = 1.0, 0.06$ for the central mass bin, $M2$. 26

2.8 Average axis ratios, $\langle q \rangle$ (left panel) and $\langle s \rangle$ (right panel) for dark matter and stellar component of subhalos as a function of mass, at redshifts $z = 1.0, 0.03$, and 0.06. 27
2.9 RMS ellipticity per component for projected shapes, $e_{\rm rms}$, for dark matter and stellar matter at $z = 1.0, 0.3$, and 0.06 as a function of cumulative subhalo mass. 27
2.10 Histogram of 3D (left panel) and 2D (right panel) misalignments at redshifts $z = 1.0, 0.3$, and 0.06 in the mass bins $M1, M2$ and $M3$. . . 30
2.11 Axis ratio distributions of stellar matter in subgroups for centrals and satellites in mass bins $M1, M2$ and $M3$. *Top panel:* Results when dividing based on the parent halo mass; *bottom panel:* when dividing based on the subhalo mass. In both rows, the left and right panels show results for q and s, respectively. 32
2.12 Histograms of misalignment angles for central and satellite subgroups in mass bins $M1, M2$ and $M3$. *Left:* Results when dividing based on the subhalo mass; *right:* when dividing based on the halo mass. . . . 33

3.1 Normalized histograms of 3D axis ratios of dark matter component in subhalos using different definitions of inertia tensor in mass bins M1, M2 and M3 at $z = 0.3$. The number of galaxies are 38768, 8438, and 267 respectively in mass bins M1, M2 and M3. *Top:* q (b/a); *Bottom:* s (c/a). 47
3.2 Normalized histograms of 3D axis ratios of stellar matter component in subhalos using different definitions of inertia tensor in mass bins M1, M2 and M3 at $z = 0.3$. *Top:* q (b/a); *Bottom:* s (c/a). 48
3.3 Normalized histograms of misalignment angles between the major axes of 3D shapes defined by the dark matter and stellar matter component in subhalos using different definitions of inertia tensor, in mass bins (M1, M2, and M3) at $z = 0.3$. Note that for uniformly distributed misalignment angles in 3D, the probability distribution is proportional to $\sin\theta$. 49
3.4 ED correlation function, $\omega(r)$, for the 3D shapes of stellar matter obtained using different definitions of inertia tensor in subhalos selected by a mass threshold. The *top* panel, shows the ED correlation function and the *bottom* panel shows the ratio of the signals obtained using iterative reduced inertia tensor with the unweighted inertia tensor. Note that in the *top* panel, the lines labeled Unweighted and Unweighted (Iterative); Reduced and Reduced (Iterative) are close enough that they cannot be easily distinguished. *Left:* $M > 10^{11}h^{-1}M_\odot$ (24648 galaxies); *Middle:* $M > 10^{12.0}h^{-1}M_\odot$ (2947 galaxies); *Right:* $M > 10^{13.0}h^{-1}M_\odot$ (267 galaxies) at $z = 0.3$. 50

3.5 w_{g+} correlation function for the projected (2D) shapes of stellar matter obtained using different definitions of inertia tensor in subhalos selected by a mass threshold at $z = 0.3$. The *top* panel, shows the w_{g+} correlation function and the *bottom* panel shows the ratio of the signals obtained using iterative reduced inertia tensor with the unweighted inertia tensor. Note that in the *top* panel, the lines labeled Unweighted and Unweighted (Iterative) are close enough that they cannot be easily distinguished. *Left:* $M > 10^{11} h^{-1} M_{\odot}$; *Middle:* $M > 10^{12.0} h^{-1} M_{\odot}$; *Right:* $M > 10^{13.0} h^{-1} M_{\odot}$. 50
3.6 Normalized histograms of 3D axis ratios of stellar matter in subhalos using iterative unweighted and iterative reduced inertia tensors with each particle weighted by its luminosity or mass. Results are shown only for the mass bin M2. *Left:* q (b/a); *Right:* s (c/a). 51
3.7 *Left:* Normalized histogram of misalignment angles using luminosity weighted shapes of stellar matter in subhalos in the mass bin, M2: $10^{11.5} - 10^{13.0} h^{-1} M_{\odot}$at $z = 0.3$. *Middle:* ED correlation of luminosity weighted shapes of stellar matter in subhalos for $M > 10^{12} h^{-1} M_{\odot}$. *Right:* w_{g+} correlation of luminosity weighted shapes of stellar matter in subhalos for $M > 10^{12} h^{-1} M_{\odot}$. For a direct comparison, the ratio of signals obtained using the mass and luminosity weighted inertia tensors are shown in the *bottom* panels. 52
3.8 Rest-frame color $(M_u - M_r)$ versus stellar mass for galaxies in the simulation at $z = 0.3$. 53
3.9 Normalized histograms of axis ratios (q, s) of dark matter and stellar matter component in subhalos for blue (6343 galaxies) and red (6343 galaxies) galaxies at $z = 0.3$. *Left:* q (b/a); *Right:* s (c/a). 54
3.10 Comparison of misalignment angles and two-point correlation function in red and blue galaxies at $z = 0.3$. *Left:* Histogram of misalignment angles; *Middle* ED position angle statistic; *Right* w_{g+} projected shape correlation function. At around $\sim 1 h^{-1}$Mpc, the correlation function becomes negative for the blue galaxies. 55
3.11 Mass dependence of two-point correlation functions for shapes defined by stellar matter in subhalos at $z = 0.3$ using iterative reduced inertia shape tensors. *Left:* Position angle statistic, ED correlation function; *Right:* Projected shape-correlation function, w_{g+}. 56
3.12 *Left:* Ratio of $\omega_{\delta}(r)$(density field traced by dark matter particles) to $\omega(r)$ *Right:* Ratio of $w_{\delta+}(r_p)$ correlation function, where the density field is traced by dark matter particles, to $w_{g+}(r_p)$ (density field traced by subhalos). 57
3.13 Ratio plot of two-point correlation functions at redshifts $z = 1.0$, 0.3 and 0.06 and various mass thresholds to the corresponding value at $z = 0.3$ for $M > 10^{11.0} h^{-1} M_{\odot}$. *Left:* ED; *Right:* w_{g+}. 59

3.14 *Left:* Normalized histogram of alignment angle of the major axis of the 2D stellar shape of a central galaxy with satellite subhalos in mass bins, $M1$, $M2$ and $M3$ of central subhalo mass at $z = 0.3$. *Right:* Normalized histogram of alignment angles of the major axis of the 2D stellar shape of satellite galaxies with host halo in mass bins, $M1$ and $M2$ of satellite subhalo mass at $z = 0.3$. 60

3.15 w_{g+} and $w_{\delta+}$ correlation function for centrals and satellites at $z = 0.3$. *Left:* M1: $10^{10-11.5}h^{-1}M_\odot$; *Middle:* M2: $10^{11.5-13.0}h^{-1}M_\odot$; *Right:* M3: $> 10^{13.0}h^{-1}M_\odot$. The labels "Cen" and "Sat" refer to the correlation functions (w_{g+}, $w_{\delta+}$) of centrals and satellites respectively. Similarly, "1h Cen" and "1h Sat" refer to the 1-halo term of $w_{\delta+}$ for central and satellite subhalos respectively. The number of central galaxies is 23014, 7415 and 255 in mass bins M1, M2 and M3 respectively. 61

3.16 Comparison of the size of Poisson and jackknife error bars in the calculation of $w_{g+}(r)$ for subhalo mass-selected samples. 64

3.17 NLA and power law fitting to $w_{\delta+}$ (top) and w_{g+} (bottom) for two different samples defined by luminosity bins. Vertical lines show the range over which we fit the NLA model ($6h^{-1}$Mpc $< r_p < 25h^{-1}$Mpc). Note that the power law is fitted only for $r_p < 1h^{-1}$Mpc, though the function is shown out to $r_p \sim 2h^{-1}$Mpc. 64

3.18 NLA amplitude, A_I, as a function of redshift for different luminosity samples. The horizontal axis indicates the average mass, luminosity or redshift of different samples. Points are colored by sample definition, while markers are set according to the redshift. 65

3.19 Comparison of power law amplitude for w_{g+} (P_A) and $w_{\delta+}$ (P_A^δ) for various samples used in this work. The dotted line shows the $x = y$ relation. $w_{\delta+}$ is observed to have systematically higher amplitude than w_{g+} for separations below $1h^{-1}$Mpc. 66

3.20 Comparison of power law index for w_{g+} (P_I) and $w_{\delta+}$ (P_I^δ) for various samples used in this work. The dotted line shows the $x = y$ relation. $w_{\delta+}$ has a systematically steeper slope than w_{g+} for separations below $1h^{-1}$Mpc. 67

3.21 w_{g+} correlation function for galaxies selected according to r-band luminosity (such that $M_r \leq -22.6$)and comparison with observational results using SDSS LRG sample. Note that the bias of the density tracer sample has been taken into account in order to make a fair comparison, by dividing w_{g+} with the large scale linear bias. 68

3.22 *Left:* $w_{\delta+}$ correlation function at redshifts $z = 0.6$ and 0.3 for galaxies selected by a luminosity threshold to match three values of comoving abundance as labeled on the plot. *Right:* Prediction of $w_{\delta+}$ for galaxies that will be used for lensing in the LSST survey, made by matching the estimated comoving abundances at $z = 1.0$ and $z = 0.6$. The shaded regions show jackknife errorbars. 69

3.23 NLA amplitude, A_I, as a function of different sample properties. The horizontal axis indicates the average mass, luminosity or redshift of different samples. Points are colored by sample definition: comoving abundance ($\bar{n}$) in units of $10^{-3}h^3\mathrm{Mpc}^{-3}$ based on a luminosity threshold, or the mass threshold of the sample (not average mass), while markers are set according to the redshift. 71

4.1 Snapshot of the MBII (left) and DMO (right) simulations in a slice of thickness $2h^{-1}$Mpc at $z = 0.06$. The shading represents the density distribution of dark matter, and the red lines show the alignment of stellar shapes in MBII. The length of the lines is proportional to the size of major axis of the ellipse representing stellar shape. 78

4.2 Snapshot of a massive halo ($\sim 10^{14}h^{-1}M_\odot$) in the MBII (left) and DMO (right) simulations, showing the density distribution of dark matter at $z = 0.06$. The blue and green circles show the virial radii of the central subhalos in MBII and DMO simulation, respectively which are centered at the location with highest density. In both the panels, 'x' and '+' indicate the locations of the central subhalo centers in the MBII and DMO simulations, respectively. The magenta circles show the virial radii of a nearby satellite subhalo. 79

4.3 Comparison of the halo mass function in MBII and DMO simulations at $z = 1.0$ and $z = 0.06$. 83

4.4 Median and scatter (defined using the 16^{th} and 84^{th} percentiles) of the fractional difference in the FOF mass of matched halos of MBII and DMO simulations at $z = 0.06$. 84

4.5 Fractional difference between the dark matter two-point correlation functions (left) and power spectra (right) in DMO and MBII simulations at $z = 1.0$ and $z = 0.06$. The shaded regions represent a deviation within $\pm 1\%$. 85

4.6 Fraction of subhalos matched at $z = 1.0$, 0.3, and 0.06 as a function of the total subhalo mass in the MBII simulation. 86

4.7 Normalized histograms of 3D axis ratios of the dark matter component in matched subhalos in the DMO and MBII simulations, with the shapes measured at different radii ($0.2R_{200}$, $0.6R_{200}$ and $1.0R_{200}$) and also the stellar matter component in MBII. The columns indicate different mass bins, while the top and bottom rows are for q (b/a) and s (c/a), respectively. 87

4.8 Median of the dark matter subhalo axis ratios (left: q, right: s) in the MBII (dashed lines) and DMO (solid lines) simulations in different mass bins, plotted against the distance to which the shape is measured, at $z = 0.06$. 88

4.9 Median and scatter (defined using the 16$^{\text{th}}$ and 84$^{\text{th}}$ percentiles) in the distribution of the axis ratios (3D and 2D) of the stellar matter component in MBII plotted against the axis ratio of the shape of matched subhalo in the DMO simulation, with the shape measured within different radii ($0.2R_{200}$, $0.6R_{200}$ and $1.0R_{200}$). *Left:* q (3D); *middle:* s (3D); *right:* q_{2d} (2D). 88

4.10 Contour plots of 3D axis ratios of the dark matter component in matched subhalos in the DMO (left) and MBII (middle) simulations, and the stellar matter component in MBII (right), in the mass bin M2 at $z = 0.06$. 89

4.11 Misalignment angle distributions for the 3D shapes of the dark matter component in matched subhalos of DMO and MBII simulations with the stellar matter component in MBII, in mass bins M1, M2 and M3 at $z = 0.06$. Also shown (green line) is the histogram of misalignment angles between the shapes of dark matter subhalos in MBII and DMO. 91

4.12 Misalignment angle distributions for 2D shapes of the dark matter component in matched subhalos of DMO and MBII with the stellar matter component in MBII, in mass bins M1, M2 and M3 at $z = 0.06$. Also shown (green line) is the histogram of misalignment angles between the shapes of dark matter subhalos in MBII and DMO. This figure is simply the 2D version of Fig. 4.11. 91

4.13 Mean of the 3D misalignment angles between the shape of the dark matter component in MBII and DMO with the shape of stellar component in MBII as a function of the triaxiality parameter, T (of the stellar matter component in MBII and the dark matter component in MBII and DMO), in the mass range, $10^{10.8} - 6.0 \times 10^{14} h^{-1} M_{\odot}$ at $z = 0.06$. The purple line shows the mean misalignment angle between the shape of dark matter component in MBII with the stellar component in MBII plotted against the triaxiality of the shape of stellar component in MBII. Similarly, the green and black lines show the mean misalignment angles between the shapes of dark matter component in MBII and DMO with the stellar component in MBII plotted against the triaxialities of the shapes of dark matter component in MBII and DMO respectively. 92

4.14 Histograms of misalignment angles of 3D shapes of dark matter subhalos in the DMO and MBII simulations (with respect to the shape of the galaxy in MBII) when measuring the subhalo shapes within different radii ($0.2R_{200}$, $0.6R_{200}$, and $1.0R_{200}$) in the mass bins M1 (left), M2 (middle), and M3 (right) at $z = 0.06$. 93

4.15 Comparison of the ED correlation function, $\omega_{\delta}(r)$, for the dark matter subhalo and stellar matter components in MBII with respect to that for dark matter subhalos in the DMO simulation, computed separately for M1 (left), M2 (midddle), and M3 (right). 94

4.16 Comparison of the projected density-shape correlation, $w_{\delta+}(r_p)$, for the dark matter subhalo and stellar matter components in MBII with respect to that for dark matter subhalos in the DMO simulation, computed separately for M1 (left), M2 (midddle), and M3 (right). 94

4.17 Comparison of $\hat{w}_{\delta+}(r_p)$ (projected shape-density correlation function without ellipticity weighting), for the dark matter subhalo and stellar matter components in MBII with respect to that for dark matter subhalos in the DMO simulation, computed separately for M1 (left), M2 (midddle), and M3 (right). 96

5.1 Comparison of galaxy stellar mass functions in MBII and Illustris at $z = 0.06$. 103

5.2 Normalized histograms of axis ratios (left: q, right: s) of the 3D shapes of galaxies in MBII and Illustris in two stellar mass bins: $10^{10.0-11.0} h^{-1} M_{\odot}$ and $10^{11.0-12.0} h^{-1} M_{\odot}$. 104

5.3 Normalized histograms of the misalignment angles between 3D shapes of galaxies and their host dark matter subhalos in MBII and Illustris in two stellar mass bins: $10^{9.0-10.5} h^{-1} M_{\odot}$ and $10^{10.5-12.0} h^{-1} M_{\odot}$. . . . 107

5.4 *Top:* Ellipticity-direction (ED) and projected shape-density ($w_{\delta+}$) correlation functions of the stellar components of galaxies in MBII and Illustris in two stellar mass bins, $10^{9.0-10.5}h^{-1}M_{\odot}$ and $10^{10.5-12.0}h^{-1}M_{\odot}$. *Left:* ED; *Right:* $w_{\delta+}$. *Bottom*: the biases, $b_{\omega\delta}$ and $b_{w\delta+}$, defined as the ratios of the ED and $w_{\delta+}$ correlations functions of stellar components to the same correlation function computed using the dark matter subhalo. 109

5.5 Ratio of ellipticity-direction (ED, *(left)*) and projected shape-density ($w_{\delta+}$, *(right)*) correlation functions of the stellar components of galaxies in MBII and Illustris in two stellar mass bins, $10^{9.0-10.5}h^{-1}M_{\odot}$ and $10^{10.5-12.0}h^{-1}M_{\odot}$. The horizontal lines represent the best fit values obtained after fitting the ratio to a straight line in the range $0.1-10h^{-1}$Mpc and the line color indicates the corresponding mass bin. . 110

5.6 Fraction of galaxies in MBII and Illustris at $z = 0.06$ for different thresholds of the bulge-to-total ratio: $BTR < 0.7$, 0.75, 0.8. Our adopted threshold for the rest of this work is that galaxies with $BTR < 0.7$ are classified as disk galaxies. 111

5.7 Mean specific angular momentum of disks and elliptical galaxies in MBII and Illustris at $z = 0.06$. 112

5.8 Comparison of the ED correlation of the orientation of disk galaxies with the location of ellipticals in MBII, Illustris, and Horizon-AGN simulations [34]. In the right panel, the ED correlation in MBII is compared using various definitions of the disk galaxy sample. In both the panels, the solid lines represent the ED correlation of the disk major axes while the dashed lines represent the correlation of the disk minor axes. 113

5.9 Normalized histogram of the axis ratios (left: q, right: s) of 3D shapes of elliptical and disk galaxies in MBII and Illustris in the stellar mass bin 10^{9}–$10^{10.5}h^{-1}M_{\odot}$. 114

5.10 RMS ellipticities of the projected shapes of elliptical and disk galaxies in MBII and Illustris based on thresholds in stellar mass. 115

5.11 Normalized histogram of the misalignment angles of 3D shapes of elliptical and disk galaxies in MBII and Illustris within two stellar mass bins: $10^{9-10.5}h^{-1}M_{\odot}$ (left) and $10^{10.5-12}h^{-1}M_{\odot}$ (right). 115

5.12 ED correlation functions of the shapes of the stellar component (*top* panel) and the dark matter component (*bottom* panel) of elliptical and disk galaxies galaxies in MBII and Illustris within two stellar mass bins: 10^9–$10^{10.5}h^{-1}M_\odot$ (left) and $10^{10.5}$–$10^{12}h^{-1}M_\odot$ (right). In the *top* panel, we only show the 1σ upper limits of the ED correlation for disk galaxies on scales above $0.1h^{-1}$Mpc, represented by the *bottom (tip)* of arrows pointing downward in Illustris ($\downarrow$) and MBII ($\Downarrow$). Note the y-axis limits are different in the top left panel compared to the other panels, which should be taken into account while comparing the figures. 118

5.13 $w_{\delta+}$ correlation functions of the shapes of the stellar component (*top* panel) and the dark matter component (*bottom* panel) of elliptical and disk galaxies in MBII and Illustris within two stellar mass bins: 10^9–$10^{10.5}h^{-1}M_\odot$ (left) and $10^{10.5}$–$10^{12}h^{-1}M_\odot$ (right). On scales above $0.1h^{-1}$Mpc, we only show the 1σ upper limits of the $w_{\delta+}$ signal for disk galaxies, represented by the *bottom (tip)* of arrows pointing downward in Illustris ($\downarrow$) and MBII ($\Downarrow$). 119

6.1 Cumulative distribution function (CDF) of the shapes b/a and c/a in two mass bins $10^{9.5-12.0}h^{-1}M_\odot$ and $10^{12.0-15.0}h^{-1}M_\odot$ of MBII-100 run and the mean CDF of the shapes of three MBII-25 simulations with different DC modes. The bands show the error of the mean CDF. . . 130

6.2 Cumulative distribution function (CDF) of the misalignment angle θ in the mass bins $10^{9.5-12.0}h^{-1}M_\odot$ and $10^{12.0-15.0}h^{-1}M_\odot$ of MBII $100h^{-1}Mpc$ and the mean CDF of the misalignment angles of $25h^{-1}Mpc$ simulations with different DC modes. The error on the mean CDF is indicated by the bands. 131

6.3 ED and $w_{\delta+}$ correlation functions in two mass bins, $10^{9.5-12.0}h^{-1}M_\odot$ and $10^{12.0-15.0}h^{-1}M_\odot$, of MBII-100 and of three independent realizations of MBII-25 box with different DC modes. The bands indicate the error in the mean ED correlation function. 132

6.4 Cumulative distribution functions of the shapes b/a and c/a in two mass bins, $10^{9.5-12.0}h^{-1}M_\odot$ and $10^{12.0-15.0}h^{-1}M_\odot$, of several $25h^{-1}Mpc$ box simulations with varied physics. Black line with the gray band is the fiducial MBII-25 model and its error, shown with red lines in the previous section. 133

6.5 Cumulative distribution function of the misalignment angles θ in two mass bins, $10^{9.5-12.0}h^{-1}M_\odot$ and $10^{12.0-15.0}h^{-1}M_\odot$, of several $25h^{-1}Mpc$ box simulations with varied physics. Black line with the gray band is the fiducial MBII-25 model and its error, shown with red lines in the previous section. 135

6.6 ED and $w_{\delta+}$ correlation functions in two mass bins, $10^{9.5-12.0}h^{-1}M_{\odot}$ and $10^{12.0-15.0}h^{-1}M_{\odot}$, of several $25h^{-1}Mpc$ box simulations with varied physics. Black line with the gray band is the fiducial MBII-25 model and its error, shown with red lines in the previous section. 136

A.1 Fits for the axis ratios of shape defined by dark matter in subhalos as a function of mass and redshift 141
A.2 Fits for the axis ratios of shape defined by stellar matter in subhalos as a function of mass and redshift 142
A.3 Fits for probability distributions of 3D misalignment angles at $z = 0.3$ 143
A.4 Fits for probability distributions of 2D misalignment angles at $z = 0.3$ 143
A.5 Fits for mean misalignment angles in 3D as a function of mass 145
A.6 Fits for mean misalignment angles in 2D as a function of mass 145

B.1 Intrinsic alignment correlation functions, $w_{\delta+}$ and w_{g+}, for different samples defined on the basis of comoving number density threshold, at redshift $z = 0.6$. There is clear evolution with number density, where samples with lower number density and hence more luminous galaxies have higher intrinsic alignments. As discussed in main text, this has important implications for future weak lensing surveys such as Euclid and LSST. 148
B.2 Intrinsic alignment correlation functions, $w_{\delta+}$ and w_{g+}, for the mass threshold sample, $M > 10^{13}h^{-}1M_{\odot}$, at redshifts, $z = 1.0$, 0.6, 0.3, and 0.06. We see some redshift evolution as $w_{\delta+}$ and w_{g+} magnitude increases at higher redshift. 154
B.3 Intrinsic alignment correlation functions, $w_{\delta+}$ and w_{g+}, for central subhalos in different mass bins, at redshift $z = 0.3$. We detect both large scale and small scale intrinsic alignments for central sub halos, with more massive sub halos also showing stronger alignments. The downturn in the lowest mass bin at small scales indicates a transition to the 1-halo term. 154
B.4 Intrinsic alignment correlation functions, $w_{\delta+}$ and w_{g+}, for satellite subhalos in different mass bins,, $M1$, $M2$ and $M3$, at redshift $z = 0.3$. Satellites show no significant alignments at large scales, though small scale alignment is very strong, consistent with the radial alignment of satellites. 155

Chapter 1

Introduction

The components of the universe and its evolution are described by the ΛCDM model. According to our current understanding, the universe is spatially flat, homogeneous and isotropic. For a discussion on cosmology in detail, see [124, 48, 175]. Recent developments indicate that currently, the universe consists of three major components, which are the collisionless dark matter component, the baryonic component made of visible matter, and perhaps a dark energy component too. The dark matter and baryonic matter together make up the total matter density of the universe. Accordingly, the set of parameters describing the ΛCDM model include the total matter density, Ω_m, baryonic matter density Ω_b, the dark energy density, Ω_Λ , the hubble parameter, h describing the expansion rate of the universe, the amplitude of matter power spectrum within a $8h^{-1}Mpc$ top hat window, σ_8 and the scalar spectral index, n_s. Here, the density parameters, Ω_m, Ω_b and Ω_Λ quantify the amount of each component expressed as a fraction of the density of each component relative to the critical density of the universe, $\rho_{crit} = \frac{3H_0^2}{8\pi G}$ where $H_0 = 100h\ kms^{-1}Mpc^{-1}$. The density fluctuations in the matter field of the early universe, thought to have been generated by some process such as inflation [63] grow due to gravitational instability and eventually formed structures such as halos. Further, it is now known that the expansion rate of universe is accelerating [130, 126] and the dark energy component which can lead to a repulsive gravitational effect is introduced as one possible explanation [128, 59, 57]. The current measurements of these quantities are $\Omega_m \sim 0.275$, $\Omega_b \sim 0.046$, $\Omega_\Lambda \sim 0.725$ [102]. However, the nature of dark matter and dark energy is not well understood and precise measurements of cosmic expansion history and growth of structure are needed to develop further understanding. An alternative to introducing a dark energy component is to modify gravity on cosmological scales [52, 27, 28]. Future surveys such as the the Large Synoptic Survey Telescope (LSST)[1], and Euclid[2], are planned to answer these questions and weak lensing is a promising probe given its sensitivity to both dark matter and dark energy.

[1]http://www.lsst.org/lsst/

[2]http://sci.esa.int/euclid/

Gravitational lensing is the distortion of the images of distant galaxies due to deflection of light by the foreground structures. Weak lensing refers to the case when the distortion of shapes and sizes of the galaxy images are small, of the order of 1%. So, the measurement of weak lensing has to be performed statistically by averaging the correlation of shapes of millions of galaxies. For reviews on weak gravitational lensing, see [10, 174]. Weak gravitational lensing, which probes the underlying matter density is a useful probe to constrain cosmological parameters since it is sensitive to both luminous and dark matter [11, 13, 74, 75, 77, 152]. In particular, weak lensing surveys can be used to provide constraints on the theories of modified gravity and also provide constraints on the properties of dark matter and dark energy [4, 174] as it is possible to probe both the expansion history and growth rate through lensing. Since dark energy affects the growth rate, weak lensing measurements of structure growth at different redshifts can help us constrain the parameters quantifying the dark energy equation of state. Upcoming surveys like LSST and Euclid aim to determine the constant and dynamical parameters of the dark energy equation of state to a very high precision using weak lensing.

However, constraining cosmological parameters with sub-percent errors in future cosmological survey requires the systematic errors to be well below those in typical weak lensing measurements with current data sets. The weak lensing analysis is based on the assumption that the intrinsic shapes and orientations of the galaxies are oriented randomly. However, in reality, the galaxy shapes are correlated with each other and the large scale density field. This intrinsic alignment (IA) of galaxy shapes with the underlying density field is an important theoretical uncertainty that contaminates weak lensing measurements [66, 41, 78, 72]. Accurate theoretical predictions of IA through analytical models and N-body simulations [72, 68, 137, 86] in the ΛCDM paradigm is difficult due to the complex nature of galaxy formations and also since, there are no galaxies in N-body simulations. However, we have to take the baryonic physics into account, as we expect it to be important given that the alignment of interest is that of the observed, baryonic component of galaxies. In the absence of baryonic physics in N-body simulations, one has to populate halos with galaxies and assign some misalignment [68] or employ semi-analytic models where an assumption is made about how the baryonic trace the dark matter [86]. So, in this study, we use the large volume, high-resolution hydrodynamic simulation, MassiveBlack-II [93] which includes the physics of galaxy formation to directly study the shapes and alignments of galaxies. Using this approach, we can consistently study the galaxy alignments and their evolution based on a given model of galaxy formation. These galaxy alignments can be incorporated into N-body simulations to mimic the results from the hydrodynamic simulation to create mock catalogs with realistic intrinsic alignments, which can be used to test the intrinsic alignment mitigation techniques for future data sets. If the feedback model is known to predict the correct scaling of intrinsic alignments, then the IA statistics can be measured from these mock catalogs using a galaxy sample selected to match the properties of the galaxies in observational data and the contaminant can be eliminated. In the sections below, I briefly overview the topics of weak lensing, intrinsic alignments, Smoothed Particle Hydrodynamics (SPH) and feedback models in MassiveBlack-II simulation.

1.1 Weak Lensing

The deflection of a light ray in the path of a spherically symmetric, compact object of mass M is given by the angle,

$$\hat{\alpha} = \frac{4GM}{\xi} \tag{1.1}$$

where, ξ is the minimum distance between the path of light ray and the object. If this deflection angle is small, assuming Born approximation, the path of the light ray can be treated as a straight line with a bend at the location of closest distance from the deflecting mass. An illustration of this is provided in Figure 1.1. When considering light propagation over a three dimensional mass distribution, the total deflection can be calculated as the sum of deflection angles due to an ensemble of point masses. Further, when the deflection angle is small compared to the scales on which the mass distribution changes significantly, the total deflection angle can be expressed in terms of the projected surface mass density,

$$\Sigma(\xi) = \int dr_3 \rho(\xi_1, \xi_2, r_3) \tag{1.2}$$

with the total deflection given by,

$$\hat{\alpha}(\xi) = 4G \int d^2\xi' \Sigma(\xi') \frac{\xi - \xi'}{|\xi - \xi'|}^{2}, \tag{1.3}$$

Here, ρ is the density, $\xi = (\xi_1, \xi_2)$ is the two dimensional impact vector in the lens plane and the deflection is independent of the coordinate, r_3 which is along the direction of propagation of the light ray. The relation of the true position of the source galaxy, η to the observed position, ξ in terms of the deflection angle is given by the lens equation. Following the notation in the Figure 1.1, the lens equation can be written as

$$\eta = \frac{D_s}{D_d}\xi - D_{ds}\alpha(\xi) \tag{1.4}$$

The above equation can be rewritten in terms of the transformed variables, $\eta = D_s\beta$, $\xi = D_d\theta$ and the scaled deflection angle, $\alpha = \frac{D_{ds}}{D_s}\hat{\alpha}$, as

$$\beta = \theta - \alpha \tag{1.5}$$

If the convergence, κ which is the dimensionless surface mass density is given by

$$\kappa(\theta) = \frac{\Sigma(D_l\theta)}{\Sigma_c}, \tag{1.6}$$

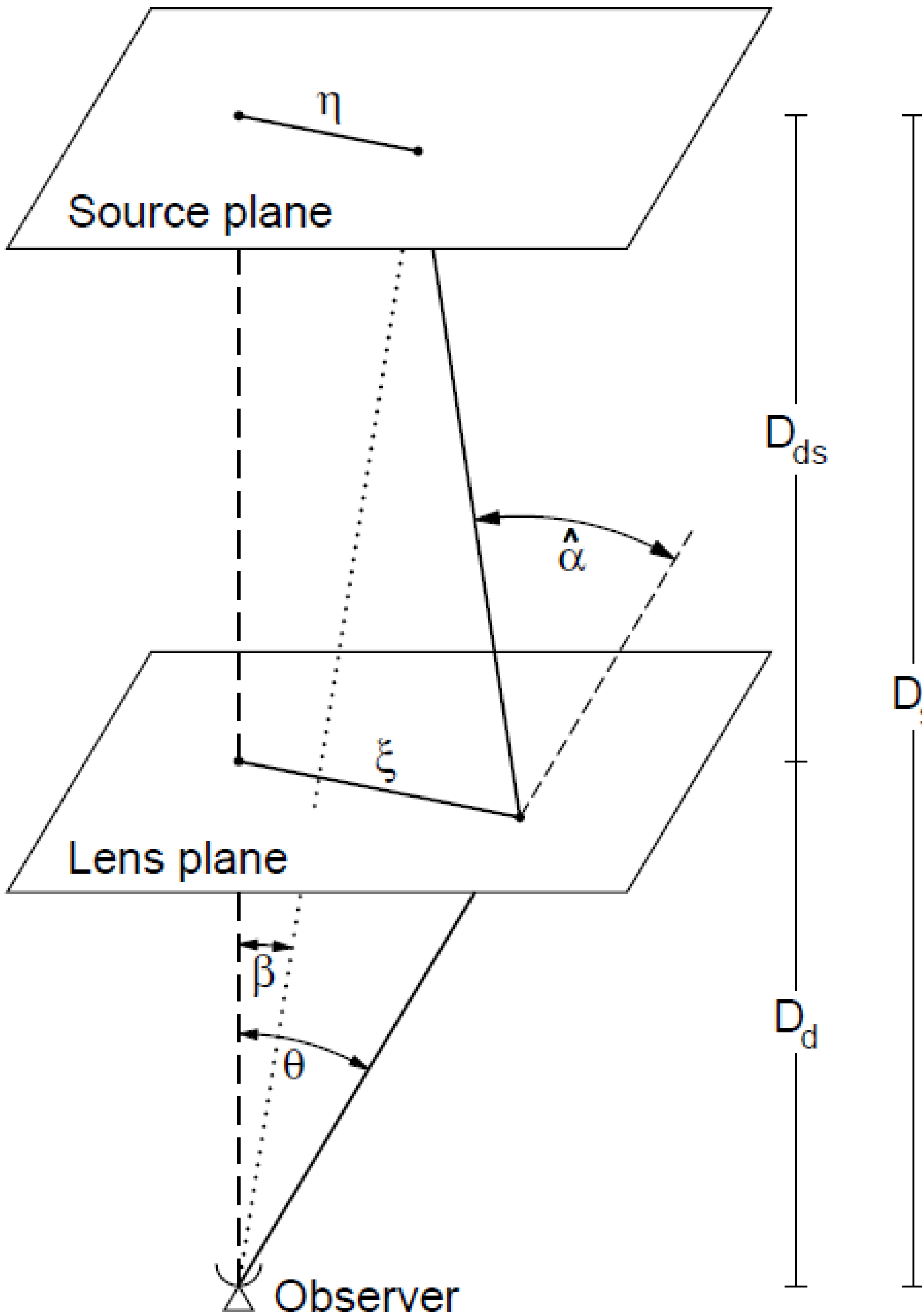

Figure 1.1: An illustration of Gravitational Lensing

where $\Sigma_c = \frac{c^2}{4\pi G}\frac{D_s}{D_d D_{ds}}$ is the critical surface mass density, the total scaled deflection angle, α is given by,

$$\alpha(\theta) = \frac{1}{\pi}\int d^2\theta' \kappa(\theta')\frac{\theta - \theta'}{|\theta - \theta'|^2} \tag{1.7}$$

Note that, $\kappa \geq 1$ for some Σ over the mass distribution is a sufficient condition to produce multiple images which leads to strong lensing. Hence, Σ_c is the parameter which defines the threshold for transition from strong lensing to weak lensing. We can write the deflection angle as a gradient of the deflection potential, Ψ which is a two-dimensional analogue of the Newtonian potential,

$$\Psi(\theta) = \frac{1}{\pi}\int d^2\theta' \log|\theta - \theta'| \tag{1.8}$$

This deflection potential satisfies the Poisson equation, $\nabla^2\Psi(\theta) = 2\kappa(\theta)$ and $\alpha = \nabla\Psi$.

For a source at angular position, β, the angular positions of the image, θ are provided by the solutions to the lens equation. If the source is much smaller than the angular scale over which the lens properties change, the mapping from source plane to the image plane can be described by a linearized Jacobian,

$$\frac{\partial\beta}{\partial\theta} = \begin{pmatrix} 1-\kappa-\gamma_1 & -\gamma_2 \\ -\gamma_2 & 1-\kappa+\gamma_1 \end{pmatrix} \tag{1.9}$$

where $\gamma = \gamma_1 + i\gamma_2 = |\gamma|e^{2i\phi}$ is the shear which describes the image distortion due to the tidal field. The observed ellipticity, ϵ of a galaxy is therefore given by

$$\epsilon = \epsilon_s + \gamma, \tag{1.10}$$

where the ϵ_s is the intrinsic ellipticity of the galaxy (I) and γ is the gravitational lensing shear distortion (G). For randomly oriented galaxies, $\langle\epsilon_s\rangle = 0$ which implies that $\langle\epsilon\rangle = \langle\gamma\rangle$. Due to the isotropy of the universe, the shear also vanishes when averaged over large patches of sky. Hence, to detect weak lensing effects, we need to measure two-point statistics described below.

Weak Lensing Power spectra

The convergence field can be expressed as a weighted projection of the linear matter density perturbations $\delta = \frac{\rho-\bar{\rho}}{\bar{\rho}}$ between the source and observer. At a given angular position, θ on the sky, and comoving horizon distance, χ_H, the convergence field is given by

$$\kappa(\theta) = \int_0^{\chi_H} d\chi W(\chi)\delta[\chi, \chi\theta] \tag{1.11}$$

For a normalized distribution of source galaxies, $p_s(\chi)$, $W(\chi)$ is the lensing weight function, defined as,

$$W(\chi) = \frac{3}{2}H_0^2 a^{-1}(\chi)\chi \int_{\chi}^{\chi_H} d\chi_s p_s(z) \frac{dz}{d\chi_s} \frac{\chi_s - \chi}{\chi_s} \tag{1.12}$$

Now, we can calculate the 2D convergence power spectrum in terms of the 3D matter power spectrum based on Limber's approximation [113, 88], where one assumes small angular separations (large l), given by

$$C(l) = \int_0^{\chi_H} d\chi \frac{W^2(\chi)}{\chi^2} P_\delta(k = \frac{l}{\chi}; \chi) \tag{1.13}$$

It is possible to split the galaxy sample into multiple redshift bins when the photometric redshift information is available and consider the auto or cross power spectra between different redshift slices. This technique is weak lensing tomography. The auto and cross power spectra are given by

$$C_{GG}^{ij}(l) = \int_0^{\chi_H} d\chi W_i(\chi) W_j(\chi) \chi^{-2} P_\delta(k = \frac{l}{\chi}; \chi), \tag{1.14}$$

where the lensing weight function, W_i is defined as

$$W_i(\chi) = \begin{cases} \frac{W_0}{\bar{n}_i} a^{-1}(\chi)\chi \int_{max(\chi,\chi_i)}^{\chi_{i+1}} d\chi_s p_s(z) \frac{dz}{d\chi_s} \frac{\chi_s - \chi}{\chi_s}, \chi \leq \chi_{i+1} \\ 0, \text{otherwise} \end{cases} \tag{1.15}$$

Here, $\bar{n}_i$ is the average number density of galaxies in the i^{th} tomographic bin.

1.2 Intrinsic Alignments

The measured weak lensing signal is contaminated by the contribution of the intrinsic shapes of galaxies whose correlations mimic that of lensing.

Consider the two-point correlation of the galaxy ellipticities at redshifts, i and j given by,

$$\langle \epsilon_i \epsilon_j \rangle = \langle \gamma_i \gamma_j \rangle + \langle \epsilon_i^s \epsilon_j^s \rangle + \langle \gamma_i \epsilon_j^s \rangle + \langle \epsilon_i^s \gamma_j \rangle \tag{1.16}$$

Here, the first term on the right hand side of the equation is referred to as the GG term, the second term is the II term and the final two terms correspond to the GI terms. If the intrinsic shapes of galaxies are randomly oriented, the II and GI terms are zero. However, galaxy shapes are correlated with each other and the large scale structure which leads to a non-zero II and GI contaminant to cosmic shear measurements. The II term arises due to the mutual alignment of galaxy shapes in close proximity [41, 66, 29]. The GI term is related to the gravitational shear - intrinsic correlation. The GI term arises due to the intrinsic alignment of a nearby galaxy with the tidal field which also lenses the source galaxy at a higher redshift [72]. In case of weak lensing tomography, the projected power spectra corresponding to the II and GI terms are given by,

$$C^{ij}_{II}(l) = \int_0^{\chi_H} d\chi \frac{p_{s,i}(\chi) p_{s,j}(\chi)}{\chi^2} P_{II}(\frac{l}{\chi}, \chi) \tag{1.17}$$

$$C^{ij}_{GI}(l) = \int_0^{\chi_H} d\chi \frac{p_{s,i}(\chi) W_j(\chi)}{\chi^2} P_{\delta I}(\frac{l}{\chi}, \chi), \tag{1.18}$$

Here, the power spectra, P_{II} and $P_{\delta I}$ quantify the correlation between the intrinsic shears and the correlation of intrinsic shear with the density field respectively. The analytical modeling of intrinsic alignment is aimed at quantifying the P_{II} and $P_{\delta I}$ signals in terms of the matter power spectrum. Modeling of intrinsic alignment signals is necessary in order to develop methods to mitigate IA signal from the weak lensing signal. Intrinsic alignment mitigation methods include nulling methods [83, 84] and methods in which free nuisance parameters of intrinsic alignment models are marginalized over, while simultaneously constraining cosmological parameters [24, 79, 18, 104]. Marginalizing requires a suitable parametrized model of the intrinsic alignment signal in terms of free parameters describing the amplitude, redshift, luminosity and scale dependence. To obtain unbiased cosmological constraints, accurate modeling of the intrinsic alignment signal to non-linear scales is needed. In the following section, a brief description of the intrinsic alignment models is provided.

1.2.1 Modeling of Intrinsic Alignments

The alignments of galaxies are generated by the interaction of galaxies with the gravitational fields. In general, analytical models describing the alignments fall into two major classes, namely, the linear and quadratic alignment models which describe the alignment of galaxies with the tidal field and the galaxy alignment with the tidal field due to tidal torquing respectively. For elliptical galaxies, the modeling is based on the linear alignment model, while the spiral galaxy alignments are described by the quadratic alignment models.

Linear Alignment Model

For elliptical galaxies, which are primarily supported by velocity dispersion and not rotation, we can assume that the orientation of the galaxy is aligned with the major axis of the tidal field. Here, it is physically reasonable to describe the alignment of an elliptical galaxy by the Linear alignment model [30, 77] which linearly relates the intrinsic shear to the tidal field, given by

$$\gamma^I = -\frac{C_1}{4\pi G}(\nabla_x^2 - \nabla_y^2, 2\nabla_x\nabla_y) S[\Psi_p] \tag{1.19}$$

where Ψ_p is the gravitational potential and S represents a filter that smooths off the fluctuations on halo scales. C_1 is a normalization constant which indicates the strength of alignment with the sign convention chosen such that a positive C_1 represents the alignment of the galaxy with the tidal field. In fourier space, the potential is related to the linear density field by

$$\Psi_P(\mathbf{k}) = -4\pi G \frac{\bar{\rho}(z)}{\bar{D}(z)} a^2 k^{-2} \delta_{lin}(\mathbf{k}) \tag{1.20}$$

From this, the shear-matter cross power spectrum can be written in terms of the matter power spectrum [77] as

$$P_{\delta I} = -\frac{C_1 \bar{\rho}}{\bar{D}} a^2 P_\delta \tag{1.21}$$

Quadratic Alignment Models

For disk galaxies, it can be assumed that the symmetric axis of the galactic disk aligns with the direction of the angular momentum of the host halo. The apparent ellipticity is then determined by the orientation of angular momentum. Under this assumption, the mean ellipticity vanishes to first order in the tidal field, while the second order contribution is given by [30, 39, 115],

$$\gamma^I = C_2(T_{xu}^2 - T_{yu}^2, 2T_{xu}T_{yu}), \tag{1.22}$$

with the tidal tensor,

$$T_{uv} = \frac{1}{4\pi G}(\nabla_u \nabla_v - \frac{1}{3}\delta_{uv}\nabla^2) S[\Psi_P] \tag{1.23}$$

In this model, the density-shear cross correlation vanishes for a linearly evolving gaussian density field [77].

1.3 Cosmological Simulations

Cosmological hydrodynamic simulations of galaxy formation include the physics of gravity, hydrodynamics and various feedback processes relevant for galaxy formation. The dynamics of the collisionless component (dark matter, stars in galaxies) is described by gravity while that of the gas component is described by gravity and hydrodynamics. In general, the numerical codes adopted to implement hydrodynamics are either the Lagrangian smoothed particle hydrodynamics (SPH) or the Eulerian mesh-based hydrodynamics. Additionally, various feedback processes involved in the galaxy formation are included as subgrid models. In particular, the MassiveBlack-II simulation[3] [93], which is studied in this thesis is implemented with SPH. The details of gravitational forces between the particles, hydrodynamics and feedback models in the MassiveBlack-II simulation are given below.

[3] http://mbii.phys.cmu.edu/

1.3.1 Gravity

The dynamics of the dark matter and star particles in the continuum limit, which can be approximated as a collisionless fluid is given by the collisionless boltzmann equation coupled to the Poisson equation in an expanding background described by the Friedman-Lemaitre model. These equations are solved by sampling the phase-space density with a finite number of tracer particles which evolve under self-gravity. For N particles with comoving coordinates x_i, corresponding canonical momenta, $p_i = a^2 m_i \dot{x}_i$, and interaction potential $\phi(x)$, the dynamics of the particles is described by the Hamiltonian,

$$H = \sum_i \frac{p_i^2}{2m_i a(t)^2} + \frac{1}{2}\sum_{ij} \frac{m_i m_j \phi(x_i - x_j)}{a(t)}, \tag{1.24}$$

In case of periodic boundary conditions, the interaction potential is the solution of the equation,

$$\nabla^2 \phi(x) = 4\pi G[\frac{1}{L^3} + \sum_n \hat{\delta}(x - nL)], \tag{1.25}$$

where, the sum is over all integer triplets and $\delta(\hat{x})$ is the single particle density distribution function. By defining the peculiar potential as $\phi(x) = \sum_i m_i \phi(x - x_i)$, we can express the dynamics of the system in terms of the peculiar potential as,

$$\nabla^2 \phi(x) = 4\pi G[\rho(x) - \bar{\rho}] \tag{1.26}$$

For N particles, the computational cost of force computation scales as N^2. So, Tree-PM method is adopted, where the peculiar potential is split in Fourier space as $\phi_k = \phi_k^{long} + \phi_k^{short}$, into long-range and short-range parts. The long range part of the potential is expressed in terms of spatial scale of the force split, r_s as,

$$\phi_k^{long} = \phi_k exp^{(-k^2 r_s^2)} \tag{1.27}$$

The long-range force is computed by mesh based fourier methods. The short range force is computed in real-space, where the potential in real space for $r_s << L$ is given by

$$\phi^{short}(x) = -G \sum_i \frac{m_i}{r_i} erfc(\frac{r_i}{2r_s}) \tag{1.28}$$

The above short range force is computed by the tree algorithm.

1.3.2 Hydrodynamics

For an inviscid ideal gas, the Lagrangian is given by

$$L = \int \rho(\frac{\mathbf{v}^2}{2} - u)dV, \tag{1.29}$$

where, ρ is the density, $\mathbf{v}$ is the velocity of the fluid and u is the thermal energy per unit mass.

From this, one can derive the Euler equations for gas dynamics representing the conservation of mass, momentum and energy which are given by

$$\frac{d\rho}{dt} + \rho\nabla.\mathbf{v} = 0 \tag{1.30}$$

$$\frac{d\mathbf{v}}{dt} + \frac{\nabla P}{\rho} = 0 \tag{1.31}$$

$$\frac{du}{dt} + \frac{P}{\rho}\nabla.\mathbf{v} = 0 \tag{1.32}$$

where, P represents the pressure.

Smoothed Particle Hydrodynamics (SPH) is a Lagrangian based technique adopted to solve the above equations of gas dynamics. The details of SPH are given in the section below.

1.3.3 Smoothed Particle Hydrodynamics (SPH)

In SPH, the continuous fluid quantities such as density, internal energy and entropy are defined by a kernel interpolation scheme using a set of discrete tracer particles which sample the gas in a Lagrangian sense. Consider N fluid elements, with positions, velocities, masses and thermal energy per unit mass denoted by $\mathbf{r}_i$, $\mathbf{v}_i$, m_i, u_i respectively. We can discretize the Lagrangian by,

$$L_{SPH} = \sum_i (\frac{1}{2} m_i \mathbf{v}_i^2 - m_i u_i) \tag{1.33}$$

Now, the density estimate in SPH at any given location, $\mathbf{r}$ is given by

$$\rho(\mathbf{r}) = \sum_i m_i W(|\mathbf{r} - \mathbf{r}_i|, h_i) \tag{1.34}$$

where, h_i is the smoothing length and $W(r,h)$ is given by

$$W(r,h) = \frac{8}{\pi h^3} \begin{cases} 1 - 6(\frac{r}{h})^2 + 6(\frac{r}{h})^3, & 0 \le \frac{r}{h} \le \frac{1}{2} \\ 2(1 - \frac{r}{h})^3, & \frac{1}{2} < \frac{r}{h} \le 1 \\ 0, & \frac{r}{h} > 1 \end{cases} \tag{1.35}$$

Here, the smoothing lengths h_i are defined such that for the estimated density, ρ_i the kernel volumes contain a constant mass with

$$\frac{4\pi}{3} h_i^3 \rho_i = N_{sph}\bar{m} \tag{1.36}$$

where, N_{sph} is the number of smoothing neighbors and $\bar{m}$ is the average mass of the particle.

The thermodynamic state of fluid element is described in terms of the entropy per unit mass and SPH manifestly conserves energy and entropy in the absence of shocks. For an entropy, A_i of each particle, the particle pressures are given by

$$P_i = A_i \rho_i^{\gamma} = (\gamma - 1)\rho_i u_i \tag{1.37}$$

From the discretized version of the Lagrangian, we can derive the SPH equations of motion, given by,

$$\frac{d\mathbf{v}_i}{dt} = -\sum_{i=1}^{N} m_i [f_i \frac{P_i}{\rho_i^2} \nabla_i W_{ij}(h_i) + f_j \frac{P_j}{\rho_j^2} \nabla_i W_{ij}(h_j)] \tag{1.38}$$

where, the coefficients, f_i are defined by,

$$f_i = (1 + \frac{h_i}{3\rho_i}\frac{\partial \rho_i}{\partial h_i})^{-1} \tag{1.39}$$

The gas dynamics described by the above equations can lead to discontinuities in the form of shocks under which the entropy of each particle is no longer constant. In order to capture these shocks, artificial viscosity is introduced with the viscous force given by,

$$\frac{d\mathbf{v}_i}{dt} = -\sum_{i=1}^{N} m_i \Pi_{ji} \nabla_i \bar{W}_{ij}, \tag{1.40}$$

where $\bar{W}_{ij} = \frac{W_{ij}(h_i) + W_{ij}(h_j)}{2}$ and Π_{ij} is a viscosity factor symmetric in i and j. This leads to the generation of entropy at the rate,

$$\frac{dA_i}{dt} = \frac{1}{2}\frac{\gamma - 1}{\rho_i^{\gamma - 1}} \sum_{j=1}^{N} m_j \Pi_{ij} v_{ij.} \nabla i \bar{W}_{ij} \tag{1.41}$$

1.3.4 Feedback Models

In addition to gravity and hydrodynamics, cosmological hydrodynamic simulations in general, also include models with the subgrid physics of galaxy formation. Here, considering the entropy formulation of SPH, the hydrodynamic force calculation is followed by updating particle velocities and the entropy is updated by accounting for feedback models. In MBII, the modeling of feedback processes is based on a multiphase ISM model described in [149]. In this model, a multiphase ISM consisting of cold clouds and hot ambient gas in equilibrium is assumed if local gas density is above a threshold density, ρ_{th} which is determined self-consistently based on the feedback parameters. Star formation proceeds by spawning individual star particles stochastically from the gas particles with density, $\rho > \rho_{th}$. The effective pressure, $P_{eff} = (\gamma - 1)(\rho_h \mu_h + \rho_c \mu_c)$, where ρ_c, ρ_h are the local densities of cold and hot phases respectively with gas density, $\rho = \rho_c + \rho_h$. μ_h, μ_c are the energy per unit mass of hot and cold components. The details of feedback models which include radiative cooling, star formation and supernova feedback, wind feedback and AGN feedback are described in the sections below. Throughout this discussion, it is to be noted that the variable, $f = 0$ for $\rho > \rho_{th}$ and $f = 1$ for $\rho < \rho_{th}$. .

1.3.5 Radiative Cooling

A thermal instability is assumed to exist between the cold phase and the hot phase. The radiative energy loss by the hot gas leads to a growth in the fraction of cold phase.
For multiphase ISM, rate of mass flux is

$$\frac{d\rho_c}{dt} = -\frac{d\rho_h}{dt} = \frac{1-f}{\mu_h - \mu_c}\Lambda_{net}(\rho_h, \mu_h) \tag{1.42}$$

Rate of energy budget of hot and cold components is given by,

$$\frac{d}{dt}(\rho_c \mu_c) = \frac{(1-f)\mu_c}{\mu_h - \mu_c}\Lambda_{net} \tag{1.43}$$

$$\frac{d}{dt}(\rho_h \mu_h) = -\frac{\mu_h - f\mu_c}{\mu_h - \mu_c}\Lambda_{net} \tag{1.44}$$

Here, Λ_{net} is the cooling function based on radiative processes for a primordial plasma of H and He [90] under ionization equilibrium in presence of UV background with reionization at $z = 6$.

1.3.6 Star formation and Supernova Feedback

Star formation converts the cold clouds into stars on a characteristic time scale, t_*. The rate of star formation is given by

$$\frac{d\rho_*}{dt} = \frac{\rho_c}{t_*} - \beta\frac{\rho_c}{t_*} \tag{1.45}$$

where, $\beta = 0.1$ is the mass fraction of short lived stars (supernova feedback) and t_* is the star formation time scale with density dependence given by,

$$t_*(\rho) = t_0^*(\frac{\rho}{\rho_{th}})^{-0.5} \tag{1.46}$$

with $t_0^* = 2.1$Gyr

Numerically, for a given time step, Δt, a star particle is spawned probabilistically if a random number uniformly distributed in $[0, 1]$ is below p_* given by,

$$p_* = \frac{m}{m_*} 1 - \exp\left[-\frac{\eta(1-\beta)x\Delta t}{t_*}\right] \tag{1.47}$$

where $m_* = \frac{m_0}{N_g}$ with N_g denoting the number of generations of stars and m, the mass of gas particle is reduced by m_*. Here $N_g = 2$ and only 2 generation of stars are feasible.

Rate of mass flux :

$$\frac{d\rho_c}{dt} = -\frac{\rho_c}{t_*} - A\beta\frac{\rho_c}{t_*} \tag{1.48}$$

$$\frac{d\rho_h}{dt} = \beta\frac{\rho_c}{t_*} + A\beta\frac{\rho_c}{t_*} \tag{1.49}$$

where A is the evaporation efficiency turning cold clouds into hot ambient gas with

$$A(\rho) = A_0\left(\frac{\rho}{\rho_{th}}\right)^{-4/5} \tag{1.50}$$

with $A_0 = 1000$. Here, it is assumed that the feedback energy from the supernovae hats the ambient hot phase.

Rate of energy budget of hot and cold components is given by,

$$\frac{d}{dt}(\rho_c\mu_c) = -\frac{\rho_c}{t_*}\mu_c - A\beta\frac{\rho_c}{t_*}\mu_c \tag{1.51}$$

$$\frac{d}{dt}(\rho_h\mu_h) = \beta\frac{\rho_c}{t_*}(\mu_{SN} + \mu_c) + A\beta\frac{\rho_c}{t_*}\mu_c \tag{1.52}$$

Here, μ_{SN} corresponds to the equivalent supernova temperature, $\mu_{SN} = \frac{3}{2}kT_{SN}$ for $T_{SN} = 10^8K$

1.3.7 Wind Feedback

Wind feedback is implemented, where it is assumed that there is no dependence on the halo mass and the wind velocity is given by ($\chi = 0.25$, $\eta = 2$),

$$v_w = \sqrt{\frac{2\beta\chi\mu_{SN}}{\eta(1-\beta)}} \tag{1.53}$$

v_w is calculated to be equal to $483.61kms^{-1}$. For a given time step, Δt, a gas particle is added to the wind probabilistically if a random number uniformly distributed in $[0, 1]$ is below p_w given by,

$$p_w = 1 - \exp\left[-\frac{\eta(1-\beta)x\Delta t}{t_*}\right] \tag{1.54}$$

The wind velocity is added to the gas particle velocity with direction chosen as isotropic or axial wind,

$$v^1 = v + v_w \mathbf{n} \tag{1.55}$$

1.3.8 AGN Feedback

Black holes are treated as collisionless particles introduced into halos of mass greater than $5.0 \times 10^{10} h^{-1} M_\odot$ at regular intervals of time separated by $\Delta \log(a) = \log(1.25)$. The densest particle is converted into a seed black hole of mass $M_{\rm BH,seed} = 5 \times 10^5 h^{-1} M_\odot$ which grows in mass by black hole accretion and mergers.
The black hole accretion rate is given by,

$$\dot{M}_{BH} = \frac{4\pi G^2 M_{\rm BH}^2 \rho}{(c_s^2 + v_{\rm BH}^2)^{3/2}} \tag{1.56}$$

where, ρ is the local gas density, c_s is the local sound speed, v is the velocity of BH relative to the gas and the accretion rate is limited to 3 times the eddington rate, $\dot{M}_{\rm Edd}$.

The AGN feedback is modeled by coupling 5% (chosen to match the slope in observed $M_{\rm BH} - \sigma$ relation [147]) of the bolometric luminosity radiated from the BH given by,

$$L_{\rm bol} = \epsilon_r \dot{M}_{\rm BH} c^2 \tag{1.57}$$

with the radiation efficiency, $\epsilon_r = 0.1$. The energy is deposited isotropically to the 64 nearest gas particles within the BH kernel.

1.4 Thesis Overview

1.4.1 Motivation

The intrinsic alignment of galaxies is an important systematic in weak lensing measurements that can bias the cosmological parameter constraints in future surveys. Further, it also provides information about the galaxy formation and evolution. So, we need to develop models to mitigate the contamination due to intrinsic alignments. However, analytical modeling of intrinsic alignmnet power spectra is difficult and N-body simulations are not sufficient to study the galaxy alignments due to the absence of baryonic physics. Recent advancements have led to the feasibility of performing high resolution, large volume cosmological hydrodynamic simulations such as MassiveBlack-II which include galaxy formation and properties such as stellar mass function are in reasonable agreement with observational measurements. This thesis is motivated by the availability of a large statistical sample of galaxies in this simulation for studying the galaxy alignments and understand the effects of baryonic feedback.

We can directly measure the shapes, alignments of the stellar component of the galaxies and their correlation with the large scale density field. Further, the dependence of the two-point statistics based on mass, luminosity, color and morphological type of the galaxies can also be explored.

1.4.2 Thesis plan

In this thesis, we present the distributions of the galaxy shapes in the MassiveBlack-II simulation and their alignments based on mass in Chapter 2. We investigative different methods of calculating shapes followed by the analysis of two-point statistics of shapes quantifying intrinsic alignments in Chapter 3. We also investigate the dependence on mass, luminosity and color in this chapter. In Chapter 4, we use a dark matter-only simulation performed with the same volume, resolution and initial conditions as the original MBII hydrodynamic simulation to compare the galaxy shapes in the hydrodynamic simulation with that of subhalo shapes in dark matter-only simulation. In Chapter 5, we compare the intrinsic alignments of disks and elliptical galaxies in MBII and Illustris simulations. Finally, in Chapter 6, we study the impact of modifying free parameters in the feedback models of MBII on the intrinsic alignments of galaxies. The conclusions and future directions are given in Chapter 7.

The works in Chapters 2, 3, 4 and 5 have been published in peer reviewed journals [156, 158, 157, 155]. The work in Chapter 6 has been submitted to a journal and is currently under review [154].

Chapter 2

Galaxy shapes and alignments

Weak gravitational lensing is a useful probe to constrain cosmological parameters since it is sensitive to both luminous and dark matter [11, 13, 74, 75, 77, 152]. In particular, weak lensing surveys can be used to probe theories of modified gravity and provide constraints on the properties of dark matter and dark energy [4, 174]. Many upcoming surveys like LSST and Euclid aim to determine the constant and dynamical parameters of the dark energy equation of state to a very high precision using weak lensing.

However, constraining cosmological parameters with sub-percent errors in future cosmological survey requires the systematic errors to be well below those in typical weak lensing measurements with current datasets. The intrinsic alignment (IA) of galaxy shapes with the underlying density field is an important theoretical uncertainty that contaminates weak lensing measurements [66, 41, 78, 72]. Accurate theoretical predictions of IA through analytical models and N-body simulations [72, 68, 137, 86] in the ΛCDM paradigm is complicated by the absence of baryonic physics, which we expect to be important given that the alignment of interest is that of the observed, baryonic component of galaxies. So, we either need simulations that include the physics of galaxy formation or N-body simulations with rules for galaxy shapes and alignments.

Proposed analysis methods to remove IA from weak lensing measurements either involve removing a fair amount of cosmological information (and require very accurate redshift information; nulling methods: [83, 84]), or involve marginalizing over parametrized models of how the intrinsic alignments affect observations as a function of scale, redshift and galaxy type e.g., [24, 79, 18]. The simultaneous fitting method, with a relatively simple intrinsic alignments model, was used for a tomographic cosmic shear analysis of CFHTLenS data [67]. The latter methods, while preserving more cosmological information than nulling methods, can only work correctly if there is a well-motivated intrinsic alignments model as a function of galaxy properties. Existing candidates for the intrinsic alignment model to be used in such an approach include the linear alignment model [72] or simple modifications of it (e.g., using the nonlinear power spectrum: [24]), N-body simulations populated with galaxies and stochastically misaligned with halos in a way that depends on galaxy type [68], and the halo model [137], which includes rules for how central and satellite galaxies are intrinsically aligned.

In this study, we use the large volume, high-resolution hydrodynamic simulation, MassiveBlack-II [94], which includes a range of baryonic processes to directly study the shapes and alignments of galaxies. In particular, we measure directly the shapes of the dark and stellar matter components of halos and subhalos (modeled as ellipsoids in three dimensional space). We examine how shapes evolve with time and as a function of halo/subhalo mass. Previous work used N-body simulations and analytical modeling to study triaxial shape distributions of dark matter halos as a function of mass and their evolution with redshift [73, 5, 107, 139]. More recently, hydrodynamic cosmological simulations have also been used to study the effects of baryonic physics on the shapes of dark matter halos [92, 8, 99, 26]. Here, using a high-resolution hydrodynamic simulation in a large cosmological volume that incorporates the physics of star formation and associated feedback as well as black hole accretion and AGN feedback, we focus on measuring directly the shapes of the stellar components of galaxies and examine the misalignments between stars and dark matter in galaxies (central and satellite). We also measure the projected (2D) shapes for comparison with observations. This study is important because the measured intrinsic alignments of galaxies are related to the projected shape correlations of the stellar component of subgroups (galaxies) by the density-ellipticity and ellipticity-ellipticity correlations [68]. By measuring the projected ellipticities of the stellar and dark matter component of simulated galaxies, we can attempt to understand the differences between these two. In addition, we can do a basic comparison of the stellar components with observational results, and validate the realism of the simulated galaxy population.

Another aspect of the problem that we consider in this paper is the relative orientation of the stellar component of the halo with its dark matter component. Many dark matter-only simulations have illustrated that dark matter halos exhibit large-scale intrinsic alignments e.g.[54, 73, 6, 68], but the prediction of galaxy intrinsic alignments from halo intrinsic alignments requires a statistical understanding of the relationship between galaxy and halo shapes. To date, there has been no direct measurement of galaxy versus halo misalignment with a large statistical sample of galaxies through hydrodynamic simulations. Recently, [50] studied the alignment between the spin of galaxies and their host filament direction using a hydrodynamical cosmological simulation of box size $100h^{-1}$Mpc. Studies of misalignment based on SPH simulations of smaller volumes detected misalignments between the baryonic and dark matter component of halos [140, 163, 64, 44]. These studies considered the correlation of spin and angular momentum of the baryonic component with dark matter. The spin correlations are arguably more relevant for the intrinsic alignments of spiral galaxies [72], whereas the observed intrinsic alignments in real galaxy samples are dominated by red, pressure-supported, elliptical galaxies [116, 81]; hence a study of the correlation of projected shapes is more relevant for the issue of weak lensing contamination. However, to make precise predictions based on the halo or subhalo mass at different redshifts, we need a hydrodynamic simulation of very large volume and high resolution. The MassiveBlack-II SPH simulation meets those requirements, making it a good choice for this kind of study.

Others arrived at constraints on misalignments using N-body simulations and calibrating the misalignments by adopting a simple parametric form to agree with observationally detected shape correlation functions [56, 122]. There are also studies of the alignment of a central galaxy with its host halo where it is assumed that the satellites trace the dark matter distribution [**?**, e.g.,]]2008MNRAS.385.1511W. By using hydrodynamic simulations, we can directly calculate the misalignment distributions for all galaxies as a function of halo mass and cosmic time. Resolution of the galaxies into centrals and satellites also helps to understand the effect of local environment.

This paper is organized as follows. In Section 6.3, we describe the SPH simulations used for this work and the methods used to obtain the shapes and orientations of groups and subgroups. In Section 2.2, we give the axis ratio distributions of dark matter and stellar matter of subgroups. In Section 2.3, we show our results for misalignments of the stellar component of subgroups with their host dark matter subgroups. In Section 2.4 we compare the shape distributions and misalignment angle between centrals and satellites. Finally, we summarize our conclusions in Section 6.6. The functional forms for our results are provided in the Appendix.

2.1 Methods

2.1.1 MassiveBlack-II Simulation

We use the MassiveBlack-II (MBII) simulation to measure shapes and alignments of dark matter and stellar components of halos and subhalos. MBII is a state-of-the-art high resolution, large volume, cosmological hydrodynamic simulation of structure formation. An extensive description of the simulation and major predictions for the halo and subhalo mass functions, their clustering, the galaxy stellar mass functions, galaxy spectral energy distribution and properties of the AGN population is presented by [94]. We refer the reader to this publication for details on MBII and briefly summarize the major relevant aspects here.

The MBII simulation was performed with the cosmological TreePM-Smooth Particle Hydrodynamics (SPH) code P-GADGET. It is a hybrid version of the parallel code, GADGET2 [147] that has been upgraded to run on Petaflop scale supercomputers. In addition to gravity and SPH, the P-GADGET code also includes the physics of multi-phase ISM model with star formation [149], black hole accretion and feedback [147, 45]. Radiative cooling and heating processes are included [90], as is photoheating due to an imposed ionizing UV background. The interstellar medium (ISM), star

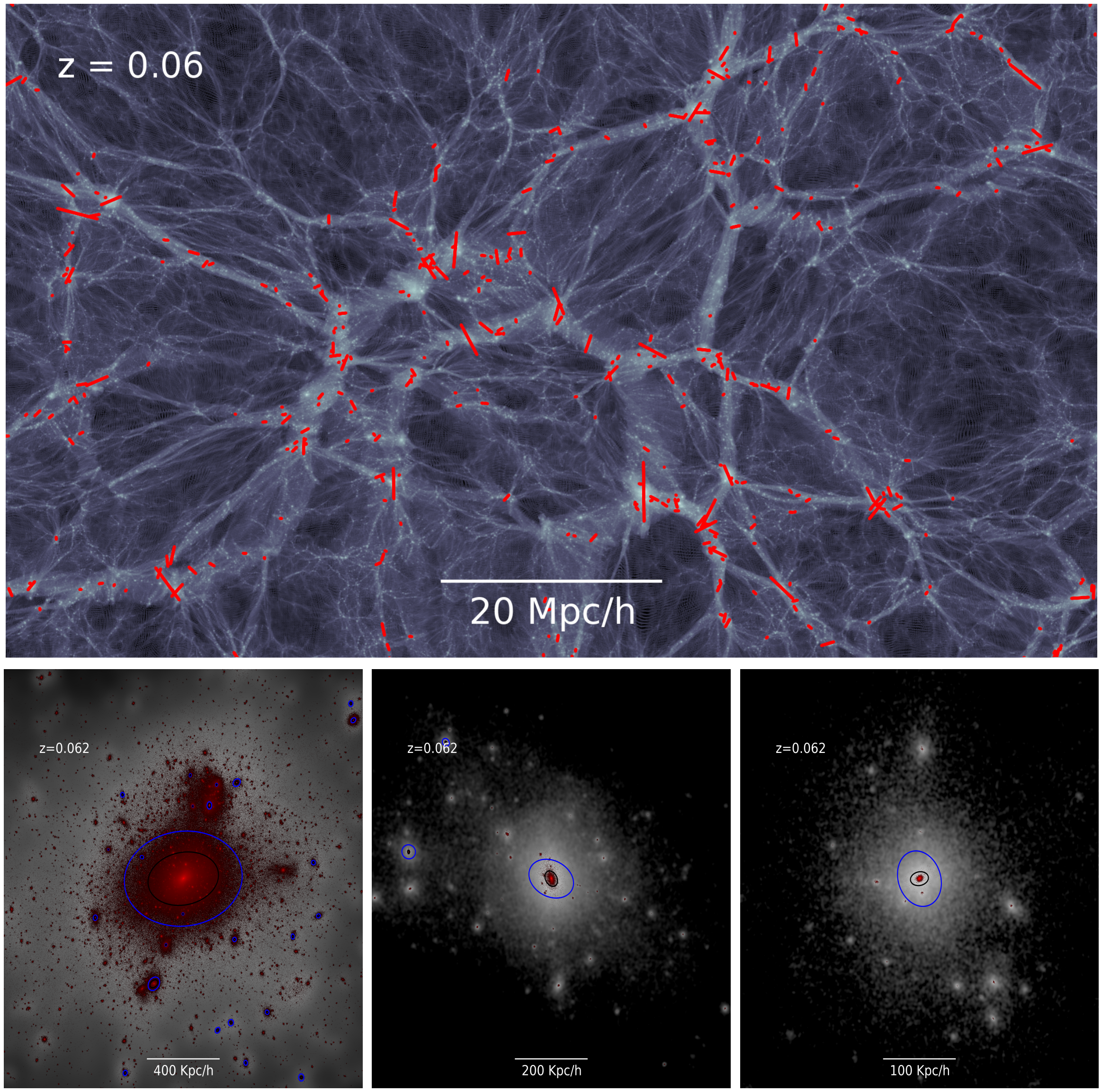

Figure 2.1: *Top:* Snapshot of the MBII simulation in a slice of thickness $2h^{-1}$Mpc at redshift $z = 0.06$. The bluish-white colored region represents the density of the dark matter distribution and the red lines show the direction of the major axis of ellipse for the projected shape defined by the stellar component. *Bottom Left:* Dark matter (shown in gray) and stellar matter (shown in red) distribution in the most massive group at $z = 0.06$ of mass $7.2 \times 10^{14} h^{-1} M_\odot$. The blue and red ellipses show the projected shapes of dark matter and stellar matter of subhalos respectively. *Bottom Middle:* Dark matter and stellar matter distribution in a group of mass $3.8 \times 10^{12} h^{-1} M_\odot$. *Bottom Right:* Dark matter and stellar matter distribution in a group of mass $1.1 \times 10^{12} h^{-1} M_\odot$.

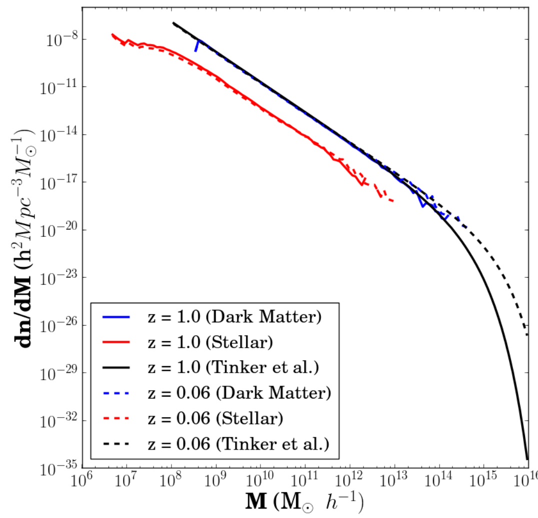

Figure 2.2: Dark matter and stellar mass function for FOF groups (halos) at $z = 0.06, 1.0$, compared with the SO-based prediction from [159] generated with $\Delta = 0.75$.

formation and supernovae feedback as well as black hole accretion and associated feedback are treated by means of previously developed sub-resolution models. In particular, the multiphase model for star forming gas we use, developed by [150], has two principal ingredients: (1) a star formation prescription and (2) an effective equation of state (EOS). A thermal instability is assumed to operate above a critical density threshold $\rho_{\rm th}$, producing a two phase medium consisting of cold clouds embedded in a tenuous gas at pressure equilibrium. Stars form from the cold clouds, and short-lived stars supply an energy of 10^{51} ergs to the surrounding gas as supernovae. This energy heats the diffuse phase of the ISM and evaporates cold clouds, thereby establishing a self-regulation cycle for star formation. $\rho_{\rm th}$ is determined self-consistently in the model by requiring that the EOS is continuous at the onset of star formation. Stellar feedback in the form of stellar winds is also included. The prescription for black hole accretion and associated feedback from massive black holes follows the one developed by [46, 148]. We represent black holes by collisionless particles that grow in mass by accreting gas (at the local dynamical timescale) from their environments. If the accretion rates reach the critical Eddington limit they are then capped at that value. A fraction f (fixed to 5% to fit the local black-hole galaxy relations) of the radiative energy released by the accreted material is assumed to couple thermally to nearby gas and influence its thermodynamic state. Black holes merge when they approach the spatial resolution limit of the simulation [150]

MBII contains $N_{\rm part} = 2 \times 1792^3$ dark matter and gas particles in a cubic periodic box of length $100h^{-1}$Mpc on a side, with a gravitational smoothing length

$\epsilon = 1.85h^{-1}$kpc in comoving units. A single dark matter particle has a mass $m_{DM} = 1.1 \times 10^7 h^{-1} M_\odot$ and the initial mass of a gas particle is $m_{gas} = 2.2 \times 10^6 h^{-1} M_\odot$. The cosmological parameters used in the simulation are as follows: amplitude of matter fluctuations $\sigma_8 = 0.816$, spectral index $\eta_s = 0.96$, mass density parameter $\Omega_m = 0.275$, cosmological constant density parameter $\Omega_\Lambda = 0.725$, baryon density parameter $\Omega_b = 0.046$, and Hubble parameter $h = 0.702$ as per WMAP7 [102].

Fig. 2.1 shows a few snapshots of the MBII simulation with dark matter and stellar matter distributions at redshift $z = 0.06$. From the top figure, we can see the formation of cosmic web with galaxies extending over the whole length of the simulation volume. The figures in the bottom panel, which are zoomed snapshots of individual halos of different masses, show the density distribution of dark matter and stellar matter.

To generate group catalogs of particles in the simulation, we used the friends of friends (FoF) group finder algorithm [43]. This algorithm identifies groups on the fly using linking length of 0.2 times the mean interparticle separation. The mass of a halo is equal to the sum of masses of all particles in the group. Fig. 2.2 shows the dark matter and stellar mass functions for groups at redshifts $z = 1.0$ and $z = 0.06$. We find good agreement with the theoretical prediction given in [159] based on Spherical Overdensity (SO) approach. This gives an idea of the mass range we are exploring by the use of this simulation. To generate subgroup catalogs, the SUBFIND code [151] is used on the group catalogs. The subgroups are defined as locally overdense, self-bound particle groups. Groups of particles are defined as subgroups when they have at least 20 gravitationally bound particles. A comparison between the properties of halos and subhalos recovered using different halo and subhalo finders can be found in [98], where it is concluded that the properties of halos and subhalos, like mass, position, velocity, two-point correlation returned by different finders agree within error bars to each other. In all the discussions in this paper, halos and subhalos are interchangeable for groups and subgroups respectively.

2.1.2 Determination of 3D and 2D shapes

Here we describe the method adopted to determine the shapes and orientations of groups and subgroups for dark matter and stellar components. For each group and subgroup, the dark matter and stellar shapes are determined by using the positions of dark matter and star particles respectively. By using the positions of all particles of the corresponding type, the halo and subhalo shapes in 3D are modelled as ellipsoids. For projected shapes, the positions of particles of corresponding type projected onto the XY plane are used to model the shapes as ellipses. We use the unweighted inertia tensor given by

$$I_{ij} = \frac{\sum_n m_n x_{ni} x_{nj}}{\sum_n m_n}, \tag{2.1}$$

where m_n represents the mass of the n^{th} particle and x_{ni}, x_{nj} represent the position coordinates of the n^{th} particle with $0 \leq i, j \leq 2$ for 3D and $0 \leq i, j \leq 1$ for 2D. It is to be noted that in this simulation, all particles of the given type (either dark matter or star particle) have the same mass. Hence the mass of a particle has no effect on the inertia tensor. The inertia tensor can also be defined by weighting the positions of particles by their luminosity instead of mass. [139] used the definition of reduced inertia tensor and investigated the radial dependance of halo shapes in the N-body simulation by considering only particles within a given fraction of the virial radius. In this paper, we are only concerned with the standard unweighted inertia tensor definition for determining shapes and defer investigation of other definitions for a future study.

Consider the 3D case. Let the eigenvectors of the inertia tensor be $\hat{e}_a, \hat{e}_b, \hat{e}_c$ and the corresponding eigenvalues be $\lambda_a, \lambda_b, \lambda_c$, where $\lambda_a > \lambda_b > \lambda_c$. The eigenvectors represent the principal axes of the ellipsoids with the lengths of the principal axes (a, b, c) given by the square roots of the eigenvalues $(\sqrt{\lambda_a}, \sqrt{\lambda_b}, \sqrt{\lambda_c})$. We now define the 3D axis ratios as

$$q = \frac{b}{a}, \; s = \frac{c}{a} \tag{2.2}$$

In 2D, the eigenvectors are $\hat{e}'_a, \hat{e}'_b$ with the corresponding eigenvalues λ'_a, λ'_b, where $\lambda'_a > \lambda'_b$. The lengths of major and minor axes are $a' = \sqrt{\lambda'_a}$, $b' = \sqrt{\lambda'_b}$ with axis ratio, $q' = b'/a'$ as defined before.

Our predictions from SPH simulations can be compared with those from N-body simulations using the full 3D shapes, while the projected shapes are useful for comparison with results from observational data. In all our results, we used groups and subgroups with a minimum of 1000 dark matter and star particles each. We describe the convergence tests performed to arrive at this cutoff in Section 2.1.3.

2.1.3 Convergence tests on axis ratios

The reliability of statements about the shapes of matter distributions depends on the number of particles used to trace those distributions. Thus, we made a convergence test to fix the minumum number of particles needed to measure shapes of halos and subhalos reliably. In Fig. 2.3, we show the histograms of shapes measured using all the dark matter particles in a given subhalo, and compared it with the histograms obtained by using a random subsample of 50, 300, 500 and 1000 particles in the subhalo. This is done in a mass range where we have enough subhalos with > 1000 particles. The plots show that using a random subsample of 1000 particles, we have a good convergence with the shapes determined using all particles. The mean axis ratio, $\langle q \rangle$ is 0.83 and $\langle s \rangle$ is 0.70 using all particles. $\langle q \rangle$ varies as $0.77, 0.82, 0.82, 0.83, 0.83$ using $50, 300, 500, 1000$ particles respectively. The corresponding values for $\langle s \rangle$ are $0.60, 0.68, 0.69, 0.70, 0.70$. Although the mean axis ratios show good convergence with 300 or 500 particles, from the plots we can see that the histograms have not converged.

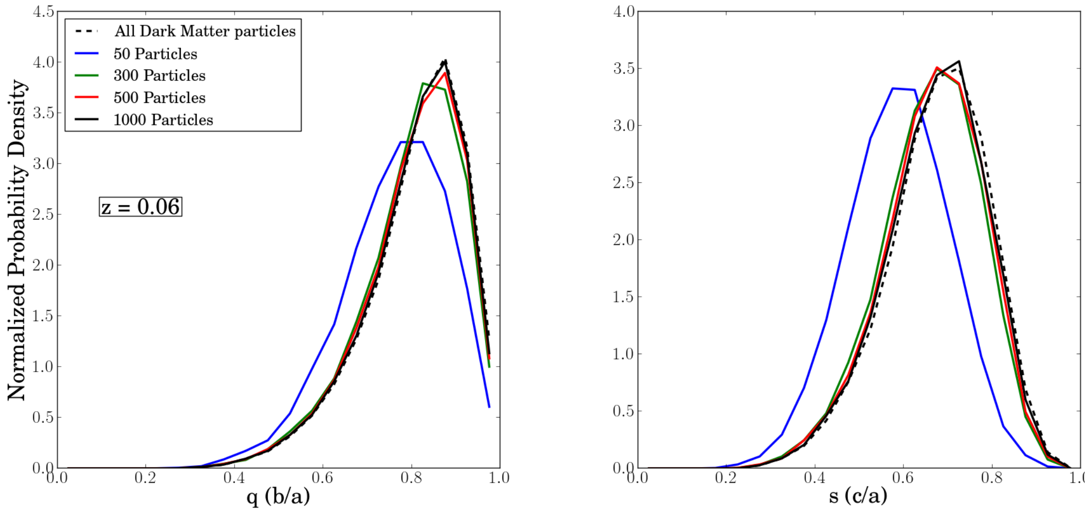

Figure 2.3: Normalized histograms of axis ratios at $z = 0.06$ showing a comparison between shapes determined by using all particles in the subhalo with those obtained using a random subsample of 50, 300, 500 and 1000 particles in the subhalo. *Left:* q (b/a); *Right:* s (c/a).

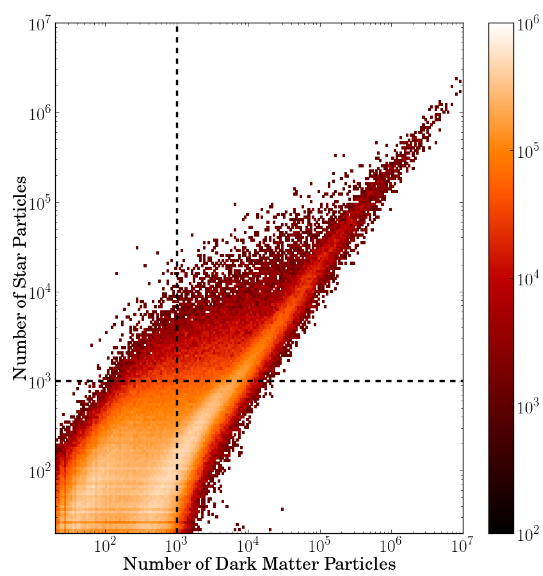

Figure 2.4: Distribution of the number of dark matter and star particles in subgroups at $z = 0.06$, where the colorbar indicates the number density of subhalos.

Hence, we choose a minimum of 1000 particles for our analysis. In Figure 2.4, we show a contour plot of the number of dark matter particles and star particles in subgroups at $z = 0.06$. The two different density peaks in the contour plot are due to different dark matter to stellar mass ratios in centrals and satellite subgroups. The right density peak corresponds to central subhalos while the left one is for satellite subgroups, which exhibit stripping of the dark matter subhalo and hence fewer dark matter particles. The lines show a cutoff of 1000 particles for dark matter and star particles. By choosing this cutoff, we are excluding subhalos of low stellar to halo mass ratio in subhalos around the low mass range $10^{10} - 10^{11.5} h^{-1} M_\odot$. So in this mass range, we are excluding a significant fraction of subhalos with low stellar mass from our analysis. However, in the high mass range, we are able to analyze a fair sample of subhalos.

2.2 Shapes of dark matter and stellar matter of subgroups

In this section, we show the axis ratio distributions of the shapes of dark matter and stellar matter component of halos and subhalos modeled as ellipsoids as described in Section 2.1.2. We investigate their dependence on the mass range of subgroups and their evolution with redshift. We also compare the relative axis ratio distributions of dark matter and stellar matter in subhalos.

2.2.1 3D axis ratio distributuions

The distributions of axis ratios, q (b/a) and s (c/a) for dark matter and stellar matter of subgroups at redshift $z = 0.06$ for different mass bins are shown in Figure 2.5. The plot shows that the axis ratios are larger for dark matter when compared to stellar matter, indicating that the dark matter component of a subgroup is more round than the stellar matter. Also, we observe that there is no significant evolution in the distribution of axis ratios in adjacent panels. We henceforth present our results in three mass bins : $10^{10.0} - 10^{11.5} h^{-1} M_\odot$, $10^{11.5} - 10^{13.0} h^{-1} M_\odot$, and $> 10^{13.0} h^{-1} M_\odot$. For convenience, we refer to these mass bins as $M1, M2$ and $M3$ respectively. In the mass bin $M3$, the largest subhalo mass is $1.4 \times 10^{14} h^{-1} M_\odot$ at $z = 1.0$, with a host halo mass of $1.6 \times 10^{14} h^{-1} M_\odot$; it grows to $6.0 \times 10^{14} h^{-1} M_\odot$ at $z = 0.06$ with a host halo mass of $7.2 \times 10^{14} h^{-1} M_\odot$.

2.2.2 Redshift evolution and mass dependence of 3D axis ratios

In Figure 2.6, we compare the distribution of axis ratios for groups and subgroups at redshift $z = 0.3$ in different mass bins. Here, we consider the dark matter component

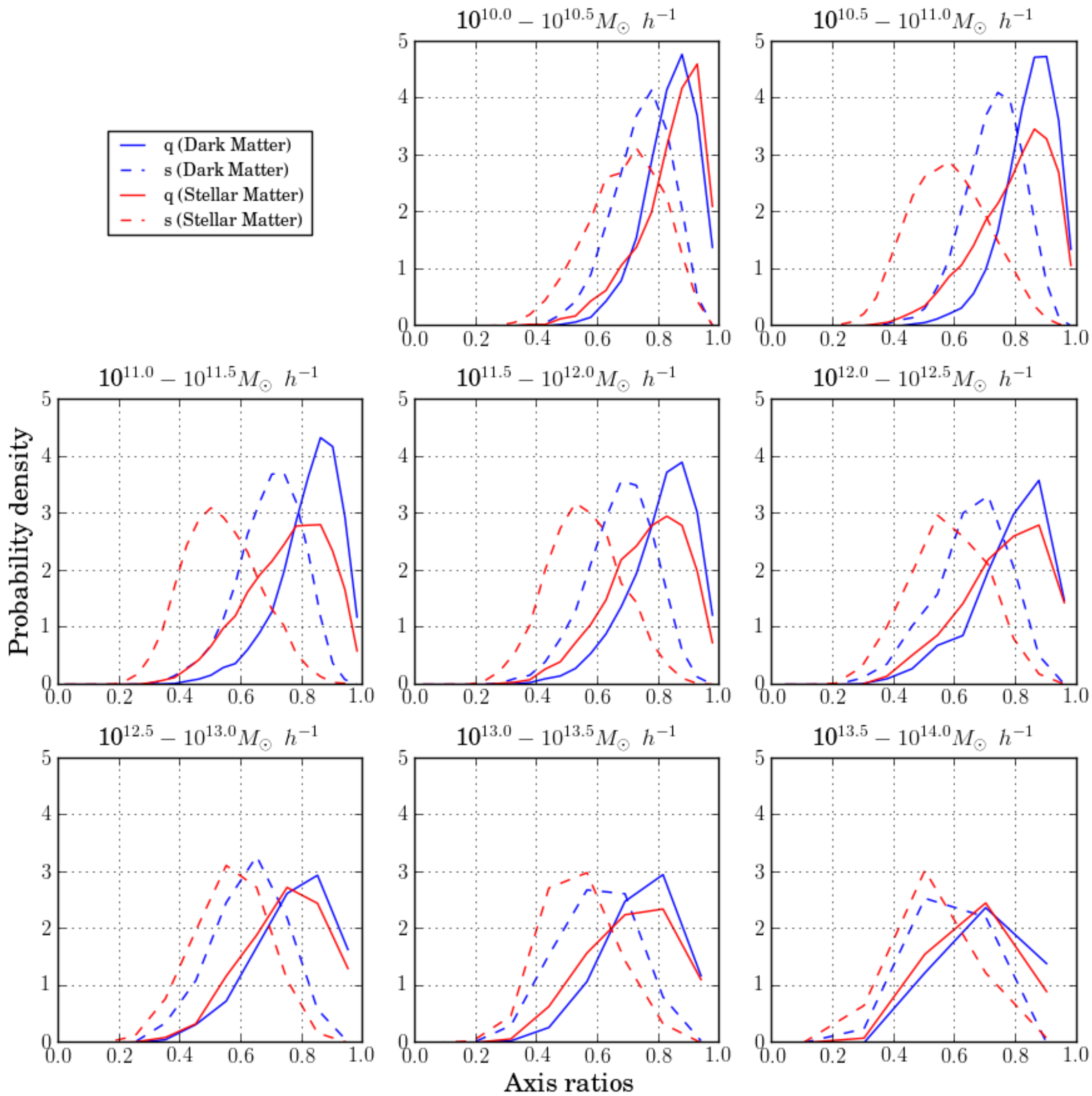

Figure 2.5: 3d axis ratio distributions of dark matter and stellar matter in subhalos at $z = 0.06$, for masses of subhaloes in the range $10^{10.0} - 10^{14.0} h^{-1} M_\odot$.

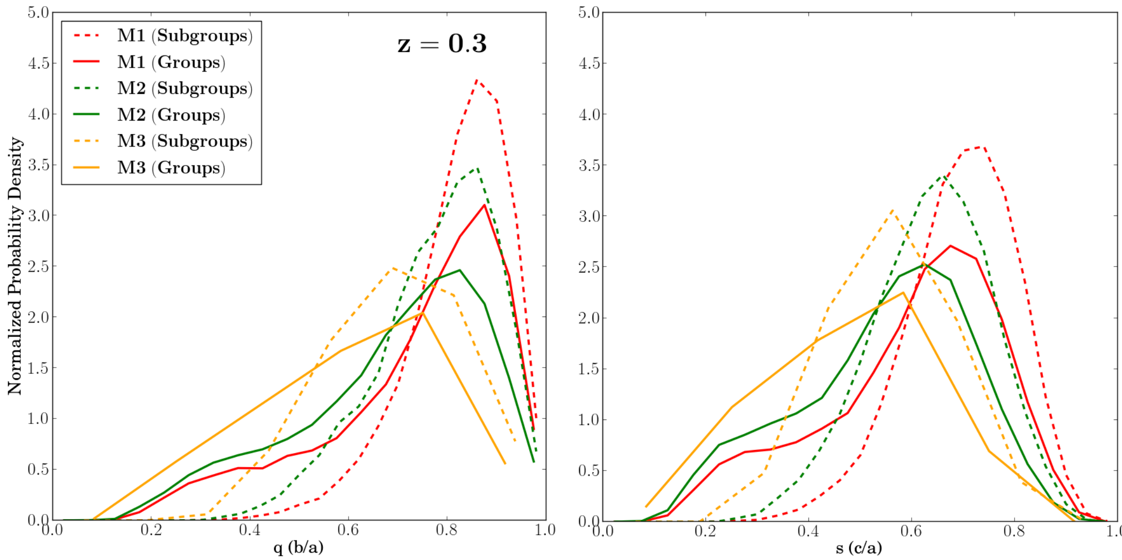

Figure 2.6: Comparison of axis ratios, q (b/a) (left panel) and s (c/a) (right panel) between dark matter subgroups and groups at $z = 0.3$ in different mass bins.

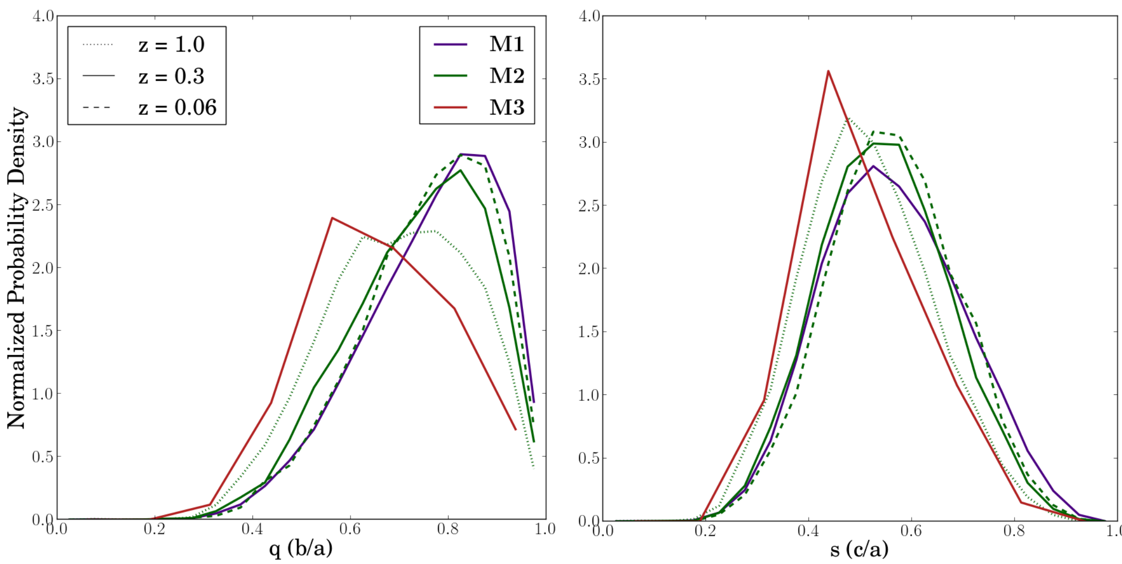

Figure 2.7: Axis ratios q (b/a) (left panel) and s (c/a) (right panel) for stellar matter of subhalos at $z = 0.3$ in mass bins ($M1, M2$ and $M3$) and at $z = 1.0, 0.06$ for the central mass bin, $M2$.

of groups and subgroups only. From the plot, we can see that for groups, as we go to higher masses, the axis ratios decrease for both groups and subgroups. Comparing

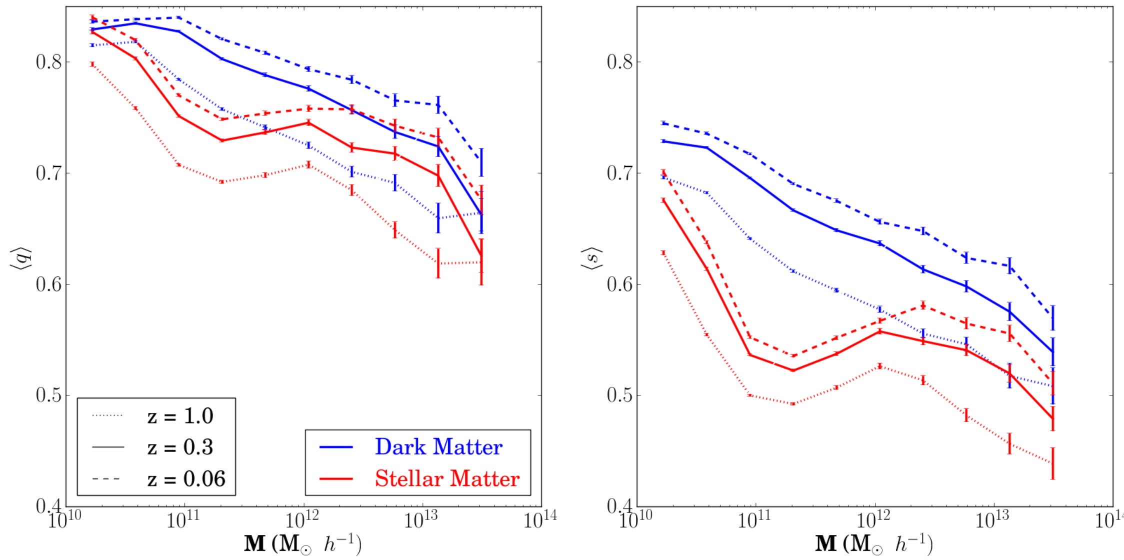

Figure 2.8: Average axis ratios, $\langle q \rangle$ (left panel) and $\langle s \rangle$ (right panel) for dark matter and stellar component of subhalos as a function of mass, at redshifts $z = 1.0, 0.03$, and 0.06.

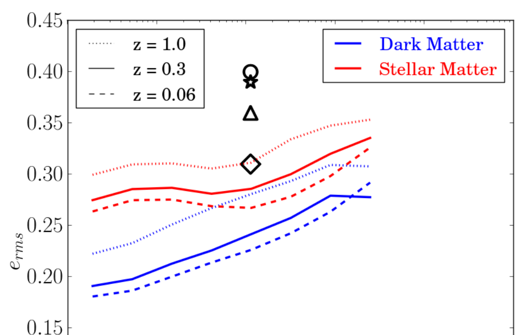

Figure 2.9: RMS ellipticity per component for projected shapes, e_{rms}, for dark matter and stellar matter at $z = 1.0, 0.3$, and 0.06 as a function of cumulative subhalo mass.

the shape distributions between groups and subgroups, we can conclude that the shapes of subgroups are more round when compared to groups in any given mass bin, in agreement with the findings of [105] using dark matter-only simulation. Even in hydrodynamic simulations, [92] found that dark matter subhalos are more round than halos. We can also see that as we go to higher mass bins, the axis ratios of dark matter halos and subhalos decrease in agreement with the findings of [101].

To investigate the mass dependence of axis-ratio distributions for the stellar matter component of subgroups, we plot the axis ratios (q, s) at redshifts $z = 0.3$ in the mass bins $M1, M2$ and $M3$ in Fig. 2.7. The plot shows that as we go to higher mass bins, the shapes of subhalos get more flattened. Using the distribution of satellites and Monte Carlo simulations, [172] reached the same conclusion for dark matter halos. We find that the shapes of stellar matter also follow a similar trend. To understand the redshift evolution of shapes, we also show the shape distributions at $z = 1.0$, and 0.06 for the middle mass bin, $10^{11.5} - 10^{13.0} h^{-1} M_{\odot}$. The lines show that at lower redshifts, the shapes tend to become rounder. [139], [5], and [73] used N-body simulations and considered the axis ratio distributions as a function of mass and redshift. Their results show that at a given mass, halos are more round at lower redshift, and more massive halos are more flattened which is consistent with our findings. In Fig. 2.8, we show the average axis ratios, $\langle q \rangle$ and $\langle s \rangle$ as a function of mass at different redshifts $z = 1.0, 0.3$, and 0.06 for the dark matter and stellar component. We also provide fitting functions for the average axis ratios of the dark matter and stellar component of subhalos as a function of mass and redshift in Appendix A.1. The plots for average axis ratios of the dark matter component can be compared against [5]. Our results agree with theirs qualitatvely in that the average axis ratios, $\langle q \rangle$ and $\langle s \rangle$, increase as we go to lower redshifts and lower masses for the dark matter component. Their curves show a lower average $\langle s \rangle$ which may be because of the different criteria used in the determination of halo shapes, changes in dark matter shapes from the effect of baryons, and different cosmological parameters. Also, they measured average axis ratios for halos, while our results are for subhalos. For the stellar matter, we can see that in general, the average axis ratios decrease with subhalo mass. However, we observe bumps where, there is an increase in the intermediate mass range around $\sim 10^{11} h^{-1} M_{\odot}$ followed by a decreasing trend once again. We will investigate the dependence of this trend on the type and color of galaxies in a future study.

To compare the axis ratio distributions of projected shapes defined by stellar matter of subhalos with results from observational measurements, we use the statistic, rms ellipticity. The rms ellipticity per single component, $e_{\rm rms}$, is given by

$$e_{\rm rms}^2 = \frac{\sum_i \left(\frac{1-q_i'^2}{1+q_i'^2}\right)^2}{2N}, \tag{2.3}$$

where $q_i' = \frac{b_i'}{a_i'}$ for the i^{th} subgroup and N is the total number of subgroups considered. In Fig 2.9, we show the projected rms ellipticity $e_{\rm rms}$ as a function of cumulative mass of subhalos (by considering all subhalos of mass greater a given mass) for redshifts $z = 1.0, 0.3$, and 0.06. Our results can be compared against those from observations in the Sloan Digital Sky Survey (SDSS) given in [129]. For stellar matter, we obtained $e_{\rm rms} = 0.28$ at $z = 0.3$ for $M_{\rm subhalo} > 10^{12} h^{-1} M_{\odot}$, which is smaller than the observed value of 0.36, but reasonably close (and larger than that expected for dark matter component). The catalogue used by [129] has been corrected for measurement noise, but it has some selection effects that bias it slightly in the direction of eliminating small round galaxies, thus boosting the RMS ellipticity in the sample of galaxies selected in the data compared to a fair sample. Also, in observations, the shape estimator is weighted towards the inner part of the luminosity distribution in a galaxy, while our shape measurements are obtained by considering all the particles of a given type in the subhalo, emphasizing the shape of stellar matter at large radii. Given the known differences between how the measurements in data and simulations were carried out, it is difficult to make a quantitative comparison, however, there are no red flags for a major discrepancy.

2.3 Misalignments between stellar matter and dark matter shapes of subhalos

In this section, we compare the major axis orientations of the stellar components and dark matter components of subhalos, in 3D and 2D, in order to quantify the degree of misalignment between them. We investigate the dependence of the probability distribution of the misalignments on the mass range of subhalos and redshift. We also discuss the change in misalignments in going from 3D, as defined by the physics, to 2D, which is what we observe for real galaxies. Finally, the misalignments are compared for centrals and satellite subgroups.

2.3.1 Definition of misalignment angle

For each subgroup, we determined the relative orientation of the major axis of its dark matter subhalo with its stellar component. If $\hat{e}_{ga}$ and $\hat{e}_{da}$ are the major axes of the stellar and dark matter components, respectively, then the misalignment angle is given by

$$\theta_m = \arccos(|\hat{e}_{da} \cdot \hat{e}_{ga}|) \tag{2.4}$$

The same definition can be used to determine the misalignment angle in 2D. It is to be noted here that the major axis is not well defined for ellipsoids which are nearly spherical. However, we verified that our results for misalignment angles do not change significantly when we exclude subhalos with q and $s > 0.95$ for shapes defined by the dark matter or stellar matter.

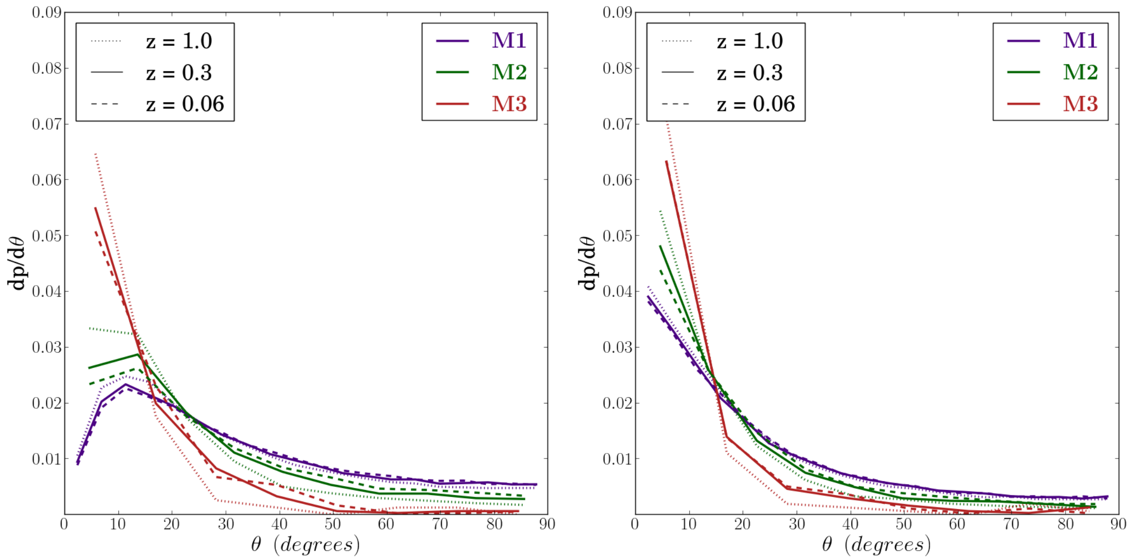

Figure 2.10: Histogram of 3D (left panel) and 2D (right panel) misalignments at redshifts $z = 1.0, 0.3$, and 0.06 in the mass bins $M1, M2$ and $M3$.

Table 2.1: Mean 3D misalignments in subgroups at redshifts $z = 1.0, 0.3$, and 0.06 in the mass bins $M1, M2$ and $M3$.

Mass ($h^{-1}M_\odot$)	Mean 3D misalignment angle		
	$z = 1.0$	$z = 0.3$	$z = 0.06$
$M1 : 10^{10.0} - 10^{11.5}$	31.61°	33.47°	34.10°
$M2 : 10^{11.5} - 10^{13.0}$	20.98°	25.20°	27.73°
$M3 : \ > 10^{13.0}$	10.00°	13.04°	13.87°

Table 2.2: Mean 2D misalignments in subgroups at redshifts $z = 1.0, 0.3$, and 0.06 in mass bins $M1, M2$ and $M3$

Mass ($h^{-1}M_\odot$)	Mean 2D misalignment angle		
	$z = 1.0$	$z = 0.3$	$z = 0.06$
$M1 : 10^{10.0} - 10^{11.5}$	22.61°	23.78°	23.88°
$M2 : 10^{11.5} - 10^{13.0}$	15.51°	17.89°	19.41°
$M3 : \ > 10^{13.0}$	8.74°	10.73°	11.00°

2.3.2 Mass and redshift dependence of misalignments

In Fig. 2.10, we show the misalignment probability distributions for subgroups at redshifts $z = 1.0, 0.3$, and 0.06 in mass bins $M1, M2$ and $M3$. From the plots, we see that in the massive bins, the stellar component is more strongly aligned with its dark matter subhalos. The mean 3D misalignments for each mass bin are listed in Table 6.1. As we go from lower to higher mass bins, the mean misalignments decrease from 34.10° to 13.87°. For a given mass bin, the misalignment strength increases towards lower redshifts, as shown in the plot and table; however, the trend with mass is far stronger than the trend with redshift. When comparing 3D and 2D misalignments, we find that the misalignments are more prominent in the 3D situation. This is mainly due to decrease in misalignment angle by projecting along a particular direction. Also, if we consider random distribution of misalignment angles, it can be inferred geometrically that the probability increases with angle of misalignment in 3D, while the distribution is uniform in 2D. In Appendix A.2, we give fitting functions for the probability distributions of 3D and 2D misalignment angles in different mass bins at redshifts $z = 1.0, 0.3, 0.06$. These probability distributions of misalignment angles are useful in predicting intrinsic alignment signals and estimating the parameter, C_1 in linear alignment model[19]. Table 6.2 shows the mean misalignments in 2D. The fitting functions for mean misalignment angles as a function of mass are given in Appendix A.3. The misalignment distribution for masses $M_{\text{subhalo}} > 10^{13}h^{-1}M_{\odot}$ shows that the stellar shapes are well aligned with their host dark matter subhalos with a mean misalignment angle of 10.00° at $z = 1$ and 13.87° at $z = 0.06$. In a similar mass range, using N-body simulations, [122] assumed a gaussian distribution of misalignment angle with zero mean and constrained the width, σ_θ, to be around 35° so as to match the observed ellipticity correlation functions for central LRGs. This corresponds to an absolute mean misalignment angle of $\sim$ 28°. The galaxies used by [122] have masses corresponding to our highest mass bin, for which we predict a stronger alignment between dark matter halo and galaxy; however, because of the different methodology used to indirectly derive their misalignment angle compared to our direct prediction from simulations, a detailed comparison is difficult.

2.4 Shape distributions and misalignments for central vs. satellite galaxies

Here we consider the axis ratio distributions and misalignment probability distributions for central and satellite subgroups in different mass bins, divided in two ways: based on the parent halo mass and based on the individual subhalo mass.

In the top panel of Fig. 2.11, we show normalized histograms of q and s for centrals and satellites binned according to their parent halo mass, for the bins, $M1, M2$ and $M3$. In the bottom panel, we show the same thing, but dividing based on the subgroup masses. The plots show that satellite subgroups are more round than central subgroups. For satellites, we see that the axis ratio distributions show a strong dependence on the subhalo mass and, for s, the parent halo mass. These trends go in the opposite direction: satellites tend to have a lower value of s when their parent

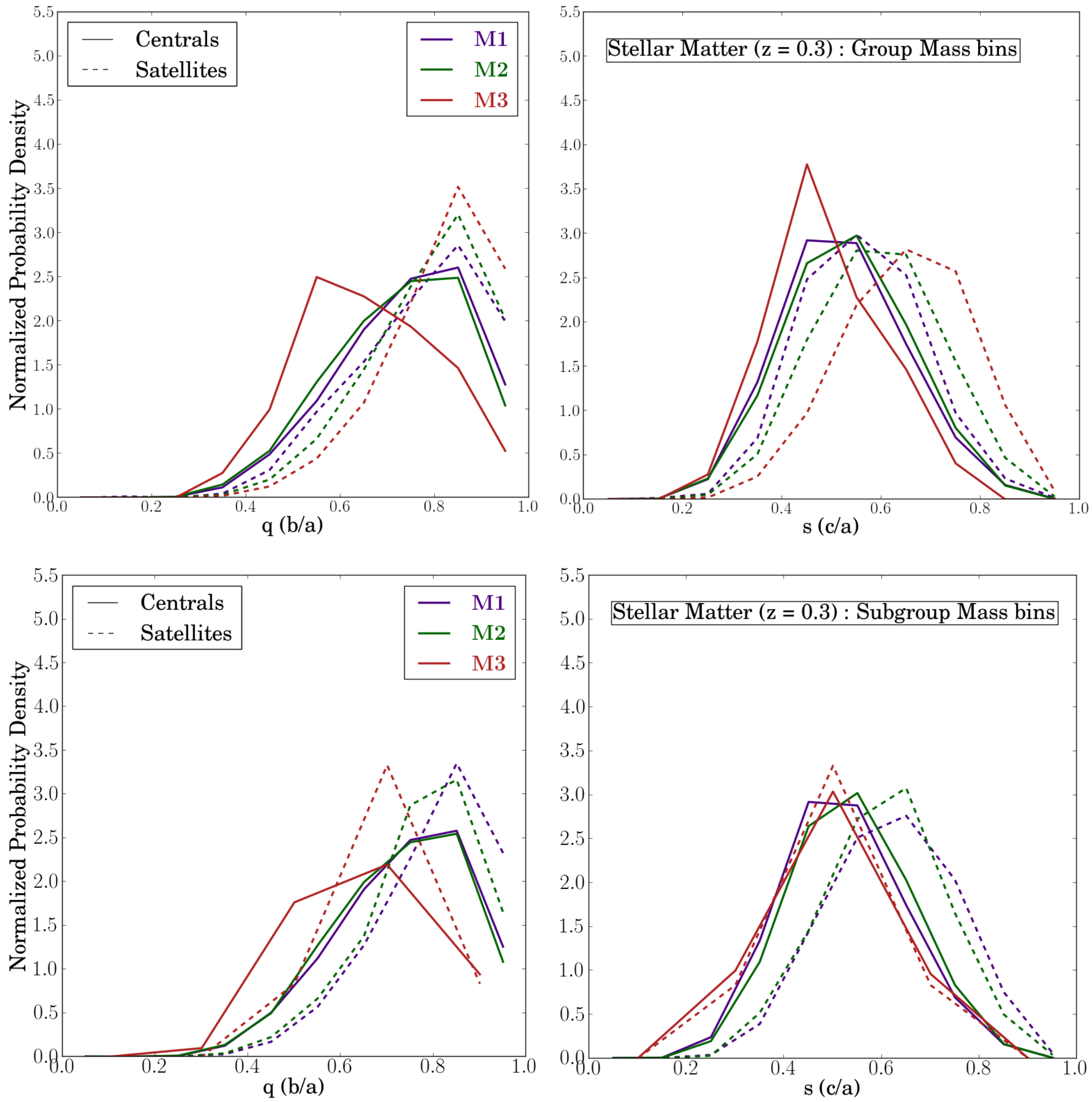

Figure 2.11: Axis ratio distributions of stellar matter in subgroups for centrals and satellites in mass bins $M1, M2$ and $M3$. *Top panel:* Results when dividing based on the parent halo mass; *bottom panel:* when dividing based on the subhalo mass. In both rows, the left and right panels show results for q and s, respectively.

halo mass is low, or when their subhalo mass is high. If we compare the top and bottom right figures, the minor-to-major axis ratio distributions for centrals exhibit little mass dependence when binning by subhalo mass, but more mass dependence when binning by parent halo mass, suggesting an interesting environment dependence.

In Fig. 2.12, we show the distributions of the misalignment angles for central and

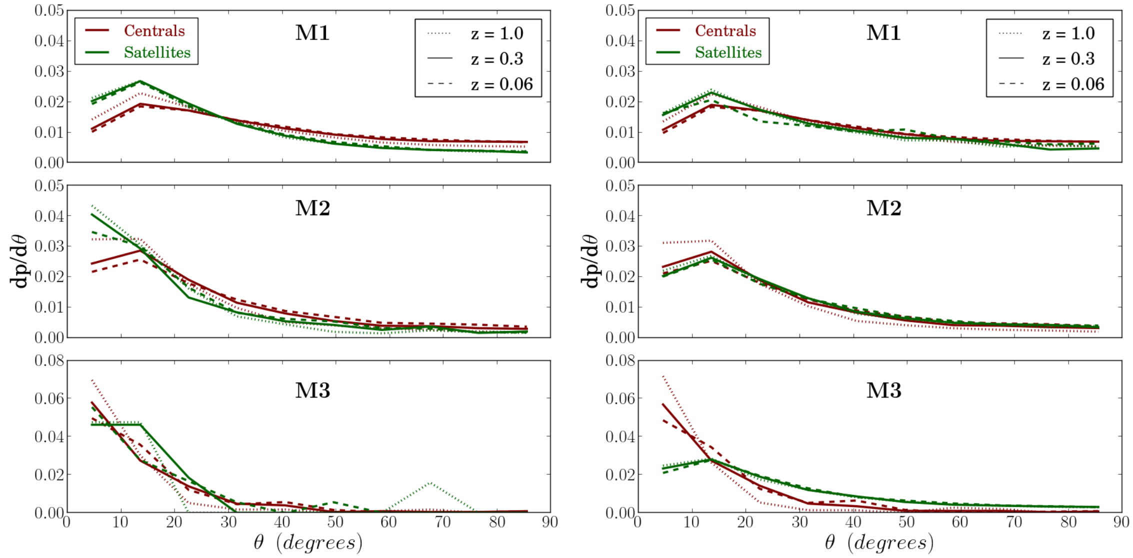

Figure 2.12: Histograms of misalignment angles for central and satellite subgroups in mass bins $M1, M2$ and $M3$. *Left:* Results when dividing based on the subhalo mass; *right:* when dividing based on the halo mass.

Table 2.3: Mean 3D misalignments in central and satellite subgroups at redshifts $z = 1.0, 0.3$, and 0.06 in subhalo mass bins $M1, M2$ and $M3$.

	$z = 1.0$		$z = 0.3$		$z = 0.06$	
Subhalo Mass ($h^{-1}M_\odot$)	Centrals	Satellites	Centrals	Satellites	Centrals	Satellites
$M1: 10^{10.0} - 10^{11.5}$	33.42°	28.21°	37.07°	28.22°	37.83°	29.00°
$M2: 10^{11.5} - 10^{13.0}$	21.30°	18.03°	25.85°	20.43°	28.68°	21.54°
$M3: \ > 10^{13.0}$	9.61°	17.17°	13.11°	11.73°	14.00°	12.03°

Table 2.4: Mean 3D misalignments in central and satellite subgroups at redshifts $z = 1.0, 0.3$, and 0.06 in parent halo mass bins $M1, M2$ and $M3$.

	$z = 1.0$		$z = 0.3$		$z = 0.06$	
Halo Mass ($h^{-1}M_\odot$)	Centrals	Satellites	Centrals	Satellites	Centrals	Satellites
$M1: 10^{10.0} - 10^{11.5}$	33.88°	32.88°	37.39°	32.71°	38.12°	35.60°
$M2: 10^{11.5} - 10^{13.0}$	21.98°	27.76°	26.61°	28.52°	29.10°	29.32°
$M3: \ > 10^{13.0}$	10.33°	26.10°	13.47°	26.48°	14.76°	27.36°

satellite subgroups in different mass bins at redshifts $z = 1.0, 0.3$, and 0.06. In the right panel, the binning is based on halo mass, while in the left panel, the binning is according to subhalo mass. We can see that both centrals and satellites exhibit the same qualitative features in the distributions of misalignment angles as the whole sample of subgoups in Fig. 2.10. Tables 5.2 and 6.3 show the mean misalignment angles of centrals and satellites binned binned according to their subhalo and parent halo masses, respectively. Considering mass bins based on individual masses of subhalos, we see that in general, the degree of alignment is larger for satellites than for centrals for all mass bins. However, if we bin based on the mass of the parent halo, then at higher halo masses, central subgroups tend to have larger alignments than the satellite subgroups. This effect may be due to the centrals having higher masses than the satellites, which tends to correlate with having a higher degree of alignment.

2.5 Conclusions

In this study, we used the MBII cosmological hydrodynamic simulation to study halo and galaxy shapes and alignments, which are relevant for determining the intrinsic alignments of galaxies, an important contaminant for weak lensing measurements with upcoming large sky surveys. While N-body simulations have been used in the past to study intrinsic alignments, it is also important to study the effects due to inclusion of the physics of galaxy formation; this includes effects both on the overall shapes (ellipticities) of the galaxies and halos, but also on any misalignment between them. In order to study this particular issue, we measured the shapes of dark matter and stellar component of groups and subgroups.

Previous studies have used N-body simulations to study the mass dependence and redshift evolution of the shapes of dark matter halos and subhalos [107, 5, 105, 172, 101, 139]. Our results are qualitatively consistent with several trends identified in previous work. The first such trend that we confirm using SPH simulations is that subhalos are more round than halos [105, 92]. The second trend that we confirm is that the shapes of less massive subhalos are more round than more massive subhalos [101, 172] and as we go to lower redshifts, the subhalos also tend to become rounder [139, 5, 73].

The effect of including baryonic physics on the shapes of dark matter halos was studied previously using hydrodynamic simulations in a box of smaller size and resolution compared to ours [92, 99, 26]. [92] found that the axis ratios of dark matter halos increase due to the inclusion of gas cooling, star formation, metal enrichment, thermal supernovae feedback and UV heating. [26] found that there is no major effect on shapes under strong feedback, but they observed a significant change in the inner halo shape distributions. [99] found that there is no effect on the shapes of dark matter subhaloes, where they included gas dynamics, cooling, star formation and supernovae feedback. Here, we took advantage of the extremely high resolution of MBII to directly study the mass dependence and redshift evolution of the shapes of the stellar component of subhalos in addition to dark matter. However, we did not study the effect of baryonic physics on dark matter shapes by comparison with a reference dark matter only simulation in this work.

We found that the shapes of the dark matter component of subhalos are more round than the stellar component. Similar to dark matter subhalo shapes, the shapes of the stellar component also become more round as we go to lower masses of subhalos and lower redshifts. We are also able to calculate the projected rms ellipticity per single component for stellar matter of subhalos, which can be directly compared with observational results in [129]. While the observed result is 0.36 at the given mass range, from our simulation, we measured a value of 0.28 at $z = 0.3$ for $M > 10^{12}h^{-1}M_{\odot}$, which is close, particularly given the uncertainties that result from observational selection effects that are not present in the simulations and that drive the RMS ellipticity to larger values, and given the different radial weighting in the two measurements.

By modelling subhalos as ellipsoids in 3D, we are able to calculate the misalignment angle between the orientation of dark matter and stellar component. Previous studies of misalignments in simulations used either low-resolution hydrodynamic simulations, or N-body simulations with a scheme to populate halos with galaxies and assign a stochastic misalignment angle and other assumptions [140, 68, 56, 122, 64, 44]. By direct calculation from our high-resolution simulation data, we found that in massive subhalos, the stellar component is more aligned with that of dark matter, qualitatively similar to results that have been inferred previously through other means. For instance, at $z = 0.06$, the mean misalignment angles in mass bins from $10^{10.0}-10^{11.5}h^{-1}M_{\odot}$, $10^{11.5}-10^{13.0}h^{-1}M_{\odot}$, and $10^{13.0}-10^{15.0}h^{-1}M_{\odot}$ are 34.10°, 27.73°, 13.87°, respectively. The amplitude of misalignment increases as we go to lower redshifts. The total mean misalignment angle of 30.05°, 30.86°, 32.71° at $z = 1.0$, 0.3, 0.06 respectively shows an increasing trend, though the trend is far weaker than trends with mass at fixed redshift. We also found that the misalignments are larger for 3D shapes when compared to projected shapes. It is to be noted here that we have not split our sample of subhalos according to the type of galaxy. The dependence of our results on galaxy type or color will be investigated in a future study.

Finally, we considered the axis ratios and misalignments in central and satellite subgroups according to their parent halo mass and individual mass of subgroups. We concluded that the shape of stellar component of satellites is more round than that of centrals. We also conclude that the satellite subgroups are more aligned when compared to centrals in similar mass range. Observationally, it is not possible to directly measure the misalignments in centrals and satellites. Misalignment studies for central galaxies were done earlier by [172, 122]. Using data and Monte Carlo simulations, [172] predict a Gaussian distribution of misalignment angle with zero mean and a standard deviation of 23° for their sample of red and blue centrals. [122] used N-body simulations and an HOD model for assigning galaxies to halos. The alignment of central LRG's with host halos is assumed to follow a Gaussian distribution with zero mean. Okumura et al. arrived at a standard deviation of 35° to match the observed ellipticity correlation. Our predictions of misalignments for central and satellite subgroups are direct measurements that could be done through hydrodynamic simulations which include the physics of star formation.

In conclusion, we found that the axis ratios of the shapes of stellar component of subhalos are smaller when compared to that of dark matter. The shapes of both dark matter and stellar component tend to become more round at low masses and low redshifts. We measured the misalignment between the shapes of dark matter and stellar component and found that the misalignment angles are larger at lower masses and increase slightly towards lower redshifts. We found that the dependence is more on the mass of subhalo than redshift. Finally, we split our subhalos sample into centrals and satellites and found that in similar mass range, the satellites have smaller misalignment angles.

We initiated this study with the goal of predicting intrinsic alignments and constraining their impact on weak gravitational lensing measurements. In this paper, we presented our results on the axis ratios and orientations of both the dark matter and stellar matter of subhalos. Future work will include the dependence of these results on the radial weighting function used to measure the inertia tensor (as in [139]), galaxy type and the difference between the shape of the stellar mass versus of the luminosity distribution. We will also present our results on the intrinsic alignment two-point correlation functions in a future paper. Finally, future work should include investigation of the impact of changes in the prescription for including baryonic physics in the simulations.

Chapter 3

Analysis of Two-point Statistics

Upcoming cosmological surveys such as the Large Synoptic Survey Telescope (LSST)EuclidWFIRST-AFTApotential to constrain cosmological parameters such as the dark energy equation of state to percent levels (or better) using weak gravitational lensing. The sensitivity of weak gravitational lensing to both luminous and dark matter [11, 13, 74, 75, 77, 152] makes it a powerful way to probe the nature of dark matter, dark energy and modified theories of gravity [4, 174]. However, the potential to constrain cosmological parameters to sub-percent levels can only be realized if the systematic errors in lensing surveys are even smaller than that.

An important astrophysical systematic that contaminates weak lensing measurements is the intrinsic alignment of galaxies [e.g.][][66, 41, 78, 72]. Weak lensing analysis is based on the assumption that the intrinsic shapes and orientations of galaxies are randomly aligned. In reality, the galaxy shapes are correlated with each other and with the underlying density field, mimicking the same coherent shape alignments that are the signature of weak gravitational lensing. This systematic, called the intrinsic alignment of galaxies, if ignored, can cause a deviation of $\sim 25\%$ when estimating the dark energy equation of state parameter [81]. While several schemes for mitigating intrinsic alignments have been proposed, such as nulling [83], self-calibration [178], and joint modeling of cosmological parameters and weak lensing [e.g.,][96], the methods that remove the least amount of cosmological information often involve modeling the intrinsic alignments as a function of scale, redshift, luminosity and environment.

The complex nature of the physics of galaxy formation makes it very difficult to model the intrinsic alignments analytically. Popular analytic models include the linear alignment model [72], modifications of it based on the non-linear power spectrum [24], and the halo model [137], which makes assumptions about the alignment of centrals and satellites. Numerical studies based on N-body simulations have studied intrinsic alignments by populating the halos with galaxies and assigning a misalignment angle [68] or by using semi-analytic models [86]. In general, methods designed to remove intrinsic alignments from observational data [83, 84, 24, 79, 18] are based on these models or require accurate redshift information which leads to considerable loss of cosmological information. A further understanding of intrinsic alignments requires the use of cosmological numerical simulations that include the physics of galaxy formation to validate the theoretical predictions.

Here, we make use of a large volume, high-resolution cosmological hydrodynamic simulation, MassiveBlack-II (MB-II) [94] to directly study the intrinsic alignment due to the stellar matter component in galaxies. Recent hydrodynamic simulations of comparable volume that form galaxies include the Horizon-AGN [50] and Illustris [169]. In a previous paper [156], we studied the shapes of stellar matter component in galaxies and their alignment with the shape of the host dark matter subhalo using MassiveBlack-II. We extend this work further in this paper, by studying the two-point correlation functions. This study allow us to both (a) compare our results from MB-II with observational measurements at high luminosity, to validate the use of these simulations for intrinsic alignment studies; and (b) to predict intrinsic alignment signals for lower luminosity galaxies that will be used in upcoming weak lensing surveys.

The intrinsic alignments of galaxies in the simulation are based on the shapes and orientations of stellar matter component in galaxies. The shape of a galaxy is determined by the radial weighting used for measuring the inertia tensor, and also the mass or luminosity weighting given to each star particle while calculating the inertia tensor. We previously studied the distributions of shapes determined by dark matter and stellar matter component in galaxies using the unweighted inertia tensor by weighting each star particle by its mass [156]. Using N-body simulations, [139] found radial dependence in the axis ratios of the shapes of dark matter halos. [16] studied the axis ratios of dark matter halos in N-body simulations using different definitions of the inertia tensor. In this paper, we extend our previous work to investigate the dependence of axis ratio distributions of the shapes of stellar matter determined using the unweighted and reduced forms of inertia tensor (defined in Sec. 3.1.2). We also consider the effect of weighting star particles by their luminosity instead of mass, which is more appropriate for comparison with observations. In addition to studying shape distributions, we check the impact of choices made when calculating the per-galaxy inertia tensor on the predicted intrinsic alignment two-point functions.

The main focus of this paper is the investigation of two-point correlation functions using the shapes of stellar matter component in galaxies. For comparison with previous results based on N-body simulations, we can study the position angle statistics, while the projected shape correlations are necessary for comparison with many observational results. The position-angle statistics study the correlation of shapes by considering only their orientation. Using N-body simulations, [109] and [73] investigated the mass dependence and redshift evolution of the alignment of halos with each other. Due to the mass dependence of the misalignment angle of the shape of stellar matter component of a galaxy with its host subhalo shape, we have to investigate this dependence by using the shapes of stellar matter. [37] used the Horizon-AGN simulation to understand intrinsic alignments of simulated galaxies at redshift $z = 1.2$

using the spin of stellar matter component.

As we know both the ellipticity and orientation of stellar matter component in galaxies, it is possible to compute the cross correlations of the projected shapes with each other or the underlying density field statistic. We investigate the mass and redshift dependence of the intrinsic shape-density cross-correlation function in the subhalo mass range of $10^{11} - 10^{14}h^{-1}M_{\odot}$ and at redshifts $z = 1.0, 0.3$, and 0.06. The availability of spectral energy distributions (SED) of star particles in the simulation [94] also allows us to calculate the luminosities of each galaxy in a given band and study intrinsic alignments for galaxy samples selected with a luminosity threshold. It is possible to divide the galaxies in the simulation into centrals and satellites and calculate the intrinsic alignment separately, for comparison in a given mass bin. The dependence of intrinsic alignments on the color of galaxies (red and blue) has been investigated observationally, for example by [71] and [116]. These results indicate larger intrinsic alignments for red galaxies. Here, we will use SEDs to determine colors that we can use to approximately divide our sample of galaxies into red and blue types, to confirm the consistency with the observational findings on the importance of color in determining intrinsic alignments.

This paper is organized as follows. In Section 6.3, we describe the simulation, MB-II, used in this study and the different methods adopted to obtain the shapes and orientations of the stellar matter component in subhalos. In Section 3.2, we define the two-point correlation functions analyzed in this paper. In Section 3.3, we show how the axis ratios and two-point correlation functions depend on the choices made when computing the inertia tensor, while Section 3.3.4 discusses the effect of using luminosity weighted inertia tensor. In Section 3.4, we analyze the color dependence of shapes and two-point correlation functions by dividing the galaxy sample into red and blue types. In Section 3.5, we investigate the mass and redshift dependence of intrinsic alignment two-point correlation functions. A comparison of intrinsic alignments in centrals and satellites is made in Section 3.6. In Section 3.7, we compare our results with observations and make predictions for intrinsic alignments in upcoming weak lensing surveys. Finally, our conclusions are summarized in Section 3.8. In addition, we also provide fitting functions for the intrinsic alignment signals in different mass and luminosity bins at different redshifts in Appendix B.1.

3.1 Methods

3.1.1 MassiveBlack-II Simulation

In this study, we used the MassiveBlack-II (MB-II) hydrodynamic simulation to predict the intrinsic alignment of the shapes of stellar matter component in galaxies. MB-II is a state-of-the-art high resolution, large volume, cosmological hydrodynamic simulation of structure formation. This simulation has been performed with P-GADGET, which is a hybrid version of the parallel code, GADGET2 [147] upgraded to run on

Petaflop scale supercomputers. In addition to gravity and smoothed-particle hydrodynamics (SPH), the P-GADGET code also includes the physics of multiphase ISM model with star formation [149], black hole accretion and feedback [147, 45]. Radiative cooling and heating processes are included [as in][][90], as is photoheating due to an imposed ionizing UV background. The details of this simulation can be found in [94].

MB-II contains $N_{\mathrm{part}} = 2 \times 1792^3$ dark matter and gas particles in a cubic periodic box of length $100h^{-1}$Mpc on a side, with a gravitational smoothing length $\epsilon = 1.85h^{-1}$kpc in comoving units. A single dark matter particle has a mass $m_{\mathrm{DM}} = 1.1 \times 10^7 h^{-1} M_{\odot}$ and the initial mass of a gas particle is $m_{\mathrm{gas}} = 2.2 \times 10^6 h^{-1} M_{\odot}$, with the mass of each star particle being $m_{\mathrm{star}} = 1.1 \times 10^6 h^{-1} M_{\odot}$. The cosmological parameters used in the simulation are as follows: amplitude of matter fluctuations $\sigma_8 = 0.816$, spectral index $\eta_s = 0.96$, mass density parameter $\Omega_m = 0.275$, cosmological constant density parameter $\Omega_\Lambda = 0.725$, baryon density parameter $\Omega_b = 0.046$, and Hubble parameter $h = 0.702$ as per WMAP7 [102].

Halo catalogs of particles in the simulation are generated using the friends of friends (FoF) halo finder algorithm [43]. The FoF algorithm identifies halos on the fly using a linking length of 0.2 times the mean interparticle separation. The subhalo catalogs are generated using the SUBFIND code [151] on the halo catalogs. The subhalos are defined as locally overdense, self-bound particle groups. In this paper, we will be concerned with the analysis of shapes and their two-point correlation functions. Groups of particles are identified as subhalos if they have at least 20 gravitationally bound particles; however, based on convergence tests in [156], we only use their measured shapes if there are ≥ 1000 particles. In this paper, we identify the galaxies to be the subhalos and only consider the shape defined by the stellar component while computing 1-point and 2-point statistics as it is directly relevant to observational measurements. A comparison of the properties of galaxies identified by different subfinder codes (such as Subfind, Structure finder, etc.) in cosmological simulations that include baryonic physics can be found in [100]. They find that various galaxy properties agree among the different subfinder codes. However, the impact on shapes in high resolution cosmological simulations is not investigated yet.

3.1.2 Shapes of galaxies and dark matter halos

In this section, we give the details of the different methods adopted to find the shape defined by the dark matter and stellar matter component in subhalos. We model the shapes of the dark matter and stellar matter components of subhalos as ellipsoids in three dimensions by using the eigenvalues and eigenvectors of the inertia tensor, which describes the mass or luminosity distribution. In the interest of comparison with observations, we also project the halos and subhalos onto the XY plane and model the shapes as ellipses. These are needed to compute projected shape correlation functions, which we will define in Sec. 3.2.2. In 3D, consider the eigenvectors of the inertia tensor to be $\hat{e}_a, \hat{e}_b, \hat{e}_c$ with the corresponding eigenvalues being $\lambda_a, \lambda_b, \lambda_c$, where $\lambda_a > \lambda_b > \lambda_c$. The eigenvectors represent the principal axes of the ellipsoid with the lengths of the principal axes (a, b, c) given by the square roots of the eigenvalues $(\sqrt{\lambda_a}, \sqrt{\lambda_b}, \sqrt{\lambda_c})$. The 3D axis ratios are defined as

$$q = \frac{b}{a}, \ s = \frac{c}{a} \tag{3.1}$$

In 2D, the eigenvectors are $\hat{e}'_a, \hat{e}'_b$ with the corresponding eigenvalues λ'_a, λ'_b, where $\lambda'_a > \lambda'_b$. The lengths of major and minor axes are $a' = \sqrt{\lambda'_a}$, $b' = \sqrt{\lambda'_b}$ with axis ratio $q' = \frac{b'}{a'}$.

We explore several different ways of computing the inertia tensor based on the mass or luminosity, and the radial weighting given to each particle. The unweighted inertia tensor (used for all results in [156]) is given by

$$I_{ij} = \frac{\sum_n m_n x_{ni} x_{nj}}{\sum_n m_n}, \tag{3.2}$$

where m_n represents the mass of the n^{th} particle and x_{ni}, x_{nj} represent the position coordinates of the n^{th} particle with $0 \le i, j \le 2$ in 3D and $0 \le i, j \le 1$ in 2D. Here all particles are given equal weight irrespective of their distance from the center of a subhalo. We can also use the reduced inertia tensor, which gives more weight to particles which are closer to the center:

$$\widetilde{I}_{ij} = \frac{\sum_n m_n \frac{x_{ni} x_{nj}}{r_n^2}}{\sum_n m_n} \tag{3.3}$$

where

$$r_n^2 = \sum_i x_{ni}^2 \tag{3.4}$$

Unlike for N-body simulations where it is natural to let each equally-weighted dark matter particle contribute equally to the inertia tensor, for simulated galaxies it is natural to consider weighting each particle by its luminosity, considering that flux is what we actually see when we observe the galaxy. This results in another definition for the inertia tensor:

$$I_{ij}^{(\mathrm{lum})} = \frac{\sum_n l_n x_{ni} x_{nj}}{\sum_n l_n}, \tag{3.5}$$

where each stellar particle is weighted by its luminosity, l_n instead of its mass. The definition presented here refers to the luminosity-weighted form of unweighted inertia tensor given in Eq. 3.2. In our analysis, we also use the shapes obtained using the luminosity-weighted form of reduced inertia tensor (Eq. 6.8) defined analogously.

Instead of determining axis ratios with a single calculation, we can also adopt iterative methods for finding the shapes using unweighted and reduced inertia tensors. In the unweighted iterative and reduced iterative methods, we first determine the axis ratios by the standard definitions of the corresponding inertia tensors using all the particles of a given type in the subhalo. Keeping the enclosed volume constant [139], the lengths of the principal axes of ellipsoids are rescaled accordinglyNote that some authors instead keep the length of the major axis fixed [5, 16]. After this rescaling, we determine the shapes again, discarding particles outside the ellipsoidal volume. This process is repeated until convergence is reached. Our convergence criterion is that the fractional change in axis ratios must be below 1%. It is to be noted here that although we only use subhalos that initially have at least 1000 dark matter and star particles to calculate shapes, the use of iterative methods results in some low mass subhalos having fewer than 1000 particles in the enclosed volume. But, since this is a very low fraction (less than 0.5%) and the number of particles remaining is very close to 1000, we include them for further analysis.

We will investigate the dependence of using these different definitions on the probability distributions of axis ratios and the two-point correlation functions. Having outlined the differences, we will present the rest of our predictions from the simulation based on the reduced iterative inertia tensor alone.

3.1.3 Misalignment angle

To study the relative orientation between the shapes defined by dark matter and stellar matter component in subhalos, we compute the probability distributions of misalignment angles as in [156]. Let $\hat{e}_{da}$ and $\hat{e}_{ga}$ be the major axes of the shapes defined by dark matter and stellar matter components respectively. We can then define the misalignment angle by

$$\theta_m = \arccos(|\hat{e}_{da} \cdot \hat{e}_{ga}|). \tag{3.6}$$

3.2 Two-point correlation functions

Here we define the intrinsic alignment two-point correlation functions that we use in this work. Intrinsic alignments can arise due to the correlation of intrinsic shapes of galaxies with each other (II term) or the correlation of the gravitational shear and intrinsic ellipticity (GI term). The two-point statistics discussed in this paper concern the GI term.

3.2.1 Position angle statistics

The position angle statistics, Ellipticity-Ellipticity (EE) and Ellipticity-Direction (ED) correlation functions, are useful to quantify the correlations between the position angles of galaxies or halos with each other and with the large-scale density field as a function of mass and redshift. These can then be compared against results for halos in N-body simulations. We follow the notation of [109] to define the EE and ED correlations.

If $\hat{e}_a(\mathbf{x})$ is the direction of the major axis of the shape of the dark matter or stellar matter component of a subhalo centered at position $\mathbf{x}$, then the EE correlation function in 3D, $\eta(r)$, is given by

$$\eta(r) = \langle | \ \hat{e}_a(\mathbf{x}) \cdot \hat{e}_a(\mathbf{x}{+}\mathbf{r}) \ |^2 \rangle - \frac{1}{3}. \tag{3.7}$$

Here, $\langle . \rangle$ means an average over pairs of galaxies separated by a distance, r. For galaxies or halos randomly oriented according to a uniform distribution, the expectation value of this quantity is zero.

The ED correlation function cross-correlates the orientation of the major axis of the shape of a subhalo with the large-scale density field. For a subhalo centered at position $\mathbf{x}$ with major axis direction $\hat{e}_a$, let the unit vector in the direction of the tracer of the matter density field at a distance r be $\hat{\mathbf{r}} = \mathbf{r}/r$. Then the ED cross-correlation function is given by

$$\omega(r) = \langle | \ \hat{e}_a(\mathbf{x}) \cdot \hat{\mathbf{r}}(\mathbf{x}) \ |^2 \rangle - \frac{1}{3} \tag{3.8}$$

which is again zero in the case of no intrinsic alignments.

We can represent the tracers of the matter density field using either the positions of dark matter particles (in which case the correlation function is denoted by the symbol ω_δ) or the positions of subhalos (in which case it includes a factor of the subhalo bias, and is simply denoted ω).

3.2.2 Projected shape correlation functions

The projected shape correlation functions are computed to directly compare our results from simulations with observations. Here, we follow the notation of [117] to give formulae for the calculation of galaxy-intrinsic shear correlation function ($\hat{\xi}_{g+}(r_p, \Pi)$) and the projected statistic, w_{g+}. Here, r_p is the comoving transverse separation of a pair of galaxies in the XY plane and Π is their separation along the Z direction.

If $q' = \frac{b'}{a'}$ is the axis ratio of the projected shape of the dark matter or stellar matter component of a subhalo and ϕ is the position angle of the major axis of the ellipse, the components of the ellipticity are given by

$$(e_+, e_\times) = \frac{1 - q'^2}{1 + q'^2} \left[\cos(2\phi), \sin(2\phi)\right], \tag{3.9}$$

where e_+ refers to the radial component of ellipticity and $e_\times$ is the component at 45° rotation. The galaxy-intrinsic shear correlation function cross-correlates the ellipticity of galaxies with the density field. The "shape sample" denoted by S_+ is selected on the basis of a threshold or binning in subhalo mass, stellar mass, band luminosity and other properties of the galaxies in the simulation, while all the subhalos are used to trace the density field, forming a "density sample" denoted by D. The cross-correlation function is then computed using

$$\hat{\xi}_{g+}(r_p, \Pi) = \frac{S_+D - S_+R}{RR} \tag{3.10}$$

where r_p is the transverse separation of the galaxy points and Π is the radial red-shift space separation (here, it is the separation along the Z direction), and S_+D is the sum over all pairs with separations r_p and Π:

$$S_+D = \sum_{i \neq j | r_p, \Pi} \frac{e_+(j \mid i)}{2\mathcal{R}}, \tag{3.11}$$

where $e_+(j|i)$ is the + component of the ellipticity of a galaxy (j) from the shear sample relative to the direction of a tracer of density field (i) selected from the density sample. Here, $\mathcal{R} = (1-e_{rms}^2)$ is the shear responsivity that converts from distortion to shear with e_{rms}, the rms ellipticity per component of the shape sample. Alternatively, we can also define the ellipticity by $e = \frac{1-q'}{1+q'}$, in which case we do not have to take the responsivity correction into account. However, using this definition decreases the intrinsic alignment signal by only about $\sim 6\%$. So, in the rest of this paper, we employ the former definition as it makes it easier for comparison with observations. S_+R is defined by a similar equation for the correlation of the data sample with a random density field distribution to remove observational systematics in the shear estimates, and hence we can neglect this term here. The projected correlation function, $w_{g+}(r_p)$ is now given by

$$w_{g+}(r_p) = \int_{-\Pi_{\max}}^{+\Pi_{\max}} \hat{\xi}_{g+}(r_p, \Pi)\, \mathrm{d}\Pi \tag{3.12}$$

We calculated the correlation functions over the whole length of the box ($100h^{-1}$Mpc) with $\Pi_{\max} = 50h^{-1}$Mpc, in 25 bins of size $4h^{-1}$Mpc each. The projected correlation functions are obtained by summing over the galaxy-intrinsic and intrinsic-intrinsic shear correlation functions with the integrand replaced by a summation. Note that the w_{g+} signal can also be calculated using projected shapes along some other plane instead of XY. However, we did not observe significant differences in the signal for $w_{g+}(r_p)$ calculated by projecting along YZ and XZ planes. Thus, all reported results use shapes projected on the XY plane.

An alternative way to trace the density field for the calculation of w_{g+} is to use the positions of all dark matter particles in the simulation instead of subhalos. The correlation function obtained in this way is denoted by $w_{\delta+}$. The former is what we can compare with observations, but we can use the latter to test the standard conversion that is used between the two (dividing the observational signals by the linear galaxy bias).

The observable, w_{g+} is related to the GI term which is discussed further in the section below. We do not discuss the intrinsic shear-shear correlation functions,

($\hat{\xi}_{++}(r_p, \Pi)$, $\hat{\xi}_{\times\times}(r_p, \Pi)$) and their corresponding projected statistics, (w_{++}, $w_{\times\times}$) in this paper due to their being extremely noisy. Moreover, it has been shown in multiple theoretical studies [e.g.,][][72] that if intrinsic alignments are caused by something like the tidal alignment model, the II contamination to cosmic shear signals will be quite subdominant to the GI contamination. Given that all measurements to date of strong intrinsic alignments on large scales have been made with red galaxies, and are consistent with the tidal alignment model [e.g.,][][19], we mainly focus on the GI-type intrinsic alignment contamination here. As a practical matter, there is additional motivation to focus on measuring w_{g+} rather than w_{++}, because for alignments consistent with the tidal alignment model, the signal-to-noise ratio for the former will be higher than for the latter (see section 4.1 of [142]). Finally, for this type of alignment, measurements of GI provide a unique prediction for II, so our measurements are equally informative about both given that they appear completely consistent with the tidal alignment.

3.2.3 Formalism: Linear Alignment Model

The linear alignment model is the standard formalism used to study intrinsic alignments of galaxy shapes at large scales [30, 72, 19, 35]. The observational measurements of intrinsic alignments on large scales can be reproduced using this model. In this section, we briefly describe the main features of the model.

The linear alignment model is based on the assumption that the intrinsic shear of galaxies is determined by the tidal field at the time of formation of the galaxy [**?**, assumed to be during matter domination,]]Catelan2001. Thus we can write the intrinsic shear in terms of the primordial potential as

$$\gamma^I = (\gamma_+^I, \gamma_\times^I) = -\frac{C_1}{4\pi G}(\partial_x^2 - \partial_y^2, \partial_x\partial_y)\phi_p \tag{3.13}$$

[72] derived the 2-point matter-intrinsic alignments power spectra, relating them to the linear matter power spectrum, P_δ^{lin}

$$P_{g+}(\vec{k}, z) = A_I b \frac{C_1\rho_{\mathrm{crit}}\Omega_m}{D(z)} \frac{k_x^2 - k_y^2}{k^2} P_\delta^{\mathrm{lin}}(\vec{k}, z) \tag{3.14}$$

$$P_{++}(\vec{k}, z) = \left(A_I \frac{C_1\rho_{\mathrm{crit}}\Omega_m}{D(z)} \frac{k_x^2 - k_y^2}{k^2}\right)^2 P_\delta^{\mathrm{lin}}(\vec{k}, z) \tag{3.15}$$

$$P_{g\times}(\vec{k}, z) = A_I b \frac{C_1\rho_{\mathrm{crit}}\Omega_m}{D(z)} \frac{k_x k_y}{k^2} P_\delta^{\mathrm{lin}}(\vec{k}, z) \tag{3.16}$$

Following [82], we fix $C_1\rho_{\mathrm{crit}} = 0.0134$ and use the arbitrary constant A_I to describe the amplitude of intrinsic alignments for different samples. $D(z)$ is the linear growth factor, normalized to unity at $z = 0$.

[25] suggested using the full non-linear matter power spectrum P_δ^{nl} in Eq. (3.14) to extend the linear alignment model to quasi-linear scales. This model is called

the non-linear linear alignment model (NLA). In this work, we will use the non-linear matter power spectrum generated with the CAMB software [110], with a fixed WMAP7 cosmology [70].

Fourier transforming Eq. (3.14) and integrating over line of sight separation Π, we get the two point correlation function

$$w_{g+}(r_p) = \frac{A_I b_D C_1 \rho_{\rm crit}\Omega_m}{\pi^2} \int dz \frac{W(z)}{D(z)} \int_0^\infty dk_z \int_0^\infty$$
$$dk_\perp \frac{k_\perp^3}{(k_\perp^2 + k_z^2)k_z} P_\delta^{\rm nl}(\vec{k}, z) \sin(k_z \Pi_{max}) J_2(k_\perp r_p) \left(1 + \beta\mu^2\right) \tag{3.17}$$

b_D is the bias for density sample, $\mu = k_z/k$ and β is the linear redshift distortion parameter with $(1 + \beta\mu^2)$ accounting for the effects of redshift-space distortions [RSD,][][87, 142]. $\beta(z) = f(z)/b$, where $f(z)$ is the logarithmic growth rate at redshift z; in ΛCDM, $f(z) \sim \Omega_m(z)^{0.55}$. $w_{g\times}$ is expected to be zero by symmetry.

3.3 The impact of using different inertia tensor definitions

In this section, we compare the axis ratio distributions and misalignment angle distributions (as presented in [156]) when using the different definitions of inertia tensor defined in Sec. 3.1.2. We also consider how the two-point correlation functions vary when using different shape definitions. For convenience, we define three mass bins based on total subhalos mass, M1 ($10^{10.0} - 10^{11.5} h^{-1} M_\odot$), M2 ($10^{11.5} - 10^{13.0} h^{-1} M_\odot$), and M3 ($> 10^{13.0} h^{-1} M_\odot$).

3.3.1 Axis ratio distributions

Here, we compare the axis ratios of shapes obtained using different definitions of inertia tensor. In Figs. 3.1 and 3.2, we show the histograms of the axis ratios of the 3D shapes of dark matter (Fig. 3.1 and stellar (Fig. 3.2) matter components in subhalos using four inertia tensor calculations: unweighted and reduced, non-iterative and iterative. We considered mass bins M1, M2 and M3 with 38768, 8438, and 267 galaxies, respectively. From the plots, we can see that the axis ratio distributions obtained with non-iterative and iterative unweighted inertia tensors are essentially identical. For the reduced inertia tensor, the results for the iterative calculation are uniformly more flattened than for the non-iterative calculation. The reason for this is that the non-iterative reduced calculation implicitly imposes spherical symmetry (via the $1/r^2$ weighting), which will result in an overly-rounded shape estimate. For this reason, we do not consider the reduced non-iterative calculation to be useful.

Comparing the iterative reduced vs. unweighted results, the axis ratios of dark matter subhalos are slightly larger (rounder) when using the reduced inertia tensor

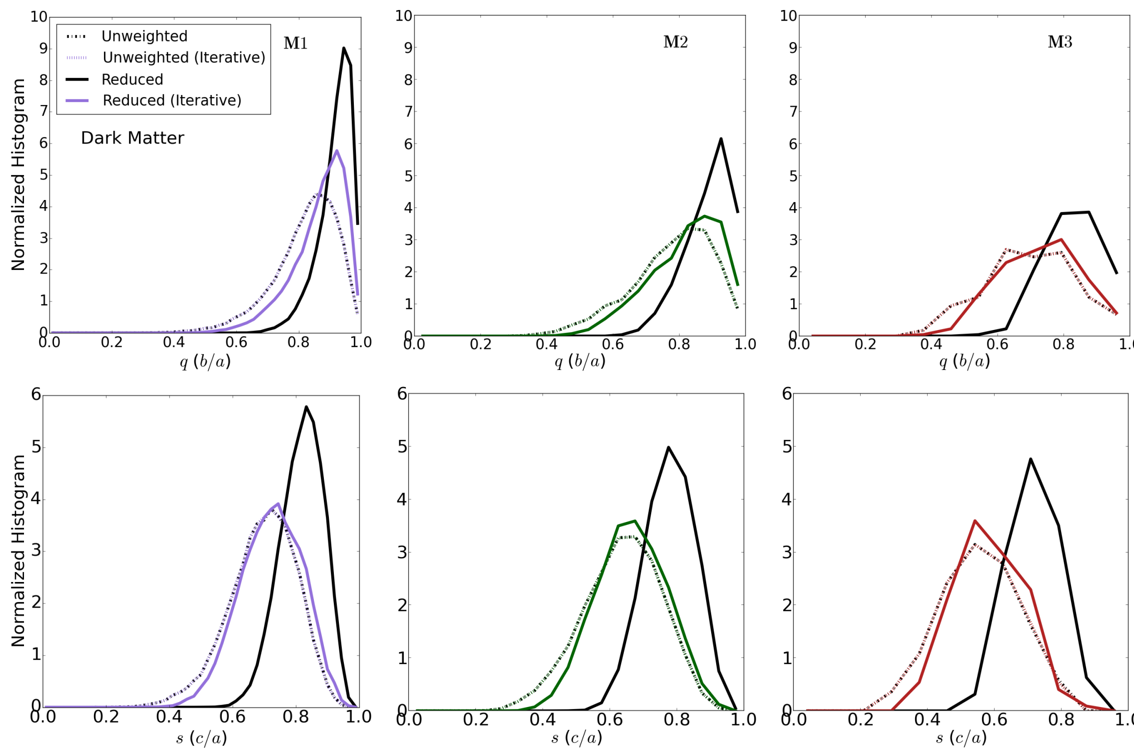

Figure 3.1: Normalized histograms of 3D axis ratios of dark matter component in subhalos using different definitions of inertia tensor in mass bins M1, M2 and M3 at $z = 0.3$. The number of galaxies are 38768, 8438, and 267 respectively in mass bins M1, M2 and M3. *Top:* q (b/a); *Bottom:* s (c/a).

than when using the unweighted one. This finding agrees qualitatively with the findings of [16] using N-body simulations. Additionally, the inclusion of baryonic physics in hydrodynamic simulations can lead to more round dark matter shapes in the inner regions of subhalos [e.g.,][][92, 26]. In future work, we will directly study the impact of baryonic physics on the shapes determined by reduced inertia tensor by comparing our results on shape distributions with those obtained with a dark matter only simulation.

When considering the stellar shapes, we see that the histograms of intermediate-to-major axis ratio, q $(\frac{b}{a})$, indicate a slight increase for the reduced inertia tensor compared to shapes obtained from the unweighted tensor, while the histograms of minor-to-major axis ratio, s $(\frac{c}{a})$, show a decrease in axis ratio. Thus the shape distributions with the reduced inertia tensor are more oblate than the ones with the unweighted inertia tensor. In a previous study [156], we found that the projected shapes of stellar matter determined using the unweighted inertia tensor are slightly smaller, but compare favorably with observational measurements using the RMS el-

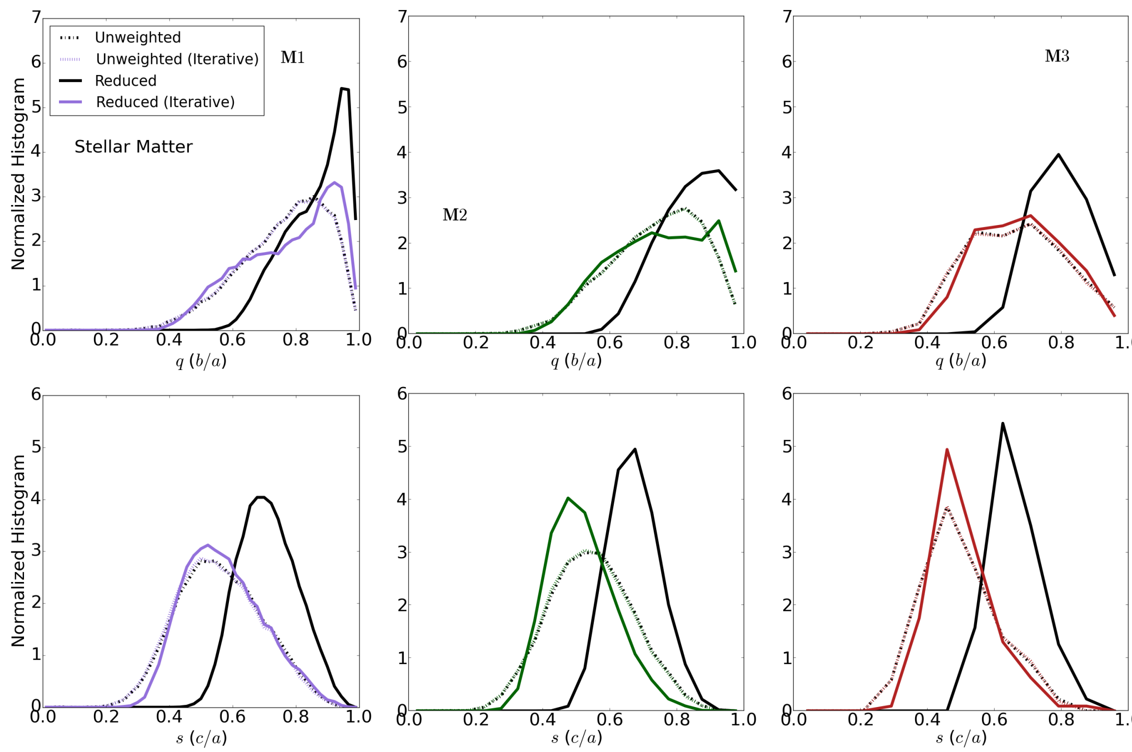

Figure 3.2: Normalized histograms of 3D axis ratios of stellar matter component in subhalos using different definitions of inertia tensor in mass bins M1, M2 and M3 at $z = 0.3$. *Top:* q (b/a); *Bottom:* s (c/a).

lipticity statistic. We note here that the projected shapes with reduced inertia tensor will have a smaller value of the RMS ellipticity statistic.

3.3.2 Misalignment angle distributions

In Fig. 6.5, we plot the normalized histograms of misalignment angles between the shapes defined by dark matter and stellar matter component in subhalos. The plots show that there is no significant difference in misalignments if we adopt an iterative or non-iterative definition of shape tensor, for both unweighted and reduced cases. For the unweighted inertia tensor, this result is consistent with the distribution of axis ratios in Sec. 3.3.1, where the histograms are similar for unweighted non-iterative and iterative definitions. For the shapes obtained using the reduced inertia tensor, the histograms of misalignment angles seem to indicate that while the axis ratios change significantly, the relative shape orientation is not altered much. Comparing misalignment histograms obtained using unweighted and reduced inertia tensor, we observe that in the lowest mass bin, M1, the misalignments are slightly smaller if we

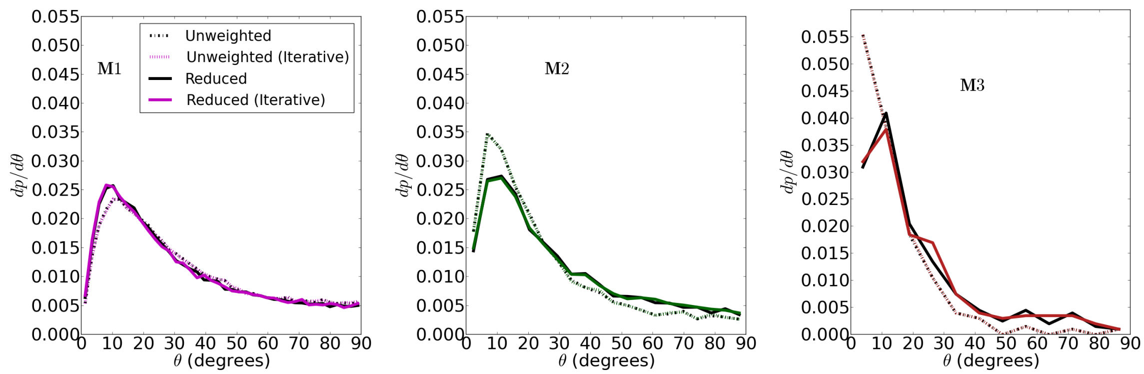

Figure 3.3: Normalized histograms of misalignment angles between the major axes of 3D shapes defined by the dark matter and stellar matter component in subhalos using different definitions of inertia tensor, in mass bins (M1, M2, and M3) at $z = 0.3$. Note that for uniformly distributed misalignment angles in 3D, the probability distribution is proportional to $\sin\theta$.

use the reduced inertia tensor to define shapes, while they are slightly higher in mass bins M2 and M3.

3.3.3 Two-point correlation functions

Here, we consider the dependence of the intrinsic alignment two-point correlation functions for the shapes of the stellar matter component in subhalos using different definitions of inertia tensor. For both ED and w_{g+} correlation functions, the errors bars shown in the plots are obtained using the jackknife variance.

In Fig. 3.4, we show the ED correlation function, $\omega(r)$, for the shapes of the stellar matter component for subhalo mass thresholds of $10^{11}h^{-1}M_{\odot}$, $10^{12}h^{-1}M_{\odot}$, and $10^{13}h^{-1}M_{\odot}$. Similar to the histograms of misalignment angles, the position-angle correlation functions are the same when we use iterative or non-iterative definitions of inertia tensor. The correlation functions are noticeably smaller if we use the reduced inertia tensor to define the shape for all the mass thresholds.

In Fig.3.5, we show the projected shape correlation function, $w_{g+}(r)$, in different mass bins. We do not observe any significant difference in the correlation function if we use the non-iterative vs. iterative unweighted inertia tensor to define shape. This is consistent with histograms of axis ratios, misalignment angles and the ED correlation function shown before. Going to the reduced definition of inertia tensor, it can be seen that w_{g+} is smaller for the shapes obtained from iterative reduced inertia tensor. This is expected due to the lower ellipticities (or higher axis ratios) obtained using the reduced inertia tensor. The values of w_{g+} for the reduced non-iterative shape tensor are even smaller due to the very high axis ratios, however as

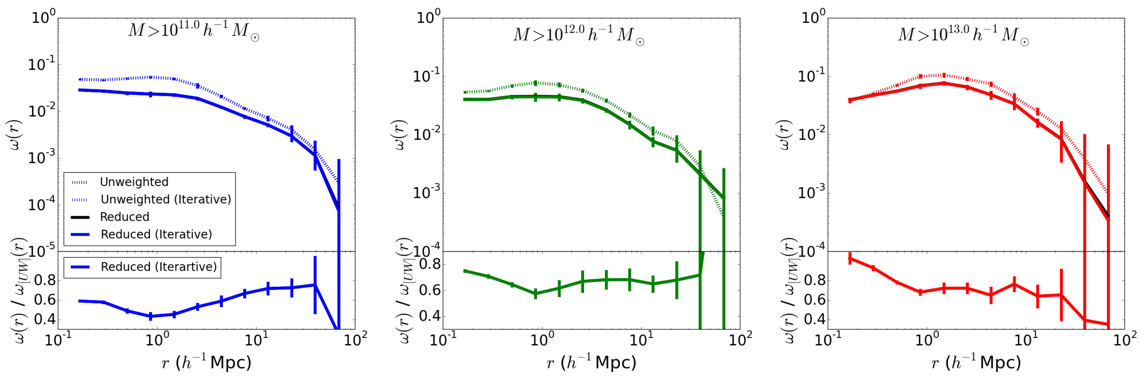

Figure 3.4: ED correlation function, $\omega(r)$, for the 3D shapes of stellar matter obtained using different definitions of inertia tensor in subhalos selected by a mass threshold. The *top* panel, shows the ED correlation function and the *bottom* panel shows the ratio of the signals obtained using iterative reduced inertia tensor with the unweighted inertia tensor. Note that in the *top* panel, the lines labeled Unweighted and Unweighted (Iterative); Reduced and Reduced (Iterative) are close enough that they cannot be easily distinguished. *Left:* $M > 10^{11} h^{-1} M_\odot$ (24648 galaxies); *Middle:* $M > 10^{12.0} h^{-1} M_\odot$ (2947 galaxies); *Right:* $M > 10^{13.0} h^{-1} M_\odot$ (267 galaxies) at $z = 0.3$.

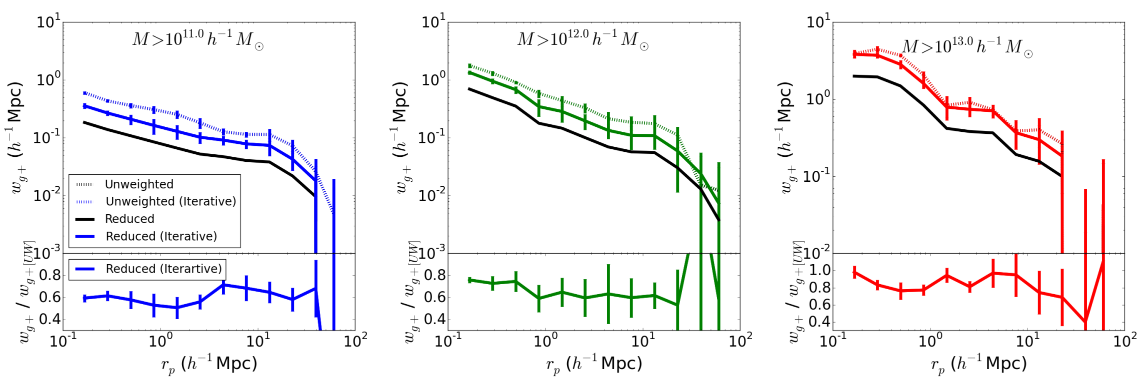

Figure 3.5: w_{g+} correlation function for the projected (2D) shapes of stellar matter obtained using different definitions of inertia tensor in subhalos selected by a mass threshold at $z = 0.3$. The *top* panel, shows the w_{g+} correlation function and the *bottom* panel shows the ratio of the signals obtained using iterative reduced inertia tensor with the unweighted inertia tensor. Note that in the *top* panel, the lines labeled Unweighted and Unweighted (Iterative) are close enough that they cannot be easily distinguished. *Left:* $M > 10^{11} h^{-1} M_\odot$; *Middle:* $M > 10^{12.0} h^{-1} M_\odot$; *Right:* $M > 10^{13.0} h^{-1} M_\odot$.

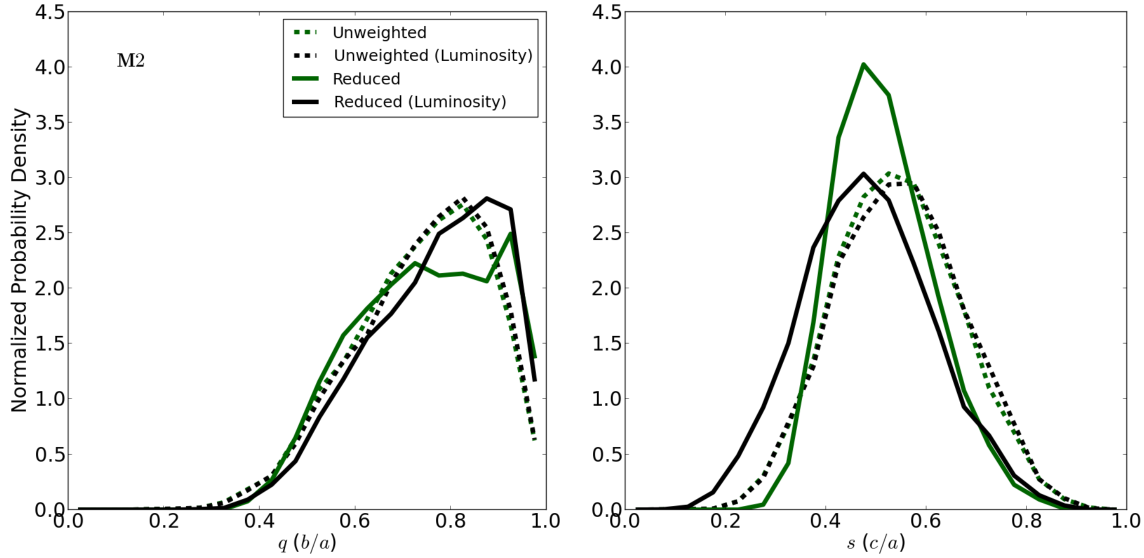

Figure 3.6: Normalized histograms of 3D axis ratios of stellar matter in subhalos using iterative unweighted and iterative reduced inertia tensors with each particle weighted by its luminosity or mass. Results are shown only for the mass bin M2. *Left:* q (b/a); *Right:* s (c/a).

mentioned previously we do not consider this a viable way of measuring shapes.

Our analysis presented in this section shows that the results from the unweighted non-iterative inertia tensor are quite similar to those obtained using the iterative tensor, so we do not have to consider this option separately. It is fair to not consider the results obtained using non-iterative reduced inertia tensor due to the expectation that it will produce overly round shapes. Based on these conclusions, our further analysis is based on the shapes obtained using only the iterative versions of unweighted and reduced inertia tensors

3.3.4 Shapes determined using luminosity weighting

In this section, we investigate the effect of weighting each stellar particle by its luminosity instead of mass while computing the inertia tensor. For the unweighted inertia tensor, we follow Eq. 3.5; the reduced form of the luminosity weighted inertia tensor can be inferred from it in a straight-forward manner. For each star particle, we use the SDSS r-band luminosity from the simulation, and determine shapes iteratively.

In Fig. 3.6, we show the histograms of axis ratios (in the M2 mass bin) of stellar matter in subhalos, computed using both the mass- and luminosity-weighted form for the unweighted and reduced inertia tensor. From the plot, we can see that there is no major change in the distribution of axis ratios due to luminosity weighting

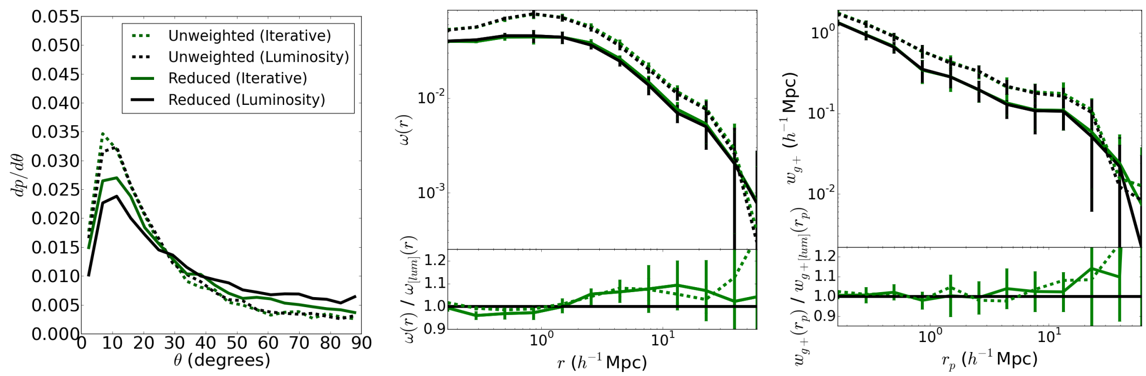

Figure 3.7: *Left:* Normalized histogram of misalignment angles using luminosity weighted shapes of stellar matter in subhalos in the mass bin, M2: $10^{11.5} - 10^{13.0} h^{-1} M_\odot$at $z = 0.3$. *Middle:* ED correlation of luminosity weighted shapes of stellar matter in subhalos for $M > 10^{12} h^{-1} M_\odot$. *Right:* w_{g+} correlation of luminosity weighted shapes of stellar matter in subhalos for $M > 10^{12} h^{-1} M_\odot$. For a direct comparison, the ratio of signals obtained using the mass and luminosity weighted inertia tensors are shown in the *bottom* panels.

for the unweighted inertia tensor. The histograms of axis ratios obtained from the reduced inertia tensor show that the luminosity weighting leads to larger values of q ($\frac{b}{a}$) and smaller values of s ($\frac{c}{a}$). Thus, the overall shapes are more oblate when using luminosity weighting. This is expected as the mass to light ratio is not constant in the inner regions of the subhalos.

Likewise, we can infer from the left panel of Fig. 3.7 that luminosity weighting has no effect on the distribution of misalignment angles in the unweighted case, while the stellar shapes obtained from reduced luminosity weighting are more misaligned with the shapes of their host dark matter subhalos. The middle panel of the same figure shows the ED correlation function, $\omega(r)$, and the right panel shows the plot of $w_{g+}(r)$. In the bottom panels, we plot the ratio of the ED and w_{g+} signals obtained using the mass weighted inertia tensor with the ones using luminosity weighted tensor. Both the plots indicate that the amplitude and shape of correlation functions obtained using luminosity-weighted shapes are consistent with the ones obtained using mass-weighted shapes. Similarly, at other mass thresholds, the effect of luminosity weighting on correlation functions is not very significant. Although the histograms of shapes and misalignment angles obtained by using the reduced form of luminosity weighted inertia tensor are different, we do not observe a significant change in the two point correlation functions, in comparison with the much stronger mass dependence of the two-point correlation shown in Sec. 3.5.1. So, we do not consider luminosity weighted inertia tensor in the rest of the sections in this paper.

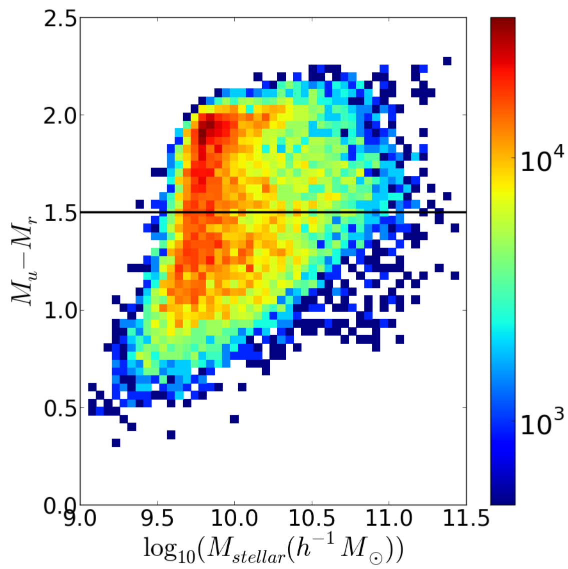

Figure 3.8: Rest-frame color $(M_u - M_r)$ versus stellar mass for galaxies in the simulation at $z = 0.3$.

3.4 Color dependence of intrinsic alignments

In this section, we investigate the color dependence of galaxy shape distributions, misalignment angle distributions, and two-point correlation functions. To do this, we roughly divide our entire sample of galaxies into red and blue types.

3.4.1 Division into blue and red galaxies

The color of a galaxy is obtained by calculating the difference in the absolute magnitudes in the SDSS u-band (M_u) and r-band (M_r) obtained from the simulation. In Fig. 3.8, we show a 2D histogram of color $(M_u - M_r)$ versus the stellar mass of subhalos at $z = 0.3$. Prior to plotting this histogram, we imposed a magnitude limit by eliminating galaxies with $M_r < -18$ and eliminated galaxies with very bright AGNs.

Our colors do not exactly match those from observations, which have a clear bimodal distribution in the color-mass contour plot. So, we choose the median of $M_u - M_r$ to roughly divide our sample of galaxies in the simulation into blue and red types. It is important to bear in mind that because of the procedure we have used, this might not be exactly analogous to the blue vs. red divisions used in studies of observed galaxies [e.g.,][][71]. Together with the fact that color and morphology are not perfectly correlated, this implies that our color based division is not same as a division into bulge-dominated and disk-dominated galaxies.

[37] used a similar definition. They used the $u - r$ rest-frame colors to divide their

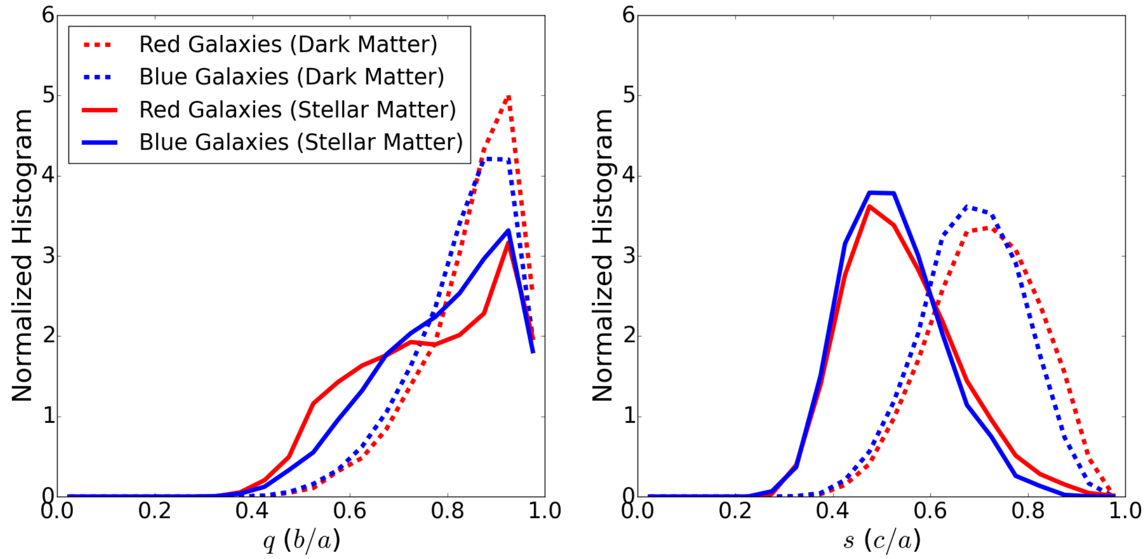

Figure 3.9: Normalized histograms of axis ratios (q, s) of dark matter and stellar matter component in subhalos for blue (6343 galaxies) and red (6343 galaxies) galaxies at $z = 0.3$. *Left:* q (b/a); *Right:* s (c/a).

sample of galaxies in the simulation into three equal bins consisting of blue, red/blue and red types. [170] divided the sample of galaxies in the Illustris simulation using the $u - i$ color into blue, green and red types based on a star formation rate threshold, but they only produce a slightly bimodal distribution in colors that is not comparable with observations.

Here, we only consider the shapes obtained from the iterative reduced inertia tensor for our analysis in this section. We obtain similar results using the unweighted inertia tensor.

3.4.2 Axis ratio distributions

The histograms of axis ratios of dark matter and stellar matter component in subhalos for the red and blue galaxies are shown in Fig. 3.9. The plots show that the red galaxies have slightly higher (rounder) axis ratios for the shapes defined by dark matter. For the shapes defined by stellar matter, the blue galaxies have slightly higher values of q $(\frac{b}{a})$ and lower values of s $(\frac{c}{a})$, indicating more oblate or disk-like shapes, as we would expect.

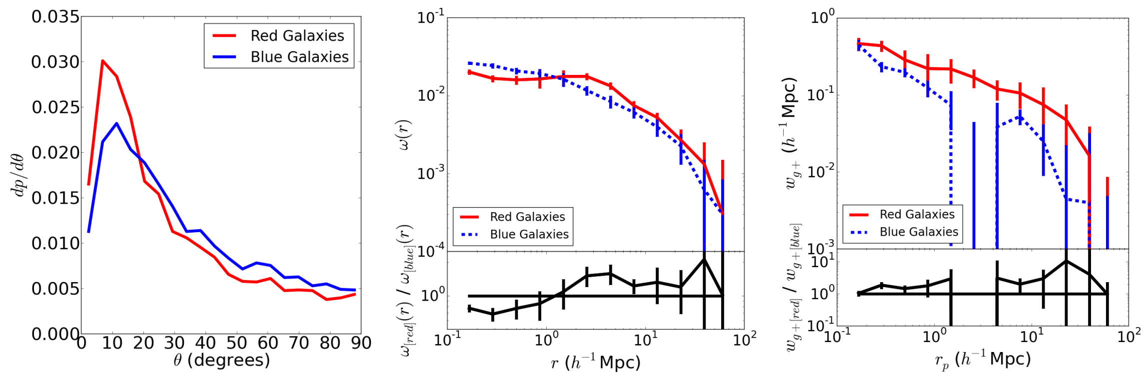

Figure 3.10: Comparison of misalignment angles and two-point correlation function in red and blue galaxies at $z = 0.3$. *Left:* Histogram of misalignment angles; *Middle* ED position angle statistic; *Right* w_{g+} projected shape correlation function. At around $\sim 1h^{-1}$Mpc, the correlation function becomes negative for the blue galaxies.

3.4.3 Misalignment angles and two-point correlation functions

The histogram of misalignment angles shown in the left panel of Fig. 3.10 indicates a larger misalignment between dark matter halo and galaxy shapes in blue galaxies. The mean misalignment angles are $29° \pm 0.3°$ and $33° \pm 0.3°$ respectively for red and blue galaxies. If we wish to interpret these differences, we have to consider other factors that might change the distribution of misalignment angles, the most important of which is the mass. The mean masses of the sample of red and blue galaxies are similar. The red (blue) sample has a mean subhalo mass of 8.0 (7.9) $\times 10^{11} h^{-1} M_{\odot}$. Given the nearly consistent masses, the larger alignment for the red sample is not entirely due to mass.

In the middle panel of Fig. 3.10 we show the ED correlation for red and blue galaxies. The w_{g+} signals are plotted in the right panel. From the ratio plots of the intrinsic alignment signals for red and blue galaxies shown in the bottom panel, we conclude that there is no significant difference for our sample of red and blue galaxies.

3.5 Mass and redshift dependence of two-point correlation functions

In this section, we show the results for intrinsic alignment two-point correlation functions for shapes defined by the stellar matter component in subhalos. We focus in particular on the mass dependence and redshift evolution of the ED and w_{g+} correlation function.

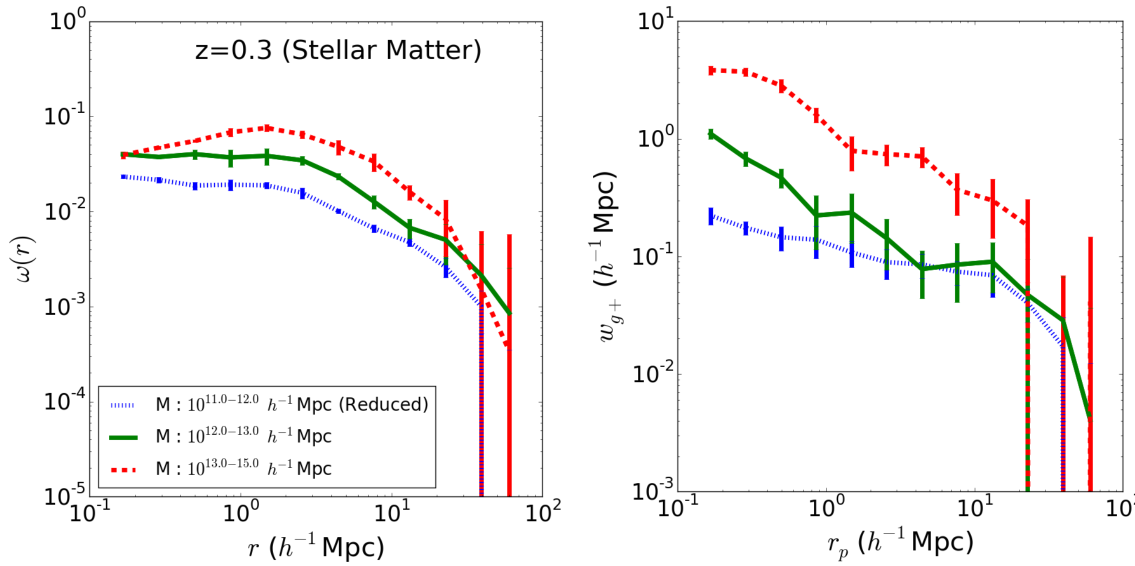

Figure 3.11: Mass dependence of two-point correlation functions for shapes defined by stellar matter in subhalos at $z = 0.3$ using iterative reduced inertia shape tensors. *Left:* Position angle statistic, ED correlation function; *Right:* Projected shape-correlation function, w_{g+}.

3.5.1 Mass dependence

In Fig. 3.11, we consider the mass dependence of two-point correlation functions for shapes defined by stellar matter in subhalos. The left panel shows the ED correlation function for shapes obtained using iterative reduced inertia tensors. The galaxy samples here are selected based on total subhalo mass in the mass bins, M : $10^{11-12}h^{-1}M_{\odot}$, $10^{12-13}h^{-1}M_{\odot}$ and $10^{13-15}h^{-1}M_{\odot}$. We observe a substantial increase in the amplitude of these correlation functions with increasing mass for both ED and w_{g+}. For M : $10^{13-15}h^{-1}M_{\odot}$, the correlation function dips at small scales, possibly indicating a slightly random alignment of satellite subhalos with the orientation of the central galaxy. In a previous study, [109] investigated the ED correlation functions from N-body simulations for shapes defined by dark matter. However, we know that the shape defined by stellar matter in galaxies is misaligned with the shape of host dark matter subhalo [156]. This can significantly change the ED correlation function of shapes obtained with stellar matter when compared with results from an N-body simulations. For instance, previous studies have noted that there is a suppression in the intrinsic alignment signal due to misalignment of galaxy shape with the host dark matter shape [68, 122, 19]. Qualitatively similar to our results of ED correlation using shapes of stellar matter component, [109] also found that the correlation of dark matter shapes with the density field increases with halo mass at all

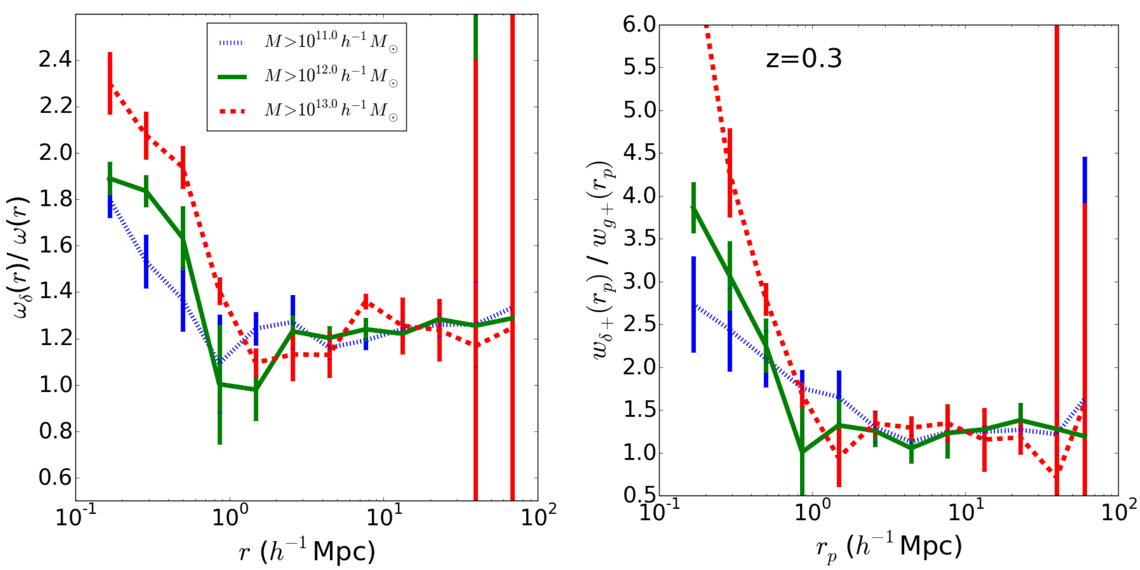

Figure 3.12: *Left:* Ratio of $\omega_\delta(r)$(density field traced by dark matter particles) to $\omega(r)$ *Right:* Ratio of $w_{\delta+}(r_p)$ correlation function, where the density field is traced by dark matter particles, to $w_{g+}(r_p)$ (density field traced by subhalos).

scales. However, [109] only measure the signal starting at $r > 1h^{-1}$Mpc. So, we cannot directly compare our results at small scales for the mass bin, $M : 10^{13-15}h^{-1}M_\odot$, where we observe a dip in the correlation.

In the right panel of Fig. 3.11, we considered the mass dependence in w_{g+} using the same mass bins. For this correlation function, the different ellipticities and orientation of shapes defined by stellar matter in galaxies can lead to a different correlation function, when compared with that obtained using dark matter shapes. For w_{g+}, we observe an increase in the amplitude of correlations with increasing subhalo mass threshold. The increase in intrinsic ellipticity-density correlation signal with halo mass is also predicted from N-body simulations [68] and semi-analytic models [86]. Unlike the ED correlation in 3D, and consistent with observations of w_{g+} for real galaxies [e.g.,][][71], we do not observe a dip in w_{g+} for $M > 10^{13}h^{-1}M_\odot$ at small scales.

Although we do not show the mass dependence of intrinsic alignments for the shapes obtained using the iterative unweighted inertia tensor, it can be inferred from the plots shown in 3.4 and 3.5 that ED and w_{g+} correlation functions have similar mass dependence using the unweighted tensor. However, for comparison with observations, we expect that the iterative reduced inertia tensor might be a better choice as it gives more weight to the particles in the inner regions of subhalos. Hence, in the rest of this paper, we only present the two-point statistics using shapes obtained from the iterative reduced inertia tensor.

Comparison of w_{g+} and $w_{\delta+}$

The projected correlation function, w_{g+}, includes a factor of the galaxy bias due to the correlation with galaxy positions. In observational data, it is necessary to estimate a large-scale galaxy bias and use the linear bias approximation to remove this galaxy bias dependency, an approach which should fail on small to intermediate scales. In order to take the effect of subhalo bias at large scales into consideration, here we considered the ratio of two-point correlation functions using the dark matter particles to trace the density field with those obtained by using the subhalos to trace the density field. In the left panel of Fig. 3.12, we plotted the $\omega_\delta(r)/\omega(r)$ correlation function at $z = 0.3$ for shapes defined by stellar matter in galaxies, for $M > 10^{11}h^{-1}M_\odot$, $M > 10^{12}h^{-1}M_\odot$, and $M > 10^{13}h^{-1}M_\odot$ using the reduced iterative inertia tensor to calculate shapes. At small scales, we observe that the $\omega_\delta(r)$ is a factor of 1.6–2 larger than $\omega(r)$, and the ratio is larger at higher mass thresholds. This result indicates that the shapes of massive galaxies are better aligned with the shape of the dark matter field than with the positions of other galaxies. The right panel shows a similar plot for the projected shape correlation function ($w_{\delta+}$). Again, we observe a larger $w_{\delta+}$ at small scales, and the ratio increases with mass threshold. In both the plots, the ratio is nearly constant at large scales for all mass thresholds, and is inversely proportional to the large-scale bias of the density tracer sample (all subhalos in the simulation). Since the simulation includes relatively low mass subhalos, their average bias is < 1 and hence the ratio that is plotted is slightly above 1.

3.5.2 Redshift evolution

We show the redshift evolution of intrinsic alignment two-point correlation functions by plotting the ratios of ED and w_{g+} at $z = 1.0$, 0.3, and 0.06 to the corresponding quantities at $z = 0.3$ for $M > 10^{11}h^{-1}M_\odot$. In the left (right) panel of Fig. 3.13, we show this ratio for the ED (w_{g+}) correlation functions with three subhalo mass threshold values. We observe that (for fixed mass threshold) the amplitude of the ED correlation function decreases significantly at all scales and for all mass thresholds as we go to lower redshifts. Using N-body simulations, [109] also found that the amplitude of the ED correlation function decreases at lower redshifts. However, the w_{g+} correlation function does not exhibit a strong dependence on redshift. This is due to a difference in the shape distributions that compensates for the redshift evolution of position angle alignments shown by the results for ω.

The linear alignment model predicts that for the range of redshifts considered here, $w_{\delta+}$ varies roughly as $(1 + z)^{-0.7}$ [71]. We do not detect any significant redshift evolution of $w_{\delta+}$ for most of our samples. However, this particular test for redshift evolution based on mass (or luminosity) threshold samples may not be fair for intrinsic alignments evolution, since we are not comparing results for a high-redshift sample of progenitors of the low-redshift sample at a given mass threshold (due to additional mergers and mass accretion). We defer the exploration of this effect to future work.

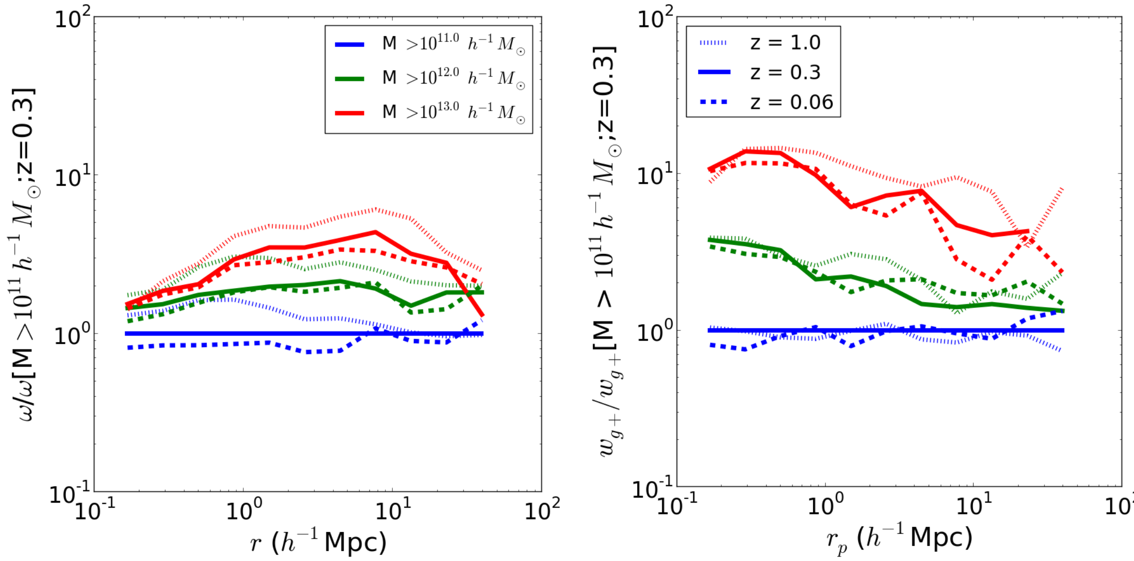

Figure 3.13: Ratio plot of two-point correlation functions at redshifts $z = 1.0$, 0.3 and 0.06 and various mass thresholds to the corresponding value at $z = 0.3$ for $M > 10^{11.0} h^{-1} M_{\odot}$. *Left:* ED; *Right:* w_{g+}.

3.6 Two point correlation functions: centrals and satellites

A central subhalo is located at or near the potential minimum of its host halo. The remaining subhalos of that host halo are satellites. Here, we investigate the intrinsic alignment two-point correlation functions for central and satellite subhalos separately, by looking at the projected shape correlation in various mass bins.

3.6.1 Alignments of central and satellite galaxies

Observationally, the distribution of satellites around central galaxies has been found to be anisotropic, with more satellites along the major axis of the central galaxy [e.g.,][][132, 23, 176, 120, 111, 171, 108]. This has also been studied through N-body simulations [55, 3, 173] and hydrodynamic simulations of smaller volume [112, 44]. However, N-body simulations overestimate the strength of the alignment signal if it is assumed that the shape of central galaxy follows the shape of dark matter halo [89, 3]. In a recent paper, [49] used a large volume hydrodynamical simulation without AGN feedback to study this problem.

Here, we explore the distribution of the location of satellite subhalos with respect to the major axis of the central subhalo in the host halo. The left panel of Fig. 3.14 shows the histogram of angle between the major axis of shapes of dark matter and

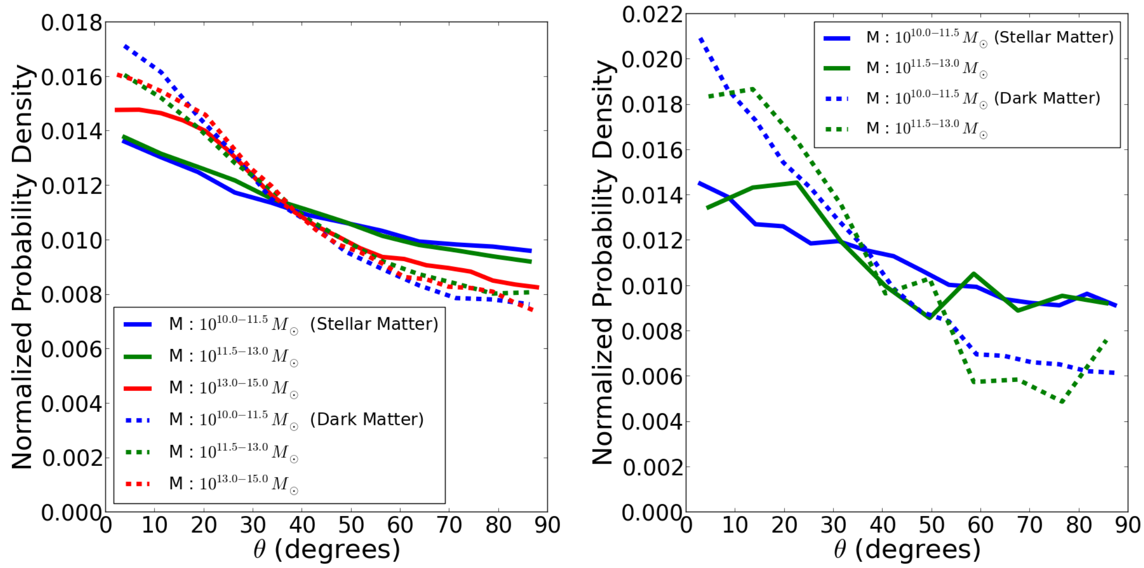

Figure 3.14: *Left:* Normalized histogram of alignment angle of the major axis of the 2D stellar shape of a central galaxy with satellite subhalos in mass bins, $M1$, $M2$ and $M3$ of central subhalo mass at $z = 0.3$. *Right:* Normalized histogram of alignment angles of the major axis of the 2D stellar shape of satellite galaxies with host halo in mass bins, $M1$ and $M2$ of satellite subhalo mass at $z = 0.3$.

stellar matter of a central subhalo with the line joining the satellite subhalos. From the plot, we can conclude that the satellite subhalos are more concentrated along the major axis of its central galaxy. Our results are qualitatively consistent with results from N-body simulations by [55, 173]. Using hydrodynamic simulations of smaller volume, [44] found that the satellites are more distributed along the axis of the shape determined by dark matter component of a central subhalo, when compared with that of stellar matter. We also confirm this finding with a large statistical sample. From the plot, we can observe that there is no significant mass dependence in the distribution of satellites along the major axis of the subhalo with shape determined using dark matter particles. On the other hand, for shapes defined by stellar matter of galaxies, we observe that the alignment increases with increasing subhalo mass with the mean alignment angles being 42.0°, 41.5° and 39.6° in the mass bins, $M1$, $M2$ and $M3$ respectively. This is due to a greater misalignment angle between the shapes defined by the dark matter and stellar matter in less massive central galaxies. [49] also studied the spatial distribution of satellite galaxies with respect to the orientation of their host central galaxy using a large volume hydrodynamical simulation. They found more alignment in massive halos with mean alignment angles varying from $45° - 40°$ in the mass range, $10^{11} - 10^{14} h^{-1} M_\odot$ which agrees qualitatively with our findings.

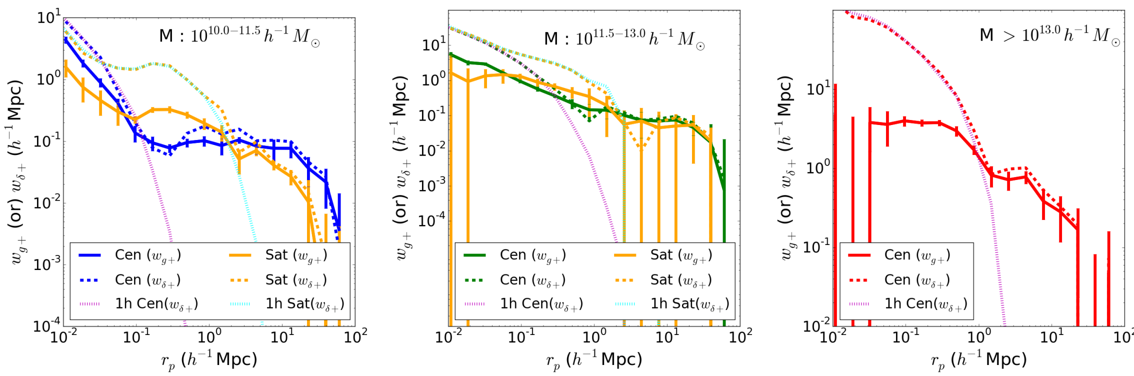

Figure 3.15: w_{g+} and $w_{\delta+}$ correlation function for centrals and satellites at $z = 0.3$. *Left:* M1: $10^{10-11.5}h^{-1}M_\odot$; *Middle:* M2: $10^{11.5-13.0}h^{-1}M_\odot$; *Right:* M3: $> 10^{13.0}h^{-1}M_\odot$. The labels "Cen" and "Sat" refer to the correlation functions (w_{g+}, $w_{\delta+}$) of centrals and satellites respectively. Similarly, "1h Cen" and "1h Sat" refer to the 1-halo term of $w_{\delta+}$ for central and satellite subhalos respectively. The number of central galaxies is 23014, 7415 and 255 in mass bins M1, M2 and M3 respectively.

We also investigate the orientation of satellite galaxies with respect to the location of its central subhalo. The right panel of Fig. 3.14 shows the alignment of the major axis of the shapes of satellite galaxies with the direction to their central subhalo. This is the radial alignment signal, which has been studied for dark matter component of satellites using N-body simulations [105, 125, 55] and hydrodynamic simulations [99]. These studies found that the orientation of satellite subhalos is not random, but point more towards the center of their host halo. Here, we observe that the shapes of stellar matter in satellites are also more aligned with the direction to their host halo. Recent observational measurements of [138, 141] have not detected radial alignment of satellite galaxies with their host halo.

3.6.2 w_{g+} and $w_{\delta+}$ for centrals and satellites

In Fig. 3.15, we show the w_{g+} and $w_{\delta+}$ correlation function for centrals and satellites in mass bins, M1 and M2. In the highest mass bin, M3, the signal for satellites is not shown due to lack of sufficient number of satellite subhalos. The figure shows that at small scales, the w_{g+} and $w_{\delta+}$ signal for satellites is larger than that for centrals for subhalos in the mass bin M1. This is interesting and could be due to following possibilities: 1. Satellite subhalos have stronger alignments with the local tidal fields than the central subhalos. Note that within a halo, tidal fields are predominantly radial, consistent with the radial alignments of satellites. More generally, since central subhalos are in reality the innermost subhalo, this could imply some radial dependence of intrinsic alignments. 2. Another possibility is that satellite and central intrinsic alignments are not very different, but the overall intrinsic alignments signal depends on the host halo mass. In this case, more massive halos with more satellite subhalos will get higher weight in satellite correlations but not in central correlations. This could also push up the w_{g+} and $w_{\delta+}$ signal for satellites. We speculate that final result is likely to be combination of these two effects, with radial dependence being the more dominant factor. In mass bin M2, the plot shows that there is no statistically significant differences in the intrinsic alignments of centrals and satellites at any scale.

At large scale, it is expected that the intrinsic alignment signal due to satellites goes to zero in the halo model [137], based on the assumption that the satellite subhalos are uniformly distributed throughout the host halo pointing towards the center. However, the latter assumption is not quite true in reality. As shown in Sec. 3.6.1, the satellite subhalos have a tendency to be distributed more along the major axis of the central galaxy and are also radially aligned. Hence, they "inherit" the large-scale intrinsic alignments of the host halo at some level. This could be the explanation for the fact that the satellite w_{g+}, while dropping on large scales, is still non-zero.

From Fig. 3.15, we can also see that as we go to higher masses, the amplitude of intrinsic alignments in central subhalos increases.

In addition, the transverse separation, r_p, where we observe a slight dip or change in the shape of the correlation function shifts to smaller values as we go to lower masses of central subhalos. This change of shape indicates a region of transition from the 1-halo term at small scales to the 2-halo term at large scales. To further illustrate our point, we also show the 1-halo term of $w_{\delta+}$ for central and satellite subhalos in these mass bins. This is directly calculated by correlating the shape of a galaxy with the location of dark matter particles that belong to its host halo. As seen from the plot, the 1-halo term follows the shape of $w_{\delta+}$ at small scales and drops to zero at large distances (on scales comparable to the virial radius), where the 2-halo term is becoming more significant.

3.7 Modeling, Comparisons and Predictions

In this section, we present the results of fitting the non-linear alignment (NLA) model to the MB-II intrinsic alignment two-point correlation functions. The NLA model has been shown to describe realistic galaxy intrinsic alignments. Comparing the results from the simulation with the NLA model will help us understand on what scales the NLA model describes the alignments in MB-II. Additionally, these fits are a much more compact way to represent our predictions, encapsulating all the information about the scale-dependence of the signal as a single amplitude parameter and a well-known physical model. On small-scales, the NLA model does not describe the signals well, so we provide simple power-law fits for these scales. We also compare the intrinsic alignment two-point correlation functions in MB-II with those in real data. There are two purposes of this comparison. The first is simply to confirm that MB-

II gives physically-reasonable results for samples for which intrinsic alignments have been robustly detected. The second is to then make predictions for samples that will be used for lensing by upcoming surveys.

3.7.1 Fitting models to MB-II correlation functions

Here we present results of fitting NLA and power law functions to our predictions for w_{g+} and $w_{\delta+}$ from MB-II. Fig. 3.17 shows an example of models fitted to the measurements for two different samples defined by luminosity bins, $M_r \leq -22.6$ and $M_r \in [-22.6, -20.3]$. More examples and tables with fit parameters can be found in Appendix B.1. We fit the NLA model in the range $6 < r_p < 25h^{-1}$Mpc. Beyond $25h^{-1}$Mpc, the MB-II predictions are dominated by cosmic variance. We fit w_{g+} and $w_{\delta+}$ simultaneously assuming the same A_I for both, and an additional large-scale (constant) subhalo bias b_D for w_{g+}. As can be seen in Fig. 3.17, the NLA model fits the data well in the fitting range and can be extended down to $r_p \sim 4h^{-1}$Mpc, below which the signal differs in both amplitude and scale dependence. We add a note of caution that we use the simple weighted least squares method to fit the model using only the diagonal terms in the covariance matrix, which underestimates the errors on the parameters when compared with the errors on data points. The errors shown on data points are calculated from jackknife variance, but due to the limited size of our simulation box, the jackknife errors on the maximum scales used are not very reliable. Fig. 3.16 shows a comparison of jackknife and Poisson error bars. The Poisson errors tend to be very small (and are certainly underestimated above a few h^{-1}Mpc scales, where cosmic variance will be important). However they are within a factor of 1.5–2 of the jackknife errors on small scales, which is reasonable. While Poisson errors are underestimated, the scale dependence of jackknife errors suggest that they are cosmic variance dominated and due to the limited size of the simulation box, the covariance matrix is very noisy. Keeping in mind the limitations of our jackknife covariance matrix, we do not attempt a more sophisticated fitting method to get better error estimates on the model parameters.

On small scales, we fit a power law function separately to w_{g+} and $w_{\delta+}$, in the range $0.1 < r_p < 1h^{-1}$Mpc. The power law function is of the form:

$$w_{g+} = P_A r_p^{P_I} \tag{3.18}$$

Fig. 3.18 shows intrinsic alignments amplitudes for w_{g+} as function of average luminosity and redshift of the sample, for different samples defined with different luminosity bins. We see clear evolution with luminosity and mild evolution with redshift. More luminous objects show stronger intrinsic alignments, qualitatively consistent with LRG observations. Within the NLA model, where it is assumed that intrinsic alignments are set at time of galaxy formation, we do not expect any redshift evolution of A_I. This is consistent with LRG observations, where no significant

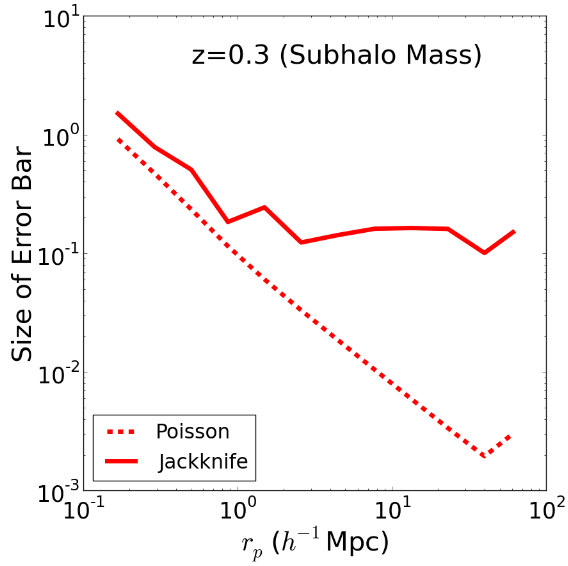

Figure 3.16: Comparison of the size of Poisson and jackknife error bars in the calculation of $w_{g+}(r)$ for subhalo mass-selected samples.

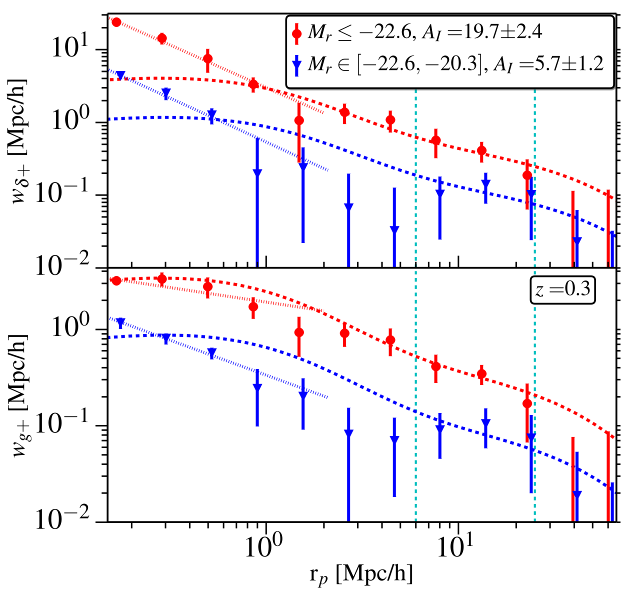

Figure 3.17: NLA and power law fitting to $w_{\delta+}$ (top) and w_{g+} (bottom) for two different samples defined by luminosity bins. Vertical lines show the range over which we fit the NLA model ($6h^{-1}$Mpc $< r_p <$ $25h^{-1}$Mpc). Note that the power law is fitted only for $r_p < 1h^{-1}$Mpc, though the function is shown out to $r_p \sim 2h^{-1}$Mpc.

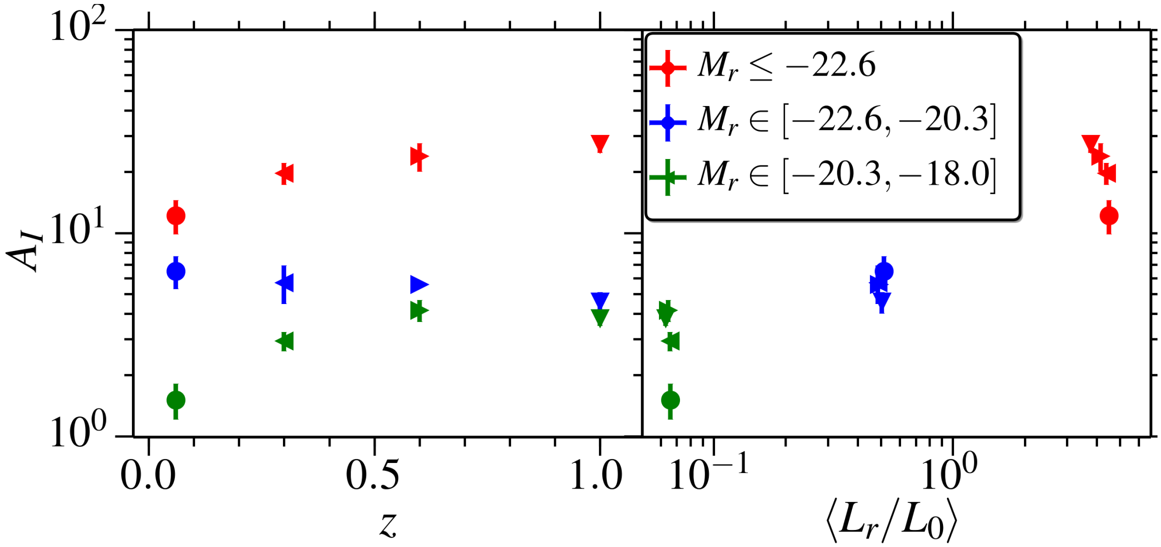

Figure 3.18: NLA amplitude, A_I, as a function of redshift for different luminosity samples. The horizontal axis indicates the average mass, luminosity or redshift of different samples. Points are colored by sample definition, while markers are set according to the redshift.

redshift dependence for A_I is detected [82], admittedly with a narrower redshift range than considered here. LRG are, however, a special population of old, very massive, passively evolving galaxies. Our sample in MB-II is much more diverse in properties and is heavily dominated by much less massive galaxies that will include a variety of formation and evolutionary histories, including recent mergers and accretion. This is expected to change the intrinsic alignments signal at all scales. We see clear redshift evolution in two of the three samples defined by luminosity bins, with the middle bin showing negligible evolution. For the brightest and faintest samples, we observe that the NLA model amplitude decreases at lower redshifts, which suggests that dynamical processes such as galactic mergers play some role in intrinsic alignments evolution at those luminosities.

To quantify the evolution of intrinsic alignments with redshift, mass and luminosity, we fit the non-linear alignment model amplitude A_I with the following functions:

$$A_I = A \left(\frac{\langle L_r \rangle}{L_0} \right)^{\alpha_L} (1+z)^{\alpha_z} \tag{3.19}$$

$\langle L \rangle$ is the average r-band luminosity, normalized by pivot luminosity L_0 corresponding to r-band magnitude $M_r = -22$. Results from the fitting are shown in Table 3.1. We also show results from similar fitting to power law amplitude and index.

Doing a similar fit to A_I in luminosity and redshift to LRG samples, [82] got

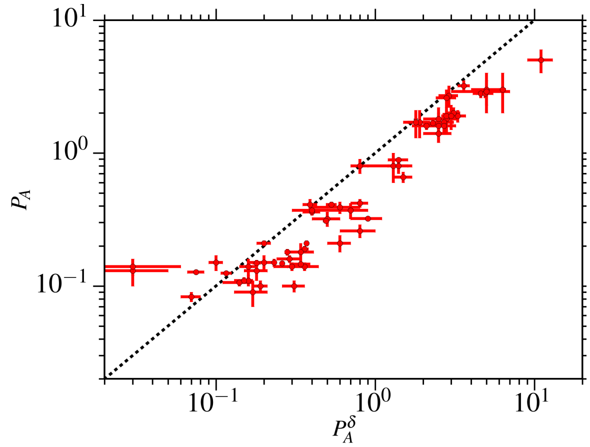

Figure 3.19: Comparison of power law amplitude for w_{g+} (P_A) and $w_{\delta+}$ (P_A^δ) for various samples used in this work. The dotted line shows the $x = y$ relation. $w_{\delta+}$ is observed to have systematically higher amplitude than w_{g+} for separations below $1h^{-1}$Mpc.

$\alpha_L = 1.13^{+0.25}_{-0.20}$ and $\alpha_z = -0.27^{+0.80}_{-0.79}$ (MegaZ-LRG + SDSS LRG + L4 + L3). Our power law indices are different, with our samples showing weaker luminosity evolution than LRGs. This is likely due to differences in the samples, since our samples do not include color cuts, and also extend to fainter luminosities. Our results are qualitatively consistent with results of [86], who used semi-analytical approach to populate dark matter halos in Millennium simulation and measured the intrinsic alignments signal. When they measured intrinsic alignments amplitudes as a function of luminosity, they found a shallower luminosity dependence at the faint end than for LRGs. Our α_z is consistent with zero within 1σ, consistent with [82] and [86].

Table 3.1: Results of fitting different parameters (luminosity bin samples only) to find their mass and luminosity evolution (Eq. 3.20 and 3.19). Different columns are the parameters that go into Eq. (3.20) and (3.19) while different rows are for different intrinsic alignments model parameters, with A_I being the NLA amplitude, P_A and P_I are power law fits (Eq. 3.18) to w_{g+} and P_A^δ and P_I^δ are power law fits to $w_{\delta+}$.

Parameter	A	α_L	α_z
A_I	6.7±1.7	0.47±0.08	0.5±0.5
P_A	0.59±0.08	0.48±0.05	-0.7±0.2
P_I	-0.49±0.08	0.09±0.06	0.5±0.3
P_A^δ	1.5±0.3	0.6±0.1	-1.7±0.5
P_I^δ	-1.1±0.1	0.1±0.03	0.1±0.2

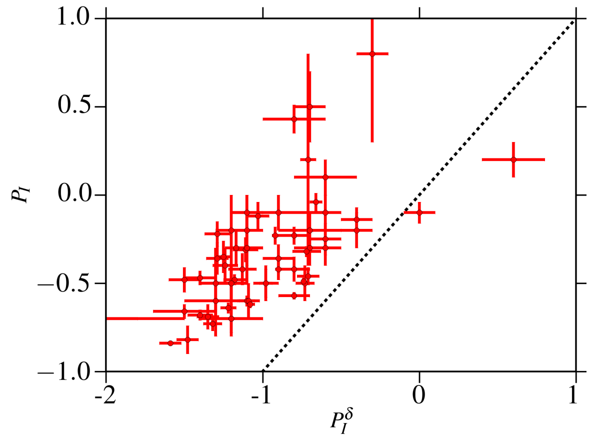

Figure 3.20: Comparison of power law index for w_{g+} (P_I) and $w_{\delta+}$ (P_I^δ) for various samples used in this work. The dotted line shows the $x = y$ relation. $w_{\delta+}$ has a systematically steeper slope than w_{g+} for separations below $1h^{-1}$Mpc.

Figs. 3.19 and 3.20 show the comparisons of power-law parameters (Eq. 3.18) fit to $w_{\delta+}$ and w_{g+} for different samples used in this work. $w_{\delta+}$ has systematically higher amplitude and steeper power-law index than w_{g+}, which implies that w_{g+} is more flattened compared to $w_{\delta+}$ below $1h^{-1}$Mpc. The flattening of w_{g+} at small scales is likely due to the effects of non-linear bias of the subhalo sample used as density tracer. However, as observed in Fig. 3.12, the ratio of $w_{\delta+}/w_{g+}$ changes for different mass threshold samples, which means that there could be some differences due to intrinsic alignments signal as well. Subhalos are biased tracers of density field and it is conceivable that intrinsic alignments signal at small scales can change when subhalos are used as the density tracers (for example, there may not be enough subhalos around a galaxy at small scales to fairly measure the intrinsic alignments signal). This can have important implications for observational studies of intrinsic alignments, where we can only use galaxies as biased tracers of the density field, so the small scale intrinsic alignments could be underestimated.

3.7.2 Comparison with luminous galaxy intrinsic alignments

In Fig. 3.21, we show the w_{g+} correlation function for the subhalos selected by luminosity in r-band such that the absolute AB magnitudes satisfy $M_r \leq -22.6$. The error bars shown here are obtained using the jackkinfe technique. The observational measurements are obtained from an SDSS LRG sample in the redshift range $0.27 < z < 0.35$, with luminosity cuts as defined in [71]. The galaxies from the simulation are selected to match the luminosity threshold of the Bright LRG sample ($M_r \leq -22.6$), against which we compare our results. The amplitude of the predicted w_{g+} for this sample is in good agreement with the observational results for the LRG

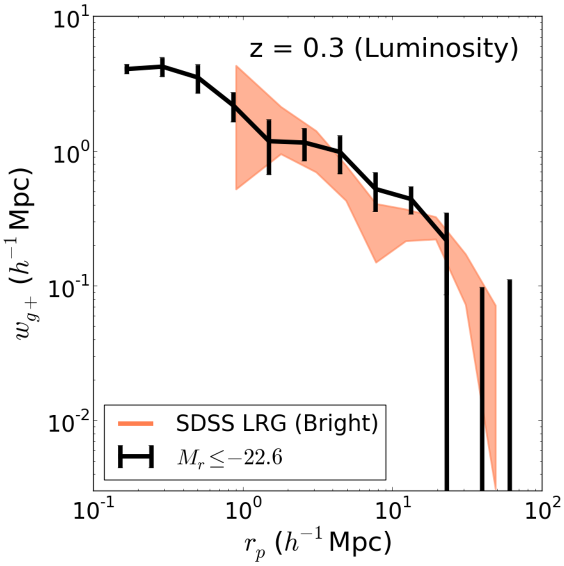

Figure 3.21: w_{g+} correlation function for galaxies selected according to r-band luminosity (such that $M_r \leq -22.6$)and comparison with observational results using SDSS LRG sample. Note that the bias of the density tracer sample has been taken into account in order to make a fair comparison, by dividing w_{g+} with the large scale linear bias.

sample[1]. The mass range of the galaxies from the simulation roughly corresponds to a subhalo mass threshold of $M > 10^{13}h^{-1}M_\odot$ which is indeed the appropriate halo mass range for LRGs. However, there is an important caveat in this comparison. The LRG sample has color cuts and so, unlike the simulated galaxies, the LRG samples are not perfectly luminosity selected. Hence, it is difficult to make an exact comparison of the the amplitude of correlation function in spite of selecting the same luminosity thresholds. If we ignore the amplitude, which is likely to be a nuisance parameter that gets marginalized over in a typical intrinsic alignment mitigation scheme, what is more important is that the scaling with transverse separation is consistent with that in real data, as is the scaling with mass that was shown earlier in this work. This confirms that MB-II can provide reasonable templates for intrinsic alignment models to be used in real data analysis.

3.7.3 Predictions for future weak lensing surveys

Using the SDSS r-band luminosity of galaxies in the simulation, we can make predictions for the $w_{\delta+}$ correlation function for upcoming surveys. However, we do not

[1]The bias of the density sample in both simulations and observations has been taken into account in this comparison.

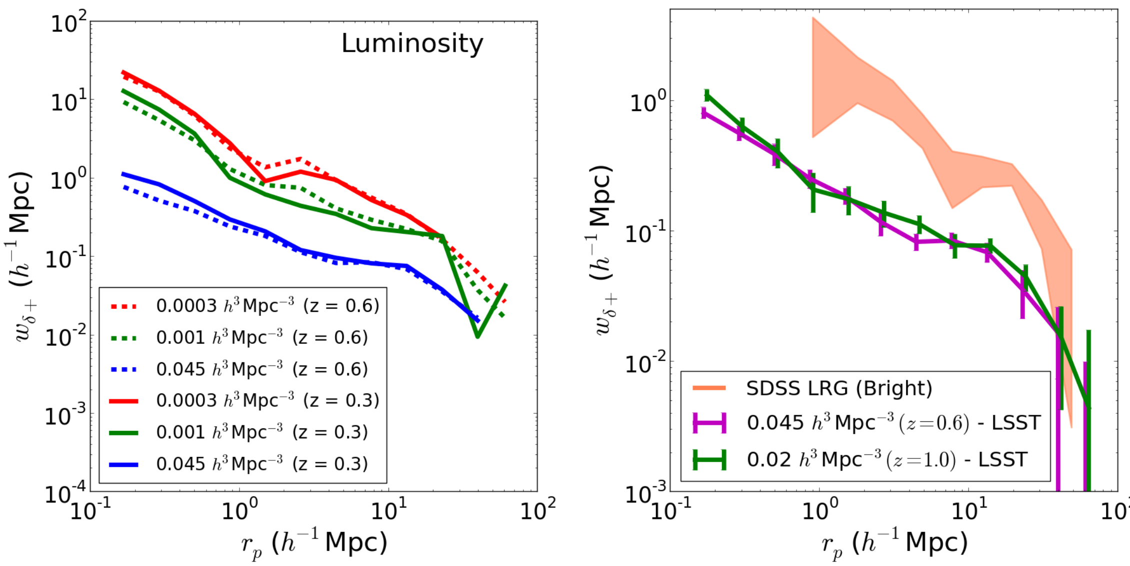

Figure 3.22: *Left:* $w_{\delta+}$ correlation function at redshifts $z = 0.6$ and 0.3 for galaxies selected by a luminosity threshold to match three values of comoving abundance as labeled on the plot. *Right:* Prediction of $w_{\delta+}$ for galaxies that will be used for lensing in the LSST survey, made by matching the estimated comoving abundances at $z = 1.0$ and $z = 0.6$. The shaded regions show jackknife errorbars.

separate the galaxies by their color. So, the IA signals shown here also include the type dependence. Here we focus on $w_{\delta+}$ rather than w_{g+} since the intrinsic alignments contamination of cosmic shear signals is caused by the entire matter density field. In the left panel of Fig. 3.22, we plotted the $w_{\delta+}$ correlation function for galaxy samples selected on the basis of a luminosity threshold with increasing comoving abundance at redshifts $z = 0.3$ and 0.6. Our results suggest that the amplitude of the $w_{\delta+}$ correlation function decreases with increasing comoving abundance at both redshifts, with the shape of the correlation function changing as well (such that the 1-halo to 2-halo transition is no longer evident for lower luminosity samples, perhaps because they occupy host halos with a wide range of masses).

In the right panel of Fig. 3.22, we show the $w_{\delta+}$ signals at $z = 0.6$ and $z = 1.0$ that help us to predict the intrinsic alignments for the galaxies that will be used to measure lensing in the upcoming LSST survey. At redshift $z = 1.0$, the comoving abundance of 0.02 $(h^{-1}\text{Mpc})^{-3}$ corresponds to the estimated number density of galaxies in the LSST. Similarly, at redshift $z = 0.6$, the estimated comoving abundance is 0.045 $(h^{-1}\text{Mpc})^{-3}$. The galaxy number densities mentioned here are based on the results from [31]. From the observational measurements of intrinsic alignments using SDSS LRGs (Fig. 3.21), we know the value of w_{g+} which would be a good match to the signal obtained from a luminosity based comoving number density threshold of

$3 \times 10^{-4} (h^{-1}\text{Mpc})^{-3}$ (left panel of Fig. 3.22). For galaxies in the LSST sample, our results predict that the intrinsic alignments decrease by a factor of ~ 18 for scales below $1h^{-1}$Mpc. At large scales, based on the NLA model fits tabulated in Appendix B.1, we predict that the amplitude of the signal decreases by a factor of ~ 5 at $z = 0.6$ compared to the measured signal using LRGs.

Fig. 3.23 shows the evolution of NLA amplitude A_I, for different samples defined by mass threshold and comoving abundance. We observe clear evolution with mass and luminosity with more massive and luminous objects having stronger alignments. We also observe mild evolution in redshift which is inconsistent with NLA assumption that intrinsic alignments are setup at time of galaxy formation, if we assume that all our galaxies formed at $z \gg 1$. This assumption is however likely to break down over the broad redshift and mass range of our sample, due to growth of structure as well as dynamical evolution of galaxies which will bring the intrinsic alignments signal down, consistent with our results. As in Sec. 3.7.1, to quantify the luminosity and redshift evolution of intrinsic alignments amplitude we fit a power law defined in Eq. (3.19) to luminosity threshold samples and a similar power law in average mass and redshift as defined in Eq. (3.20) to mass threshold samples.

$$A_I = A \left(\frac{\langle M \rangle}{10^{13} h^{-1} M_\odot} \right)^{\alpha_M} (1 + z)^{\alpha_z} \tag{3.20}$$

Since A and α_z are same for both luminosity and mass threshold samples we fit both luminosity and mass threshold samples simultaneously to get all the parameters. Parameters are given in Table 3.2. We note that our samples defined by threshold cuts are correlated and hence the values given in Table 3.2 should not be directly compared with observational results, where samples are usually defined in luminosity or mass bins. The purpose of our fits given here is to give scaling relations for overall expected intrinsic alignments for sources that will be used to measure lensing in surveys like LSST and Euclid, for which the source samples will likely be derived from taking most of the galaxies above some flux cut.

3.8 Conclusions

In this paper, we used the MB-II cosmological hydrodynamic simulation to study the intrinsic alignments of galaxies using the Ellipticity-Direction (ED) and the projected shape correlation function (w_{g+}). We are able to directly measure the shapes of the stellar matter component of the galaxies and use these to estimate the two-point correlation functions which can be compared with intrinsic alignment measurements from observations. The use of hydrodynamic simulations, which include the physics of galaxy formation, has an advantage over N-body simulations in that we do not have to make assumptions about the occupation of halos with galaxies and their alignments with the host halo. We also have information on the luminosities of galaxies in the

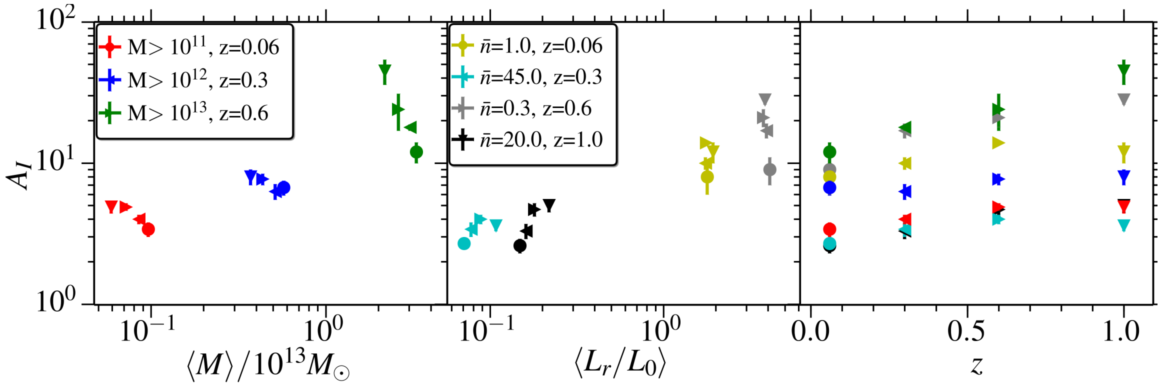

Figure 3.23: NLA amplitude, A_I, as a function of different sample properties. The horizontal axis indicates the average mass, luminosity or redshift of different samples. Points are colored by sample definition: comoving abundance ($\bar{n}$) in units of $10^{-3}h^3\mathrm{Mpc}^{-3}$ based on a luminosity threshold, or the mass threshold of the sample (not average mass), while markers are set according to the redshift.

Table 3.2: Results of fitting different parameters (for mass and luminosity threshold samples only) to find their mass and luminosity evolution (Eq. 3.20 and 3.19). Different columns are the parameters that go into Eq. (3.20) and (3.19) while different rows are for different intrinsic alignments model parameters, with A_I being the NLA amplitude, P_A and P_I are power law fits (Eq. 3.18) to w_{g+} and P_A^δ and P_I^δ are power law fits to $w_{\delta+}$.

Parameter	A	α_M	α_L	α_z
A_I	7.7±0.5	0.35±0.03	0.48±0.03	0.69±0.16
P_A	0.65±0.04	0.57±0.03	0.7±0.04	-0.2±0.2
P_I	-0.42±0.05	-0.09±0.06	0.1±0.09	0.1±0.3
P_A^δ	1.23±0.12	0.53±0.04	0.58±0.04	-1.0±0.2
P_I^δ	-1.05±0.06	0.14±0.02	0.11±0.02	0.0±0.1

simulation, which is useful for comparisons with observations and making predictions of intrinsic alignments for upcoming surveys.

It is necessary to adopt a definition for the shapes of dark matter and stellar matter components in subhalos. We investigated the variation in the distribution of axis ratios of shapes obtained using iterative and non-iterative forms of the unweighted and reduced inertia tensor. The axis ratios and orientations of the shapes obtained using unweighted iterative and non-iterative inertia tensor are very similar. For comparison with observations, it might be useful to use the reduced form of inertia tensor which gives more weight to particles in the inner regions of a subhalo. The non-iterative reduced inertia tensor produces shapes that are biased towards being very spherical and hence is not considered. The axis ratios of shapes defined by dark matter subhalos obtained using the iterative reduced inertia tensor have slightly larger axis ratios when compared with those obtained using the unweighted inertia tensor, which is in agreement with the findings of [16]. For shapes defined by stellar matter, the reduced inertia tensor produces shapes which are slightly more oblate.

We can also define a luminosity weighted unweighted and reduced inertia tensors for shapes of stellar matter. We concluded that the shapes obtained using the unweighted inertia tensor are similar when the star particle is weighted by its luminosity or mass. However, we observe noticeable changes in the distribution of axis ratios for shapes obtained using the reduced form of the inertia tensor when we weight each particle by its luminosity. This is not surprising, as it indicates that the mass to light ratio is not constant in the inner regions of galaxy, which is expected. However, our results suggest this effect of luminosity-weighting does not affect the intrinsic alignment signals which are consistent with the ED and w_{g+} determined using shapes from mass-weighted inertia tensor.

To investigate the color dependence of intrinsic alignments, the galaxies in the simulation are roughly divided into red and blue types by choosing a median value of the rest-frame color, $M_u - M_r$. By comparing the w_{g+} correlation function for red and blue galaxies, we concluded that there is no significant difference in the ED and w_{g+} correlation functions for red and blue galaxies.

We measured the dependence of the two-point correlation functions, ED (position angle statistic) and w_{g+} (projected shape correlation function), on the mass and redshift. The w_{g+} correlation function is more relevant for comparison with many observational results and for contamination of upcoming weak lensing measurements by intrinsic alignments, given that it includes the overall galaxy shape. For both ED and w_{g+}, the amplitude of the correlation function is smaller for shapes defined by the reduced form of the inertia tensor. By plotting the correlation functions for galaxy samples selected in the mass bins, $10^{11-12}h^{-1}M_{\odot}$, $10^{12-13}h^{-1}M_{\odot}$ and $10^{13-15}h^{-1}M_{\odot}$, we concluded that the amplitude of the correlation function increases strongly with increasing mass. We also consider the redshift dependence of ED and w_{g+} correlation functions. For the ED correlation function, the amplitude of the correlation function decreases at low redshifts, which indicates that the shape defined by the stellar component tends to get slightly less correlated with the density field traced by subhalos. Our findings for the mass and redshift dependence of ED correlation function using the shapes of stellar matter are similar to the conclusions of [109] based on N-body simulations. However, we do not notice a significant redshift dependence for the w_{g+} correlation function for fixed mass threshold samples.

The simulation also allows us to directly study the intrinsic alignment in centrals and satellite galaxies, as it is possible to split our subhalos into centrals and satellites. Previously, the intrinsic alignments in centrals and satellites has been modeled analytically using the halo model [137]. Here, we concluded that in low mass galaxies, the satellites have larger intrinsic alignment when compared to centrals at small scales (i.e., in the language of the halo model, the satellite galaxies have a stronger one-halo term than the centrals). At large scales, the intrinsic alignment signal for satellite galaxies goes down and is smaller than those for central galaxies (centrals have a larger two-halo term than satellites). We do not observe statistically significant differences in the intrinsic alignments of centrals and satellites in more massive galaxies.

We also fit non-linear alignment model (NLA) in the range $6h^{-1}\mathrm{Mpc} < r_p < 25h^{-1}\mathrm{Mpc}$ and study the evolution of with mass, luminosity and redshift. The NLA amplitude A_I increases with mass and luminosity, qualitatively consistent with LRGs observations though our scalings are different from LRGs observations, possibly due to our focus on lower luminosity galaxies.We also fit a simple power law model to study intrinsic alignments at small scales, and observe that intrinsic alignments signal gets lower and more flattened as we go to lower mass and luminosities. We observe that intrinsic alignments get more flattened for w_{g+} as compared to $w_{\delta+}$, which implies that sub halos don't allow a fair measurement of intrinsic alignments signal at small scales. This has important implications for observations, where we can only use galaxies to trace the density field.

Finally, we are able to make predictions for the intrinsic alignments for upcoming surveys at redshifts $z = 1.0$ and $z = 0.6$ by calculating the $w_{\delta+}$ correlation function (cross-correlation of projected shapes with density field traced by dark matter particles). For these predictions, we select galaxy samples based on a threshold in luminosity such that the comoving abundance matches the expected number density of galaxies at the given redshifts. We concluded that, as expected, the amplitude of $w_{\delta+}$ correlation decreases as we go to larger comoving abundances. This result is important as we already have the observationally measured result for w_{g+} using data from the SDSS LRG sample. Using our results from simulation, we predict that for galaxies that will be used to measure lensing in the LSST survey, the IA signal decreases by a factor of $\sim$ 5–18 depending on the radial separation (from ~ 30 down to $\sim 0.5h^{-1}\mathrm{Mpc}$) compared to the measured value for LRGs. This differs from the conclusion of [37], where they detected no intrinsic alignment signal in their sample of reddest galaxies at $z = 1.2$. The difference can be due to the fact that [37] define shapes with a spin statistic which is suitable for blue galaxies. As mentioned in their paper, spins do not fully capture the shape of a galaxy or the effects of intrinsic alignments on the two-point shear statistics. It is also to be noted that their hydrodynamics is implemented based on AMR code. As our approach is based on SPH, it will be interesting to directly compare the intrinsic alignments of galaxies using a similarly defined observable to understand the differences due to numerical implementation.

In future work, we will compare the results of our two-point correlation function with predictions from a dark matter only simulation run with the same initial conditions, in order to understand the importance of the physics of galaxy formation and processes such as feedback on the intrinsic alignments. We will also try to apply additional post-processing techniques to match the color of galaxies in our simulation to those from observational results. However, the results in this work suggest that high-resolution and large-volume SPH simulations such as MB-II will be a powerful tool for predicting and mitigating intrinsic alignments in future weak lensing surveys.

Chapter 4

Galaxy shapes and alignments in Dark matter-only simulations

4.1 Introduction

Weak gravitational lensing is a cosmological probe that has the potential to address major outstanding cosmological problems, such as understanding the connection between dark matter and galaxies, the nature of dark energy, and exploring possible variations in the theory of gravity on cosmological scales [4, 174]. Using weak lensing, upcoming surveys such as the Large Synoptic Survey Telescope[1] (LSST; [114]), Euclid[2] [106], and the Wide-Field Infrared Survey Telescope[3] (WFIRST; [145]) will to constrain cosmological parameters such as the dark energy equation of state to a very high precision. However, the most basic weak lensing analysis assumes that galaxy shapes are randomly aligned, which is not correct in reality. The galaxy shapes are correlated with each other and with the underlying density field. This intrinsic alignment of galaxy shapes is an important astrophysical systematic that contaminates measurements in weak lensing surveys [66, 41, 78, 72]. For reviews on intrinsic alignments and its impact on cosmological parameter constraints, see [161], [80], [97], and [95].

Previous studies of intrinsic alignments that made predictions out to tens of Mpc scales have generally involved analytical methods, or N-body and hydrodynamic simulations of cosmological volume. Analytical modeling involves a number of different possible models, with the one receiving the most attention for elliptical galaxies being the linear alignment model [72], an extension of it to nonlinear scales using the non-linear power spectrum ([24]; see [20] for a more recent extension that includes all non-linear terms at the same order), and a small-scale extension using the halo model [137]. N-body simulations have been used to study intrinsic alignments by

[1] http://www.lsst.org/lsst/

[2] http://sci.esa.int/euclid/, http://www.euclid-ec.org

[3] http://wfirst.gsfc.nasa.gov

[68] where halos are populated with galaxies which are stochastically misaligned, [86] with semi-analytic models, and others (see references in the review by [95]). However, the physics of galaxy formation is not taken into consideration by these analytic models and N-body simulations. Recent hydrodynamic simulations of cosmological volumes such as the MassiveBlack-II [94], the Horizon-AGN [51], and the EAGLE and cosmo-OWLS [164] simulations have made it possible to directly study the intrinsic alignments of the stellar component of galaxies and their scaling with mass, luminosity and distance.

Using the MassiveBlack-II (MBII) simulation, we previously studied the shapes of the stellar matter component of the galaxies and its alignment with the shape of the dark matter component [156]. We found that the ellipticities of the stellar components of galaxies compare favorably with those in observations, and that the shape of the stellar component is misaligned with the dark matter component, with average misalignment angles ranging from $\sim 10°$ to $30°$. In [158], we extended this study to two-point statistics and explored their dependence with mass, luminosity and distance. We found that the intrinsic alignments of massive galaxies in the simulation have a scaling with transverse distance that is consistent with results from observational measurements. Large volume hydrodynamic simulations are proving to be extremely useful in quantifying intrinsic alignment signals. However, they are also very computationally expensive. Hence, it would be useful to develop methods to paint the intrinsic alignments of galaxies onto N-body simulations. Since there is no baryonic component in N-body simulations, the shapes of galaxies are determined by modeling the subhalos as ellipsoids using only the positions of the dark matter particles belonging to them [68, 139, 85]. However, it is known that the halo shapes and orientations in N-body simulations overestimate the intrinsic alignments when compared with observational results [68]. Hence, a direct comparison of intrinsic alignments in hydrodynamic and N-body simulations is necessary. In this paper, we use the MassiveBlack-II dark matter-only (DMO) simulation that has been performed with the same resolution, box size, initial conditions, and cosmological parameters as the hydrodynamic simulation (MBII) to compare the intrinsic alignments of galaxies in MBII and halos in DMO.

To predict the intrinsic alignment of galaxies from dark matter-only simulations accurately, it is important to have an average mapping that statistically determines the ellipticity and orientation of the stellar matter component of the subhalo with respect to that of the dark matter component. Here, the radius at which the shape of the dark matter subhalo is measured matters, as it has been shown using N-body simulations that the shapes of dark matter component change with radius [5, 105, 139]. Further, it is also known that the dark matter halo shapes in hydrodynamic simulations are different from those in N-body simulations due to the effects of baryonic physics, which leads to rounder shapes [91, 26]. Here, we study the radial dependence of the distribution of dark matter halo axis ratios in the MBII and DMO simulations, and compare with the shape of the stellar matter component in MBII. We also study the orientation of the stellar shape with the shape of dark matter component in MBII and DMO measured at different radii. The change in the orientation of the dark matter shapes in the subhalos measured at different radii has been previously studied using N-body simulations [e.g.,][][9, 139]. Using small volume hydrodynamic simulations, [8], [44] and others (see references in the review by [95]) found that the inner shape of the dark matter component is well aligned with the galaxy orientation. However, it will be useful to compare the orientation of stellar shape in the hydrodynamic simulation with the shape of the dark matter component measured at different radii in the matched subhalo of a dark matter-only simulation. This comparison is what will enable the mapping of intrinsic alignments in hydrodynamic simulations onto dark matter-only simulations.

This paper is organized as follows. In Section 6.3, we describe the details of the simulations used in this study followed by the method adopted to determine the shapes of galaxies and the definitions of two-point statistics. In Section 4.3, we match the subhalos in both simulations and compare shapes and misalignment angles. A brief discussion of the comparison of mass functions and dark matter power spectrum in the two simulations is also included here. In Section 4.4, we analyze the radial dependence of shapes and orientations of the dark matter component in subhalos. In Section 4.5, we compare the two-point correlation functions using shapes defined by the dark matter component in MBII and DMO, and the stellar shapes from MBII. Note that we only discuss the correlation of galaxy shapes with the density field traced by dark matter particles. We do not discuss the correlation of galaxy shapes with each other due to the signals being extremely noisy. Further, the intrinsic alignments of galaxies are not measured as a function of morphological type, which is deferred for a future study. Finally, we summarize our conclusions in Section 6.6.

4.2 Methods

4.2.1 Simulations

Table 4.1: Simulation parameters: box size (L_{box}), force softening length (ϵ), number of particles (N_{part}), mass of dark matter particle (m_{DM}) and mass of gas particle (m_{gas})

Parameters	Hydrodynamic (MBII)	Dark Matter Only (DMO)
L_{box} (h^{-1}Mpc)	100	100
ϵ (h^{-1}kpc)	1.85	1.85
N_{part}	2×1792^3	1792^3
m_{DM} ($h^{-1}M_\odot$)	1.1×10^7	1.32×10^7
m_{gas}($h^{-1}M_\odot$)	2.2×10^6	0

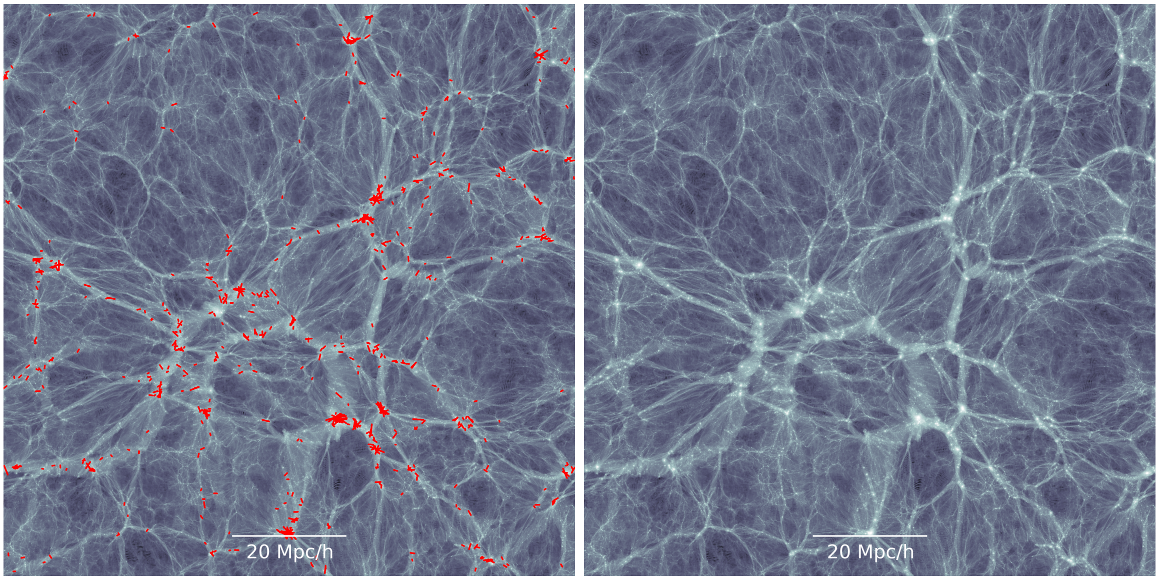

Figure 4.1: Snapshot of the MBII (left) and DMO (right) simulations in a slice of thickness $2h^{-1}$Mpc at $z = 0.06$. The shading represents the density distribution of dark matter, and the red lines show the alignment of stellar shapes in MBII. The length of the lines is proportional to the size of major axis of the ellipse representing stellar shape.

In this study, we use the MassiveBlack-II hydrodynamic (MBII, [94]) and Dark Matter Only (DMO) simulations. MassiveBlack-II is a state-of-the-art high resolution, large volume, cosmological simulation of structure formation. These simulations have been performed in a cubic periodic box of size $100h^{-1}$Mpc on a side using P-GADGET, which is a hybrid version of the parallel code, GADGET2 [147] that has been upgraded to run on Petaflop-scale supercomputers. The total number of dark matter particles in both the simulations is 1792^3 with an equal initial number of gas particles in the hydrodynamic run. The cosmological parameters are chosen according to WMAP7 [102], with amplitude of matter fluctuations $\sigma_8 = 0.816$, spectral index $n_s = 0.96$, matter density parameter $\Omega_m = 0.275$, cosmological constant density parameter $\Omega_\Lambda = 0.725$, baryon density parameter $\Omega_b = 0.046$ (in MBII), and Hubble parameter $h = 0.702$. Table 4.1 shows the box size ($\mathrm{L_{box}}$), force softening length (ϵ), total number of particles including dark matter and gas (N_{part}), mass of dark matter particle (m_{DM}) and initial mass of gas particle (m_{gas}) for the two simulations. MBII includes the physics of a multiphase interstellar medium (ISM) model with star formation [149], black hole accretion and feedback [147, 45] in addition to gravity and smoothed-particle hydrodynamics (SPH). Radiative cooling and heating processes are included [as in][][90], as is photoheating due to an imposed ionizing UV background. Further details about the hydrodynamic simulation, MBII, can be found in [94]. The

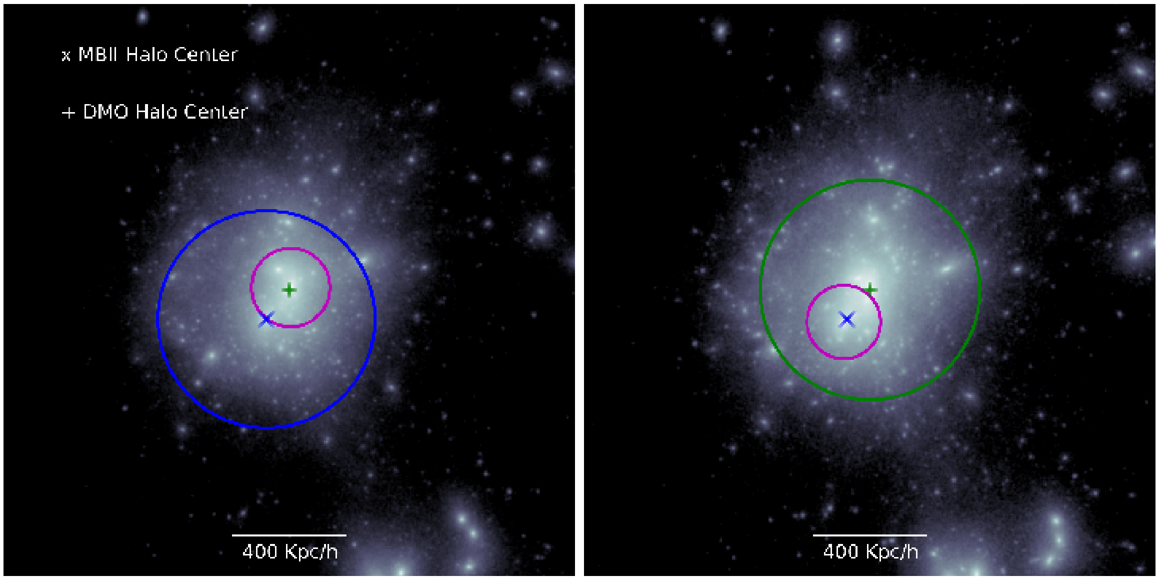

Figure 4.2: Snapshot of a massive halo ($\sim 10^{14}h^{-1}M_{\odot}$) in the MBII (left) and DMO (right) simulations, showing the density distribution of dark matter at $z = 0.06$. The blue and green circles show the virial radii of the central subhalos in MBII and DMO simulation, respectively which are centered at the location with highest density. In both the panels, 'x' and '+' indicate the locations of the central subhalo centers in the MBII and DMO simulations, respectively. The magenta circles show the virial radii of a nearby satellite subhalo.

dark matter-only simulation, DMO, is performed with the same volume, resolution, cosmological parameters and initial conditions as in MBII. Figure 4.1 shows snapshots of the dark matter distribution in a slice of $2h^{-1}$Mpc thickness at $z = 0.06$ in both the MBII and DMO simulations. As expected, the dark matter distributions appear to be nearly identical on large scales. For further comparison, we also show the dark matter distribution in an isolated halo in Figure 4.2. In the left panel, the blue and magenta circles show the virial radius of the central subhalo and a nearby satellite subhalo respectively in the MBII simulation. Similarly, the green and magenta circles depict the virial radius of the central and a nearby satellite subhalo in the DMO simulation. In both the panels, 'x' and '+' indicate the locations of the centers of central subhalos in the MBII and DMO simulations, respectively. Here, we can clearly see small differences in the distribution of dark matter within the dark matter halo virial radius which, as we shall see, can lead to changes in the shapes and orientations of the halos and subhalos.

The halo catalogs in the simulations are generated using the friends of friends (FoF) halo finder algorithm [43] with a linking length of 0.2 times the mean interparticle separation. The subhalo catalogs are generated using the SUBFIND code [151] on the halo catalogs. Here subhalos are locally overdense, self-bound groups of particles within the halo. Groups of particles are identified as subhalos if they have at least 20 gravitationally bound particles. When performing our analysis, however, we use only subhalos from the hydrodynamic simulation with at least 1000 dark matter and star particles based on the convergence test in [156].

4.2.2 Shapes of dark matter subhalos

In this section, we describe the measurements of dark matter and stellar matter component shapes in subhalos. We model these shapes as ellipsoids in three dimensions using the eigenvalues and eigenvectors of the reduced inertia tensor. The projected shapes are calculated by projecting the halos and subhalos onto the XY plane and modeling the shapes as ellipses. In 3D, the eigenvectors of the inertia tensor are $\hat{e}_a, \hat{e}_b, \hat{e}_c$ with corresponding eigenvalues $\lambda_a, \lambda_b, \lambda_c$, where $\lambda_a > \lambda_b > \lambda_c$. The eigenvectors represent the principal axes of the ellipsoid, with the lengths of the principal axes (a, b, c) given by the square roots of the eigenvalues $(\sqrt{\lambda_a}, \sqrt{\lambda_b}, \sqrt{\lambda_c})$. The 3D axis ratios are defined as

$$q = \frac{b}{a},\ \ s = \frac{c}{a} \tag{4.1}$$

In 2D, the eigenvectors are $\hat{e}'_a, \hat{e}'_b$ with corresponding eigenvalues λ'_a, λ'_b, where $\lambda'_a > \lambda'_b$. The lengths of the major and minor axes are $a' = \sqrt{\lambda'_a}$ and $b' = \sqrt{\lambda'_b}$ with axis ratio $q_{2d} = b'/a'$.

The shapes are determined using an iterative method based on the reduced inertia tensor:

$$\widetilde{I}_{ij} = \frac{\sum_n m_n \frac{x_{ni}x_{nj}}{r_n^2}}{\sum_n m_n} \tag{4.2}$$

where

$$r_n^2 = \sum_i x_{ni}^2 \tag{4.3}$$

This definition of inertia tensor gives more weight to particles that are closer to the center which is desirable since it eliminates the bias due to loosely bound particles present in the outer regions of the subhalo. In the iterative method, we first determine the axis ratios by the standard definition of the reduced inertia tensor using all the particles of a given type in the subhalo. Keeping the enclosed volume constant [as in][][139], we rescale the lengths of the principal axes of ellipsoids accordingly. After this rescaling, we determine the shapes again, discarding particles outside the ellipsoidal volume. This process is repeated until convergence is reached. Our convergence criterion is that the fractional change in axis ratios must be below 1%. We considered the impact of using different definitions of the inertia tensor on the distributions of shapes and the intrinsic alignment two-point correlation functions in a previous study [158].

4.2.3 Misalignment angle

To study the relative orientation between the shapes defined by the dark matter and stellar matter components in subhalos, we compute the probability distributions of misalignment angles as in [156]. If $\hat{e}_{da}$ and $\hat{e}_{ga}$ are the major axes of the shapes defined by the dark matter and stellar matter components, respectively, then we can define the misalignment angle by

$$\theta_m = \arccos(|\hat{e}_{da} \cdot \hat{e}_{ga}|). \tag{4.4}$$

In previous work [156, 158], we studied the distribution of misalignment angles between the shapes of the stellar component and dark matter component in the subhalos of MBII. Here, our aim is to study the misalignment angles between the shapes of stellar component in MBII and the dark matter component in the corresponding subhalo of the DMO simulation. Since the simulations have been performed with the same initial conditions, this is a well-defined comparison, and the resulting distributions will be helpful to paint galaxies onto N-body simulations by providing the necessary probability distributions from which to draw the galaxy orientation.

4.2.4 Two-point statistics

To quantify the intrinsic alignments of galaxies with the large-scale density field, we use the ellipticity-direction (ED) and the projected shape-density ($w_{\delta+}$) correlation functions. The ED correlation quantifies the position angle alignments of galaxies in 3D, while the projected shape correlation function can be used to compare against observational measurements that include the 2D shape of the galaxy.

The ED correlation function cross-correlates the orientation of the major axes of subhalos with the large-scale density field. For a subhalo centered at position $\mathbf{x}$ with major axis direction $\hat{e}_a$, let the unit vector in the direction of a tracer of the matter density field at a distance r be $\hat{\mathbf{r}} = \mathbf{r}/r$. Following the notation of [109], the ED cross-correlation function is given by

$$\omega(r) = \langle | \, \hat{e}_a(\mathbf{x}) \cdot \hat{\mathbf{r}}(\mathbf{x}) \, |^2 \rangle - \frac{1}{3} \tag{4.5}$$

which is zero for galaxies randomly oriented according to a uniform distribution.

The matter density field can be represented using either the positions of dark matter particles (in which case the correlation function is denoted by the symbol ω_δ) or the positions of subhalos (in which case it includes a factor of the subhalo bias, and is simply denoted ω). Here, we only use ω_δ to eliminate the effect of subhalo bias.

The projected shape correlation functions are computed to directly compare our results from simulations with observations. Here, we follow the notation of [117] to define the galaxy-intrinsic shear correlation function, $\hat{\xi}_{g+}(r_p, \Pi)$ and the corresponding projected two-point statistic, $w_{\delta+}$. Here, r_p is the comoving transverse separation of a pair of galaxies in the XY plane and Π is their separation along the Z direction.

If $q_{2d} = b'/a'$ is the axis ratio of the projected shape of the dark matter or stellar matter component of a subhalo, and ϕ is the major axis position angle with respect to the reference direction (tracer of the density field), the components of the ellipticity are given by

$$(e_+, e_\times) = \frac{1 - q_{2d}^2}{1 + q_{2d}^2} \left[\cos(2\phi), \sin(2\phi)\right], \tag{4.6}$$

where e_+ refers to the radial component and $e_\times$ is the component at 45°. The matter-intrinsic shear correlation function cross-correlates the ellipticity of galaxies with the matter density field,

$$\hat{\xi}_{\delta+}(r_p, \Pi) = \frac{S_+D - S_+R}{RR} \tag{4.7}$$

where S_+ represents the "shape sample" which is selected on the basis of a threshold or binning in subhalo mass. The dark matter particles used to trace the density field form a "density sample" denoted by D. S_+D is the following sum over all shape sample vs. dark matter particle pairs with separations r_p and Π:

$$S_+D = \sum_{i \neq j | r_p, \Pi} \frac{e_+(j \mid i)}{2\mathcal{R}}, \tag{4.8}$$

where $e_+(j|i)$ is the + component of the ellipticity of a galaxy (j) from the shear sample relative to the direction of a tracer of density field (i) selected from the density sample. Here, $\mathcal{R} = (1 - e_{\rm rms}^2)$ is the shear responsivity that converts from distortion to shear [14], with $e_{\rm rms}$ being the RMS ellipticity per component of the shape sample. S_+R is defined by a similar equation for the correlation of the data sample with a random density field distribution to remove observational systematics in the shear estimates, so we neglect this term here. The RR term in Eq. 6.13 is given by the expected number of randomly-distributed points in a particular (r_p, Π) bin around galaxies in the shape sample.

The projected shape correlation function, $w_{\delta+}(r_p)$ is now given by

$$w_{\delta+}(r_p) = \int_{-\Pi_{\rm max}}^{+\Pi_{\rm max}} \hat{\xi}_{\delta+}(r_p, \Pi)\, \mathrm{d}\Pi \tag{4.9}$$

We calculated the correlation functions over the whole length of the box ($100h^{-1}$Mpc) with $\Pi_{\rm max} = 50h^{-1}$Mpc. The projected correlation functions are obtained via direct summation.

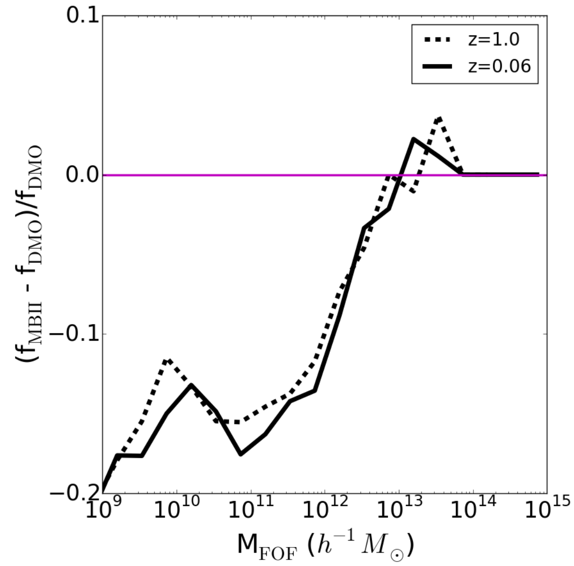

Figure 4.3: Comparison of the halo mass function in MBII and DMO simulations at $z = 1.0$ and $z = 0.06$.

4.3 Results

4.3.1 Mass function

In Figure 4.3, we compare the mass function of halos, which is defined as the number density of halos per unit mass interval, in MBII and DMO simulations at redshifts $z = 1$ and $z = 0.06$. At both redshifts, there are differences in the dark matter halo mass function in MBII. There are $\sim 10 - 20\%$ more halos in the DMO simulation at low masses ($10^9 - 10^{12} h^{-1} M_\odot$). This fraction decreases at higher masses. [167] found similar results using the OWLS simulation with resolved halos in the mass range $10^{12} - 10^{15} h^{-1} M_\odot$ (based on $M_{200}^{\rm mean}$). However, [167] find an even larger suppression in their halo mass function, possibly due to a stronger AGN feedback model. Suppression of the mass function due to baryonic effects seems to be a fairly generic finding (e.g., see also [42] and [22]) though with the amount of suppression and the masses at which it is relevant varying depending on the details of the star formation and feedback prescription. This suppression of mass function can be explained by the decrease in the FOF mass of halos in MBII. To illustrate further, we plotted the median of the fractional difference in the FOF mass of the matched halos of MBII and DMO simulation in Figure 4.4. We find that the halo mass is smaller in the hydrodynamic simulation by $\sim 10 - 20\%$ in the low mass range.

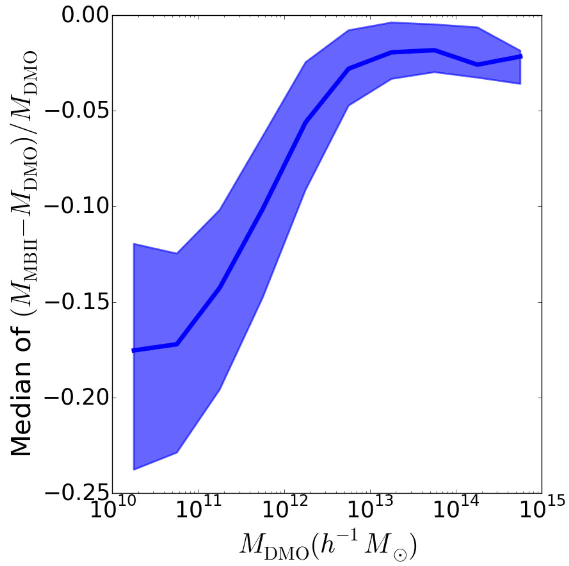

Figure 4.4: Median and scatter (defined using the 16^{th} and 84^{th} percentiles) of the fractional difference in the FOF mass of matched halos of MBII and DMO simulations at $z = 0.06$.

4.3.2 Matter correlation function and power spectrum

Figure 4.5 shows a comparison of the 3D dark matter two-point correlation function and power spectrum at $z = 1.0$ and $z = 0.06$ in the MBII and DMO simulations. To calculate the two-point correlation function, we randomly subsampled 4×10^5 dark matter particles and tested that the correlation function has already converged using a smaller subset. The power spectrum is calculated by taking the Fourier transform of the two-point correlation function,

$$P(k) = 4\pi \int_0^{\sqrt{3}\Pi_{\mathrm{max}}} \xi(r) r^2 \frac{\sin(kr)}{kr}\, \mathrm{d}r. \tag{4.10}$$

From the left panel of the figure, we observe that $\xi(r)$ is larger at small scales ($< 1h^{-1}$Mpc) in the MBII simulation, presumably due to baryonic physics. At these scales, the correlation function is larger in MBII by a factor of $\sim 10\%$, and the discrepancy is larger at lower redshift. At intermediate scales (above $\sim 1h^{-1}$Mpc), we find that the ratio of the correlation functions approaches unity with no significant redshift dependence. The enhancement of the correlation function at small scales is compensated by a decrease in clustering at scales comparable to the box size.

The right panel of Fig. 4.5 shows a comparison of the matter power spectra, demonstrating that the dark matter power spectrum in the hydrodynamic run is enhanced by $\sim 10\%$ at $k \geq 10h/$Mpc, with the effect again being stronger at low

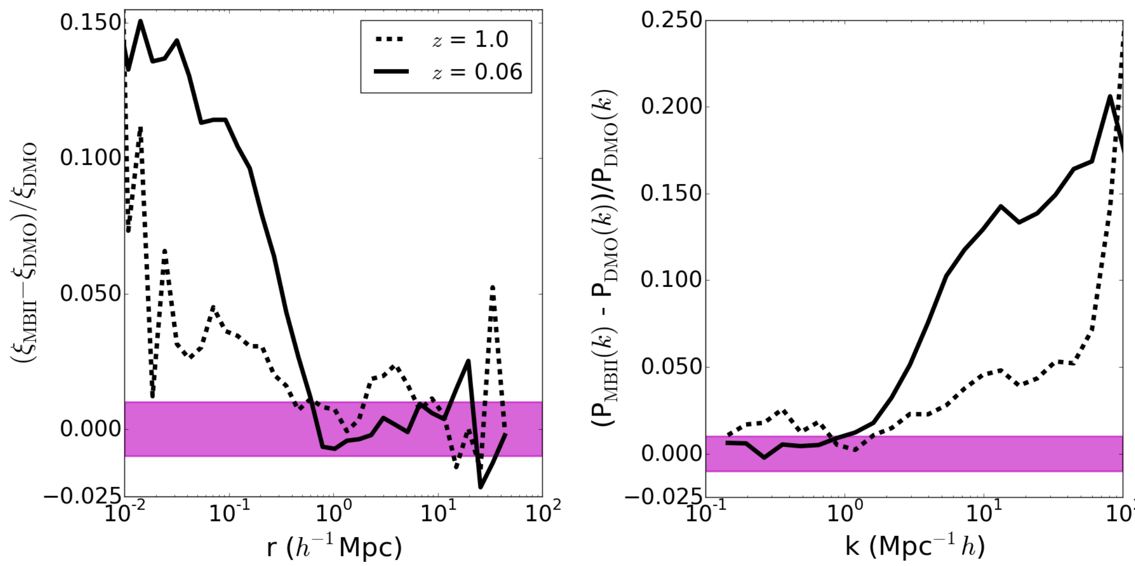

Figure 4.5: Fractional difference between the dark matter two-point correlation functions (left) and power spectra (right) in DMO and MBII simulations at $z = 1.0$ and $z = 0.06$. The shaded regions represent a deviation within $\pm 1\%$.

redshift. In contrast to our results, [162] found that the dark matter power spectrum is suppressed at intermediate scales in the OWLS simulation that included AGN feedback. However, the small scale enhancement of power seems to be fairly generic across hydrodynamic simulations (e.g., [131]). The purple band in this plot indicates the target precision of ~ 1 per cent accuracy in predictions of the matter power spectrum on scales of $0.1h$ Mpc^{-1} $< k <$ $10h$ Mpc^{-1} [76, 65]. This level of accuracy in the theoretical predictions is necessary to avoid systematic errors in constraining cosmological parameters. [177, 53] and [118] discuss approaches to mitigate the potentially large differences in the matter two-point correlations and reduce the uncertainty to the necessary level.

4.3.3 Matching subhalos in MBII and DMO

To make a fair comparison between intrinsic alignments of galaxies and halos in the MBII and DMO simulations, we matched the subhalos in both simulations. The subhalos are matched using the unique ID's of the dark matter particles in both the DMO and MBII simulations. For a given subhalo in the MBII simulation with at least 1000 dark matter and star particles, we identify the subhalo in the DMO simulation that has the highest number of dark matter particles with the same IDs as in the MBII subhalo. This subhalo in the DMO simulation is linked to the subhalo in MBII if the fraction of common dark matter particles is greater than 50% of the

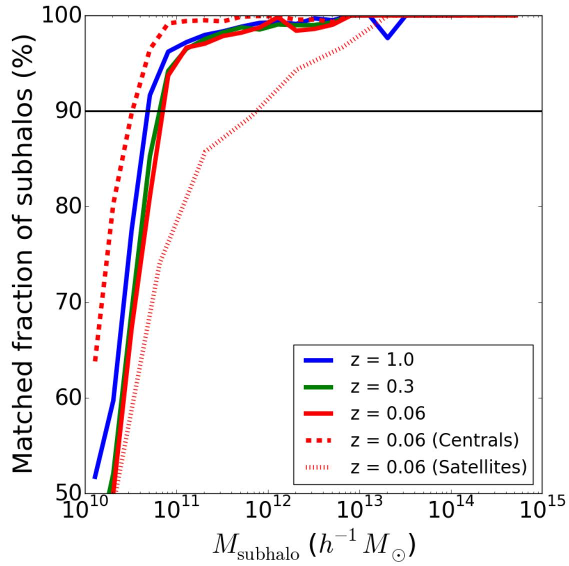

Figure 4.6: Fraction of subhalos matched at $z = 1.0$, 0.3, and 0.06 as a function of the total subhalo mass in the MBII simulation.

total number of dark matter particles in the subhalos of each simulation. Figure 4.6 shows the matched fraction of subhalos as a function of mass. We observe that the fraction of matched subhalos increases with mass and approaches unity. For the rest of this paper, we will only consider subhalos with mass greater than $10^{10.8}h^{-1}M_\odot$, where the matched fraction exceeds 90%.

The decrease in the fraction of matched subhalos at lower masses is due to an increase in the number of satellite subhalos. The fraction of central subhalos matched even in the lower mass bin, $10^{10.8-11.0}h^{-1}M_\odot$, is $\sim 99\%$. As illustrated in Figure 4.2, there are small but visible differences in the smallest subhalo population in a matched halo of mass $\sim 10^{14}h^{-1}M_\odot$ (for example, some missing or merged subhalos in MBII). We also attempted to match subhalos using only the 50 innermost dark matter particles, and obtained results that were largely consistent with the method discussed earlier. However, for a small fraction of subhalos, this new method would cause us to link subhalos in the two simulations with very different masses. For example, consider the distribution of dark matter in the MBII and DMO simulations in Figure 4.2. In the left panel, the blue and magenta circles show the virial radius of the central subhalo and a nearby satellite subhalo respectively in MBII. We can clearly see that the center of the satellite subhalo in MBII is closer to the center of the central subhalo in DMO simulation, which leads to a false match using the 50 closest particles. Hence, we use all the dark matter particles in the subhalo to obtain a consistent match. For similar reasons (such as changes in the location of density peaks), it is not possible to consistently match the satellite subhalos in low mass halos, which is the motivation

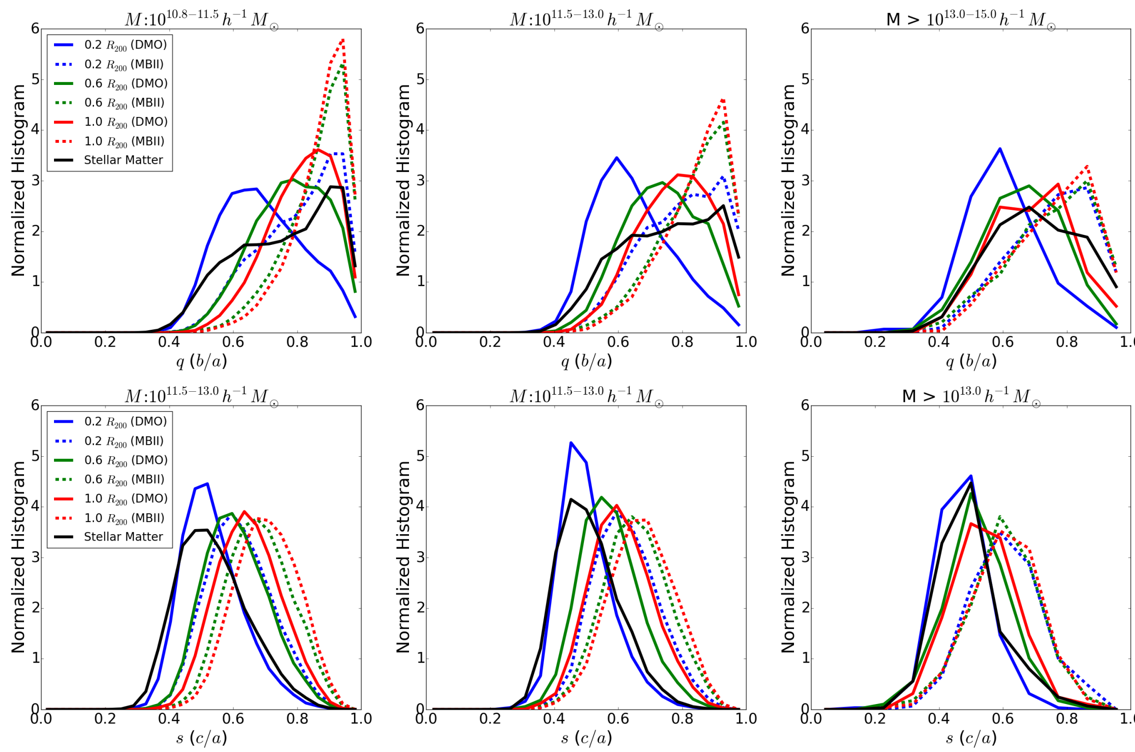

Figure 4.7: Normalized histograms of 3D axis ratios of the dark matter component in matched subhalos in the DMO and MBII simulations, with the shapes measured at different radii ($0.2R_{200}$, $0.6R_{200}$ and $1.0R_{200}$) and also the stellar matter component in MBII. The columns indicate different mass bins, while the top and bottom rows are for q (b/a) and s (c/a), respectively.

for our adoption of a lower mass limit of $10^{10.8}h^{-1}M_\odot$.

4.4 Shapes and misalignment angles

In this section, we investigate the change in the shape and orientation of the subhalos with the distance from their center, which is defined as the location of the most bound particle in the subhalo. This measurement is necessary to understand whether the shape of the stellar matter component traces the (inner) shape of the dark matter component. We show the radial dependence of the shape of the dark matter component in both the MBII and DMO simulations, and compare the orientations at various radii against that of the stellar component in MBII.

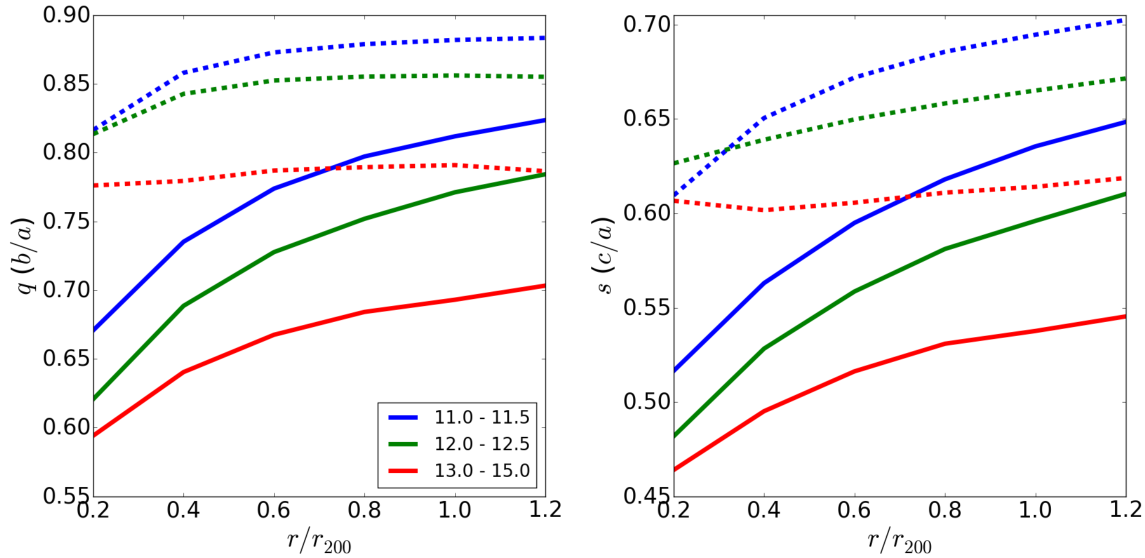

Figure 4.8: Median of the dark matter subhalo axis ratios (left: q, right: s) in the MBII (dashed lines) and DMO (solid lines) simulations in different mass bins, plotted against the distance to which the shape is measured, at $z = 0.06$.

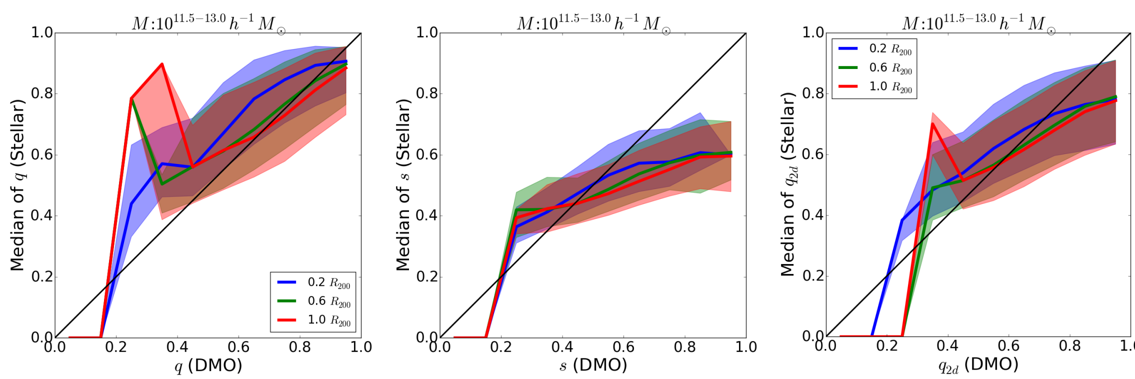

Figure 4.9: Median and scatter (defined using the 16^{th} and 84^{th} percentiles) in the distribution of the axis ratios (3D and 2D) of the stellar matter component in MBII plotted against the axis ratio of the shape of matched subhalo in the DMO simulation, with the shape measured within different radii ($0.2R_{200}$, $0.6R_{200}$ and $1.0R_{200}$). *Left:* q (3D); *middle:* s (3D); *right:* q_{2d} (2D).

4.4.1 Radial dependence of shapes

To calculate the shape of the dark matter component in the subhalo within a given radius, we start with all dark matter particles inside the spherical volume at a given

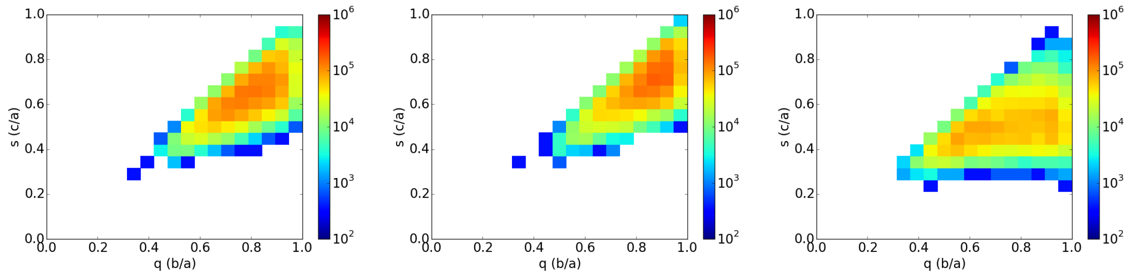

Figure 4.10: Contour plots of 3D axis ratios of the dark matter component in matched subhalos in the DMO (left) and MBII (middle) simulations, and the stellar matter component in MBII (right), in the mass bin M2 at $z = 0.06$.

distance from the center and compute the shape using the iterative reduced inertia tensor (Eq. 6.8). By using the reduced inertia tensor for shape calculation, we still provide more weight to the particles in the inner region of the subhalo, so our resulting shapes should be considered as shapes within a radius rather than at that radius. Hence, the effect of baryonic physics on the dark matter halo shapes in MBII will be evident even for shapes measured out to large radii. For the analysis of shapes, we only consider subhalos with at least 500 particles remaining after the last iteration, excluding fewer than 1% of galaxies. We will compare the distribution of shapes and alignments of the dark matter component calculated within a radial distance of $0.2R_{200}$, $0.6R_{200}$ and $1.0R_{200}$. Here R_{200} is the radius within which the spherically-calculated average density of matter is equal to 200 times the critical density.

The radial dependence of dark matter halo shapes has previously been studied using N-body simulations [e.g.,][][5, 139] and small-volume hydrodynamic simulations [e.g.,][][91, 1, 44]. As in our work, the method used to measure the shapes in [5], [44], and [139] is based on the iterative reduced inertia tensor. However, [91] measure shapes using only particles within different radial bins with the reduced inertia tensor, and [1] fit ellipsoids to the positions of dark matter particles along the isopotential contours at different radii. Hence, the comparison with some of these previous studies is only qualitative.

In Figure 4.7, we show the normalized histograms of the dark matter subhalo axis ratios in MBII and DMO calculated with different maximum radii, as well as the axis ratios of the total stellar matter component of MBII. Throughout this section, we use three mass bins: $10^{10.8-11.5}h^{-1}M_{\odot}$, $10^{11.5-13.0}h^{-1}M_{\odot}$ and $> 10^{13}h^{-1}M_{\odot}$ (M1, M2, and M3). Comparing the dark matter subhalo axis ratio distributions in MBII and DMO simulations, we observe that for a given maximum radius, the shapes measured in the hydrodynamic run are more spherical. This finding is in agreement with results from previous studies using smaller-volume hydrodynamic simulations [91, 1, 44]. Note that the histograms of the axis ratio s (c/a) of the shapes of dark matter subhalos in DMO measured within $0.2R_{200}$ are similar to those of the stellar matter component in

MBII. However, the histograms of q (b/a) are very different, which indicates different triaxiality of the shapes. We also find that the axis ratios increase as we go to larger radii, which means that the shape of the dark matter component is more flattened in the inner regions of the subhalo, again in agreement with previous findings [44, 139].

To illustrate this effect further, we plot the median axis ratios against the radius within which the shape is measured in Figure 4.8, in more narrowly-defined mass bins. From the plot, we can see that for a given mass bin, the median axis ratios are higher in MBII. The median values of q and s can be compared against those from [139], and qualitatively we reproduce their trend that they decrease at small distances from the subhalo center and at increasing mass. However, this increase in axis ratios is smaller in MB-II than in the DMO simulation. Also, at higher masses, the increase in the median axis ratio with radius is milder than at lower masses. Using smaller-volume hydrodynamical simulations, [1] found that the halo axis ratios are independent of radius, and [44] found that the shapes of dark matter halos are slightly more oblate in the inner regions. These differences are most likely due to the absence of stellar and AGN feedback in those studies, unlike in MBII.

From Figure 4.7, we see that the axis ratio histograms for the dark matter subhalos in the DMO simulation do not follow those for the galaxy stellar components in MBII, at any radius. This result can be seen more clearly in Figure 4.9, where we plot the median and scatter in the stellar matter axis ratio distributions in MBII as a function of the DMO dark matter q or s value, for different radii. We see that the scatter in the distribution of axis ratios is large for all radii, so there is no advantage in using the inner shape of the dark matter subhalo in dark matter-only simulations to predict the shape of the stellar component in MBII. For this reason, we only consider the dark matter subhalo axis ratios using all particles in our analysis of two-point statistics.

In Figure 4.10, we show the contour plot of q versus s for the dark matter shape in DMO and MBII and stellar shape in MBII in the mass bin M2 ($10^{11.5-13.0}h^{-1}M_{\odot}$). The contour plots indicate that the galaxy shapes are more prolate compared to the shapes of the dark matter component in MBII. We can use the triaxiality parameter, $T = \frac{1-q^2}{1-s^2}$ [58], to quantify the prolateness or oblateness of the shape. Large (small) values of T imply that the shape is more prolate (oblate). In the mass bin M2, the mean triaxiality of the stellar component shapes is 0.562 ± 0.003, while for dark matter shapes in MBII, the mean triaxiality is 0.538 ± 0.002. The triaxialities are larger for the dark matter shapes in the DMO simulation with a mean value of 0.600 ± 0.002, meaning that the dark matter shapes are more oblate (prolate) in hydrodynamic (dark matter-only) simulations. This conclusion is consistent with results from previous comparisons performed using simulations of smaller volume [12, 62, 1, 44].

4.4.2 Misalignment angles

In Fig. 4.11, we show the normalized histograms of the misalignment angles (Eq. 6.10) between the 3D shape defined by the stellar component of subhalos in MBII and the

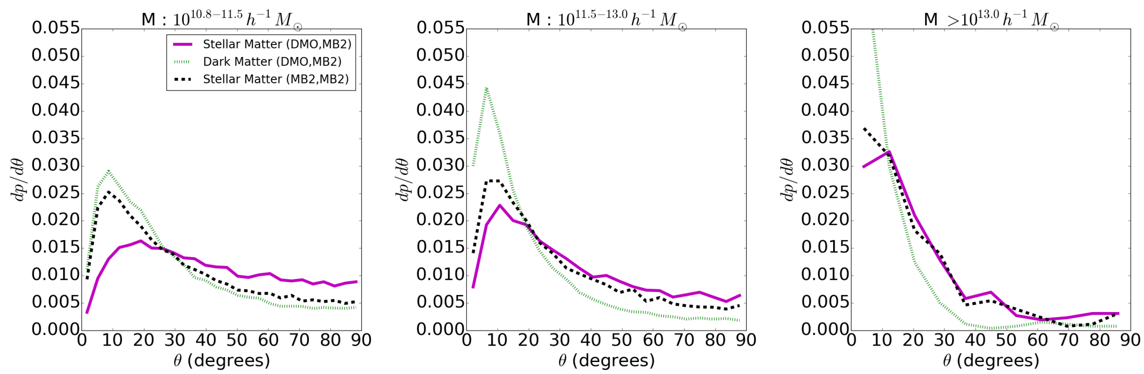

Figure 4.11: Misalignment angle distributions for the 3D shapes of the dark matter component in matched subhalos of DMO and MBII simulations with the stellar matter component in MBII, in mass bins M1, M2 and M3 at $z = 0.06$. Also shown (green line) is the histogram of misalignment angles between the shapes of dark matter subhalos in MBII and DMO.

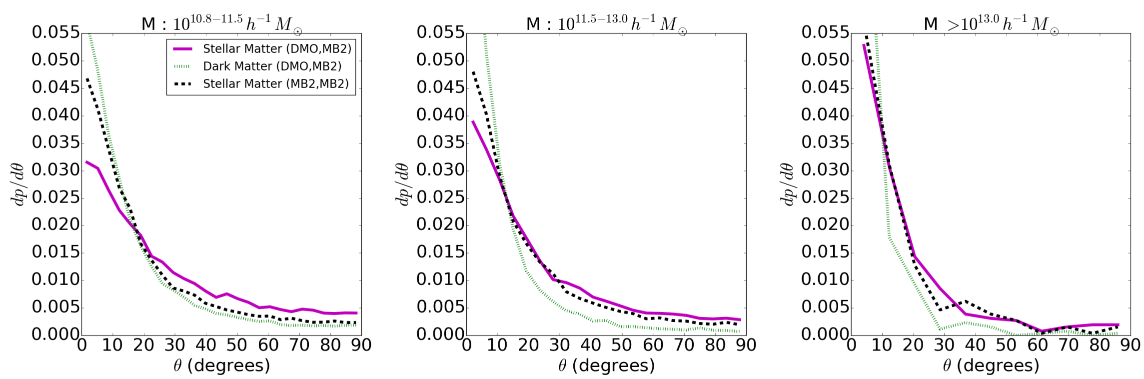

Figure 4.12: Misalignment angle distributions for 2D shapes of the dark matter component in matched subhalos of DMO and MBII with the stellar matter component in MBII, in mass bins M1, M2 and M3 at $z = 0.06$. Also shown (green line) is the histogram of misalignment angles between the shapes of dark matter subhalos in MBII and DMO. This figure is simply the 2D version of Fig. 4.11.

shape defined by the dark matter component in MBII and DMO (for mass bins M1, M2 and M3). From the plot, we can see that for M3, the alignment of stellar matter in MBII with the dark matter component in DMO (purple curve) is similar to the alignment with the dark matter component in MBII (dashed black curve). This result implies that the shapes of dark matter components in the matched subhalos of MBII and DMO have similar orientations at high mass, which is also shown directly by the green line. Fig. 4.12 shows a similar result using the projected shapes, with slightly

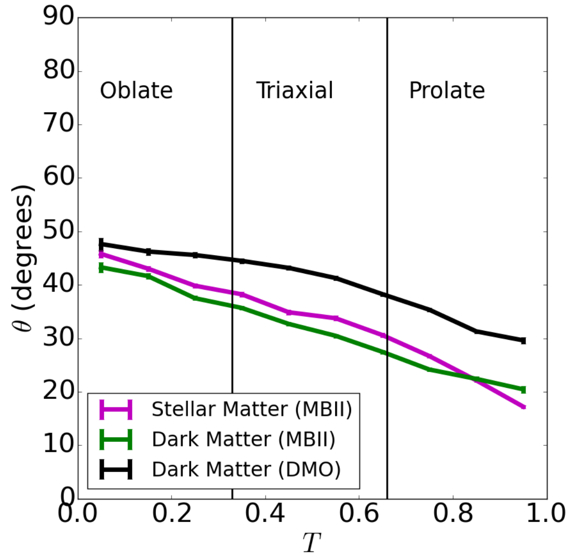

Figure 4.13: Mean of the 3D misalignment angles between the shape of the dark matter component in MBII and DMO with the shape of stellar component in MBII as a function of the triaxiality parameter, T (of the stellar matter component in MBII and the dark matter component in MBII and DMO), in the mass range, $10^{10.8} - 6.0 \times 10^{14} h^{-1} M_{\odot}$ at $z = 0.06$. The purple line shows the mean misalignment angle between the shape of dark matter component in MBII with the stellar component in MBII plotted against the triaxiality of the shape of stellar component in MBII. Similarly, the green and black lines show the mean misalignment angles between the shapes of dark matter component in MBII and DMO with the stellar component in MBII plotted against the triaxialities of the shapes of dark matter component in MBII and DMO respectively.

smaller misalignment angles. However, for M1 and M2, it is clear that the stellar matter in MBII is better aligned with the MBII dark matter subhalo than with the corresponding subhalo in DMO.

To check for a connection between galaxy shapes and misalignment angles, we consider the triaxiality parameter, T. In Figure 4.13, we plot the mean misalignment angles between the shapes of stellar matter in MBII with the dark matter shapes in DMO and MBII simulations as a function of triaxiality. From the figure, we can see that as T increases for the stellar shapes and dark matter shapes in MBII, the mean misalignment angles decrease. This means that for stellar and dark matter shapes in MBII which are more prolate, the alignment between the shapes of stellar and the dark matter components is stronger than for those with more oblate shapes. Similarly, for the more prolate dark matter shapes in the DMO simulation, the alignment with the stellar component in MBII is closer. However, the mean misalignment angles

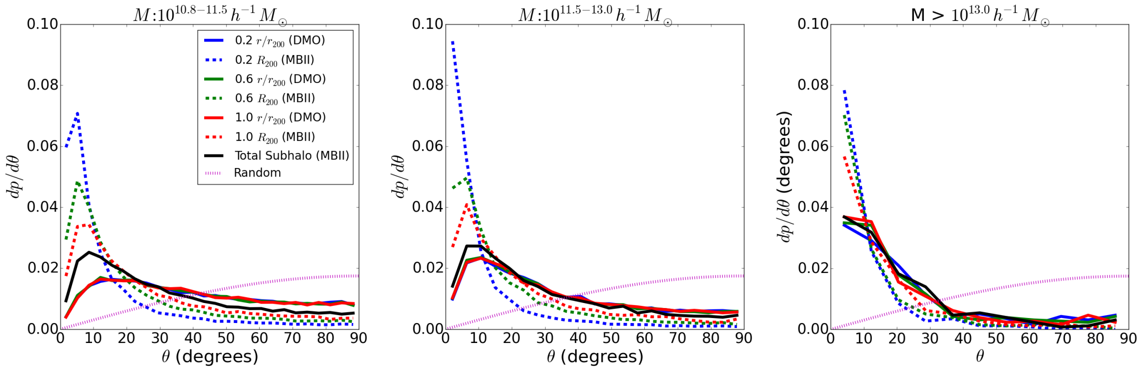

Figure 4.14: Histograms of misalignment angles of 3D shapes of dark matter subhalos in the DMO and MBII simulations (with respect to the shape of the galaxy in MBII) when measuring the subhalo shapes within different radii ($0.2R_{200}$, $0.6R_{200}$, and $1.0R_{200}$) in the mass bins M1 (left), M2 (middle), and M3 (right) at $z = 0.06$.

decreases by only $\sim 27\%$ while going from $T < 0.33$ to $T > 0.66$ in DMO, which is less than the decrease of $\sim 45\%$ for stellar shapes in MBII. When using galaxy shapes, it is tempting to interpret more oblate shapes as relating to disk galaxies, and thus inferring that disk galaxy shapes are more misaligned with their host dark matter halos than elliptical galaxies. However, we defer a more detailed comparison of the morphologies of galaxies and the connection to misalignment angle distributions in future work.

4.4.3 Radial dependence of misalignment angles

Next, we investigate radial trends in the orientation of the shape of the stellar component in MBII with respect to the dark matter component at different radii in MBII and DMO. Histograms of the misalignment angles when defining the dark matter halo shape within various radii are shown in Figure 4.14. For comparison, we also show the prediction for a purely random distribution of misalignment angles in 3D. From the plots, we see that in the MBII simulation, the alignment of the stellar component with the dark matter subhalo shape increases as we limit ourselves to smaller radii within the dark matter subhalo. This is expected, as the stellar matter is coupled to the distribution and shape of the dark matter in the inner regions of the subhalo. However, there is no corresponding trend in the DMO simulation, where the misalignment angle distributions have very little dependence on the maximum radius.

From this plot, we can conclude that it is not advantageous to use the inner shape of the dark matter subhalo in a dark matter-only simulation when trying to define mock galaxy shapes and alignments. Since the distribution of misalignment angles with respect to the total dark matter subhalo orientation is not consistent with a

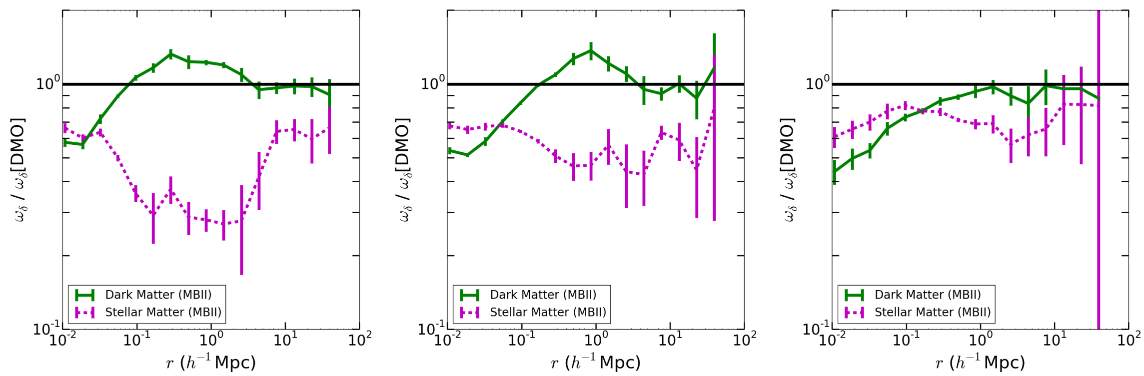

Figure 4.15: Comparison of the ED correlation function, $\omega_\delta(r)$, for the dark matter subhalo and stellar matter components in MBII with respect to that for dark matter subhalos in the DMO simulation, computed separately for M1 (left), M2 (midddle), and M3 (right).

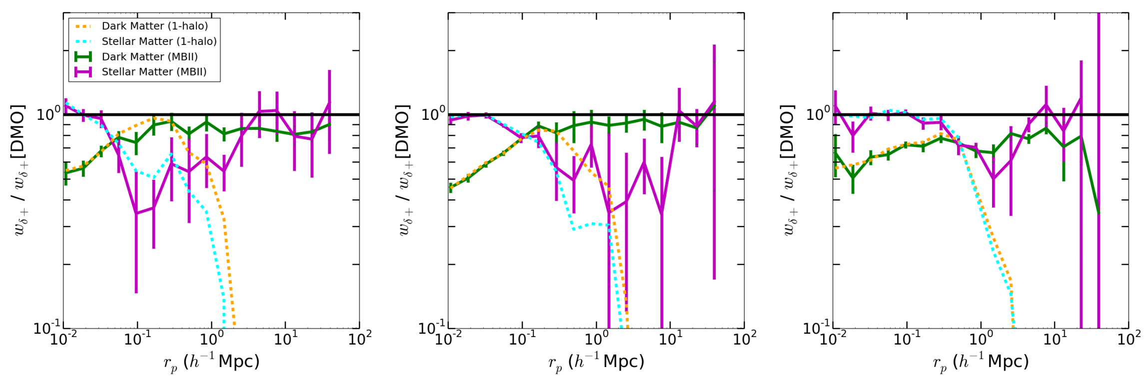

Figure 4.16: Comparison of the projected density-shape correlation, $w_{\delta+}(r_p)$, for the dark matter subhalo and stellar matter components in MBII with respect to that for dark matter subhalos in the DMO simulation, computed separately for M1 (left), M2 (midddle), and M3 (right).

uniform random distribution, we can still use these distributions in different mass bins to assign shapes and orientations to galaxies painted onto N-body simulations.

4.5 Intrinsic alignment two-point correlation functions

In this section, we compare the intrinsic alignments in MBII and DMO simulations by analysing the two-point statistics, ellipticity-direction (ED) and the projected density-shape ($w_{\delta+}$) correlation functions defined in Section 5.3.3. In Figure 4.15, we compare the ED correlation for the shapes of the dark matter subhalo and stellar matter component in MBII with that for the dark matter subhalos in the DMO simulation, mass bins M1 ($10^{10.8-11.5}h^{-1}M_{\odot}$), M2 ($10^{11.5-13.0}h^{-1}M_{\odot}$), and M3 ($> 10^{13.0}h^{-1}M_{\odot}$). The ED correlation function for the dark matter subhalos in MBII is comparable to that in the DMO simulation on large scales. However, on small scales, we observe a tens of percent decrease in the ED correlation function for the MBII simulation. This finding is possibly due to the dark matter subhalos in MBII being rounder than in DMO, which implies that the dark matter particles assume a distribution within the halos that is closer to spherical, reducing the ED correlation function at smaller scales.

The ED correlation computed using the shape of the stellar matter component in MBII is smaller than that of the dark matter component in DMO (by tens of percent, on all scales). This result is due to the misalignment of the stellar shape with the dark matter subhalo shapes that are determined by the density field. This ratio is relatively scale-independent in the higher mass bins M2 and M3, unlike the ratio of ED for the dark matter subhalos in MBII vs. in DMO. On $0.5 - 5h^{-1}$Mpc scales, the fractional difference of this ratio is on average $\sim 72\%$, 53% and 29% in the mass bins M1, M2, and M3, respectively.

In Fig. 4.16, we compare the projected shape-density correlation function, $w_{\delta+}$, for the dark matter and stellar matter shapes in MBII with that of the dark matter shape in DMO. Here, $w_{\delta+}$ for the dark matter shape in DMO is higher than the other correlations at all values of r_p and for all mass bins. This finding is expected when comparing the DMO and MBII dark matter subhalos, since the alignment of the dark matter shape with the density field is similar in both simulations, but the dark matter subhalos in MBII are rounder, reducing $w_{\delta+}$ for MBII. If we consider the $w_{\delta+}$ computed using the shapes of the stellar matter components, we observe that at small scales, it is close to the $w_{\delta+}$ of the dark matter shapes in the DMO simulation. This similarity derives from the compensation of two competing effects: the stellar shapes are more misaligned with the density field, lowering $w_{\delta+}$, but the stellar shapes have a larger ellipticity, raising $w_{\delta+}$. However, the correlation function computed using stellar component shapes is still $\sim 30 - 40\%$ smaller than that using DMO subhalos for $0.5 < r_p < 5h^{-1}$Mpc. Due to the limited size of the simulation volume, the uncertainties are large beyond $\sim 5h^{-1}$Mpc. At intermediate scales, we can also see the transition from the 1-halo term to the 2-halo term for the stellar component, whereas for the dark matter component, it is not clearly evident. To illustrate further, we also show the ratio for the 1-halo terms corresponding to $w_{\delta+}$ of the shapes of dark matter and stellar component in MBII. In the lowest mass bin, which has a fairly equal mix of central and satellite subhalos, we observe a change in the shape of the 1-halo term at $\sim 1h^{-1}$Mpc for the stellar component. As the stellar component is more aligned with the inner regions of the dark matter distribution in the subhalo, the 1-halo term drops more significantly in the intermediate scales in

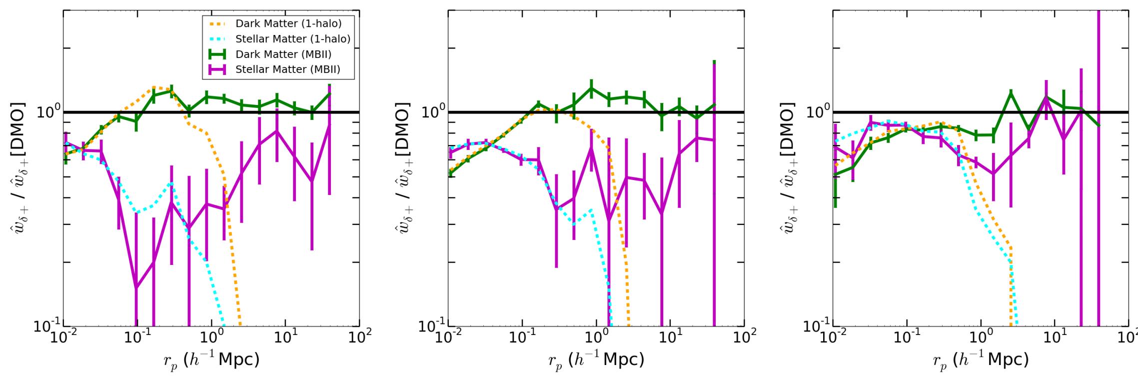

Figure 4.17: Comparison of $\hat{w}_{\delta+}(r_p)$ (projected shape-density correlation function without ellipticity weighting), for the dark matter subhalo and stellar matter components in MBII with respect to that for dark matter subhalos in the DMO simulation, computed separately for M1 (left), M2 (midddle), and M3 (right).

comparison to that of the dark matter component.

For a more direct understanding of the effects of alignment versus different shape distributions, we compute a new statistic, $\hat{w}_{\delta+}$, which is defined as the projected shape-density correlation function without ellipticity weighting (i.e., setting $|e| = 1$ for all objects in the shape sample). The results are shown in Figure 4.17. For the stellar component in MBII, $\hat{w}_{\delta+}$ is smaller than that of the dark matter component in DMO at all scales. For $0.5 < r_p < 5h^{-1}$Mpc, the fractional differences in the correlation function are $\sim$ 60%, 49% and 38% in the mass bins M1, M2, and M3, respectively. Clearly, since the shapes have been normalized to the same value, this must be due only to misalignments between galaxy shapes and the density field. Similarly, the correlation functions for the dark matter subhalo shapes agree on large scales, but that for MBII is smaller than that for DMO on small scales, due to the rounder shapes of the dark matter subhalos (just as was seen for the ED correlation).

4.6 Conclusions

In this paper, we carried out a comparison of halo and subhalo populations in the MassiveBlack-II (MBII) simulation, and a corresponding dark matter-only simulation (DMO) with the same cosmology, resolution, volume, and initial conditions. First, considering basic halo properties, we compared the halo mass function of the MBII simulation with that of DMO. The mass function is suppressed in the hydrodynamic run by $\sim$ 10% at $10^{12}h^{-1}M_{\odot}$, increasing to 20% at $10^{9}h^{-1}M_{\odot}$. This agrees qualitatively with the findings from the OWLS simulation [167]. The two-point correlation function for the dark matter particles in the two simulations is similar on large scales. On small scales, the two-point correlations are larger for the hydrodynamic run, corresponding to an increased dark matter power spectrum at large k values.

Identifying matching subhalos in the two simulations enables us to directly compare the distribution of axis ratios and shape alignments to understand the effects of baryonic physics. The fraction of matched subhalos decreases as we go to lower masses, but is above 90 per cent for the mass range used in this work. These shapes are also used to calculate and compare the intrinsic alignment two-point statistics.

We measured the shapes of dark matter subhalos in MBII and DMO simulations as a function of radius, by only using particles within a certain distance from the center based on a fixed fraction of the subhalo R_{200}. We analyzed the distributions of axis ratios and alignments of shapes measured within $0.2R_{200}$, $0.6R_{200}$, and $1.0R_{200}$. In both simulations, we found that the axis ratios increase with the distance from center, which agrees with previous results in N-body simulations [139]. We also found that the dark matter subhalo axis ratios in the MBII simulation are higher (rounder) than those in the DMO simulation at all mass ranges due to the effects of baryonic physics, in agreement with previous findings [e.g.,][][91, 1, 44]. The galaxy stellar components in MBII have smaller axis ratios than the dark matter subhalos in both simulations, with the fractional difference being larger for the minor-to-major axis ratio, s.

The degree of alignment of the stellar component in MBII with the dark matter component in DMO is larger in subhalos of high mass and decreases at lower masses. This trend is qualitatively similar to that of the alignment of the stellar component with the dark matter component in MBII. In subhalos of higher mass, the shapes of the dark matter component in MBII and DMO simulation are well aligned with each other. This alignment is stronger than the alignment of the dark matter shape in MBII with that of stellar component in the same simulation. Comparing the misalignment of the stellar component with shapes of dark matter component measured within different radial distances in MBII, we find that the misalignment angles increase as we go to larger radii within the dark matter subhalo. However, we do not notice a significant change in the misalignment of the stellar component with the shape of dark matter component in DMO measured for different radii. Based on our results from axis ratios and misalignment angles, we concluded that when mapping galaxy alignments from hydrodynamic simulations onto subhalos in dark matter-only simulations, it is not useful to measure the shape of dark matter component at smaller radii in order to trace the shape and orientation of the stellar component. Hence, for the comparison of two-point statistics, we only consider the shapes of dark matter subhalos obtained using all the particles in the subhalo.

Using the shapes of matched subhalos, we compared the intrinsic alignments two-point statistics (ellipticity-direction correlation, or ED, and the projected-shape density correlation, $w_{\delta+}$) of the dark matter and stellar matter in MBII with that of the dark matter component in DMO simulation. The ED correlations of the dark matter component in MBII and DMO agree on large scales. On small scales, the ED correlation function decreases in MBII due to a change in the dark matter profile caused by baryonic physics. For the stellar component, the ED correlation is smaller on all scales due to the misalignment of the stellar component with the dark matter component. This corresponds to a fractional difference ranging from $\sim 30-70\%$ for scales around $0.5-5h^{-1}$Mpc, and the decrease is larger in subhalos of lower mass. The $w_{\delta+}$ correlation function for the shapes of dark matter component in MBII are smaller when compared to that of the DMO simulation due to the smaller values of ellipticities, since the shapes are rounder in MBII. For the stellar component, we find that the $w_{\delta+}$ is comparable on large scales and small scales with the $w_{\delta+}$ of the dark matter component in DMO. However, for scales around $0.5-5h^{-1}$Mpc, $w_{\delta+}$ is still smaller for the stellar component by $\sim 30-40\%$. At intermediate scales, we find a transition from the 1-halo to 2-halo term that causes a decrease in $w_{\delta+}$ computed using stellar shapes, but this feature is not clearly evident for the $w_{\delta+}$ of the dark matter shape in MBII.

Our results in this paper suggest that the scatter in the distribution of axis ratios of the dark matter subhalo shapes in the DMO simulation is large compared to that of the stellar component in MBII, with significant misalignment in the orientation of shapes. However, the alignments between the galaxies in MBII and the corresponding matched subhalos in the DMO simulation are still significant compared to a uniform random distribution. In future work, we will use these measurements to map the intrinsic alignments of the stellar matter component in hydrodynamic simulations onto dark-matter-only simulations. This is an important step in producing N-body based mock catalogs that have realistically-complicated intrinsic alignments for tests of weak lensing analysis methods in future surveys.

Chapter 5

Intrinsic alignments of disk and elliptical galaxies

5.1 Introduction

Weak lensing is a promising cosmological probe that can help in understanding the nature of dark matter, dark energy and modified theories of gravity [4, 174]. Future weak lensing surveys such as the Large Synoptic Survey Telescope[1] (LSST; [114]), Euclid[2], http://www.euclid-ec.org [106], and the Wide-Field Infrared Survey Telescope[3] (WFIRST; [145]) should constrain cosmological parameters such as the dark energy equation of state to sub-percent levels. However, the intrinsic alignment of galaxies, the coherent correlations of the galaxy shapes with each other and with the underlying density field, is a significant astrophysical systematic in weak lensing analysis [66, 41, 78, 72]. Ignoring the effects of intrinsic alignments on a weak lensing analysis can bias the estimation of the dark energy equation of state parameter. [103] find that without marginalizing over intrinsic alignments, this bias in the value of w can be up to $\sim 80\%$ of its value. Hence, an understanding of intrinsic alignments and their scaling with galaxy mass, luminosity, redshift and morphological type is necessary to develop effective mitigation strategies. Further, studies of intrinsic alignments can also help in understanding the physics of galaxy formation and evolution [136, 36, 135]. For reviews of intrinsic alignments, see [161], [80], [97], and [95].

[1] http://www.lsst.org/lsst/
[2] http://sci.esa.int/euclid/
[3] http://wfirst.gsfc.nasa.gov

Intrinsic alignments have been studied analytically using the linear alignment model [72], extensions that include nonlinear contributions [24, 20] and the halo model [137]. N-body simulations have also been used to study IA by stochastically populating halos with galaxies with a random orientation or by using semi-analytic methods [68, 86]. Recently, hydrodynamic simulations of cosmological volumes, such as the MassiveBlack-II [93], Horizon-AGN [51], EAGLE [134] and Illustris [169, 170, 61] simulations have emerged as a useful tool to study intrinsic alignments. They enable direct predictions of intrinsic alignments of the stellar component of galaxies using a large statistical sample, including the physics of galaxy formation [156, 158, 38, 164, 166, 34]. In previous work [156], we studied the shapes of the stellar component of the galaxies using the MassiveBlack-II cosmological hydrodynamic simulation and compared our results with observational measurements finding good agreement. In a follow up study [158], we measured the two-point correlations of the galaxy shapes with the density field and found that the scaling of the correlation function measured in the simulations is consistent with observational results and, on large scales, with predictions of the tidal alignment model.

However, none of these studies have considered morphological divisions of the galaxy sample into disks and ellipticals. There are theoretical and observational motivations for such a split. The galaxies for which intrinsic alignments have been robustly measured in real data [117, 71, 122, 81, 67, 143] are predominantly elliptical galaxies, for which alignments on large scales are well described by the linear alignment model [19]. Observationally, there has been no significant detection of intrinsic alignment shape correlations for disk galaxies [71, 116], except for a hint of a detection for the most luminous blue sample in [71] at low significance. Due to the importance of angular momentum in the formation of disk galaxies, their intrinsic alignments are likely described by the quadratic alignment model, for which the shape-density correlation vanishes in the case of a Gaussian density field [72]. However, in general, due to the non-linear evolution of the density field, we expect a non-zero correlation.

Given the different mechanisms for the alignments of elliptical and disk galaxies, it will be interesting to investigate these differences in a large-volume hydrodynamic simulation simulation. The alignments of disk galaxies have been studied previously using small volume hydrodynamic simulations [e.g.,][][8, 17, 64, 44]. The most recent hydrodynamic simulations with cosmological volumes have a resolution high enough to enable dynamical classification of galaxies into disks and ellipticals using a method described in [2]. Recently, the galaxies in the Illustris simulation (based on a moving mesh code) have been found to have a disk galaxy fraction that compares favorably with observations [170], so it will be interesting to study the intrinsic alignments of disk galaxies using this simulation. Further, it has been shown that disk galaxies in simulations based on SPH and moving mesh techniques differ in properties such as disk scale lengths and angular momentum [160]. Since MassiveBlack-II is an SPH-based hydrodynamic simulation, we can similarly explore differences in properties such as the disk galaxy fraction, specific angular momentum and alignments. In this paper, we first compare the intrinsic alignments of galaxies in MBII and Illustris for galaxies in a similar stellar mass range. This comparison will show how different implementations of hydrodynamics or baryonic physics, and box size effects, can affect predictions of galaxy intrinsic alignments. We then compare the alignments for galaxy subsamples that have been kinematically classified into disks and ellipticals.

This paper is organized as follows. In Section 5.2, we describe the details of the MassiveBlack-II and Illustris simulations used in the study. In Section 5.3, we describe the methods adopted to measure the shapes of galaxies, quantify intrinsic alignments, and kinematically classify galaxies. In Section 5.4, we compare the galaxy shapes in MBII and Illustris and their two-point correlations in a similar stellar mass range. In Section 5.5, we show the results for galaxy shapes and their intrinsic alignments separately for disks and elliptical galaxies in both simulations. Finally, a summary of our conclusions is given in Section 6.6.

5.2 Simulations

In this study, we use the MassiveBlack-II (MB-II) hydrodynamic simulation and publicly-released data from the Illustris simulation [119].

5.2.1 MassiveBlack-II Simulation

MB-II is a state-of-the-art high resolution, large volume, cosmological hydrodynamic simulation of structure formation. This simulation has been performed with P-GADGET, which is a hybrid version of the parallel code, GADGET2 [147] upgraded to run on Petaflop scale supercomputers. In addition to gravity and smoothed-particle hydrodynamics (SPH), the P-GADGET code also includes the physics of multiphase ISM model with star formation [149], black hole accretion and feedback [147, 45]. Radiative cooling and heating processes are included [as in][][90], as is photoheating due to an imposed ionizing UV background. The black hole accretion and feedback are modeled according to [47] based on quasar-mode feedback. Here, a fixed fraction (5%) of the radiative energy release by the accreted gas is assumed to couple thermally to the nearby gas and this is independent of the accretion rate. The details of this simulation can be found in [93].

MB-II contains $N_{\rm part} = 2 \times 1792^3$ dark matter and gas particles in a cubic periodic box of length $100h^{-1}$Mpc on a side, with a gravitational smoothing length $\epsilon = 1.85h^{-1}$kpc in comoving units. A single dark matter particle has a mass $m_{\rm DM} = 1.1 \times 10^7 h^{-1} M_\odot$ and the initial mass of a gas particle is $m_{\rm gas} = 2.2 \times 10^6 h^{-1} M_\odot$, with the mass of each star particle being $m_{\rm star} = 1.1 \times 10^6 h^{-1} M_\odot$. The cosmological parameters used in the simulation are as follows: amplitude of matter fluctuations $\sigma_8 = 0.816$, spectral index $\eta_s = 0.96$, mass density parameter $\Omega_m = 0.275$, cosmological constant density parameter $\Omega_\Lambda = 0.725$, baryon density parameter $\Omega_b = 0.046$, and Hubble parameter $h = 0.702$ as per WMAP7 [102].

5.2.2 Illustris Simulation

The Illustris simulation is performed with the AREPO TreePM-moving-mesh code [146] in a box of volume $(75h^{-1}\mathrm{Mpc})^3$. The simulation follows 1820^3 dark matter particles and an approximately equal number of baryonic elements with a gravitational smoothing length of 1.4 comoving kpc for the dark matter particles. The mass of each dark matter particle is $4.41 \times 10^6 h^{-1} M_\odot$ and the initial baryonic mass resolution is $8.87 \times 10^5 h^{-1} M_\odot$. The galaxy formation physics includes subgrid-model for star formation and associated supernova feedback, black hole accretion and feedback. Here, the black hole accretion and feedback are modeled according to quasar-mode feedback at high accretion rates and radio-mode feedback at low accretion rates. In the radio-mode feedback, it is assumed that the accretion periodically produces an AGN jet that inflates hot bubbles in the surrounding gas. When the black hole has increased its mass by a certain fraction, an AGN-driven bubble is created. The accretion rate and current black hole mass determine the duty cycle of bubble injection, energy content and radius of bubbles. This model is different from that of MBII where the radio-mode feedback is absent and the quasar-mode feedback is independent of accretion rate. A detailed description of the models adopted in Illustris can be found in [168]. The cosmological parameters are as follows: $\sigma_8 = 0.809$, $\eta_s = 0.963$, $\Omega_m = 0.2726$, $\Omega_\Lambda = 0.7274$, $\Omega_b = 0.0456$, $h = 0.704$.

5.2.3 Galaxy and halo catalogs

In both simulations, halo catalogs are generated using the friends of friends (FoF) halo finder algorithm [43]. The FoF algorithm identifies halos on the fly using a linking length of 0.2 times the mean interparticle separation. The subhalo catalogs are generated using the SUBFIND code [151] on the halo catalogs. The subhalos are defined as locally overdense, self-bound particle groups. In this paper, we analyze the shapes of the stellar components in the subhalos and their two-point correlation functions. Based on convergence tests in [156], we only analyze the measured stellar shapes if there are ≥ 1000 dark matter and star particles. As a result, we exclude $\sim 10\%$ (1%) of the galaxies in MBII (Illustris) in the 10^9–$10^{10} h^{-1} M_\odot$ stellar mass bin due to their subhalo masses being low enough that they do not have 1000 dark matter particles. This fraction reduces to $< 1\%$ in the stellar mass bin from 10^{10}–$10^{11} h^{-1} M_\odot$, while no galaxies are discarded for $M* > 10^{11} h^{-1} M_\odot$.

5.3 Methods

Here we describe the methods used to measure galaxy shapes, quantify intrinsic alignments, and kinematically classify the galaxies into disk and elliptical samples.

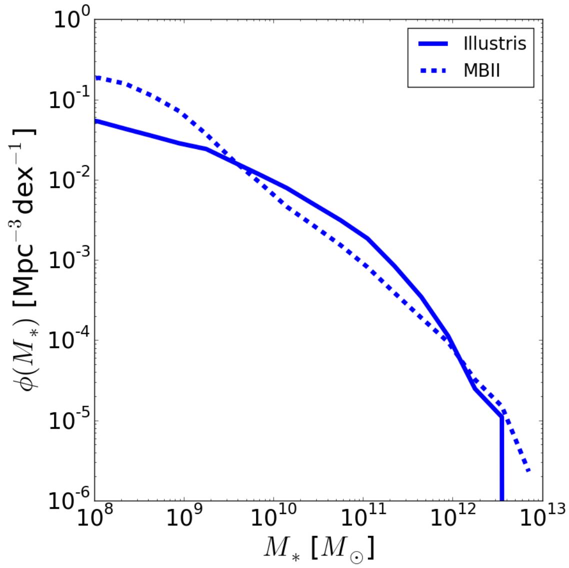

Figure 5.1: Comparison of galaxy stellar mass functions in MBII and Illustris at $z = 0.06$.

5.3.1 Galaxy shapes

The shapes of the stellar matter component in subhalos are modeled as ellipsoids in three dimensions using the eigenvalues and eigenvectors of the iterative version of the reduced inertia tensor given by :

$$\widetilde{I}_{ij} = \frac{\sum_n m_n \frac{x_{ni} x_{nj}}{r_n^2}}{\sum_n m_n} \tag{5.1}$$

where the summation is over particles indexed by n, and

$$r_n^2 = \frac{x_{n0}^2}{a^2} + \frac{x_{n1}^2}{b^2} + \frac{x_{n2}^2}{c^2}. \tag{5.2}$$

where a, b, c are half-lengths of the principal axes of the ellipsoid and are all equal to 1 in the first iteration. The reduced inertia tensor gives more weight to particles that are closer to the center, which reduces the influence of loosely bound particles present in the outer regions of the subhalo. Additionally, this method corresponds more closely to observational shape measurements such as the ones based on weighted quadrupole moments (see [97]) where more weight is given to particles in the inner regions. The eigenvectors of the inertia tensor are $\hat{e}_a, \hat{e}_b, \hat{e}_c$ with corresponding eigenvalues $\lambda_a > \lambda_b > \lambda_c$. The eigenvectors represent the principal axes of the ellipsoid, with the half-lengths of the principal axes (a, b, c) given by $(\sqrt{\lambda_a}, \sqrt{\lambda_b}, \sqrt{\lambda_c})$. The 3D axis ratios are

$$q = \frac{b}{a}, \ \ s = \frac{c}{a}. \tag{5.3}$$

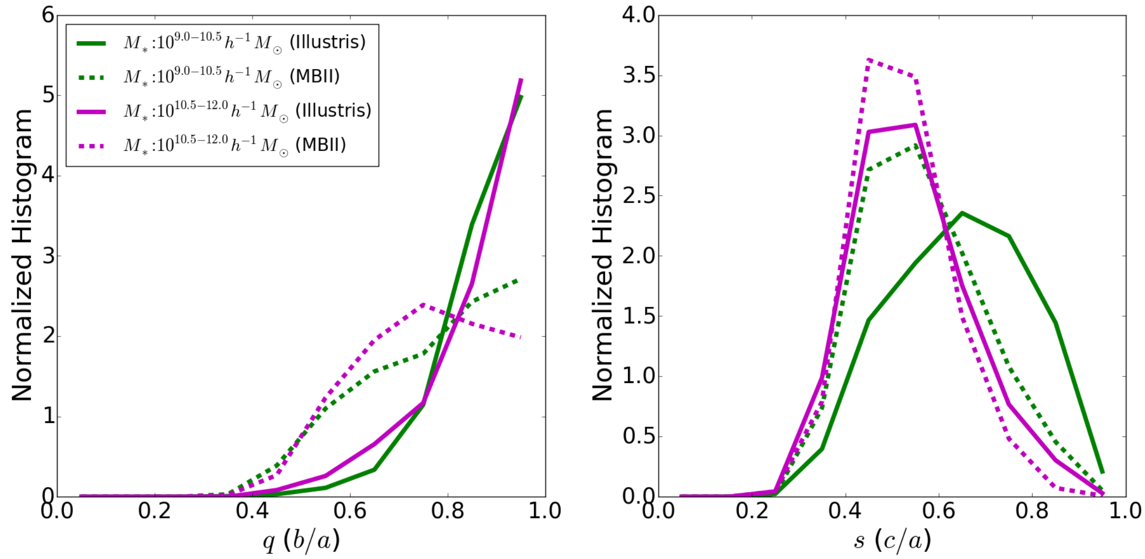

Figure 5.2: Normalized histograms of axis ratios (left: q, right: s) of the 3D shapes of galaxies in MBII and Illustris in two stellar mass bins: $10^{10.0-11.0}h^{-1}M_\odot$ and $10^{11.0-12.0}h^{-1}M_\odot$.

The projected shapes are calculated by projecting the positions of the particles onto the XY plane and modeling the shapes as ellipses.

We note here that without using the iterative scheme, the reduced inertia tensor will lead to shape estimates that are biased to rounder values due to the spherical symmetry imposed by the $1/r^2$ weighting. This has been discussed in [158]; a detailed description of the iterative procedure and further details regarding other definitions of the inertia tensor used to calculate shapes and their impact on intrinsic alignments can also be found there.

5.3.2 Misalignment angle

To study the relative orientation between the shapes defined by the dark matter and stellar matter components in subhalos, we compute the probability distributions of misalignment angles as in [156]. If $\hat{e}_{da}$ and $\hat{e}_{ga}$ are the major axes of the shapes defined by the dark matter and stellar matter components, respectively, then we define the misalignment angle by

$$\theta_m = \arccos(|\hat{e}_{da} \cdot \hat{e}_{ga}|). \tag{5.4}$$

5.3.3 Two-point statistics

The intrinsic alignments of galaxies with the large-scale density field are quantified using the ellipticity-direction (ED) and the projected shape-density ($w_{\delta+}$) correlation functions. The ED correlation quantifies the position angle alignments of galaxies in 3D, while the projected shape correlation function can be used to compare against observational measurements that include the 2D shape of the galaxy.

The ED correlation function cross-correlates the orientation of the major axes of subhalos with the large-scale density field. For a subhalo centered at position $\mathbf{x}$ with major axis direction $\hat{e}_a$, let the unit vector in the direction of a tracer of the matter density field at a distance r be $\hat{\mathbf{r}} = \mathbf{r}/r$. Following the notation of [109], the ED cross-correlation function is given by

$$\omega(r) = \langle | \hat{e}_a(\mathbf{x}) \cdot \hat{\mathbf{r}}(\mathbf{x}) |^2 \rangle - \frac{1}{3} \tag{5.5}$$

which is zero for galaxies randomly oriented according to a uniform distribution.

The matter density field can be represented using either the positions of dark matter particles (in which case the correlation function is denoted by the symbol ω_δ) or the positions of subhalos (in which case it is simply denoted ω). Here, we only use ω_δ to eliminate the effect of subhalo bias.

The projected shape correlation functions are computed to directly compare our results from simulations with observations. Here, we follow the notation of [117] to define the galaxy-intrinsic shear correlation function, $\hat{\xi}_{g+}(r_p, \Pi)$ and the corresponding projected two-point statistic, $w_{\delta+}$. Here, r_p is the comoving transverse separation of a pair of galaxies in the XY plane and Π is their separation along the Z direction.

The projected shape correlation function, $w_{\delta+}(r_p)$ is given by

$$w_{\delta+}(r_p) = \int_{-\Pi_{\max}}^{+\Pi_{\max}} \hat{\xi}_{\delta+}(r_p, \Pi)\, \mathrm{d}\Pi \tag{5.6}$$

We calculated the correlation functions over the whole length of the box, L_{box} with $\Pi_{\max} = L_{box}/2$, where the length of the box is $100h^{-1}$Mpc and $75h^{-1}$Mpc in MBII and Illustris respectively. The details regarding the calculation of $\hat{\xi}_{\delta+}(r_p, \Pi)$ using the projected shapes and density field traced by dark matter particles can be found in [158]. The projected correlation functions are obtained via direct summation. The error bars for the ED and $w_{\delta+}$ correlation functions are calculated using the jackknife method, where the correlation function for each jackknife sample is calculated by eliminating one eighth of the volume of the box.

5.3.4 Bulge-to-disk decomposition

In order to identify a galaxy according to its morphological type, we follow the procedure from [133] and define a circularity parameter for each star within 10 times the stellar half-mass radius, $\epsilon = j_z/j_{\rm circ}(r)$. Here j_z is the component of the specific angular momentum of the star in the direction of the total angular momentum of the galaxy calculated using all star particles within 10 times the stellar half-mass radius. $j_{\rm circ}(r)$ is the specific angular momentum of a circular orbit at the same radius as the star,

$$j_{\rm circ}(r) = rV_{\rm circ}(r) = \sqrt{\frac{GM(<r)}{r}}. \tag{5.7}$$

All stars with $\epsilon > 0.7$ are identified as disk stars. We then define the bulge-to-total ratio as $BTR = 1 - f_{\epsilon>0.7}$, where $f_{\epsilon>0.7}$ is the fraction of stars belonging to the disk. In this paper, we classify the galaxies with $BTR < 0.7$ as disk galaxies and the galaxies with BTR greater than this value as elliptical galaxies. However, we will briefly explore the results of varying this threshold in Sec. 5.5.1.

5.4 Galaxy shapes and alignments in Illustris and MBII

5.4.1 Galaxy stellar mass function

Before examining the galaxy shape distributions and alignments in the two simulations, we first present some background about the simulated galaxy samples.

In Figure 5.1, we compare the galaxy stellar mass function in MBII and Illustris at $z = 0.06$. At lower masses, the density of galaxies is higher in MBII, while at higher masses the two simulations are similar. [93] compare the galaxy stellar mass function in MBII with observations, noting that MBII overpredicts the mass function at $z = 0.06$ at both low and high mass. The lower mass over-prediction can be resolved by only considering galaxies with a non-zero star-formation rate, which suggests a need for a star formation and stellar feedback model with an associated mass dependent wind [e.g.,][][123, 121]. [170] discuss the stellar mass function of Illustris simulation in greater detail, where they also report a higher galaxy density at the fainter end compared with observations. As shown, both MBII and Illustris contain a reasonably-sized galaxy population for the stellar mass range $10^{9.0-12.0}h^{-1}M_\odot$. For the rest of this paper, we use this stellar mass range, which is also consistent with our convergence criterion (≥ 1000 star particles).

5.4.2 Shapes and misalignment angles

In this section, we explore the differences in the shapes and orientations of galaxies in MBII and Illustris, focusing on the mass dependence without including a morphological classification. In Fig. 6.4, we compare the distribution of axis ratios q (b/a) and s (c/a) in Illustris and MBII in two stellar mass bins, $10^{9.0-10.5}h^{-1}M_\odot$ and $10^{10.5-12.0}h^{-1}M_\odot$. Both axis ratios ($q$ and s) are larger in Illustris, which means that

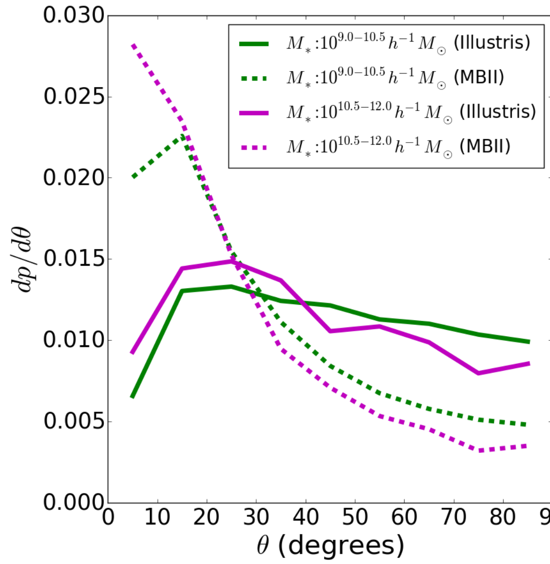

Figure 5.3: Normalized histograms of the misalignment angles between 3D shapes of galaxies and their host dark matter subhalos in MBII and Illustris in two stellar mass bins: $10^{9.0-10.5}h^{-1}M_\odot$ and $10^{10.5-12.0}h^{-1}M_\odot$.

within the same broad mass range, galaxy shapes are rounder compared to MBII. Further, the shapes are rounder in galaxies of lower mass, consistent with results presented in [156]. Table 5.1 shows the mean axis ratios, $\langle q \rangle$ and $\langle s \rangle$, within the two stellar mass bins. The mean values of q in Illustris are larger by a factor of $\sim 12-14\%$ when compared with MBII, while the mean values of s differ by $\sim 4-11\%$.

We compare the normalized histograms of 3D misalignment angles (Eq. 6.10) between the orientations of the galaxy shape and the corresponding dark matter subhalo in Figure 5.3. The mass dependence of the misalignment angles is similar in Illustris and MBII, with the galaxies being more misaligned in the lower mass range. However, the galaxy shapes are significantly more misaligned with their host dark matter subhalos in the Illustris simulation, with the mean misalignment angles differing by $\sim 50-60\%$ when compared with MBII. The mean misalignment angles in the two stellar mass bins are given in Table 5.2.

Table 5.1: Mean axis ratios, $\langle q \rangle$ and $\langle s \rangle$, for galaxies in Illustris and MBII.

	Illustris		MBII	
M_* ($h^{-1}M_\odot$)	$\langle q \rangle$	$\langle s \rangle$	$\langle q \rangle$	$\langle s \rangle$
$10^{9.0}-10^{10.5}$	0.88	0.65	0.78	0.56
$10^{10.5}-10^{12.0}$	0.87	0.54	0.76	0.52

Table 5.2: Mean 3D misalignment angles, $\langle\theta\rangle$ (degrees), between the major axis of galaxies and their host dark matter subhalos in Illustris and MBII.

M_* ($h^{-1}M_\odot$)	Illustris	MBII
$10^{9.0} - 10^{10.5}$	$45.04 \pm 0.16°$	$31.33 \pm 0.11°$
$10^{10.5} - 10^{12.0}$	$41.51 \pm 0.54°$	$26.49 \pm 0.46°$

5.4.3 Two-point statistics

The correlation of galaxy shapes with the density field can be quantified using the two-point statistics, ED and $w_{\delta+}$, defined in Section 5.3.3. In the top left panel of Figure 5.4, we compare the ED correlation functions in Illustris and MBII in two stellar mass bins, $10^{9.0-10.5}h^{-1}M_\odot$ and $10^{10.5-12.0}h^{-1}M_\odot$. Due to the larger misalignment of the stellar shapes in Illustris with their host dark matter subhalos (shown in Fig. 5.3), the amplitude of these two-point correlation functions is lower than in MBII for the same stellar mass range. The radial scaling of the ED correlation function is similar for the two simulations in the higher mass bin and increases with mass in MBII. Given that the differences in the mean misalignment angles of Illustris are smaller in between the two mass bins when compared with MBII, the mass dependence of the ED correlation function in Illustris is less significant. In the top right panel of Figure 5.4, we compare the $w_{\delta+}$ correlation functions in the same stellar mass bins. The amplitude of $w_{\delta+}$ is smaller in Illustris than in MBII for two reasons: the larger misalignment of the stellar shapes with the dark matter subhalos, and fact that the galaxy shapes are rounder in Illustris. However, the radial scaling and mass dependence is similar to that of MBII. To further understand and quantify the radial scaling of the correlation functions in the two simulations, we plot the ratio of ED and $w_{\delta+}$ in Illustris to those of MBII in Figure 5.5. Given the similarity of the radial scaling in the highest mass bin for ED and both the mass bins for $w_{\delta+}$, it is possible to fit the ratio of correlation functions in the range $0.1-10h^{-1}$Mpc to a straight line. In the mass bin, $10^{9.0-10.5}h^{-1}M_\odot$, we can see from the figure that the radial scaling of ED is not similar between the two simulations and hence, we do not fit the ratio to a straight line in this mass bin. We find that the ED correlation in Illustris is smaller by a factor of ~ 2.4 in the stellar mass bin $10^{10.5-12.0}h^{-1}M_\odot$. Similarly the $w_{\delta+}$ correlation function in Illustris is smaller by a factor of ~ 2.8 and 3.1 in the lower and higher mass bins respectively.

In addition to the differences in galaxy shapes and alignments, the effects due to box size for MBII and Illustris should be considered as a possible cause of differences in two-point correlation function amplitude. Since the Illustris simulation has a smaller volume, the correlation function is suppressed due to the absence of large scale modes [e.g.,][][7, 127] and the dark matter correlation function is smaller in Illustris by as much as $\sim 20\%$, with some scale dependence. In order to take this into account, we compute the ratio of the correlation functions of the shapes of the stellar matter with

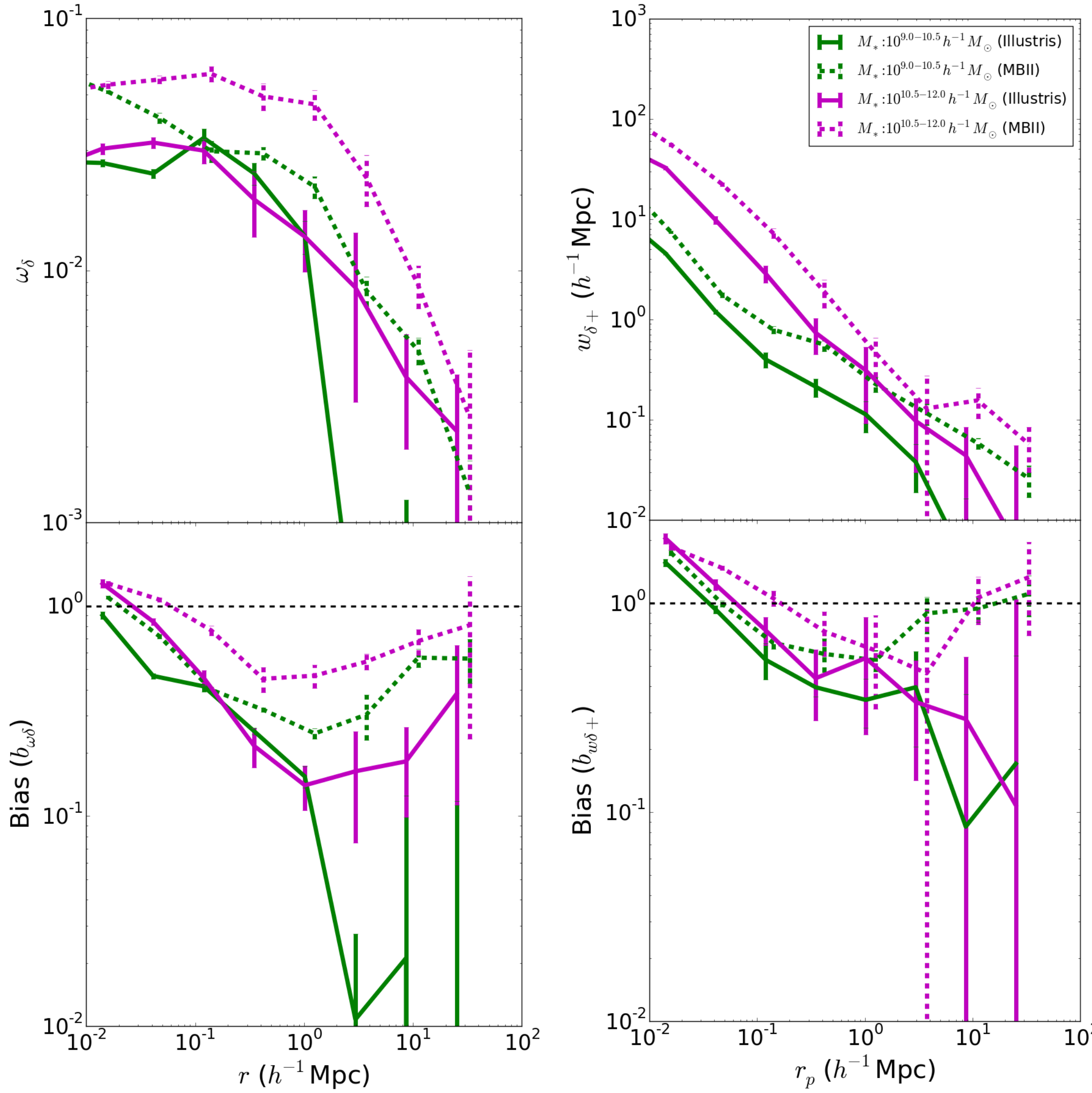

Figure 5.4: *Top:* Ellipticity-direction (ED) and projected shape-density ($w_{\delta+}$) correlation functions of the stellar components of galaxies in MBII and Illustris in two stellar mass bins, $10^{9.0-10.5}h^{-1}M_\odot$ and $10^{10.5-12.0}h^{-1}M_\odot$. *Left:* ED; *Right:* $w_{\delta+}$. *Bottom*: the biases, $b_{\omega\delta}$ and $b_{w\delta+}$, defined as the ratios of the ED and $w_{\delta+}$ correlations functions of stellar components to the same correlation function computed using the dark matter subhalo.

the correlation functions of the shapes of dark matter within the same simulation. This ratio should essentially divide out such box size effects.

In the bottom left panel of Figure 5.4, we compare this ratio for the ED correlation,

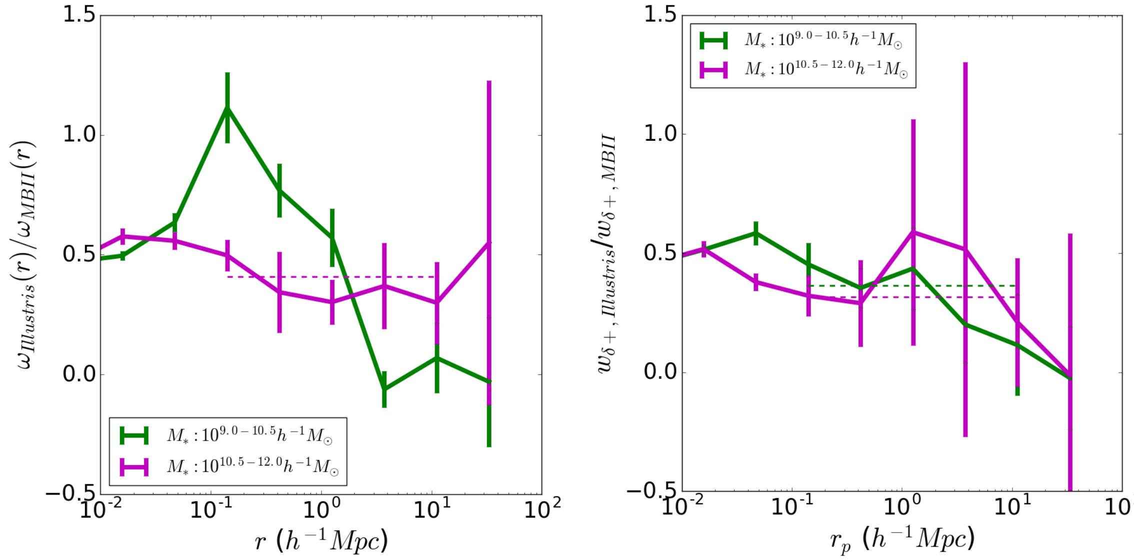

Figure 5.5: Ratio of ellipticity-direction (ED, *(left)*) and projected shape-density ($w_{\delta+}$, *(right)*) correlation functions of the stellar components of galaxies in MBII and Illustris in two stellar mass bins, $10^{9.0-10.5}h^{-1}M_\odot$ and $10^{10.5-12.0}h^{-1}M_\odot$. The horizontal lines represent the best fit values obtained after fitting the ratio to a straight line in the range $0.1-10h^{-1}$Mpc and the line color indicates the corresponding mass bin.

which we denote $b_{\omega\delta}$. On small scales, the differences in the amplitude of $b_{\omega\delta}$ in MBII and Illustris are relatively smaller than the differences in the ED correlation itself. However, on large scales, the ED correlation for the shapes of dark matter is similar for MBII and Illustris within the same stellar mass bins, and hence we observe a significantly smaller value of $b_{\omega\delta}$ in Illustris. In the bottom right panel, we show the bias, $b_{w\delta+}$, which is obtained by normalizing the $w_{\delta+}$ for the shapes of stellar component with that of the shapes of dark matter component. There are smaller differences in amplitude when comparing this quantity in Illustris and MBII, especially in the higher stellar mass bin at small scales from $\sim 10^{-2}$ to 1 h^{-1}Mpc, but there are significant differences in the lower stellar mass bin at all scales. Considering all factors together, we conclude that in addition to box size effects, differences in the distributions of shapes and misalignment angles also lower the amplitude of density-shape correlation functions in Illustris compared to those for comparable samples in MBII.

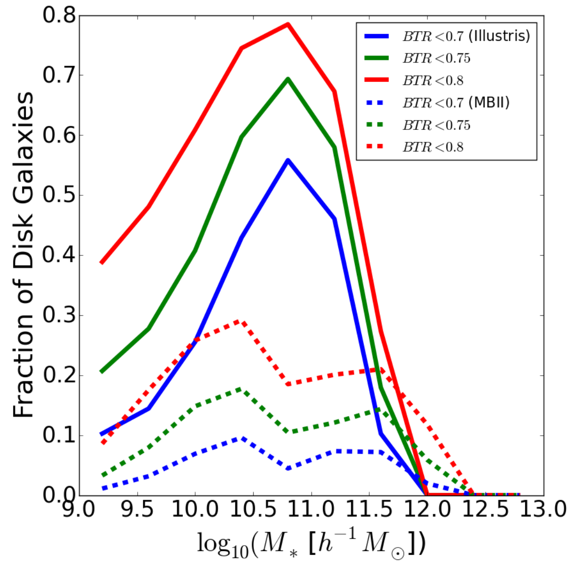

Figure 5.6: Fraction of galaxies in MBII and Illustris at $z = 0.06$ for different thresholds of the bulge-to-total ratio: $BTR < 0.7$, 0.75, 0.8. Our adopted threshold for the rest of this work is that galaxies with $BTR < 0.7$ are classified as disk galaxies.

5.5 Morphological Classification in Illustris and MBII

Here, we present the results of classifying the galaxies in Illustris and MBII into disks and ellipticals using the kinematic bulge-to-disk decomposition. We then compare the shape distributions and two-point intrinsic alignments statistics of disks and elliptical galaxies.

5.5.1 Fraction of disk galaxies

Using the method described in Section 5.3.4, we calculated the bulge-to-total ratio for each of the simulated galaxies in Illustris and MBII. We note that the threshold adopted to classify galaxies as disks based on the bulge-to-total ratio varies across different studies based on simulations. For instance, [170] classify galaxies with $BTR < 0.7$ as disks while [40] adopt a threshold of $BTR < 0.8$. Figure 5.6 shows the fraction of galaxies in Illustris and MBII for different thresholds in the bulge-to-total ratio with $BTR < 0.7, 0.75$, and 0.8. For our adopted threshold of 0.7, the fraction of disk galaxies in Illustris varies from $10 - 50\%$ in the stellar mass range 10^9–$10^{12} h^{-1} M_\odot$, while it is below 10% for galaxies in MBII. It rises to 20% with a smaller threshold, such as $BTR < 0.8$. We also note that using a smaller threshold on the BTR can lead to some differences in the distributions of axis ratios and misalignment angles. However, the changes in the two-point statistics are not

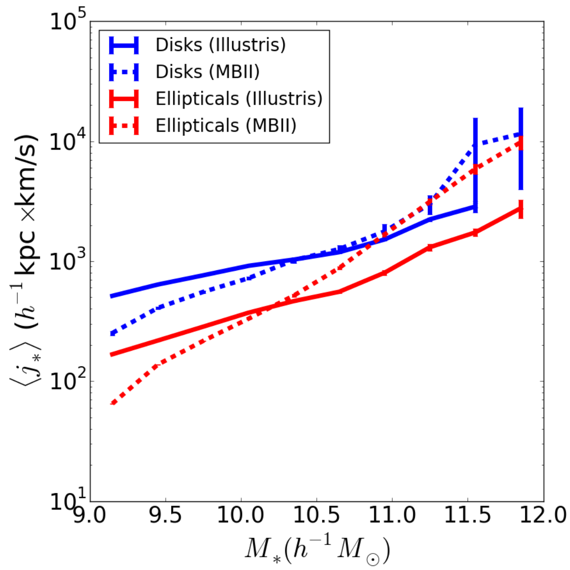

Figure 5.7: Mean specific angular momentum of disks and elliptical galaxies in MBII and Illustris at $z = 0.06$.

significant. Hence, in the rest of this paper, we only show results of morphological classification such that galaxies with $BTR < 0.7$ are classified as disk galaxies and the rest as ellipticals.

To further understand the differences between the properties of disks and elliptical galaxies, we compare their mean specific angular momenta as a function of stellar mass in Figure 5.7. The mean specific angular momenta of disks and elliptical galaxies were found to be consistent with observations in the Illustris simulation [60], with disks having a larger specific angular momentum. Here, we observe that the disk galaxies in MBII also have a larger specific angular momentum than ellipticals at lower mass. However, at high stellar mass, the mean specific angular momenta of disks and ellipticals in MBII are very similar. When we change the threshold on BTR to 0.75 or 0.8, the specific angular momentum of disk galaxies decreases $\sim 10-20\%$ for subhalos of stellar mass below $\sim 10^{10.5}h^{-1}M_\odot$ and increases by a similar amount for subhalos of higher stellar mass.

Comparing the specific angular momentum in MBII and Illustris for fixed galaxy type, we see that it is smaller in MBII at low stellar masses, but higher in MBII at higher stellar mass. It has been shown in [60] that the radio mode decreases the specific angular momentum by $\sim 20-50\%$. Thus, the difference at high stellar mass may be due to the absence of radio-mode in the MBII simulation, and also an increase in the number of baryonic particles at higher stellar mass, which can account for the numerical resolution effects which reduce angular momentum in SPH simulations.

We also compared the angle of orientation between the directions of the angular

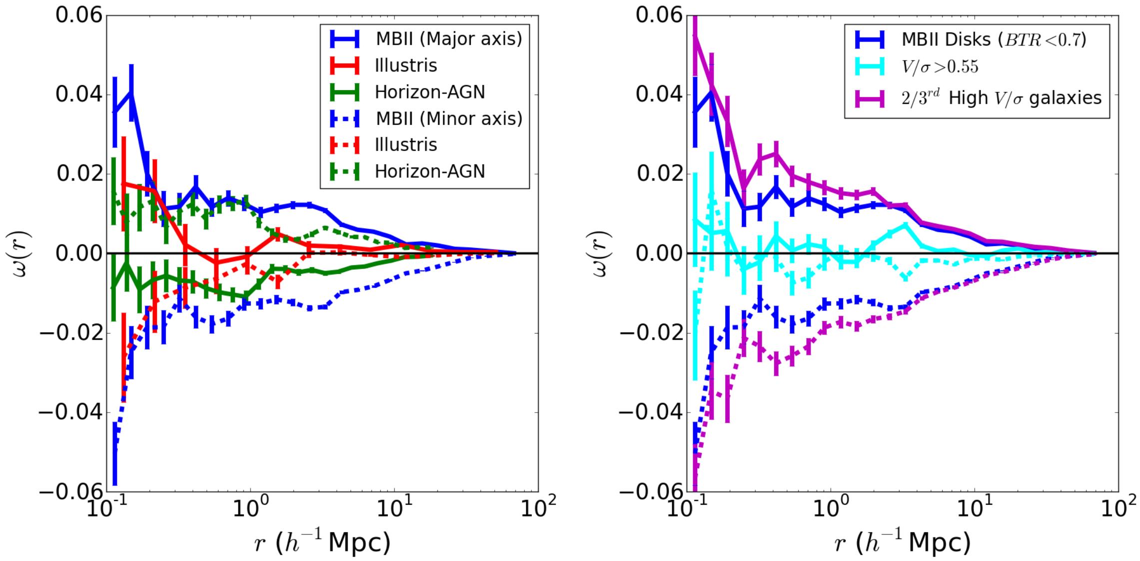

Figure 5.8: Comparison of the ED correlation of the orientation of disk galaxies with the location of ellipticals in MBII, Illustris, and Horizon-AGN simulations [34]. In the right panel, the ED correlation in MBII is compared using various definitions of the disk galaxy sample. In both the panels, the solid lines represent the ED correlation of the disk major axes while the dashed lines represent the correlation of the disk minor axes.

momentum of stellar component with the angular momentum of dark matter component of the subhalo. We found that in both MBII and Illustris, the alignment of the angular momentum of star particles with that of dark matter particles is larger in disk galaxies than ellipticals. This is consistent with the findings of [153], who analyzed disks and elliptical galaxies in the Magneticum Pathfinder Simulations. Recently, [34] analyzed the 3D orientations of disk galaxies in the Horizon-AGN simulation with respect to the location of elliptical galaxies at $z = 0.5$, and found that the orientation of the disk major axis is anti-correlated with the location of ellipticals. We made a similar analysis at $z = 0.6$ using the disk galaxies in MBII and Illustris with our adopted disk classification. In the left panel of Figure 5.8, we plot the ED correlation of the orientation of disk major and minor axis with respect to the location of ellipticals as a function of separation. Comparing with the results of [34] as shown on the plot, we observe that unlike the disks in Horizon-AGN, the major axes of disk galaxies in both MBII and Illustris are positively correlated with the location of ellipticals. The minor axes of the disk galaxies are tangentially oriented towards the direction of ellipticals. The direction of the spin or angular momentum of the stellar component of the galaxy is more aligned with the minor axis when compared with the major axes. So, similar to the disk minor axes, the angular momentum of disks

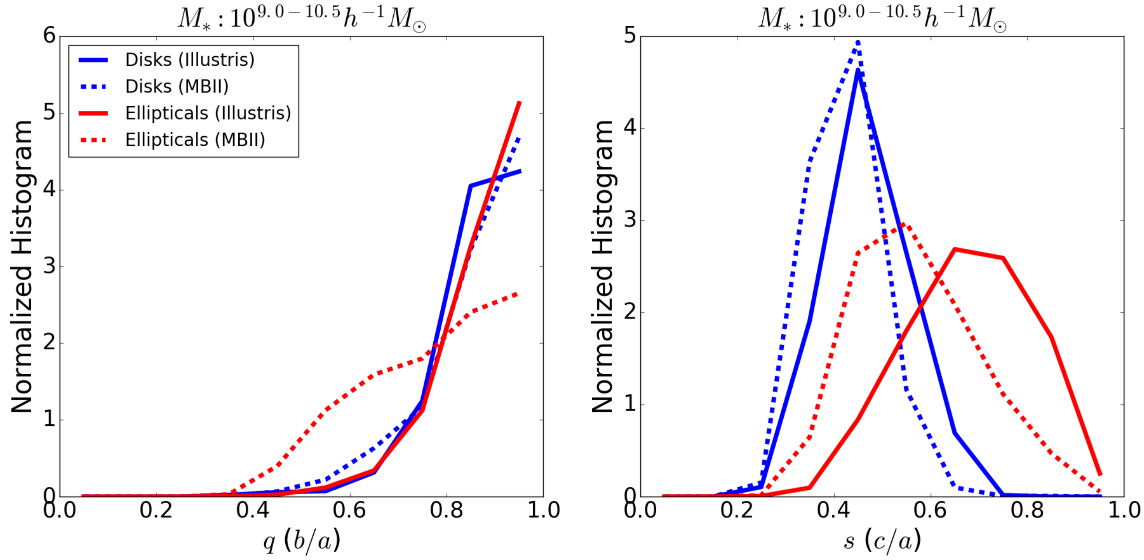

Figure 5.9: Normalized histogram of the axis ratios (left: q, right: s) of 3D shapes of elliptical and disk galaxies in MBII and Illustris in the stellar mass bin 10^9–$10^{10.5}h^{-1}M_\odot$.

is tangentially aligned with respect to ellipticals.

Note that [34] used the ratio of mean azimuthal velocity of stars to their velocity dispersion, V/σ and classified all galaxies with $V/\sigma > 0.55$ as disks. This threshold is chosen such that 2/3 of their galaxy sample is classified as disks. We verified that our results do not change sign when adopting a different morphological classifies for disk galaxies. In the right panel of Figure 5.8, we compare the results in MBII using the galaxies classified as disks using $BTR < 0.7$ (our adopted selection throughout this work) with two other disk galaxy selection criteria: the galaxies for which $V/\sigma > 0.55$, and 2/3 of the sample with the highest V/σ. The results are qualitatively similar with these different definitions, so the difference in sign observed in Horizon-AGN compared with MBII and Illustris is unlikely to arise from differences in morphological classifiers. We conclude that differences in properties of disk galaxies in SPH and AMR simulations and also for different choices of sub-grid physics using the same hydrodynamical code should be explored further.

5.5.2 Shapes and misalignment angles of disks and elliptical galaxies

We compare the shapes and misalignment angles of the kinematically-classified disks and elliptical galaxies in Illustris and MBII. In Figure 5.9, we plot the normalized histograms of the axis ratios, q (b/a) and s (c/a) for galaxies with stellar mass in the

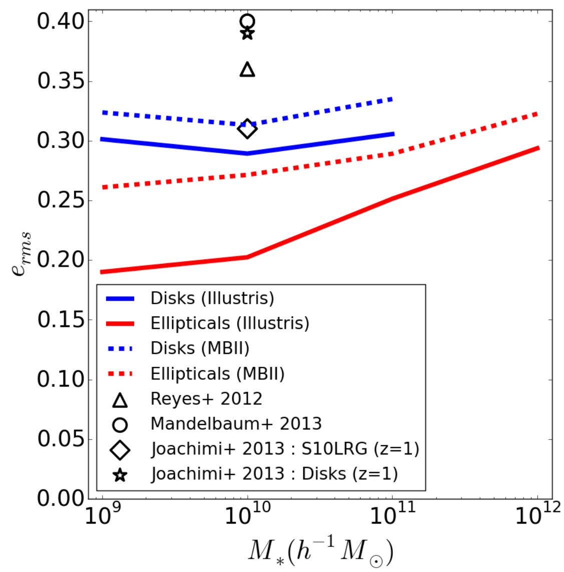

Figure 5.10: RMS ellipticities of the projected shapes of elliptical and disk galaxies in MBII and Illustris based on thresholds in stellar mass.

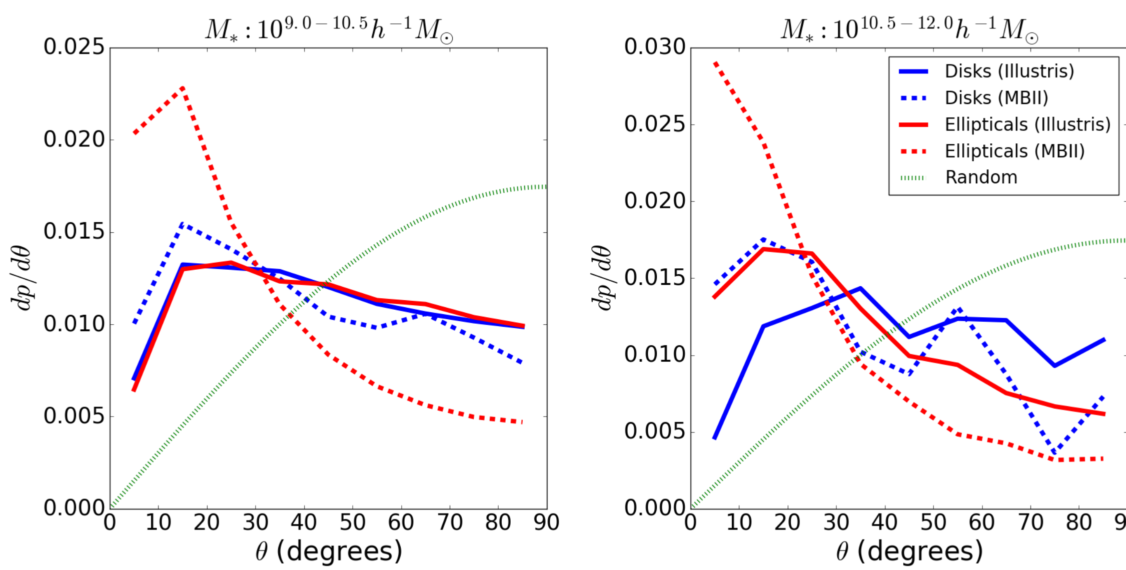

Figure 5.11: Normalized histogram of the misalignment angles of 3D shapes of elliptical and disk galaxies in MBII and Illustris within two stellar mass bins: $10^{9-10.5}h^{-1}M_\odot$ (left) and $10^{10.5-12}h^{-1}M_\odot$ (right).

range 10^9–$10^{10.5}h^{-1}M_\odot$. Disk galaxies have larger values of q and smaller values of s than elliptical galaxies in both Illustris and MBII. This reflects the fact that disk

Table 5.3: Mean axis ratios, $\langle q \rangle$ and $\langle s \rangle$, of disks and elliptical galaxies in Illustris and MBII.

	Illustris		MBII	
M_* ($h^{-1}M_\odot$)	Disks	Ellipticals	Disks	Ellipticals
		$\langle q \rangle$		
$10^9 - 10^{10.5}$	0.87	0.88	0.86	0.77
$10^{10.5} - 10^{12}$	0.90	0.84	0.91	0.75
		$\langle s \rangle$		
$10^9 - 10^{10.5}$	0.47	0.68	0.42	0.57
$10^{10.5} - 10^{12}$	0.47	0.61	0.43	0.53

Table 5.4: Mean misalignment angles in 3D, $\langle \theta \rangle$ (degrees), of disks and elliptical galaxies in Illustris and MBII.

M_* ($h^{-1}M_\odot$)	Illustris		MBII	
	Disks	Ellipticals	Disks	Ellipticals
$10^9 - 10^{10.5}$	$44.61 \pm 0.40°$	$45.13 \pm 0.18°$	$41.42 \pm 0.68°$	$31.01 \pm 0.11°$
$10^{10.5} - 10^{12}$	$46.46 \pm 0.74°$	$36.68 \pm 0.75°$	$36.85 \pm 2.07°$	$25.85 \pm 0.47°$

galaxies have a more oblate shape than elliptical galaxies. Comparing the axis ratios in Illustris and MBII, we find that elliptical galaxies are rounder in Illustris, consistent with the earlier results when considering mass dependence alone (Sec. 5.4.2).

However, the distributions for disk galaxies show that disks in MBII have slightly larger values of q but smaller values of s than in Illustris. This implies that disk galaxies in MBII are thinner (more oblate) compared to those in Illustris. Galaxies in a higher stellar mass bin, $10^{10.5}$–$10^{12} h^{-1} M_\odot$ (not shown), follow similar trends with respect to axis ratios. The mean axis ratios, $\langle q \rangle$ and $\langle s \rangle$, for disks and ellipticals in Illustris and MBII for the two stellar mass bins are given in Table 5.3. Similarly, in the case of projected shapes, the RMS ellipticities for disk galaxies in MBII are larger. The RMS ellipticities based on a stellar mass threshold are shown in Figure 5.10 and compared with observations. Note that when compared to observational measurements, the RMS ellipticities are smaller even for disk galaxies in MBII. However, a direct quantitative comparison with observations is difficult due to different methods adopted to measure the observed and simulated galaxy shapes. A detailed discussion on this comparison can be found in [156].

In order to understand the orientation of disks and ellipticals with the shape of their host dark matter subhalos, we compare the histograms of misalignment angles in Figure 5.11. In general, disk galaxies are more misaligned with their host dark matter shapes when compared with elliptical galaxies. The mean misalignment angles are provided in Table 5.4. Note that disks and ellipticals in the lower mass bin of

Illustris, 10^9–$10^{10.5}h^{-1}M_\odot$, have similar histograms of misalignment angles. This may be a mass-dependent effect where misalignments increase as we go to lower masses. If we increase the lower mass threshold of the bin, the histograms are shifted such that disks tend to be more misaligned than ellipticals.

Based on the results shown in this section, we find that the disk and elliptical galaxies in the MBII and Illustris simulations have qualitatively similar shapes and misalignment angle distributions. However, there are differences in the disk fraction and the amplitude of misalignments in the galaxies of the two simulations. This is likely due to the differences in sub-grid physics in the two simulations. A detailed study considering the effects of various baryonic feedback implementations in simulations on the galaxy alignments is deferred for future study.

5.5.3 Two-point intrinsic alignment statistics of disks and elliptical galaxies

Using the measured shapes of disks and elliptical galaxies, we compare the two-point shape correlation functions of disk galaxies with those of ellipticals in both simulations.

Figure 5.12 shows the ED correlation function in two stellar mass bins: 10^9–$10^{10.5}h^{-1}M_\odot$ and $10^{10.5}$–$10^{12}h^{-1}M_\odot$. As shown, the disk galaxies have a smaller ED correlation function than ellipticals; indeed, the correlation function is consistent with zero for disk galaxies in both simulations and mass bins on scales above $\sim 100h^{-1}$kpc. Hence, we only show the 1σ upper limits of the signal on these scales, represented by the *bottom (tip)* of arrows pointing downward in Illustris ($\downarrow$) and MBII ($\Downarrow$). The disk vs. elliptical difference is due to the larger misalignment of disk galaxy shapes with their host dark matter subhalo shapes. As discussed further below, we find that the ED correlation is similar for the shapes of dark matter subhalos of disks and ellipticals, while the galaxy misalignment suppresses the correlation. For the same reason, the correlation functions are larger in MBII than in Illustris for all samples.

To further understand the differences in the ED correlations of disks and ellipticals, we compare the ED correlations of the dark matter subhalos of disks and ellipticals in the bottom panels of Figure 5.12. In both Illustris and MBII, the ED correlation function of the dark matter subhalos hosting disk galaxies is significant even on large scales, and has similar radial scaling compared with that of ellipticals. The small differences in amplitude might relate to the slightly different subhalo mass distributions for disk and elliptical galaxies within these mass bins. The strong similarity between the results for subhalos hosting disk and elliptical galaxies reinforces our conclusion that the suppression in the ED correlation for the stellar components of disk galaxies is largely due to stronger misalignment with the shape of their host dark matter subhalo.

In Figure 5.13, we compare the projected shape-density ($w_{\delta+}$) correlation function in the same two stellar mass bins. Similar to the ED correlation, the $w_{\delta+}$ for disk

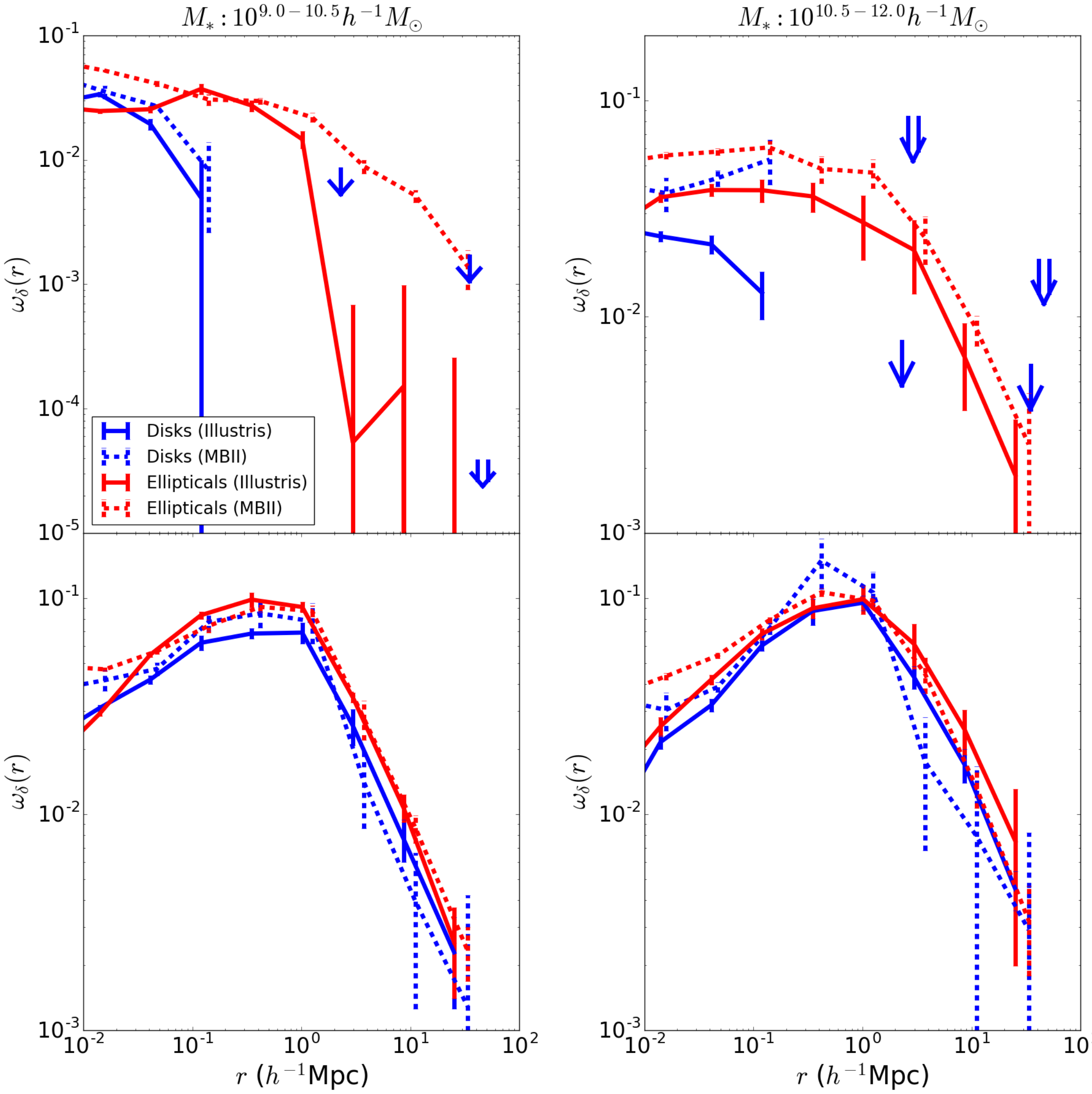

Figure 5.12: ED correlation functions of the shapes of the stellar component (*top* panel) and the dark matter component (*bottom* panel) of elliptical and disk galaxies galaxies in MBII and Illustris within two stellar mass bins: 10^9–$10^{10.5}h^{-1}M_\odot$ (left) and $10^{10.5}$–$10^{12}h^{-1}M_\odot$ (right). In the *top* panel, we only show the 1σ upper limits of the ED correlation for disk galaxies on scales above $0.1h^{-1}$Mpc, represented by the *bottom (tip)* of arrows pointing downward in Illustris ($\downarrow$) and MBII ($\Downarrow$). Note the y-axis limits are different in the top left panel compared to the other panels, which should be taken into account while comparing the figures.

galaxies is noisy on scales above $0.1h^{-1}$Mpc, and only the upper limits of the signal

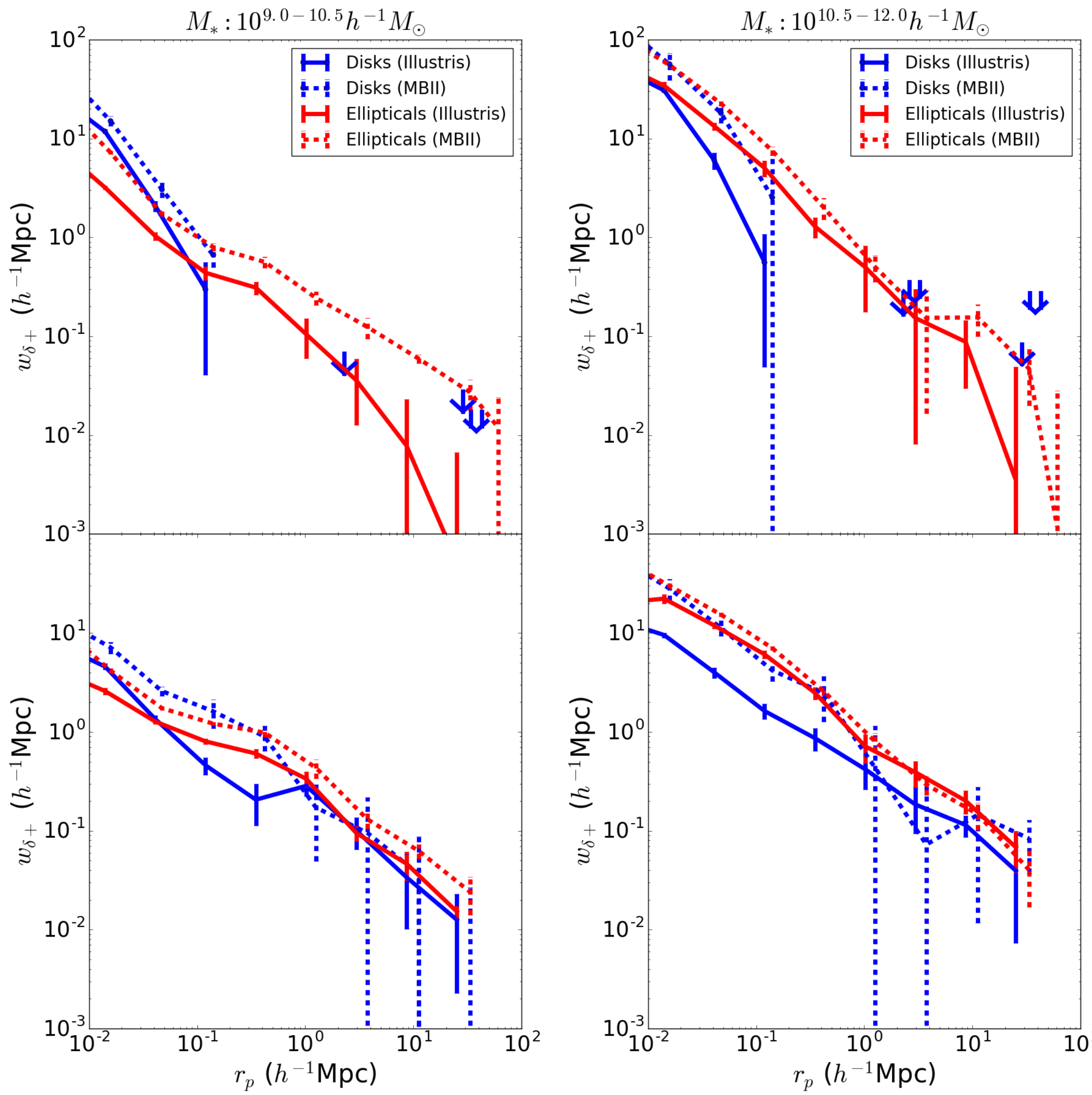

Figure 5.13: $w_{\delta+}$ correlation functions of the shapes of the stellar component (*top* panel) and the dark matter component (*bottom* panel) of elliptical and disk galaxies in MBII and Illustris within two stellar mass bins: 10^9–$10^{10.5}h^{-1}M_\odot$ (left) and $10^{10.5}$–$10^{12}h^{-1}M_\odot$ (right). On scales above $0.1h^{-1}$Mpc, we only show the 1σ upper limits of the $w_{\delta+}$ signal for disk galaxies, represented by the *bottom (tip)* of arrows pointing downward in Illustris ($\downarrow$) and MBII ($\Downarrow$).

are shown above these scales. However, on smaller scales, the amplitude of $w_{\delta+}$ for disk galaxies is larger than that for ellipticals in both simulations, due to the fact that disk galaxies have larger ellipticities than elliptical galaxies.

These predictions for disk galaxies can be compared against the measurements of [71], which has a null detection of w_{g+} for most of their blue galaxy samples, but a weak detection of intrinsic alignments for their most luminous blue galaxy sample, consistent with the amplitude of red galaxy w_{g+} in the same luminosity bin. While the amplitude of $w_{\delta+}$ is comparable for disks and ellipticals at small scales around $0.1h^{-1}$Mpc, we do not detect the signal for disks at scales around $1-10h^{-1}$Mpc, where the measurements in [71] are made. We also note here that [116] investigated the intrinsic alignments of blue galaxies from the WiggleZ sample at $z \sim 0.6$ and find a null detection for $1-10h^{-1}$Mpc. However, when considering the stellar mass bin 10^{11}–$10^{12}h^{-1}M_{\odot}$ (not shown), the $w_{\delta+}$ for disk galaxies in MBII is higher than for both samples shown in this section, and is comparable in magnitude with the amplitude of the weak signal detected for blue galaxies in [71] at scales around $\sim 1h^{-1}$Mpc.

5.6 Conclusions

In this paper, we studied the shapes and intrinsic alignments of disk and elliptical galaxies in the MassiveBlack-II and Illustris simulations. The galaxy stellar mass function is similar in both the simulations at high mass range, while at lower stellar masses, MBII has a higher number density of galaxies. We restrict our analysis to stellar masses ranging from 10^9–$10^{12}h^{-1}M_{\odot}$, for which the galaxies have a minimum of 1000 star particles.

We first compared the galaxy shapes and alignments in Illustris and MBII based on stellar mass alone, without considering disks and ellipticals separately. While the two simulations show similar trends in galaxy shapes with stellar mass (rounder at lower stellar mass), the galaxy shape distributions are rounder in Illustris than in MBII at fixed mass. By measuring the orientation of the shape of the stellar component with respect to the major axis of the host dark matter subhalo, we find that both simulations show similar trends with mass, with stronger misalignments at lower mass. However, at fixed mass, galaxies are more misaligned with their host subhalo shapes in the Illustris simulation than in MBII.

Due to the larger misalignment of the galaxy stellar components with the density field, the ellipticity-direction (ED) correlation function has a smaller amplitude in Illustris at fixed stellar mass. At around $1h^{-1}$Mpc, the correlation function is larger in MBII by a factor of $\sim 1.5-3.5$. Similarly, the amplitude of the projected shape-density correlation function, $w_{\delta+}$, is smaller in Illustris by a factor of $\sim 1.5-2.0$ at transverse separation of $1h^{-1}$Mpc due to both the larger misalignments and the smaller ellipticities. These differences in the amplitudes of the intrinsic alignment correlation functions are significant even after accounting for the bias in the dark matter correlations due to the smaller volume in Illustris. We further find that the mass- and scale-dependence of the $w_{\delta+}$ two-point statistic is similar in Illustris and MBII, in spite of the different implementations of hydrodynamics and baryonic physics. However, the scale dependence is significantly different in the ED correlation of low mass galaxies. This can be due to the different implementations of hydrodynamic or differences in baryonic feedback models. We find signs of different physics behind intrinsic alignments of disk galaxies in MBII and Illustris compared to findings from the Horizon-AGN simulation [34], which suggests possible differences in SPH vs. AMR simulations that warrant further investigation. Based on our findings, we conclude that hydrodynamic simulations are a promising tool to study intrinsic alignments. For higher mass galaxies, our results suggest that hydrodynamic simulations can be used to generate templates for the scale-dependence of intrinsic alignment two-point correlations for use by upcoming surveys that must remove this effect from weak lensing measurements, provided that the amplitude of the effect is marginalized over (given observational priors). However, further study on understanding the differences in various simulations is needed to confirm the validity of this conclusion at lower mass and to confirm that it applies with greater statistical precision at high mass.

Galaxies in MBII and Illustris are classified into disks and ellipticals by a dynamical bulge-disk decomposition method following the procedure adopted in [133], resulting in a larger fraction of disk galaxies in Illustris than in MBII at fixed stellar mass. The disk galaxies in both simulations are more oblate than the elliptical galaxies. However, the disk galaxies in MBII are more oblate than those in Illustris.

Comparing the alignments of the disk galaxies with their host dark matter subhalos, we find that disk galaxies are more misaligned than ellipticals in both MBII and Illustris by $\sim 20-30\%$ on average. Due to this larger misalignment, the disks have a smaller amplitude of ED correlation when compared with ellipticals (and compared to the ED correlations of their host dark matter subhalo shapes). Indeed, this correlation function is consistent with zero for the disk samples (within our errorbars) above $\sim 100h^{-1}$kpc. However, the disk galaxies also have larger ellipticities, which increases the $w_{\delta+}$ correlation on the small scales where it is detected. Thus, the amplitude of $w_{\delta+}$ for disks is comparable with that of ellipticals at the same mass for scales below $0.1h^{-1}$Mpc, while on large scales it is consistent with a null detection. While exploration with larger-volume simulations that have more disks and hence lower statistical errors is warranted, our results currently support the commonly-made assumption [e.g.,][][103] that large-scale intrinsic alignments for early-type galaxies are stronger than those for late-type galaxies. This finding bodes well for future weak lensing surveys that will be dominated by galaxies at $z \geq 0.6$, where the disk galaxy fraction is larger than it is at later times.

Chapter 6

Impact of Baryonic Physics

6.1 Introduction

The intrinsic shapes and orientations of galaxies are correlated with each other and the large scale density field. This intrinsic alignment of galaxies is an important astrophysical systematic in weak lensing measurements [66, 41, 29, 78, 72] of upcoming surveys such as the Large Synoptic Survey Telescope [1] (LSST; [114]) and Euclid [2] [106]. Ignoring intrinsic alignments in weak lensing analysis can significantly bias the constraints on cosmological parameters such as the dark energy equation of state parameter [104]. Therefore, intrinsic alignments have been studied with analytical models and also cosmological simulations including N-body and hydrodynamic simulations which can help in mitigating this contaminant signal. Analytically, intrinsic alignments have been modeled with a linear alignment model [29, 72] and modifications of the model which includes the non-linear evolution of the density field [24, 21]. However, it is difficult to analytically describe the alignments of a galaxy's stellar component by accurately considering the physics of galaxy formation. There are also limitations to the use of N-body simulations as one has to populate halos with galaxies by assigning a random orientation [68] or employ semi-analytic methods [86]. Recently, intrinsic alignments of galaxies in large volume hydrodynamic simulations have been extensively studied with simulations of galaxy formation such as MassiveBlack-II [93], Horizon-AGN [51], EAGLE [134] and Illustris [169, 170, 61].

Cosmological hydrodynamic simulations of galaxy formation are an important tool to study intrinsic alignments as it is directly possible to measure the shape and orientation of the stellar component of galaxies in the simulations. In a precursor of this paper, [158] studied the galaxy shapes and two-point statistics in the MassiveBlack-II cosmological hydrodynamic simulation. This study was extended to compare the galaxy alignments based on their morphological type in MassiveBlack-II and Illustris simulations [155]. [32] used the Horizon-AGN simulation, an Adaptive Mesh Refine-

[1] `http://www.lsst.org/lsst/`
[2] `http://sci.esa.int/euclid/`, `http://www.euclid-ec.org`

ment (AMR) based hydrodynamic simulation of galaxy formation to study intrinsic alignments of spirals and elliptical galaxies. The redshift and luminosity evolution of alignments in the same simulation was studied in [33]. Recently, [69] studied the mass and redshift dependence of intrinsic alignments in the Illustris simulation and their dependence on stellar mass, luminosity, redshift and photometric type. Qualitatively, the properties of galaxy shapes and alignments have a similar trend with mass across different simulations. However, differences have been noted in the amplitude of galaxy alignments and morphological fraction of disk galaxies in MassiveBlack-II and Illustris [155], as well as qualitative differences in the comparison of alignments of spirals with the over-density and the redshift dependence of intrinsic alignments in the Horizon-AGN simulation [32, 33]. Given the differences in the models of subgrid physics adopted in these simulations and also the numerical implementations of hydrodynamics, it is important to understand the details of the subgrid physics responsible for changes in the galaxy alignments and to explore the robustness of simulation results.

In a previous study, [165] studied intrinsic alignments using the EAGLE suite of simulations with variations in the strength of feedback. Here, we undertake a parameter space study of the subgrid model adopted in the MassiveBlack-II simulation using a suite of small volume simulations with box size of $25h^{-1}Mpc$ on a side. We vary the free parameters in the feedback models of the simulation and test the robustness of the galaxy shapes, orientations and two-point statistics of shape correlations to variations in these parameters. Since high resolution hydrodynamic simulations of large volume are computationally expensive, we also test the usefulness of using small volume simulations to capture the sensitivity of intrinsic alignment statistics to variations in the feedback parameters.

This paper is organized as follows. In Section 6.2, we describe the simulations used in this study along with a brief overview of the feedback models adopted in the MassiveBlack-II simulation. Section 6.3 provides the details of the methods adopted to calculate shapes and intrinsic alignment statistics studied in this paper. In Section 6.4 we compare the results from the suite of small volume simulations with the fiducial MBII model and different amplitudes of the DC mode with those of the original $100h^{-1}Mpc$ box size MBII simulation. The intrinsic alignment statistics in the small volume runs with different feedback parameters are compared with those from the fiducial model in Section 6.5. Finally, we provide a summary of our conclusions in Section 6.6

6.2 Simulations and Feedback Models

In this paper, we use the MassiveBlack-II (MBII) simulation [93], a high resolution cosmological hydrodynamic simulation performed in a box of volume $(100h^{-1}Mpc)^3$, which includes galaxy formation physics as our base model. We complement MassiveBlack-II with smaller volume simulations of size $25h^{-1}Mpc$, in which we vary the key parameters of the star formation and stellar and AGN feedback model. We denote the smaller volume simulations as MBII-25. The simulations are performed with the TreePM-Smoothed Particle Hydrodynamics (SPH) code, P-Gadget, a modified version of GADGET2 [147]. The same version of the code has been used earlier to perform the large volume MBII simulation [93]. The simulations include the wide range of physical effects thought to be crucial for properly modeling galaxy formation, such as multiphase ISM, star formation, supernova and stellar wind feedback, as well as black hole accretion and feedback. Radiative cooling and heating are included as in [90], along with photoheating due to an imposed ionizing UV background.

Initial conditions are generated at $z = 159$ and simulations are evolved to $z = 0$ with an equal initial number of gas and dark matter particles. The cosmological parameters are chosen with the WMAP7 cosmology[102]: $h = 0.701$, $\Omega_m = 0.275$, $\Omega_b = 0.046$, $\Omega_\Lambda = 0.725$, $\sigma_8 = 0.816$, spectral index, $\eta_s = 0.968$ The mass of each dark matter particle is $1.1 \times 10^7 h^{-1} M_\odot$. The smaller volume simulations are performed with the same mass and spatial resolution as the original simulation. Accordingly, the initial number of gas and dark matter particles are equal to 2×1792^3 and 2×448^3 in the $100 h^{-1} Mpc$ and $25 h^{-1} Mpc$ box size simulations respectively. We note that all the small volume simulations have been started with the same initial conditions at $z = 159$. The details of the star formation and feedback models of the simulation and the changes adopted in the small volume runs are described below.

6.2.1 Star formation and Stellar and AGN Feedback

The star formation and feedback model adopted in the simulation is based on an earlier multiphase ISM model of Springel & Hernquist [149]. Specifically, if the local gas density ρ is greater than a critical density threshold ρ_{th}, a multiphase ISM consisting of cold clouds in pressure equilibrium with a hot ambient gas is assumed. The effective pressure P_{eff} is defined as $P_{eff} = (\gamma - 1)(\rho_h \mu_h + \rho_c \mu_c)$ [149], where ρ_c, ρ_h are the local densities of cold and hot phases respectively, $\rho = \rho_c + \rho_h$, and μ_h and μ_c are specific energies of hot and cold components. The threshold density ρ_{th} is determined self consistently by requiring that the effective pressure is a continuous function of density.

Star formation is modeled by spawning individual stellar particles stochastically from the cold clouds. The rate of star formation is given by

$$\frac{d\rho_*}{dt} = \frac{\rho_c}{t_*} - \beta \frac{\rho_c}{t_*} \tag{6.1}$$

where $\beta = 0.1$ is the mass fraction of short lived stars and t_* is the star formation time scale with density dependence given by

$$t_*(\rho) = t_0^*(\frac{\rho}{\rho_{th}})^{-0.5}, \tag{6.2}$$

where $t_0^* = 2.1$Gyr.

The energy released by supernovae heats the ambient gas and the heating rate is set by the energy balance condition

$$\frac{d}{dt}(\rho_h \mu_h) = \beta \frac{\rho_c}{t_*}(\mu_{SN}). \tag{6.3}$$

Here $\mu_{SN} = \frac{3}{2}kT_{SN}$ where T_{SN} is the equivalent supernova temperature which is equal to 10^8 K in the fiducial model.

6.2.2 Wind Feedback

Galactic winds are implemented with the wind velocity given by

$$v_w = \sqrt{\frac{2\beta\chi\mu_{SN}}{\eta(1-\beta)}}, \tag{6.4}$$

where $\chi = 1.0$ is the fraction of supernova energy carried by the wind and $\eta = 2.0$ is the wind loading factor. For a given time step Δt, a gas particle is added to the wind probabilistically with the probability

$$p_w = 1 - \exp\left[-\frac{\eta(1-\beta)x\Delta t}{t_*}\right]. \tag{6.5}$$

6.2.3 AGN Feedback

The simulations also include the physics of black hole accretion and feedback, based on the models of [147] and [47]. Black holes are treated as collisionless particles introduced into halos of mass greater than $5.0 \times 10^{10} h^{-1} M_\odot$ at regular time intervals, separated by $\Delta \log(a) = \log(1.25)$. The densest particle is converted into a seed black hole of mass $M_{BH,seed} = 5 \times 10^5 h^{-1} M_\odot$ which grows in mass by black hole accretion and mergers. The black hole accretion rate is given by the modified Bondi rate formula

$$\dot{M}_{BH} = \frac{4\pi\alpha G^2 M_{BH}^2 \rho}{(c_s^2 + v_{BH}^2)^{3/2}}, \tag{6.6}$$

where ρ is the local gas density, c_s is the local speed of sound, v is the velocity of BH relative to the gas. The accretion rate is limited to 2 times the Eddington rate, $\dot{M}_{Edd}$. A dimensionless parameter α is set to 100; that value has been found experimentally to approximately correct for the gas density close to the black hole, which is reduced in the effective sub-resolution model of the ISM.

The AGN feedback is modeled by coupling 5% (the value chosen to match the slope in the observed $M_{BH} - \sigma$ relation [147]) of the bolometric luminosity radiated from the BH,

$$L_{bol} = \epsilon_r \dot{M}_{BH} c^2, \tag{6.7}$$

with the radiation efficiency $\epsilon_r = 0.1$. The energy is deposited isotropically to the 64 nearest gas particles within the BH particle kernel.

6.2.4 Parameters Space Study

In the simulations analyzed here, we vary the key parameters in the star formation and stellar and AGN feedback models. In particular, we consider the effect of a lower or higher star formation efficiency by increasing and decreasing the star formation timescale t_0^* by a factor of 3. We also consider the effects of increasing the AGN feedback by increasing the scaling parameter α in the AGN feedback model to 300, which triples the black hole accretion rate. Similarly, the effect of wind velocity is weakened by decreasing the wind loading factor 10 times to study the effects of wind feedback.

6.3 Methods

In this section, we describe the method adopted to calculate shapes and the also provide details of the intrinsic alignment statistics explored in this paper.

6.3.1 Calculation of shapes

The 3D shapes of the dark matter and stellar components in subhalos are determined using the the eigenvalues and eigenvectors of the reduced inertia tensor given by

$$\widetilde{I}_{ij} = \frac{\sum_n m_n \left(x_{ni} x_{nj}\right) / r_n^2}{\sum_n m_n}, \tag{6.8}$$

where the summation is over particles index n, and

$$r_n^2 = \frac{x_{n0}^2}{a^2} + \frac{x_{n1}^2}{b^2} + \frac{x_{n2}^2}{c^2}. \tag{6.9}$$

Here a, b, and c are half-lengths of the principal axes of the ellipsoid.

The eigenvectors of the inertia tensor are $\hat{e}_a, \hat{e}_b, \hat{e}_c$ with corresponding eigenvalues $\lambda_a > \lambda_b > \lambda_c$. The eigenvectors represent the principal axes of the ellipsoid, with the half-lengths of the principal axes (a, b, c) given by $(\sqrt{\lambda_a}, \sqrt{\lambda_b}, \sqrt{\lambda_c})$. The 3D axis ratios are b/a and c/a.

Similarly, in 2D, the projected shapes are calculated by projecting the positions of the particles onto the XY plane and modeling the shapes as ellipses. Here, we denote the eigenvectors as $\hat{e}'_a, \hat{e}'_b$ with corresponding eigenvalues $\lambda'_a > \lambda'_b$. The lengths of the semi-major and semi-minor axes are $a' = \sqrt{\lambda'_a}$ and $b' = \sqrt{\lambda'_b}$ with the axis ratio b'/a'.

The details of the iterative method for measuring axis ratios can be found in [158]. In the first iteration, we start with the half-lengths of the principal axes all equal to 1 and determine the eigenvalues and eigenvectors of the ellipsoid. After each iteration, the lengths of the principal axes of ellipsoids are rescaled such that the enclosed volume is constant and particles outside the ellipsoidal volume are discarded. This process is repeated until convergence is reached such that the fractional change in axis ratios is below 1%.

In addition to the distribution of the axis ratios, b/a and c/a of the stellar components of subhalos, we are also interested in the orientation of the major axis of the stellar shape with the shape of dark matter in subhalos. So, we compute the probability distribution of the misalignment angle

$$\theta_m = \arccos(|\hat{e}_{da} \cdot \hat{e}_{ga}|), \tag{6.10}$$

where $\hat{e}_{da}$ and $\hat{e}_{ga}$ are the major axes of the shapes defined by the dark matter and stellar matter components respectively.

6.3.2 Two-point statistics

In this paper we quantify the intrinsic alignments of galaxies with the large-scale density field using the ellipticity-direction (ED) and the projected shape-density ($w_{\delta+}$) correlation functions.

The ED correlation function cross-correlates the orientation of the major axes of the 3D shapes of dark matter or stellar component of galaxies with the large-scale density field. Consider a subhalo centered at position $\mathbf{x}$ with the major axis direction $\hat{e}_a$. Let the unit vector in the direction of a tracer of the matter density field at a distance r be $\hat{\mathbf{r}}(\mathbf{x})$. Based on the notation in [109], the ED correlation function is given by

$$\omega_\delta(r) = \langle | \hat{e}_a(\mathbf{x}) \cdot \hat{\mathbf{r}}(\mathbf{x}) |^2 \rangle - \frac{1}{3}, \tag{6.11}$$

which is zero for randomly oriented galaxies in a uniform distribution. In the simulations the matter density field is traced using the positions of dark matter particles.

The projected shape correlation function, $w_{\delta+}$ is directly related to the correlation function measured in observations. Following the notation of [117], we define the the matter-intrinsic shear correlation function $\hat{\xi}_{\delta+}(r_p, \Pi)$ and the corresponding projected two-point statistic $w_{\delta+}$. In this paper, r_p is the comoving transverse separation of a pair of galaxies in the XY plane and Π is their separation along the Z direction.

The components of the projected ellipticities of a galaxy are given by

$$(e_+, e_\times) = \frac{1 - (b'/a')^2}{1 + (b'/a')^2} \left[\cos(2\phi), \sin(2\phi)\right], \tag{6.12}$$

where b'/a' is the axis ratio of the projected shape of the stellar component of a galaxy, and ϕ is the position angle of the major axis with respect to the reference direction (position of the dark matter particle). Here, e_+ refers to the radial component and $e_\times$ is the component rotated at 45°. The matter-intrinsic shear correlation function is given by,

$$\hat{\xi}_{\delta+}(r_p, \Pi) = \frac{S_+ D}{RR} \tag{6.13}$$

where S_+ represents the “shape sample”, selected on the basis of a binning in subhalo mass and the “density sample” labeled by D consists of the dark matter particles used to trace the matter density field. S_+D is given by the following sum over all galaxy - dark matter particle pairs with separations r_p and Π:

$$S_+D = \sum_{i \neq j | r_p, \Pi} \frac{e_+(j \mid i)}{2\mathcal{R}}, \tag{6.14}$$

where $e_+(j|i)$ is the $+$ component of the ellipticity of a galaxy (j) from the shape sample relative to the direction of a dark matter particle (i) selected from the density sample. Here, $\mathcal{R} = (1 - e_{\rm rms}^2)$ is the shear responsivity that converts from distortion to shear [15], with $e_{\rm rms}$ being the RMS ellipticity per component of the shape sample. The RR term in Eq. (6.13) refers to the expected number of randomly-distributed pairs in a particular (r_p, Π) bin around galaxies in the shape sample.

The projected shape correlation function $w_{\delta+}(r_p)$ is given by

$$w_{\delta+}(r_p) = \int_{-\Pi_{\rm max}}^{+\Pi_{\rm max}} \hat{\xi}_{\delta+}(r_p, \Pi)\, {\rm d}\Pi. \tag{6.15}$$

We calculate the matter-intrinsic shear correlation function over the whole length of the box, L_{box} with $\Pi_{\rm max} = L_{box}/2$, where the length of the box is $100h^{-1}$Mpc or $25h^{-1}$Mpc. The projected correlation functions are obtained via direct summation.

6.4 Intrinsic alignments in a smaller volume box including DC mode in the fiducial model

To study the effects of modifying baryonic feedback parameters, we use small volume simulations, as larger simulation volumes would not be feasible at present. Smaller volume simulations, however, will be a subject to larger cosmic variance, and so may be biased relative to the larger box.

In order to estimate the error we are going to incur by using smaller boxes, we use the DC mode formalism [144] that allows one to approximately quantify the effect of the missing large-scale power. Ideally, one would need to run a whole ensemble of the simulations with randomly chosen DC modes. However, due to limited computational resources, we only perform three independent realizations of the $25h^{-1}Mpc$ box with the amplitude of DC mode set to zero and to $\pm\Delta_0$, where Δ_0 is the rms density fluctuations in a cubic $25h^{-1}Mpc$ box at $z = 0$. For any of our statistical measures we then can use the spread between the three realizations as an, admittedly crude, estimate of the uncertainty due to the limited simulation volume.

For the WMAP7 cosmological parameters and the box size of $25h^{-1}Mpc$ box size $\Delta_0 = 0.585$. In a most general case accounting for the DC mode requires modifications to the simulation code. However, [144] showed that for the cosmology that includes only matter, the cosmological constant, and, optionally, curvature, the DC mode can be accounted for by a simple rescaling of cosmological parameters. In this paper we use such a rescaling to include the DC mode in P-Gadget that does not support the DC mode explicitly.

6.4.1 Distribution of Shapes and Misalignment angles

Table 6.1: Mean 3D shapes b/a and c/a of the stellar component of the fiducial MBII-100 simulation and three MBII-25 simulations with different DC modes of 0 and $\pm 1\sigma$

	MBII-100	MBII-25: $\Delta_{\rm DC} = 0$	$\Delta_{\rm DC} = +1\sigma$	$\Delta_{\rm DC} = -1\sigma$
$M_{subhalo}$ $(h^{-1}M_{\odot})$	$\langle b/a \rangle$	$\langle b/a \rangle$	$\langle b/a \rangle$	$\langle b/a \rangle$
$10^{9.5} - 10^{12.0}$	0.79 ± 0.0	0.78 ± 0.0	0.75 ± 0.0	0.795 ± 0.003
$10^{12.0} - 10^{15.0}$	0.74 ± 0.0	0.76 ± 0.02	0.73 ± 0.02	0.77 ± 0.02
$M_{subhalo}$ $(h^{-1}M_{\odot})$	$\langle c/a \rangle$	$\langle c/a \rangle$	$\langle c/a \rangle$	$\langle c/a \rangle$
$10^{9.5} - 10^{12.0}$	0.61 ± 0.0	0.60 ± 0.0	0.56 ± 0.0	0.62 ± 0.0
$10^{12.0} - 10^{15.0}$	0.525 ± 0.002	0.524 ± 0.015	0.515 ± 0.013	0.51 ± 0.015

In Figure 6.1 we show a comparison between the cumulative distribution functions (CDF) for the shapes, b/a and c/a in two mass bin for the original $100h^{-1}Mpc$ MBII-100 run and our three $25h^{-1}Mpc$ MBII-25 simulations with different DC modes. The mean values for the shapes are tabulated in Table 6.1. Because of the limited size of our simulation volumes, we are only able to consider two mass bins. However, this may be sufficient to notice a really strong trend with halo mass; more subtle trends are missed by us and will have to be explored in the future with more precise simulations. Throughout this paper, the galaxy shapes and alignments are analyzed at $z = 0.3$.

Table 6.2: Mean 3D misalignment angles, $\langle \theta \rangle$ (degrees), between the major axis of galaxies and their host dark matter subhalos in the MBII simulation of $100h^{-1}Mpc$ size box and simulations of $25h^{-1}Mpc$ box with DC-modes : 0, $\pm 1\sigma$

$M_{subhalo}$ $(h^{-1}M_{\odot})$	MBII-100	MBII-25: $\Delta_{\rm DC} = 0$	$\Delta_{\rm DC} = +1\sigma$	$\Delta_{\rm DC} = -1\sigma$
$10^{9.5} - 10^{12.0}$	$33.259 \pm 0.078°$	$31.151 \pm 0.603°$	$31.761 \pm 0.662°$	$28.153 \pm 0.545°$
$10^{12.0} - 10^{15.0}$	$27.157 \pm 0.409°$	$31.785 \pm 3.525°$	$25.505 \pm 2.701°$	$26.49 \pm 4.35°$

For three smaller volume simulations we can both the compute the mean over the three realization, and the error in that mean, which we show in these and all subsequent figures with lines and bands respectively. Since the small box simulations

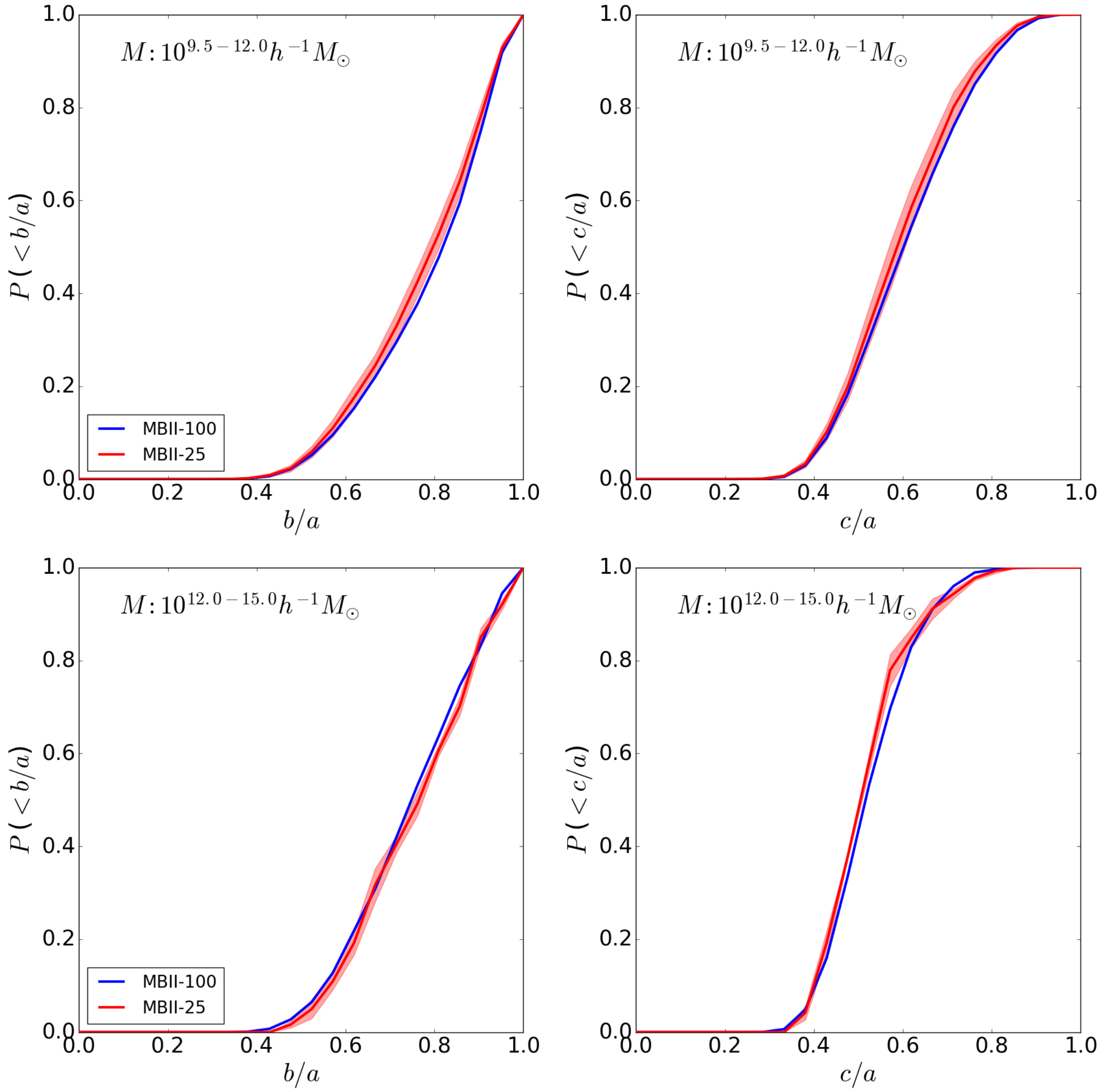

Figure 6.1: Cumulative distribution function (CDF) of the shapes b/a and c/a in two mass bins $10^{9.5-12.0}h^{-1}M_\odot$ and $10^{12.0-15.0}h^{-1}M_\odot$ of MBII-100 run and the mean CDF of the shapes of three MBII-25 simulations with different DC modes. The bands show the error of the mean CDF.

may be biased and/or insufficiently accurate, we use the error in the mean as the estimate of our theoretical error due to the limited box size. For example, from Fig. 6.1 it is clear that the differences between the mean of three MBII-25 runs and the original MBII-100 run are comparable to the error on MBII-25, and that error is reasonably modest, about 2%. Hence, by using smaller boxes we do introduce a bias, but the bias is modest and is comparable to the statistical error of the simulation

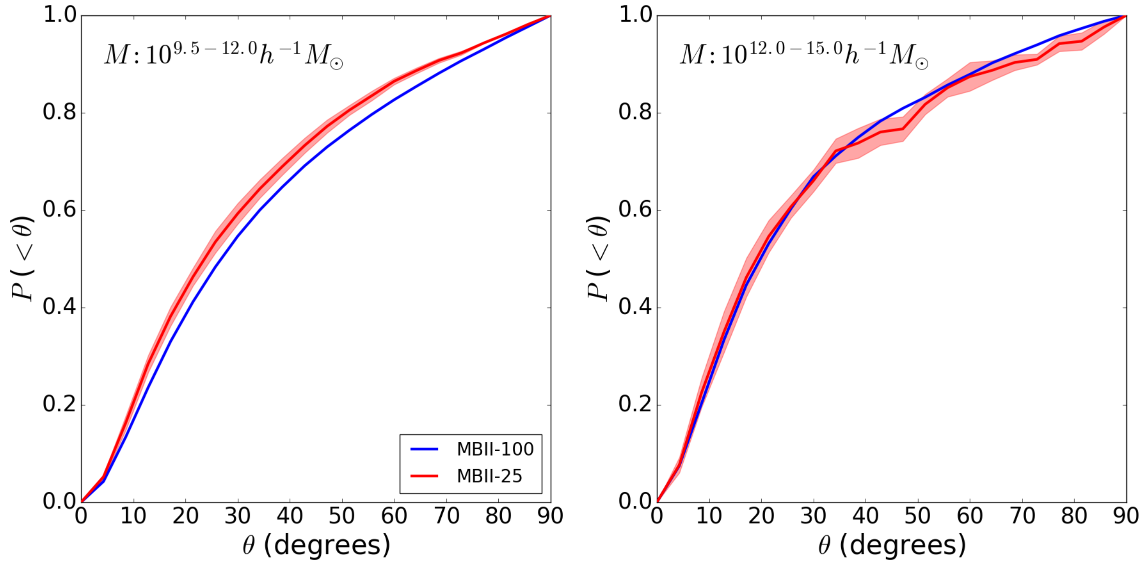

Figure 6.2: Cumulative distribution function (CDF) of the misalignment angle θ in the mass bins $10^{9.5-12.0}h^{-1}M_\odot$ and $10^{12.0-15.0}h^{-1}M_\odot$ of MBII $100h^{-1}Mpc$ and the mean CDF of the misalignment angles of $25h^{-1}Mpc$ simulations with different DC modes. The error on the mean CDF is indicated by the bands.

results.

The distributions of misalignment angles in the same two mass bins are shown in Figure 6.2, and their mean values are given in Table 6.2. We find that the galaxies in the lower mass bin of smaller volume simulations are more aligned, at about 2σ level, than in the fiducial MBII-100 run, and in the high mass bins low abundance of halos becomes appreciable. In both cases, however, the bias in using smaller boxes is still sufficiently modest (less than 3^o) to justify our use of smaller boxes in this first, exploratory work.

The two-point statistics ED and $w_{\delta+}$ are shown in Figure 6.3. The ED and $w_{\delta+}$ correlation functions in the MBII-100 simulation and in the mean of MBII-25 runs are in good agreement on small scales and in the high mass bin. The agreement is worse at large scales in the low mass bin, but the measurements there are also noisy. The formal error on the mean of three MBII-25 runs is smaller than the difference between the two box sizes, but since the error is estimated from just three runs, it may itself be inaccurate.

Overall, we find that our $25h^{-1}Mpc$ boxes are a suitable, albeit not ideal and moderately biased, tool for exploring the sensitivity of the simulation predictions to the parameters of the star formation and feedback model.

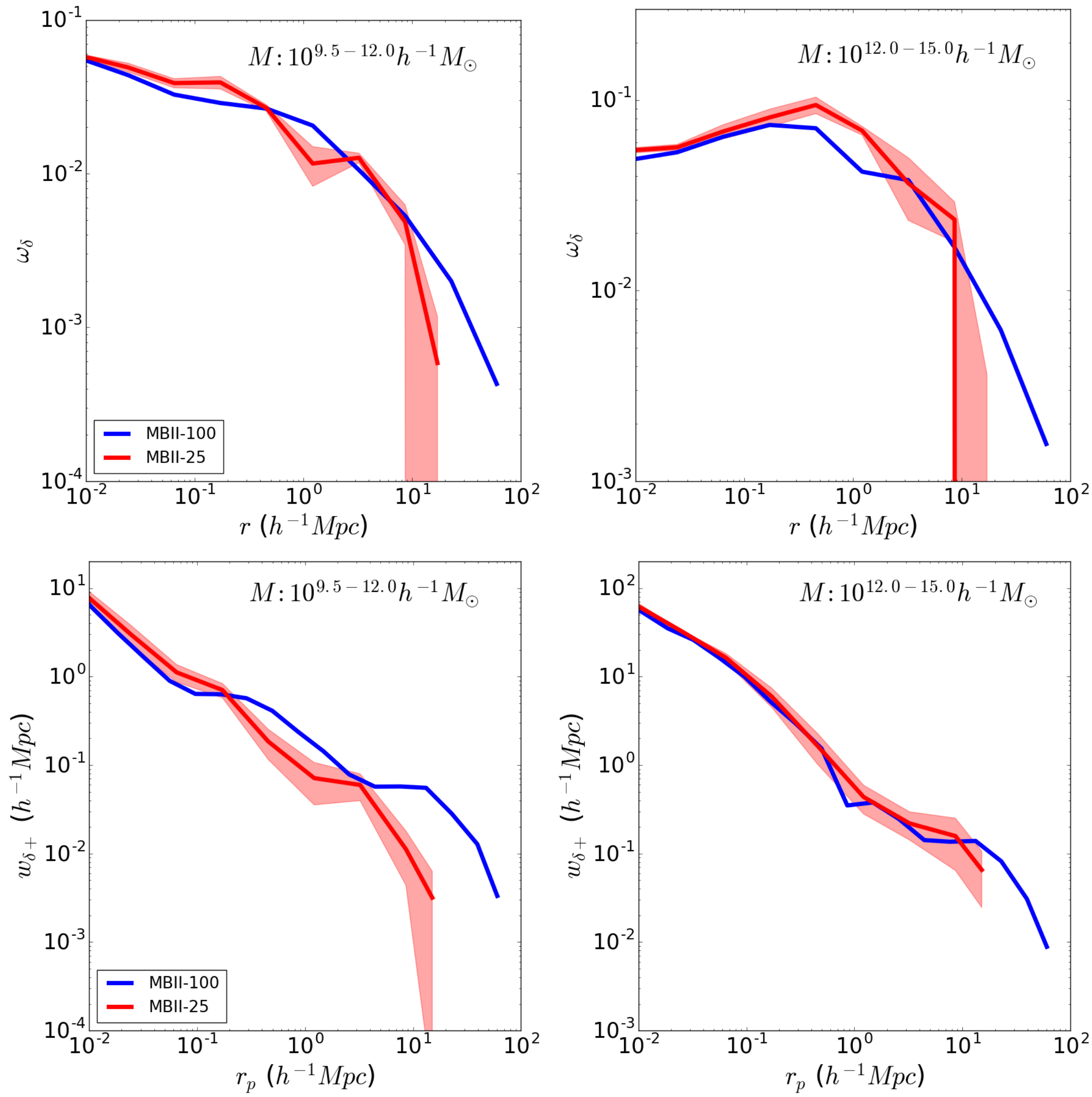

Figure 6.3: ED and $w_{\delta+}$ correlation functions in two mass bins, $10^{9.5-12.0}h^{-1}M_\odot$ and $10^{12.0-15.0}h^{-1}M_\odot$, of MBII-100 and of three independent realizations of MBII-25 box with different DC modes. The bands indicate the error in the mean ED correlation function.

6.5 Baryonic effects : parameter variation in the fiducial model

In this section, we explore the effects of modifying the feedback parameters in the simulation on the galaxy shapes and two-point statistics. We follow the methodology of

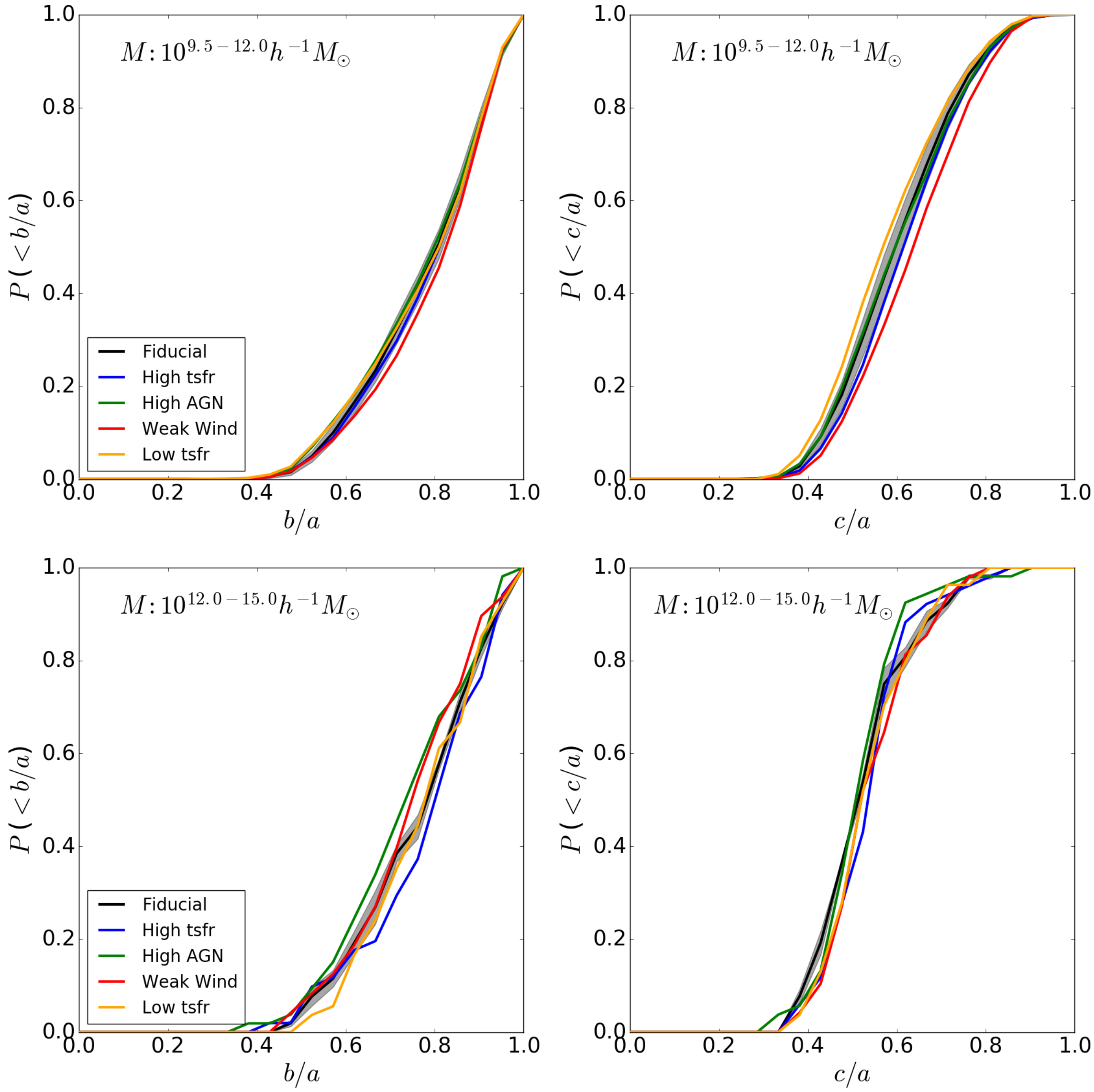

Figure 6.4: Cumulative distribution functions of the shapes b/a and c/a in two mass bins, $10^{9.5-12.0}h^{-1}M_\odot$ and $10^{12.0-15.0}h^{-1}M_\odot$, of several $25h^{-1}Mpc$ box simulations with varied physics. Black line with the gray band is the fiducial MBII-25 model and its error, shown with red lines in the previous section.

the previous section, and use the three MBII-25 runs with different DC models as our new fiducial simulation set against which we compare runs with varied physics. The details about which parameter is varied in a given model are provided in Section 6.2.4.

The cumulative shape distributions are plotted in Figure 6.4 in two mass bins of $10^{9.5-12.0}h^{-1}M_\odot$ and $10^{12.0-15.0}h^{-1}M_\odot$. Comparing the distributions and the mean

Table 6.3: Mean of b/a, c/a, and θ of the stellar shape of galaxies for simulations with varying star formation feedback.

	$10^{9.5} - 10^{12.0}(h^{-1}M_\odot)$		
Simulation	b/a	c/a	θ
MBII-25	0.779 ± 0.004	0.603 ± 0.003	31.151 ± 0.603
tsfr-High	0.783 ± 0.003	0.618 ± 0.003	31.883 ± 0.557
tsfr-Low	0.775 ± 0.004	0.582 ± 0.003	33.306 ± 0.648
AGN-High	0.773 ± 0.004	0.604 ± 0.003	30.265 ± 0.600
Wind-High	0.793 ± 0.002	0.636 ± 0.002	37.783 ± 0.427
	$10^{12.0} - 10^{15.0}(h^{-1}M_\odot)$		
Simulation	b/a	c/a	θ
MBII-25	0.76 ± 0.0195	0.524 ± 0.015	31.785 ± 3.525
tsfr-High	0.777 ± 0.02	0.532 ± 0.014	32.512 ± 3.490
tsfr-Low	0.767 ± 0.017	0.533 ± 0.013	30.747 ± 2.973
AGN-High	0.73 ± 0.02	0.513 ± 0.013	29.725 ± 3.18
Wind-High	0.747 ± 0.02	0.535 ± 0.014	32.512 ± 3.49

values shown in Table 6.3, we that in the lower mass bin the axis ratio b/a is larger for the simulation with weaker wind feedback, although the effect is not large, within 2σ of the fiducial model - the deviation comparable to the difference between the mean of three MBII-25 runs and the original MBII-100 run.

Despite all deviations being moderate and not highly significant, some trends are nevertheless intriguing. For example, in the low mass bin weaker feedback makes galaxies rounder, while in the high mass bin the (mild) deviation is in the opposite direction.

The cumulative distributions of misalignment angles are shown in Figure 6.5. The effect of the lower wind loading factor is larger on the angles than on the shapes for lower mass galaxies - since the wind carries away linear and angular momenta, it can directly affect the orientation of the stellar distribution without affecting the shape that much. For more massive galaxies the effect disappears, however, as in that mass bin the feedback is dominated by AGN. One can hypothesize that AGN, being centrally located, are not able to eject large amounts of angular momentum.

If such interpretation of our findings is valid, then the critical quantity that controls the distributions of shapes and angles is the angular momentum of the wind; once simulations get it right, their predictions for intrinsic alignment become robust and accurate.

In a previous study, [165] explored the variation in the ellipticities and misalignments, compared with their fiducial model of EAGLE simulation for three different feedback implementations. [165] investigated models with weaker and stronger stellar feedback and no AGN feedback. They also found that shapes are affected much less

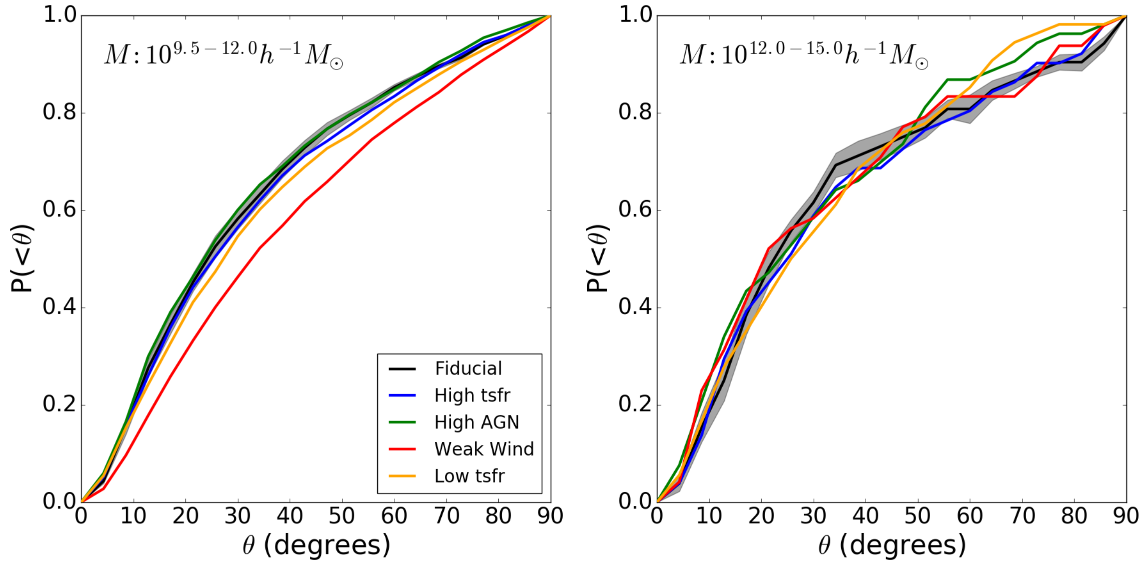

Figure 6.5: Cumulative distribution function of the misalignment angles θ in two mass bins, $10^{9.5-12.0}h^{-1}M_\odot$ and $10^{12.0-15.0}h^{-1}M_\odot$, of several $25h^{-1}Mpc$ box simulations with varied physics. Black line with the gray band is the fiducial MBII-25 model and its error, shown with red lines in the previous section.

than angles, consistent with our hypothesis above. However, they find a larger effect of the stellar feedback on misalignment angles in more massive ($> 10^{12}M_\odot$) galaxies, while their measurements for lower mass galaxies are too noisy to be conclusive.

Overall, however, we find a good agreement with EAGLE simulations, which is encouraging, but not particularly surprising - modern simulations reproduce many observed properties of galaxies fairly.

Two point statistics for simulations with varied physics are shown in Figure 6.6. Differences between various models are similar to the level of difference between MBII-100 and MBII-25 runs: correlation functions agree well on small scales and in the high mass bin, but exhibit significant variations on scales between $0.1h^{-1}$Mpc and $1h^{-1}$Mpc. These variations are non-monotonic and unsystematic, and are likely caused by the lack of statistics in our small box runs. However, just as in previous statistics, we find the largest difference in the run with the low wind mass loading factor.

In particular, the dip in the w_δ correlation function at $\sim 0.3h^{-1}$Mpc appears to be real - it is insensitive to the numerical details of computing the correlation function such as binning, sample selection, etc. The dip is located close to the radius where the one-halo term transitions to the two-halo term, and may reflect physical processes occurring at the halo-IGM interface. Unfortunately, our simulations volumes are too small to make any strongly statistically significant claim.

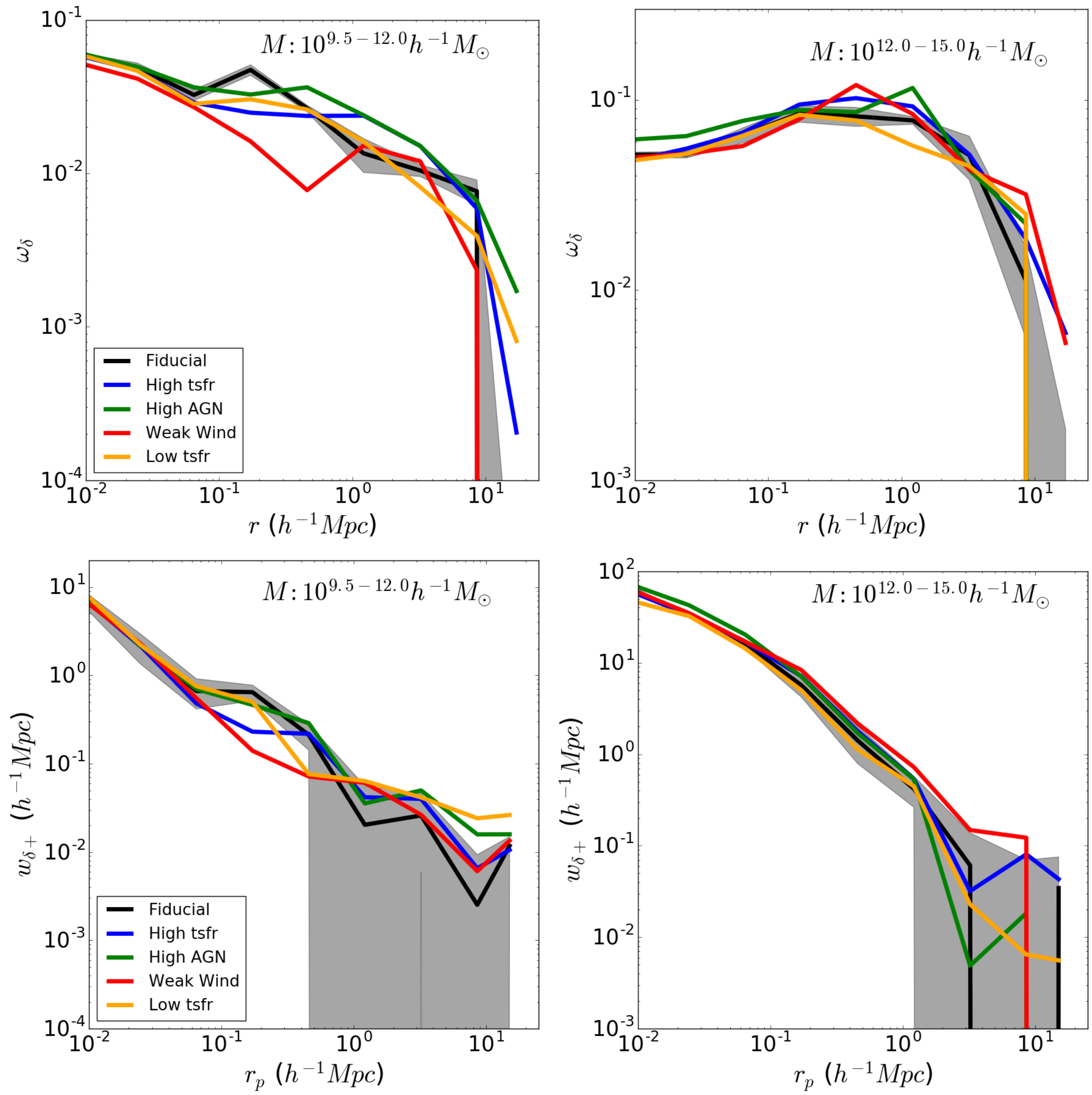

Figure 6.6: ED and $w_{\delta+}$ correlation functions in two mass bins, $10^{9.5-12.0}h^{-1}M_{\odot}$ and $10^{12.0-15.0}h^{-1}M_{\odot}$, of several $25h^{-1}Mpc$ box simulations with varied physics. Black line with the gray band is the fiducial MBII-25 model and its error, shown with red lines in the previous section.

6.6 Conclusions

Our primary goal in this paper is to explore the effects of model parameters in the star formation and feedback models on the galaxy shapes and alignments using small volume simulations of size $25h^{-1}Mpc$ on a side. As our fiducial model for the simulation, we adopted the same star formation and feedback model as in the MassiveBlack-II hydrodynamic simulation of galaxy formation [93], which is performed in a box of volume $(100h^{-1}Mpc)^3$.

Simulations with significantly (by factors of of 3 - 10) varying feedback show remarkable consistency with the fiducial run. Within the statistical precision we are able to achieve in our small volume runs, most of observational probes are insensitive to the details of subgrid physical modeling, with the exception of misalignment angles. We hypothesize that the angular momentum ejected by galactic winds is the most crucial physical quantity that determines the alignment of stellar shapes, and it remains one of the least robust quantities predicted in modern simulations of galaxy formation.

Our conclusions are also in good agreement with similar exploration of the role of subgrid physics on intrinsic alignments by the EAGLE simulation team.

Chapter 7

Conclusion and Future Work

7.1 Conclusions

The availability of large volume cosmological hydrodynamic simulations such as MassiveBlack-II, Illustris, EAGLE, and Horizon-AGN has made it possible to directly explore the intrinsic alignments of the shape of stellar component of a large statistical sample of galaxies. In this thesis, we study the intrinsic alignments of galaxies in the MBII hydrodynamic simulation and explore their scaling with mass, luminosity, redshift and morphology. First, we found that the measured ellipticities of the shapes of stellar component of galaxies in the simulation compare well with observations than the shapes of the dark matter component. We found a significant mass dependent trend in the shapes and alignments of the galaxies. The stellar component of the galaxies of low mass are found to be more misaligned with the shape of their host dark matter subhalo and rounder when compared to massive galaxies. This translates to a mass dependence in the correlation of galaxy shapes with the large scale density field quantified by the ED and $w_{\delta+}$ two-point statistics which tend to increase with mass. The amplitude of alignments increases with luminosity which is similar to that of mass. This is qualitatively similar to the scaling of intrinsic alignments with luminosity based on LRG observations. Further, the mass dependent trend of intrinsic alignments is also consistent with results from other hydrodynamic simulations including Illustris, Horizon-AGN and EAGLE. We also find a morphology dependent trend for the intrinsic alignments in MBII and Illustris. Here, the disk galaxies are found to be more oblate and misaligned when compared with elliptical galaxies. The two-point statistics of disk galaxies on scales above $0.1h^{-1}Mpc$ are consistent with null detection which is in agreement with current observational measurements.

While some of the trends of the predictions of intrinsic alignments in MBII are consistent with the predictions of other simulations, there are notable differences in the properties of galaxies in between these simulations. In particular, we found that the amplitude of alignments in MBII are larger when compared with Illustris, a simulation based on moving mesh hydrodynamics and in which, the implementations of baryonic feedback models are also different from MBII models. We also found that the galaxy shapes are rounder in Illustris with a greater fraction of disk galaxies. Additionally, in MBII, we do not find a dependence of the $w_{\delta+}$ signal with redshift which is not consistent with the predictions of the linear alignment model. This is different when compared with that of Horizon-AGN simulation, where they find an increase in the amplitude of $w_{\delta+}$ as we go to lower redshifts. Further, the disk galaxies in MBII and Illustris are found to be radially aligned with the location of ellipticals, while in the Horizon-AGN simulation, the disks are found to be tangentially aligned. A detailed study comparing intrinsic alignments with varying baryonic feedback models in the simulations is needed to understand these differences. As a first step, we did an initial study using small volume simulations, where we vary the free parameters in the feedback models of MBII. This study indicates that the wind feedback has a significant effect on the galaxy alignments when compared with the star formation efficiency or AGN feedback.

We also compared the intrinsic alignments of the stellar component of galaxies in the MBII simulation with an identical dark matter-only (DMO) simulation. By matching subhalos in the two simulations, we tested if the inner shape of the subhalo in the DMO simulation can be used to trace the shape of stellar component in MBII. While this approach is not encouraging, we find that the distribution of misalignment angles is not identical to a random distribution and hence, the distributions are still useful to map alignments from the hydrodynamic to dark matter-only simulations.

7.2 Future Work

This thesis presents a detailed study of intrinsic alignments of the stellar component of galaxies using large volume hydrodynamic simulations, MassiveBlack-II and Illustris. Based on our findings, we can identify directions for future work in this area. From [155], we observe differences in the amplitude of galaxy misalignments and correlation functions when comparing MassiveBlack-II and Illustris simulations. Further, there are differences in the morphological properties such as the fraction of disk galaxies in between various hydrodynamic simulations. So, a detailed study of the impact of variations in the baryonic feedback models on the intrinsic alignments is needed along with an exploration of the effects of different numerical implementations of hydrodynamics, such as the differences between SPH and AMR codes. However, these studies require high resolution simulations of large volume to accurately estimate the effects of changes in feedback models and numerical implementations.

In our comparison of the ellipticities of the simulations with observational measurements, we have used the data in which the noise from systematics have been removed. Alternatively, we can also mimic observational systematics on the simulated data to create synthetic galaxy images which can be directly compared with the properties of the observed galaxy population and test the correctness of the feedback model in reproducing the observed population. While comparing two-point statistics, we verified that the radial scaling of intrinsic alignment signals in hydrodynamic simulations matches with the comparisons of observational measurements, where the samples in both have been selected to match in luminosities. However, these galaxy samples correspond to bright luminous galaxies and if the feedback model adopted in the simulation is to be trusted such that predictions of intrinsic alignment signals from the simulation are to be directly used for intrinsic alignment mitigation in weak lensing analysis, we need further comparisons of these predictions with observational measurements. In particular, it is necessary to test the predictions of the intrinsic alignment signal at low luminosities and compare the scaling in amplitude as we go from higher to lower luminosities. Due to the lack of spectroscopic redshift information on the galaxies at lower luminosities, it is not currently feasible to observationally measure IA of galaxies at low luminosities and has to be explored with future data sets. Given that there is a sign difference in the prediction of disk galaxy alignment with respect to the location of ellipticals in MBII and Illustris simulations when compared with Horizon-AGN, a statistically significant measurement of this signal in observations with data from future surveys can rule out the incorrect model and give more confidence in which feedback model and numerical implementation of hydrodynamics has to be adopted.

In order to test the intrinsic alignment mitigation techniques for weak lensing measurements in upcoming surveys, we need mock catalogs of N-body simulations with realistic models of the intrinsic galaxy shapes and alignments incorporated. The predictions of the orientation of the stellar component and their ellipticities from the hydrodynamic simulations can be used to populate these N-body simulations based on their halo properties and also assign galaxy luminosities and morphological type. From these mock catalogs, the intrinsic alignment signals matching the results in hydrodynamic simulation can be predicted for a galaxy sample defined by certain selection criteria such as threshold in luminosity. The study presented in [157] is relevant to make galaxy mocks and suitable mapping techniques have to be developed. If the feedback model is known to be correct such that it accurately reproduces the scale dependence of the intrinsic alignments, then the intrinsic alignment signal from these mocks can be directly used in weak lensing likelihood analysis with an amplitude scaling parameter which is marginalized over. We can also use these mock catalogs in testing IA mitigation techniques where the signal from the hydrodynamic simulations can be incorporated so as to mimic the intrinsic alignment signal seen in real data. To assess the impact of scale dependent differences in the predicted intrinsic alignments in different hydrodynamic simulations with variations in galaxy formation model (including different feedback models, numerical implementations and parameter space exploration of the free parameters in a given feedback models), we can create mocks from all these simulations, which can be applied in constraining cosmological parameters to quantify the level of degradation in the parameter constraints.

Appendix A

A.1 Functional forms for dark matter and stellar matter shapes

Here, we give the functional forms for the average axis ratios (q, s) of shapes defined by dark matter and stellar matter in subhalos as a function of mass and redshift. The parameters are given in Table A.1. The plots showing fits for mean axis ratios of the shapes of dark matter and stellar matter are given in Figs. A.1 and A.2 respectively.

The fitting functions for average axis ratios are given by,

$$\langle q, s \rangle = (1+z)^{\gamma} \sum_i a_i \left[\log(\frac{M}{M_{piv}}) \right]^i \tag{A.1}$$

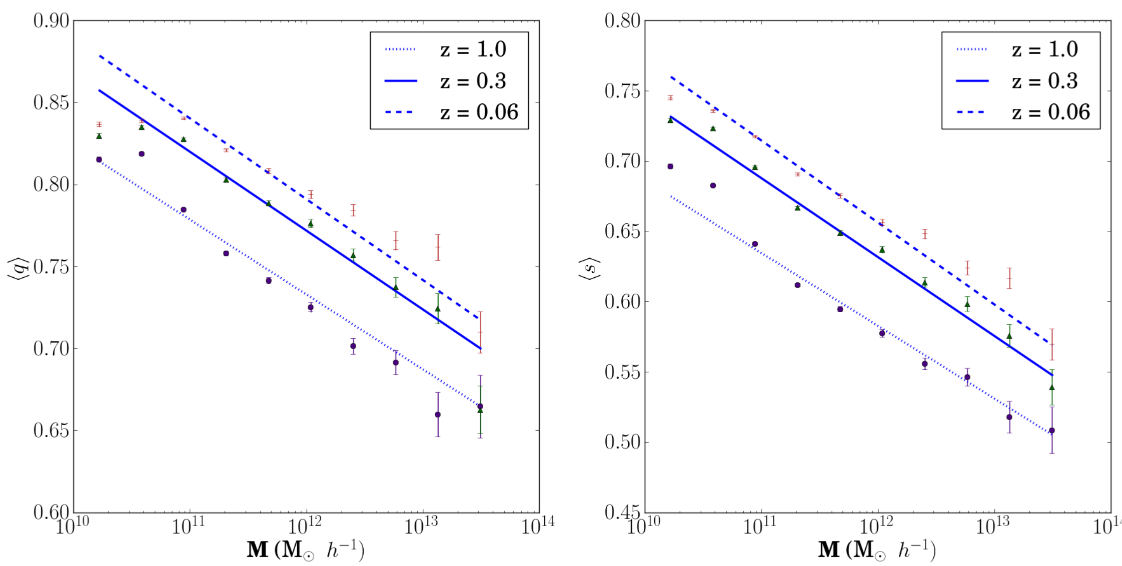

Figure A.1: Fits for the axis ratios of shape defined by dark matter in subhalos as a function of mass and redshift

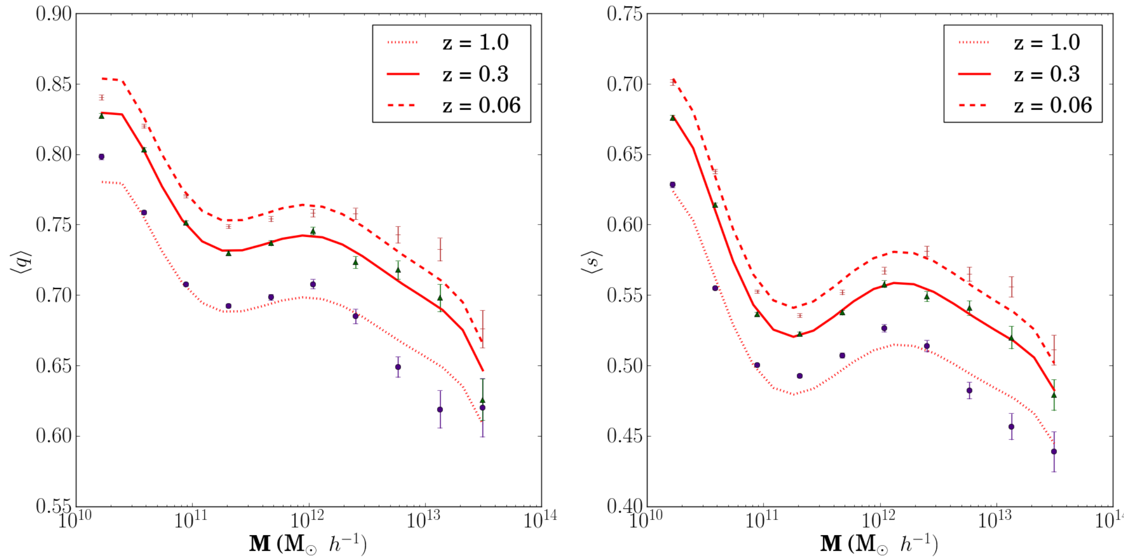

Figure A.2: Fits for the axis ratios of shape defined by stellar matter in subhalos as a function of mass and redshift

Table A.1: Parameters, γ and a_i for mean axis ratios, $\langle q\rangle$ and $\langle s\rangle$ in mass range, $10^{10.0} - 10^{14.0}h^{-1}M_{\odot}$

Axis ratio	γ	a_0	a_1	a_2	a_3	a_4	a_5	a_6
q (Dark Matter)	-0.12	0.797	-0.049	-	-	-	-	-
s (Dark Matter)	-0.19	0.663	-0.059	-	-	-	-	-
q (Stellar Matter)	-0.14	0.771	-0.004	-0.068	-0.017	-0.061	-0.003	-0.015
s (Stellar Matter)	-0.19	-0.585	0.031	-0.089	-0.034	0.075	-0.001	-0.016

where, M_{piv} is $10^{12}h^{-1}M_{\odot}$.

The fitting functions are linear in $\log(\frac{M}{M_{piv}})$ for shapes of dark matter with $i = 0, 1$ and polynomial to 6^{th} degree in $\log(\frac{M}{M_{piv}})$ with $i = 0, 1, 2, 3, 4, 5, 6$ for shapes defined by stellar component in subhalos.

A.2 Functional forms for probability distributions of 3D and 2D misalignment angles

The probability distributions for 3D misalignment angles in the two lower mass bins $10^{10.0} - 10^{11.5}h^{-1}M_{\odot}$ and $10^{11.5} - 10^{13.0}h^{-1}M_{\odot}$ are given by

$$\frac{dp}{d\theta} = A_z(1 - e^{-\gamma_z\theta})e^{-B_z\theta} + (1 - e^{-\alpha_z\theta})C_z \tag{A.2}$$

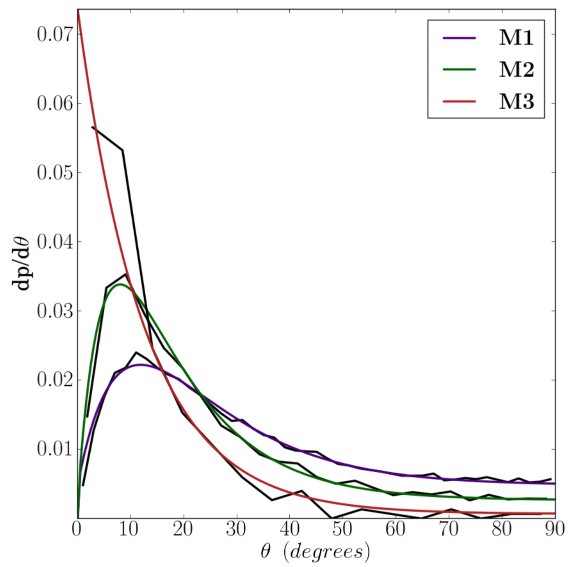

Figure A.3: Fits for probability distributions of 3D misalignment angles at $z = 0.3$

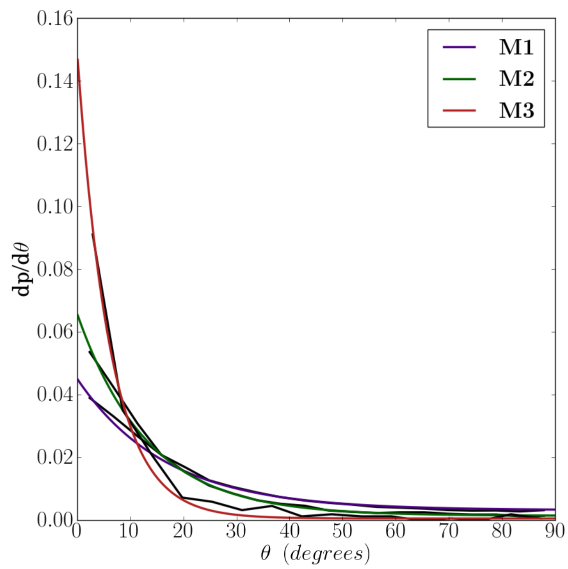

Figure A.4: Fits for probability distributions of 2D misalignment angles at $z = 0.3$

In the highest mass bin, $10^{13.0} - 10^{15.0} h^{-1} M_{\odot}$ the fitting function is,

$$\frac{dp}{d\theta} = A_z e^{-B_z \theta} \tag{A.3}$$

The probability distributions for 2D misalignment angles in different mass bins

Table A.2: Parameters for probability distributions of 3D misalignment angles at redshifts $z = 1.0, 0.3,$ and 0.06 for subhalos in the mass bins $M1 : 10^{10.0} - 10^{11.5}h^{-1}M_\odot$, $M2 : 10^{11.5} - 10^{13.0}h^{-1}M_\odot$ and $M3 : > 10^{13.0}h^{-1}M_\odot$.

	$z = 1.0$					$z = 0.3$				
Mass bin	A_z	B_z	C_z	γ_z	α_z	A_z	B_z	C_z	γ_z	α_z
$M1$	0.211	0.079	0.004	0.023	100	0.146	0.071	0.005	0.028	100
$M2$	0.122	0.088	0.002	0.134	100	0.091	0.074	0.003	0.121	100
$M3$	0.115	0.119	0.004	–	–	0.073	0.079	–	–	–

	$z = 0.06$				
Mass bin	A_z	B_z	C_z	γ_z	α_z
$M1$	0.055	0.052	0.004	0.071	100
$M2$	0.058	0.057	0.003	0.166	100
$M3$	0.064	0.070	–	–	–

Table A.3: Parameters for probability distributions of 2D misalignment angles at redshifts $z = 1.0, 0.3,$ and 0.06 for subhalos in the mass bins $M1 : 10^{10.0} - 10^{11.5}h^{-1}M_\odot$, $M2 : 10^{11.5} - 10^{13.0}h^{-1}M_\odot$ and $M3 : > 10^{13.0}h^{-1}M_\odot$.

	$z = 1.0$			$z = 0.3$			$z = 0.06$		
Mass bin	A_z	B_z	C_z	A_z	B_z	C_z	A_z	B_z	C_z
$M1$	0.044	0.060	0.003	0.042	0.060	0.003	0.041	0.056	0.003
$M2$	0.077	0.089	0.001	0.064	0.075	0.002	0.056	0.069	0.002
$M3$	0.2	0.211	0.0	0.146	0.162	0.0	0.133	0.137	0.0

are given by

$$\frac{dp}{d\theta} = A_z e^{-B_z\theta} + C_z \tag{A.4}$$

The fits for the probability distributions in 3D and 2D are shown in Fig. A.3 and Fig. A.4 respectively and the parameters are given in Tables A.2 and A.3.

A.3 Functional forms for mean misalignment angles in 3D and 2D

The mean misalignment angle in 3D and 2D are given by,

$$\theta(M) = (a_{0z} - a_{1z}e^{-(\frac{\log(M)-d_{0z}}{b_{0z}})})(c_{0z}\log(M) + c_{1z}) \tag{A.5}$$

The plots showing fits for mean misalignments in 3D and 2D are shown in Fig. A.5 and Fig. A.6 respectively. The corresponding parameters are given in Tables A.4 and A.5.

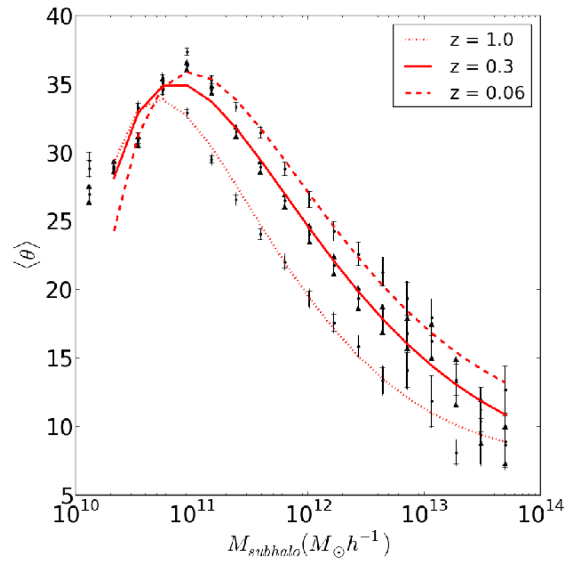

Figure A.5: Fits for mean misalignment angles in 3D as a function of mass

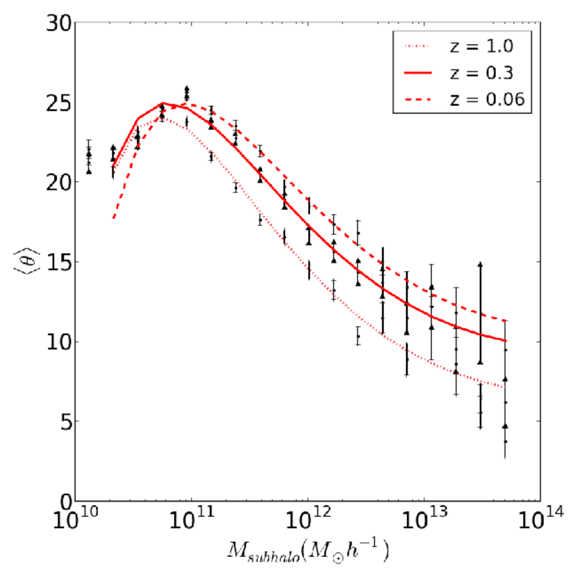

Figure A.6: Fits for mean misalignment angles in 2D as a function of mass

Table A.4: Parameters for mean misalignment angles in 3D at redshifts $z = 1.0, 0.3$ and 0.06 for subhalos in the mass range, $10^{10.0} - 10^{14.0}\ h^{-1}M_{\odot}$.

z	a_{0z}	a_{1z}	b_{0z}	c_{0z}	c_{1z}	d_{0z}
1.0	1.19	-64.35	0.79	1.18	-11.70	10.19
0.3	0.88	-53.72	0.97	1.16	-11.46	10.27
0.06	1.09	-28.58	0.96	1.38	-13.74	10.84

Table A.5: Parameters for mean misalignment angles in 2D at redshifts $z = 1.0, 0.3$ and 0.06 for subhalos in the mass range, $10^{10.0} - 10^{14.0}\ h^{-1}M_{\odot}$.

z	a_{0z}	a_{1z}	b_{0z}	c_{0z}	c_{1z}	d_{0z}
1.0	1.44	-89.84	0.82	0.79	-7.77	9.92
0.3	1.86	-79.50	0.89	0.89	-8.75	9.84
0.06	2.07	-43.40	0.91	0.90	-8.99	10.47

Appendix B

B.1 Fitting Results

Here we present results of fitting the NLA and power law models to different samples for which w_{g+} and $w_{\delta+}$ were measured. These are helpful to produce IA signals that scale with mass, luminosity and transverse signals according to predictions from the MBII simulation. At linear and quasi-linear scales ($6h^{-1}$Mpc $< r_p < 25h^{-1}$Mpc) we fit $w_{\delta+}$ and w_{g+} simultaneously for amplitude A_I and subhalo linear bias b_D in w_{g+}. b_D values are not shown in tables but we get b_D consistent with values expected for ξ_{gg} and ξ_{mm} measurements. The power-law was fitted separately to w_{g+} and $w_{\delta+}$ for $r_p < 1h^{-1}$Mpc, with two free parameters, amplitude P_A and index P_I. A subscript δ on power-law parameters denotes a fit to $w_{\delta+}$. Power-law parameters evolve with mass and luminosity, with the function becoming more shallow for lower mass and luminosity. As discussed in Sec. 3.7.1, there are also differences in power law fits to $w_{\delta+}$ and w_{g+}, with the function being more shallow for w_{g+}. See Sec. 3.7.1 for more a detailed discussion.

Table B.1 presents results for different samples defined by their comoving abundance. Fig. B.1 shows the intrinsic alignments signal for some of the samples at $z = 0.6$. The intrinsic alignments amplitude generally increases with decreasing comoving abundance, consistent with the fact that more massive and brighter objects have stronger intrinsic alignments.

Table B.2 presents results for different samples defined by subhalo mass threshold. Average subhalo mass are given for each sample. Fig. B.2 shows the signal for $M > 10^{13}h^{-1}M_\odot$ sample at different redshift. Samples with more massive subhalos show stronger intrinsic alignments, along with some redshift evolution as discussed in the main text.

Table B.3 and Table B.4 present results for satellite and central subhalos, with sample selection using different mass thresholds. Fig. B.3 and Fig. B.4 also show signal for some of the samples. We observe clear large scale alignments for central subhalos, also with clear mass evolution. Satellite subhalos on the other hand show very little or no alignments at large scales with A_I consistent with zero or at least much smaller than that for central subhalos at the same redshift and in the same

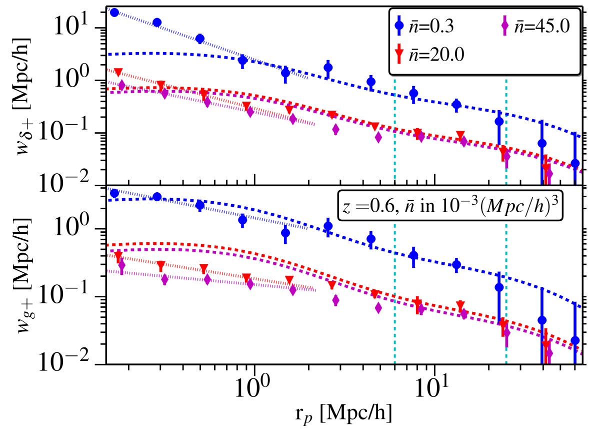

Figure B.1: Intrinsic alignment correlation functions, $w_{\delta+}$ and w_{g+}, for different samples defined on the basis of comoving number density threshold, at redshift $z = 0.6$. There is clear evolution with number density, where samples with lower number density and hence more luminous galaxies have higher intrinsic alignments. As discussed in main text, this has important implications for future weak lensing surveys such as Euclid and LSST.

mass range. These results are consistent with the halo model, as satellites show radial alignments within the halo and hence their large scale signal is much weaker.

Table B.5 presents results for samples defined by luminosity bins. We observe evolution of intrinsic alignments with luminosity, with more luminous objects having stronger alignments and there is also some redshift evolution observed in two of the three luminosity bins. See section 3.7.1 for more detailed discussion.

Table B.1: Model fits to samples defined by a luminosity threshold, including all galaxies above some lower luminosity limit such that a given comoving abundance is achieved. A_I is the NLA model amplitude, P_A and P_I are the power law parameters. The power-law is fit separately to w_{g+} and $w_{\delta+}$, with superscript δ indicating the fits to $w_{\delta+}$. $\langle L/L_0 \rangle$ gives average luminosity for the sample, normalized by pivot luminosity L_0, corresponding to r-band magnitude $M_{r,0} = -22$.

$\bar{n}$	z	A_I	P_A	P_I	P_A^δ	P_I^δ	$\langle L/L_0 \rangle$
1.0×10^{-4}	0.06	18±2	2.8±0.2	-0.22±0.07	4.6±0.5	-1.29±0.08	7.8
1.0×10^{-4}	0.3	36±4	3±1	-0.2±0.2	5±1	-1.2±0.1	7.5
1.0×10^{-4}	0.6	30±10	2.8±0.2	-0.31±0.07	4.9±0.6	-1.11±0.08	7.0
1.0×10^{-4}	1.0	50±10	3.2±0.3	-0.12±0.08	3.6±0.3	-1.03±0.07	6.7
3.0×10^{-4}	0.06	9±2	1.9±0.2	-0.35±0.09	2.8±0.2	-1.25±0.05	4.1
3.0×10^{-4}	0.3	17±2	1.6±0.4	-0.4±0.1	2.5±0.3	-1.24±0.08	3.9
3.0×10^{-4}	0.6	21±3	1.4±0.2	-0.5±0.1	2.5±0.5	-1.2±0.1	3.8
3.0×10^{-4}	1.0	28±2	1.7±0.4	-0.3±0.2	1.8±0.3	-1.1±0.1	3.8
1.0×10^{-3}	0.06	8±2	0.89±0.03	-0.48±0.03	1.4±0.2	-1.18±0.07	1.8
1.0×10^{-3}	0.3	10±1	0.8±0.2	-0.6±0.2	1.3±0.4	-1.3±0.2	1.7
1.0×10^{-3}	0.6	13.9±0.3	0.8±0.1	-0.6±0.1	1.4±0.2	-1.09±0.07	1.8
1.0×10^{-3}	1.0	12±2	0.8±0.1	-0.5±0.1	0.8±0.1	-1.2±0.1	1.9
2.0×10^{-2}	0.06	2.6±0.3	0.21±0.01	-0.23±0.05	$(37.0\pm0.9)\times10^{-2}$	-0.92±0.02	1.5×10^{-1}
2.0×10^{-2}	0.3	3.3±0.4	0.14±0.01	0.43±0.08	0.36±0.08	-0.8±0.2	1.6×10^{-1}
2.0×10^{-2}	0.6	4.7±0.5	0.18±0.01	-0.42±0.06	$(28.0\pm0.9)\times10^{-2}$	-0.9±0.02	1.8×10^{-1}
2.0×10^{-2}	1.0	5.0±0.5	$(14.9\pm0.8)\times10^{-2}$	-0.5±0.08	0.18±0.01	-0.98±0.04	2.2×10^{-1}
4.5×10^{-2}	0.06	2.7±0.2	0.19±0.01	-0.04±0.05	0.36±0.02	-0.66±0.04	7.1×10^{-2}
4.5×10^{-2}	0.3	3.4±0.4	0.1±0.01	0.5±0.2	0.31±0.05	-0.7±0.1	7.8×10^{-2}
4.5×10^{-2}	0.6	4.0±0.3	0.15±0.01	-0.2±0.1	$(23.2\pm0.6)\times10^{-2}$	-0.7±0.02	8.8×10^{-2}
4.5×10^{-2}	1.0	3.6±0.3	0.11±0.01	-0.5±0.1	0.16±0.01	-0.73±0.06	1.1×10^{-1}

Table B.2: Model fits to samples defined by mass threshold subhalo mass. $\langle M/h^{-1}M_{\odot}\rangle$ is the average subhalo mass with in the sample. See Table B.1 for description of different parameters.

$\log(M/h^{-1}M_{\odot})$	z	A_I	P_A	P_I	P_A^{δ}	P_I^{δ}	$\langle M/h^{-1}M_{\odot}\rangle$
>11	0.06	3.4±0.4	0.15±0.02	-0.36±0.08	0.2±0.04	-0.9±0.1	9.6×10^{11}
>11	0.3	4.0±0.3	$(14.8\pm0.4)\times10^{-2}$	-0.49±0.02	$(26.0\pm0.3)\times10^{-2}$	$(-74.0\pm0.7)\times10^{-2}$	8.5×10^{11}
>11	0.6	4.9±0.3	0.14±0.02	-0.5±0.1	0.16±0.02	-0.98±0.08	7.2×10^{11}
>11	1.0	4.9±0.5	$(12.5\pm0.3)\times10^{-2}$	-0.6±0.03	$(11.6\pm0.9)\times10^{-2}$	-1.1±0.05	5.9×10^{11}
>12	0.06	6.7±0.8	0.36±0.02	-0.68±0.03	0.4±0.05	-1.4±0.08	5.7×10^{12}
>12	0.3	6.3±0.8	0.39±0.04	-0.7±0.08	0.6±0.2	-1.2±0.2	5.1×10^{12}
>12	0.6	7.7±0.7	0.41±0.02	-0.64±0.03	0.53±0.04	-1.22±0.05	4.3×10^{12}
>12	1.0	8±1	0.41±0.04	-0.69±0.07	0.39±0.04	-1.35±0.07	3.7×10^{12}
>13	0.06	12±2	1.68±0.08	-0.47±0.04	2.3±0.3	-1.4±0.1	3.3×10^{13}
>13	0.3	17.9±0.9	1.8±0.4	-0.5±0.2	2.5±0.5	-1.3±0.1	3.0×10^{13}
>13	0.6	24±7	1.9±0.2	-0.42±0.09	3.3±0.4	-1.13±0.09	2.6×10^{13}
>13	1.0	45±9	2.7±0.5	-0.1±0.1	2.9±0.4	-1.1±0.1	2.2×10^{13}

Table B.3: Model fits to central galaxy intrinsic alignment correlation functions. $\langle M/h^{-1}M_{\odot}\rangle$ is the average subhalo mass with in the sample. See Table B.1 for description of different parameters.

$\log(M/h^{-1}M_{\odot})$	z	A_I	P_A	P_I	P_A^{δ}	P_I^{δ}	$\langle M/h^{-1}M_{\odot}\rangle$
$\in [10.0, 11.5]$	0.06	3.7±0.4	0.09±0.02	0.1±0.2	0.17±0.04	1.9±0.9	1.3×10^{11}
$\in [10.0, 11.5]$	0.3	4.2±0.5	0.1±0.01	0.2±0.1	0.19±0.02	0.6±0.2	1.3×10^{11}
$\in [10.0, 11.5]$	0.6	4.7±0.3	$(10.6\pm0.6)\times10^{-2}$	-0.1±0.06	0.14±0.03	$(-0.0\pm0.1)\times10^{0}$	1.2×10^{11}
$\in [10.0, 11.5]$	1.0	4.1±0.4	$(8.3\pm0.7)\times10^{-2}$	-0.2±0.1	0.07±0.01	-0.4±0.1	1.1×10^{11}
$\in [11.5, 13.0]$	0.06	3.1±0.8	0.14±0.02	-0.7±0.1	0.03±0.03	-2.1±0.6	1.3×10^{12}
$\in [11.5, 13.0]$	0.3	4.0±0.6	$(12.7\pm0.3)\times10^{-2}$	-0.84±0.01	$(7.5\pm0.9)\times10^{-2}$	-1.59±0.07	1.2×10^{12}
$\in [11.5, 13.0]$	0.6	5.8±0.5	0.13±0.03	-0.7±0.2	0.03±0.02	-2.1±0.3	1.2×10^{12}
$\in [11.5, 13.0]$	1.0	5.5±0.8	0.15±0.02	-0.82±0.08	0.1±0.01	-1.48±0.07	1.1×10^{12}
$\in [13.0, 15.0]$	0.06	11±2	1.6±0.1	-0.48±0.07	2.1±0.4	-1.5±0.1	3.4×10^{13}
$\in [13.0, 15.0]$	0.3	18±1	1.8±0.4	-0.5±0.2	2.8±0.5	-1.3±0.1	3.1×10^{13}
$\in [13.0, 15.0]$	0.6	24±5	1.7±0.3	-0.5±0.1	2.7±0.4	-1.2±0.1	2.6×10^{13}
$\in [13.0, 15.0]$	1.0	49±9	2.6±0.4	-0.2±0.2	2.8±0.4	-1.1±0.1	2.2×10^{13}

Table B.4: Model fits to satellite galaxy intrinsic alignment correlation functions. $\langle M/h^{-1}M_\odot\rangle$ is the average subhalo mass with in the sample. See Table B.1 for description of different parameters.

$\log(M/h^{-1}M_\odot)$	z	A_I	P_A	P_I	P_A^δ	P_I^δ	$\langle M/h^{-1}M_\odot\rangle$
$\in [10.0, 11.5]$	0.06	0.9±0.3	0.26±0.03	0.1±0.1	0.8±0.2	-0.6±0.2	6.5×10^{10}
$\in [10.0, 11.5]$	0.3	1.7±0.1	0.21±0.03	-0.25±0.09	0.6±0.1	-0.6±0.1	6.2×10^{10}
$\in [10.0, 11.5]$	0.6	1.6±0.2	0.18±0.03	-0.1±0.1	0.34±0.07	-0.6±0.1	6.1×10^{10}
$\in [10.0, 11.5]$	1.0	2.0±0.4	0.14±0.01	-0.3±0.1	0.3±0.07	-0.6±0.1	5.7×10^{10}
$\in [11.5, 13.0]$	0.06	-1±1	0.42±0.03	-0.23±0.05	0.8±0.1	-0.8±0.1	1.0×10^{12}
$\in [11.5, 13.0]$	0.3	4.1±0.7	$(32.1\pm0.8)\times10^{-2}$	-0.57±0.02	0.9±0.2	-0.8±0.1	1.0×10^{12}
$\in [11.5, 13.0]$	0.6	3±1	0.66±0.06	-0.14±0.07	1.5±0.2	-0.4±0.1	9.9×10^{11}
$\in [11.5, 13.0]$	1.0	$(0.0\pm0.3)\times10^{1}$	0.37±0.05	-0.2±0.1	0.7±0.2	-0.7±0.2	9.0×10^{11}
$\in [13.0, 15.0]$	0.06	10±10	2.9±0.6	-0.1±0.1	5±2	-0.9±0.3	2.2×10^{13}
$\in [13.0, 15.0]$	0.3	20±20	$(0.0\pm0.2)\times10^{0}$	-3±2	$(0.0\pm0.3)\times10^{7}$	$(0.0\pm0.2)\times10^{6}$	1.7×10^{13}
$\in [13.0, 15.0]$	0.6	40±30	5±1	0.8±0.5	11±2	-0.3±0.1	2.3×10^{13}
$\in [13.0, 15.0]$	1.0	-40±20	3±1	0.2±0.6	6.3±0.3	-0.71±0.05	2.1×10^{13}

Table B.5: Model fits to intrinsic alignments measurements for samples defined in luminosity bins. See Table B.1 for description of different parameters.

M_r	z	A_I	P_A	P_I	P_A^δ	P_I^δ	$\langle L/L_0\rangle$
≤ -22.6	0.06	12±2	2.0±0.2	-0.36±0.09	3.1±0.3	-1.29±0.07	4.5
≤ -22.6	0.3	20±2	1.9±0.4	-0.3±0.1	3.0±0.3	-1.17±0.07	4.4
≤ -22.6	0.6	24±4	1.6±0.2	-0.5±0.1	2.7±0.5	-1.2±0.1	4.1
≤ -22.6	1.0	27±2	1.7±0.4	-0.3±0.2	1.9±0.3	-1.1±0.1	3.8
$\in [-22.6, -20.3]$	0.06	6±1	0.37±0.02	-0.66±0.04	0.4±0.1	-1.5±0.2	5.2×10^{-1}
$\in [-22.6, -20.3]$	0.3	6±1	0.32±0.04	-0.7±0.1	0.5±0.1	-1.2±0.2	4.9×10^{-1}
$\in [-22.6, -20.3]$	0.6	5.6±0.2	0.31±0.01	-0.62±0.02	0.49±0.02	-1.08±0.03	4.9×10^{-1}
$\in [-22.6, -20.3]$	1.0	4.6±0.5	0.21±0.01	-0.73±0.04	0.2±0.02	-1.32±0.06	5.0×10^{-1}
$\in [-20.3, -18.0]$	0.06	1.5±0.3	$(14.6\pm0.5)\times10^{-2}$	-0.32±0.03	0.34±0.05	-0.72±0.09	6.6×10^{-2}
$\in [-20.3, -18.0]$	0.3	2.9±0.3	0.16±0.01	-0.42±0.07	0.29±0.05	-0.8±0.1	6.6×10^{-2}
$\in [-20.3, -18.0]$	0.6	4.2±0.5	0.13±0.02	-0.3±0.1	0.18±0.03	-0.7±0.1	6.5×10^{-2}
$\in [-20.3, -18.0]$	1.0	3.8±0.3	$(11.0\pm0.6)\times10^{-2}$	-0.46±0.05	0.15±0.02	-0.71±0.07	6.3×10^{-2}

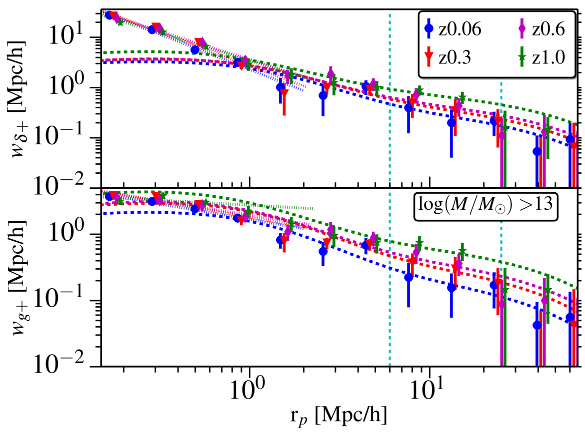

Figure B.2: Intrinsic alignment correlation functions, $w_{\delta+}$ and w_{g+}, for the mass threshold sample, $M > 10^{13}h^{-1}1M_{\odot}$, at redshifts, $z = 1.0$, 0.6, 0.3, and 0.06. We see some redshift evolution as $w_{\delta+}$ and w_{g+} magnitude increases at higher redshift.

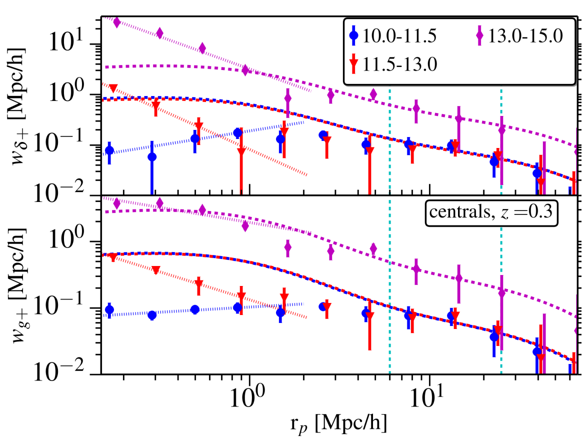

Figure B.3: Intrinsic alignment correlation functions, $w_{\delta+}$ and w_{g+}, for central sub-halos in different mass bins, at redshift $z = 0.3$. We detect both large scale and small scale intrinsic alignments for central sub halos, with more massive sub halos also showing stronger alignments. The downturn in the lowest mass bin at small scales indicates a transition to the 1-halo term.

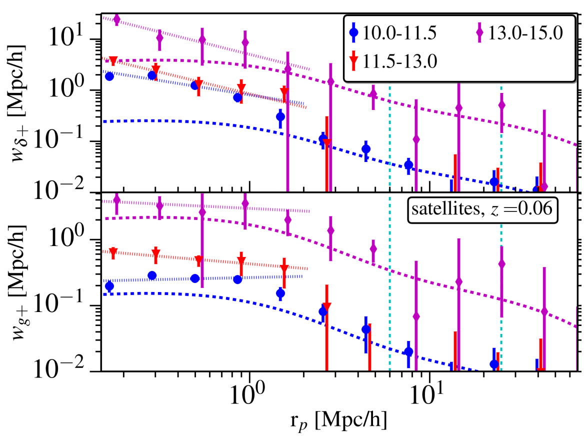

Figure B.4: Intrinsic alignment correlation functions, $w_{\delta+}$ and w_{g+}, for satellite subhalos in different mass bins,, $M1$, $M2$ and $M3$, at redshift $z = 0.3$. Satellites show no significant alignments at large scales, though small scale alignment is very strong, consistent with the radial alignment of satellites.

Bibliography

[1] M. G. Abadi, J. F. Navarro, M. Fardal, A. Babul, and M. Steinmetz. Galaxy-induced transformation of dark matter haloes. MNRAS, 407:435–446, September 2010.

[2] M. G. Abadi, J. F. Navarro, M. Steinmetz, and V. R. Eke. Simulations of Galaxy Formation in a Λ Cold Dark Matter Universe. II. The Fine Structure of Simulated Galactic Disks. ApJ, 597:21–34, November 2003.

[3] I. Agustsson and T. G. Brainerd. Anisotropic Locations of Satellite Galaxies: Clues to the Orientations of Galaxies within their Dark Matter Halos. ApJ, 709:1321–1336, February 2010.

[4] A. Albrecht, G. Bernstein, R. Cahn, W. L. Freedman, J. Hewitt, W. Hu, J. Huth, M. Kamionkowski, E. W. Kolb, L. Knox, J. C. Mather, S. Staggs, and N. B. Suntzeff. Report of the Dark Energy Task Force. *ArXiv Astrophysics e-prints*, September 2006.

[5] B. Allgood, R. A. Flores, J. R. Primack, A. V. Kravtsov, R. H. Wechsler, A. Faltenbacher, and J. S. Bullock. The shape of dark matter haloes: dependence on mass, redshift, radius and formation. MNRAS, 367:1781–1796, April 2006.

[6] G. Altay, J. M. Colberg, and R. A. C. Croft. The influence of large-scale structures on halo shapes and alignments. MNRAS, 370:1422–1428, August 2006.

[7] J. S. Bagla and S. Ray. Comments on the size of the simulation box in cosmological N-body simulations. MNRAS, 358:1076–1082, April 2005.

[8] J. Bailin, D. Kawata, B. K. Gibson, M. Steinmetz, J. F. Navarro, C. B. Brook, S. P. D. Gill, R. A. Ibata, A. Knebe, G. F. Lewis, and T. Okamoto. Internal Alignment of the Halos of Disk Galaxies in Cosmological Hydrodynamic Simulations. ApJ, 627:L17–L20, July 2005.

[9] J. Bailin and M. Steinmetz. Internal and External Alignment of the Shapes and Angular Momenta of ΛCDM Halos. ApJ, 627:647–665, July 2005.

[10] M. Bartelmann and P. Schneider. Weak gravitational lensing. Phys.Rep., 340:291–472, January 2001.

[11] K. Benabed and L. van Waerbeke. Constraining dark energy evolution with gravitational lensing by large scale structures. Phys.Rev.D, 70(12):123515, December 2004.

[12] I. Berentzen and I. Shlosman. Growing Live Disks within Cosmologically Assembling Asymmetric Halos: Washing Out the Halo Prolateness. ApJ, 648:807–819, September 2006.

[13] G. Bernstein and B. Jain. Dark Energy Constraints from Weak-Lensing Cross-Correlation Cosmography. ApJ, 600:17–25, January 2004.

[14] G. M. Bernstein and M. Jarvis. Shapes and Shears, Stars and Smears: Optimal Measurements for Weak Lensing. AJ, 123:583–618, February 2002.

[15] G. M. Bernstein and M. Jarvis. Shapes and Shears, Stars and Smears: Optimal Measurements for Weak Lensing. AJ, 123:583–618, February 2002.

[16] P. Bett. Halo shapes from weak lensing: the impact of galaxy-halo misalignment. MNRAS, 420:3303–3323, March 2012.

[17] P. Bett, V. Eke, C. S. Frenk, A. Jenkins, and T. Okamoto. The angular momentum of cold dark matter haloes with and without baryons. MNRAS, 404:1137–1156, May 2010.

[18] J. Blazek, R. Mandelbaum, U. Seljak, and R. Nakajima. Separating intrinsic alignment and galaxy-galaxy lensing. JCAP, 5:41, May 2012.

[19] J. Blazek, M. McQuinn, and U. Seljak. Testing the tidal alignment model of galaxy intrinsic alignment. JCAP, 5:10, May 2011.

[20] J. Blazek, Z. Vlah, and U. Seljak. Tidal alignment of galaxies. JCAP, 8:15, August 2015.

[21] J. Blazek, Z. Vlah, and U. Seljak. Tidal alignment of galaxies. JCAP, 8:015, August 2015.

[22] S. Bocquet, A. Saro, K. Dolag, and J. J. Mohr. Baryon impact on the halo mass function: Fitting formulae and implications for cluster cosmology. *ArXiv e-prints*, February 2015.

[23] T. G. Brainerd. Anisotropic Distribution of SDSS Satellite Galaxies: Planar (Not Polar) Alignment. ApJ, 628:L101–L104, August 2005.

[24] S. Bridle and L. King. Dark energy constraints from cosmic shear power spectra: impact of intrinsic alignments on photometric redshift requirements. *New Journal of Physics*, 9:444, December 2007.

[25] S. Bridle and L. King. Dark energy constraints from cosmic shear power spectra: impact of intrinsic alignments on photometric redshift requirements. *New Journal of Physics*, 9:444, December 2007.

[26] S. E. Bryan, S. T. Kay, A. R. Duffy, J. Schaye, C. Dalla Vecchia, and C. M. Booth. The impact of baryons on the spins and shapes of dark matter haloes. MNRAS, 429:3316–3329, March 2013.

[27] S. Capozziello and L. Z. Fang. Curvature Quintessence. *International Journal of Modern Physics D*, 11:483–491, 2002.

[28] S. M. Carroll, V. Duvvuri, M. Trodden, and M. S. Turner. Is cosmic speed-up due to new gravitational physics? Phys.Rev.D, 70(4):043528, August 2004.

[29] P. Catelan, M. Kamionkowski, and R. D. Blandford. Intrinsic and extrinsic galaxy alignment. MNRAS, 320:L7–L13, January 2001.

[30] P. Catelan, M. Kamionkowski, and R. D. Blandford. Intrinsic and extrinsic galaxy alignment. MNRAS, 320:L7–L13, January 2001.

[31] C. Chang, M. Jarvis, B. Jain, S. M. Kahn, D. Kirkby, A. Connolly, S. Krughoff, E.-H. Peng, and J. R. Peterson. The effective number density of galaxies for weak lensing measurements in the LSST project. MNRAS, 434:2121–2135, September 2013.

[32] N. Chisari, S. Codis, C. Laigle, Y. Dubois, C. Pichon, J. Devriendt, A. Slyz, L. Miller, R. Gavazzi, and K. Benabed. Intrinsic alignments of galaxies in the Horizon-AGN cosmological hydrodynamical simulation. MNRAS, 454:2736–2753, December 2015.

[33] N. Chisari, C. Laigle, S. Codis, Y. Dubois, J. Devriendt, L. Miller, K. Benabed, A. Slyz, R. Gavazzi, and C. Pichon. Redshift and luminosity evolution of the intrinsic alignments of galaxies in Horizon-AGN. MNRAS, 461:2702–2721, September 2016.

[34] N. E. Chisari, S. Codis, C. Laigle, Y. Dubois, C. Pichon, J. Devriendt, A. Slyz, L. Miller, R. Gavazzi, and K. Benabed. Intrinsic alignments of galaxies in the Horizon-AGN cosmological hydrodynamical simulation. *ArXiv e-prints*, July 2015.

[35] N. E. Chisari and C. Dvorkin. Cosmological information in the intrinsic alignments of luminous red galaxies. JCAP, 12:29, December 2013.

[36] N. E. Chisari and C. Dvorkin. Cosmological information in the intrinsic alignments of luminous red galaxies. JCAP, 12:29, December 2013.

[37] S. Codis, R. Gavazzi, Y. Dubois, C. Pichon, K. Benabed, V. Desjacques, D. Pogosyan, J. Devriendt, and A. Slyz. Intrinsic alignment of simulated galaxies in the cosmic web: implications for weak lensing surveys. *ArXiv e-prints*, June 2014.

[38] S. Codis, R. Gavazzi, Y. Dubois, C. Pichon, K. Benabed, V. Desjacques, D. Pogosyan, J. Devriendt, and A. Slyz. Intrinsic alignment of simulated galaxies in the cosmic web: implications for weak lensing surveys. MNRAS, 448:3391–3404, April 2015.

[39] R. G. Crittenden, P. Natarajan, U.-L. Pen, and T. Theuns. Spin-induced Galaxy Alignments and Their Implications for Weak-Lensing Measurements. ApJ, 559:552–571, October 2001.

[40] R. A. C. Croft, T. Di Matteo, V. Springel, and L. Hernquist. Galaxy morphology, kinematics and clustering in a hydrodynamic simulation of a Λ cold dark matter universe. MNRAS, 400:43–67, November 2009.

[41] R. A. C. Croft and C. A. Metzler. Weak-Lensing Surveys and the Intrinsic Correlation of Galaxy Ellipticities. ApJ, 545:561–571, December 2000.

[42] W. Cui, S. Borgani, K. Dolag, G. Murante, and L. Tornatore. The effects of baryons on the halo mass function. MNRAS, 423:2279–2287, July 2012.

[43] M. Davis, G. Efstathiou, C. S. Frenk, and S. D. M. White. The evolution of large-scale structure in a universe dominated by cold dark matter. ApJ, 292:371–394, May 1985.

[44] A. J. Deason, I. G. McCarthy, A. S. Font, N. W. Evans, C. S. Frenk, V. Belokurov, N. I. Libeskind, R. A. Crain, and T. Theuns. Mismatch and misalignment: dark haloes and satellites of disc galaxies. MNRAS, 415:2607–2625, August 2011.

[45] T. Di Matteo, N. Khandai, C. DeGraf, Y. Feng, R. A. C. Croft, J. Lopez, and V. Springel. Cold Flows and the First Quasars. ApJ, 745:L29, February 2012.

[46] T. Di Matteo, V. Springel, and L. Hernquist. Energy input from quasars regulates the growth and activity of black holes and their host galaxies. Nature, 433:604–607, February 2005.

[47] T. Di Matteo, V. Springel, and L. Hernquist. Energy input from quasars regulates the growth and activity of black holes and their host galaxies. Nature, 433:604–607, February 2005.

[48] S. Dodelson. *Modern cosmology*. 2003.

[49] X. Dong, W. Lin, X. Kang, Y. O. Wang, A. A. Dutton, and A. V. Macciò. The Distribution of Satellites Around Central Galaxies in a Cosmological Hydrodynamical Simulation. *ArXiv e-prints*, July 2014.

[50] Y. Dubois, C. Pichon, C. Welker, D. Le Borgne, J. Devriendt, C. Laigle, S. Codis, D. Pogosyan, S. Arnouts, K. Benabed, E. Bertin, J. Blaizot, F. Bouchet, J.-F. Cardoso, S. Colombi, V. de Lapparent, V. Desjacques, R. Gavazzi, S. Kassin, T. Kimm, H. McCracken, B. Milliard, S. Peirani, S. Prunet, S. Rouberol, J. Silk, A. Slyz, T. Sousbie, R. Teyssier, L. Tresse, M. Treyer, D. Vibert, and M. Volonteri. Dancing in the dark: galactic properties trace spin swings along the cosmic web. *ArXiv e-prints*, February 2014.

[51] Y. Dubois, C. Pichon, C. Welker, D. Le Borgne, J. Devriendt, C. Laigle, S. Codis, D. Pogosyan, S. Arnouts, K. Benabed, E. Bertin, J. Blaizot, F. Bouchet, J.-F. Cardoso, S. Colombi, V. de Lapparent, V. Desjacques, R. Gavazzi, S. Kassin, T. Kimm, H. McCracken, B. Milliard, S. Peirani, S. Prunet, S. Rouberol, J. Silk, A. Slyz, T. Sousbie, R. Teyssier, L. Tresse, M. Treyer, D. Vibert, and M. Volonteri. Dancing in the dark: galactic properties trace spin swings along the cosmic web. MNRAS, 444:1453–1468, October 2014.

[52] G. Dvali, G. Gabadadze, and M. Porrati. 4D gravity on a brane in 5D Minkowski space. *Physics Letters B*, 485:208–214, July 2000.

[53] T. Eifler, E. Krause, S. Dodelson, A. Zentner, A. Hearin, and N. Gnedin. Accounting for baryonic effects in cosmic shear tomography: Determining a minimal set of nuisance parameters using PCA. *ArXiv e-prints*, May 2014.

[54] A. Faltenbacher, S. Gottlöber, M. Kerscher, and V. Müller. Correlations in the orientations of galaxy clusters. A&A, 395:1–9, November 2002.

[55] A. Faltenbacher, Y. P. Jing, C. Li, S. Mao, H. J. Mo, A. Pasquali, and F. C. van den Bosch. Spatial and Kinematic Alignments between Central and Satellite Halos. ApJ, 675:146–155, March 2008.

[56] A. Faltenbacher, C. Li, S. D. M. White, Y.-P. Jing, Shu-DeMao, and J. Wang. Alignment between galaxies and large-scale structure. *Research in Astronomy and Astrophysics*, 9:41–58, January 2009.

[57] P. G. Ferreira and M. Joyce. Structure Formation with a Self-Tuning Scalar Field. *Physical Review Letters*, 79:4740–4743, December 1997.

[58] M. Franx, G. Illingworth, and T. de Zeeuw. The ordered nature of elliptical galaxies - Implications for their intrinsic angular momenta and shapes. ApJ, 383:112–134, December 1991.

[59] J. A. Frieman, C. T. Hill, A. Stebbins, and I. Waga. Cosmology with Ultralight Pseudo Nambu-Goldstone Bosons. *Physical Review Letters*, 75:2077–2080, September 1995.

[60] S. Genel, S. M. Fall, L. Hernquist, M. Vogelsberger, G. F. Snyder, V. Rodriguez-Gomez, D. Sijacki, and V. Springel. Galactic Angular Momentum in the Illustris Simulation: Feedback and the Hubble Sequence. ApJ, 804:L40, May 2015.

[61] S. Genel, M. Vogelsberger, V. Springel, D. Sijacki, D. Nelson, G. Snyder, V. Rodriguez-Gomez, P. Torrey, and L. Hernquist. Introducing the Illustris project: the evolution of galaxy populations across cosmic time. MNRAS, 445:175–200, November 2014.

[62] M. Gustafsson, M. Fairbairn, and J. Sommer-Larsen. Baryonic pinching of galactic dark matter halos. Phys.Rev.D, 74(12):123522, December 2006.

[63] A. H. Guth. Inflationary universe: A possible solution to the horizon and flatness problems. Phys.Rev.D, 23:347–356, January 1981.

[64] O. Hahn, R. Teyssier, and C. M. Carollo. The large-scale orientations of disc galaxies. MNRAS, 405:274–290, June 2010.

[65] A. P. Hearin, A. R. Zentner, and Z. Ma. General requirements on matter power spectrum predictions for cosmology with weak lensing tomography. JCAP, 4:34, April 2012.

[66] A. Heavens, A. Refregier, and C. Heymans. Intrinsic correlation of galaxy shapes: implications for weak lensing measurements. MNRAS, 319:649–656, December 2000.

[67] C. Heymans, E. Grocutt, A. Heavens, M. Kilbinger, T. D. Kitching, F. Simpson, J. Benjamin, T. Erben, H. Hildebrandt, H. Hoekstra, Y. Mellier, L. Miller, L. Van Waerbeke, M. L. Brown, J. Coupon, L. Fu, J. Harnois-Déraps, M. J. Hudson, K. Kuijken, B. Rowe, T. Schrabback, E. Semboloni, S. Vafaei, and M. Velander. CFHTLenS tomographic weak lensing cosmological parameter constraints: Mitigating the impact of intrinsic galaxy alignments. MNRAS, 432:2433–2453, July 2013.

[68] C. Heymans, M. White, A. Heavens, C. Vale, and L. van Waerbeke. Potential sources of contamination to weak lensing measurements: constraints from N-body simulations. MNRAS, 371:750–760, September 2006.

[69] S. Hilbert, D. Xu, P. Schneider, V. Springel, M. Vogelsberger, and L. Hernquist. Intrinsic Alignments in the Illustris Simulation. *ArXiv e-prints*, June 2016.

[70] G. Hinshaw, D. Larson, E. Komatsu, D. N. Spergel, C. L. Bennett, J. Dunkley, M. R. Nolta, M. Halpern, R. S. Hill, N. Odegard, L. Page, K. M. Smith, J. L. Weiland, B. Gold, N. Jarosik, A. Kogut, M. Limon, S. S. Meyer, G. S. Tucker, E. Wollack, and E. L. Wright. Nine-year Wilkinson Microwave Anisotropy Probe (WMAP) Observations: Cosmological Parameter Results. ApJS, 208:19, October 2013.

[71] C. M. Hirata, R. Mandelbaum, M. Ishak, U. Seljak, R. Nichol, K. A. Pimbblet, N. P. Ross, and D. Wake. Intrinsic galaxy alignments from the 2SLAQ and SDSS surveys: luminosity and redshift scalings and implications for weak lensing surveys. MNRAS, 381:1197–1218, November 2007.

[72] C. M. Hirata and U. Seljak. Intrinsic alignment-lensing interference as a contaminant of cosmic shear. Phys.Rev.D, 70(6):063526, September 2004.

[73] P. F. Hopkins, N. A. Bahcall, and P. Bode. Cluster Alignments and Ellipticities in ΛCDM Cosmology. ApJ, 618:1–15, January 2005.

[74] W. Hu. Dark synergy: Gravitational lensing and the CMB. Phys.Rev.D, 65(2):023003, January 2002.

[75] D. Huterer. Weak lensing, dark matter and dark energy. *General Relativity and Gravitation*, 42:2177–2195, September 2010.

[76] D. Huterer and M. Takada. Calibrating the nonlinear matter power spectrum: Requirements for future weak lensing surveys. *Astroparticle Physics*, 23:369–376, May 2005.

[77] M. Ishak, C. M. Hirata, P. McDonald, and U. Seljak. Weak lensing and CMB: Parameter forecasts including a running spectral index. Phys.Rev.D, 69(8):083514, April 2004.

[78] Y. P. Jing. Intrinsic correlation of halo ellipticity and its implications for large-scale weak lensing surveys. MNRAS, 335:L89–L93, October 2002.

[79] B. Joachimi and S. L. Bridle. Simultaneous measurement of cosmology and intrinsic alignments using joint cosmic shear and galaxy number density correlations. A&A, 523:A1, November 2010.

[80] B. Joachimi, M. Cacciato, T. D. Kitching, A. Leonard, R. Mandelbaum, B. M. Schäfer, C. Sifón, H. Hoekstra, A. Kiessling, D. Kirk, and A. Rassat. Galaxy Alignments: An Overview. Space Sci.Rev., July 2015.

[81] B. Joachimi, R. Mandelbaum, F. B. Abdalla, and S. L. Bridle. Constraints on intrinsic alignment contamination of weak lensing surveys using the MegaZ-LRG sample. A&A, 527:A26, March 2011.

[82] B. Joachimi, R. Mandelbaum, F. B. Abdalla, and S. L. Bridle. Constraints on intrinsic alignment contamination of weak lensing surveys using the MegaZ-LRG sample. A&A, 527:A26, March 2011.

[83] B. Joachimi and P. Schneider. The removal of shear-ellipticity correlations from the cosmic shear signal via nulling techniques. A&A, 488:829–843, September 2008.

[84] B. Joachimi and P. Schneider. The removal of shear-ellipticity correlations from the cosmic shear signal. Influence of photometric redshift errors on the nulling technique. A&A, 507:105–129, November 2009.

[85] B. Joachimi, E. Semboloni, P. E. Bett, J. Hartlap, S. Hilbert, H. Hoekstra, P. Schneider, and T. Schrabback. Intrinsic galaxy shapes and alignments - I. Measuring and modelling COSMOS intrinsic galaxy ellipticities. MNRAS, 431:477–492, May 2013.

[86] B. Joachimi, E. Semboloni, S. Hilbert, P. E. Bett, J. Hartlap, H. Hoekstra, and P. Schneider. Intrinsic galaxy shapes and alignments - II. Modelling the intrinsic alignment contamination of weak lensing surveys. MNRAS, 436:819–838, November 2013.

[87] N. Kaiser. Clustering in real space and in redshift space. MNRAS, 227:1–21, July 1987.

[88] N. Kaiser. Weak gravitational lensing of distant galaxies. ApJ, 388:272–286, April 1992.

[89] X. Kang, F. C. van den Bosch, X. Yang, S. Mao, H. J. Mo, C. Li, and Y. P. Jing. The alignment between satellites and central galaxies: theory versus observations. MNRAS, 378:1531–1542, July 2007.

[90] N. Katz, D. H. Weinberg, and L. Hernquist. Cosmological Simulations with TreeSPH. ApJS, 105:19, July 1996.

[91] S. Kazantzidis, A. V. Kravtsov, A. R. Zentner, B. Allgood, D. Nagai, and B. Moore. The Effect of Gas Cooling on the Shapes of Dark Matter Halos. ApJ, 611:L73–L76, August 2004.

[92] S. Kazantzidis, A. R. Zentner, and D. Nagai. The Effect of Baryons on Halo Shapes. In G. A. Mamon, F. Combes, C. Deffayet, and B. Fort, editors, *EAS Publications Series*, volume 20 of *EAS Publications Series*, pages 65–68, 2006.

[93] N. Khandai, T. Di Matteo, R. Croft, S. Wilkins, Y. Feng, E. Tucker, C. DeGraf, and M.-S. Liu. The MassiveBlack-II simulation: the evolution of haloes and galaxies to z$\sim$0. MNRAS, 450:1349–1374, June 2015.

[94] N. Khandai, T. Di Matteo, R. Croft, S. M. Wilkins, Y. Feng, E. Tucker, C. DeGraf, and M.-S. Liu. The MassiveBlack-II Simulation: The Evolution of Halos and Galaxies to z˜0. *ArXiv e-prints*, February 2014.

[95] A. Kiessling, M. Cacciato, B. Joachimi, D. Kirk, T. D. Kitching, A. Leonard, R. Mandelbaum, B. M. Schäfer, C. Sifón, M. L. Brown, and A. Rassat. Galaxy alignments: Theory, modelling and simulations. *ArXiv e-prints*, April 2015.

[96] L. J. King. Cosmic shear as a tool for precision cosmology: minimising intrinsic galaxy alignment-lensing interference. A&A, 441:47–53, October 2005.

[97] D. Kirk, M. L. Brown, H. Hoekstra, B. Joachimi, T. D. Kitching, R. Mandelbaum, C. Sifón, M. Cacciato, A. Choi, A. Kiessling, A. Leonard, A. Rassat, and B. M. Schäfer. Galaxy alignments: Observations and impact on cosmology. *ArXiv e-prints*, April 2015.

[98] A. Knebe, S. R. Knollmann, S. I. Muldrew, F. R. Pearce, M. A. Aragon-Calvo, Y. Ascasibar, P. S. Behroozi, D. Ceverino, S. Colombi, J. Diemand, K. Dolag, B. L. Falck, P. Fasel, J. Gardner, S. Gottlöber, C.-H. Hsu, F. Iannuzzi, A. Klypin, Z. Lukić, M. Maciejewski, C. McBride, M. C. Neyrinck, S. Planelles, D. Potter, V. Quilis, Y. Rasera, J. I. Read, P. M. Ricker, F. Roy, V. Springel, J. Stadel, G. Stinson, P. M. Sutter, V. Turchaninov, D. Tweed, G. Yepes, and M. Zemp. Haloes gone MAD: The Halo-Finder Comparison Project. MNRAS, 415:2293–2318, August 2011.

[99] A. Knebe, N. I. Libeskind, S. R. Knollmann, G. Yepes, S. Gottlöber, and Y. Hoffman. The impact of baryonic physics on the shape and radial alignment of substructures in cosmological dark matter haloes. MNRAS, 405:1119–1128, June 2010.

[100] A. Knebe, N. I. Libeskind, F. Pearce, P. Behroozi, J. Casado, K. Dolag, R. Dominguez-Tenreiro, P. Elahi, H. Lux, S. I. Muldrew, and J. Onions. Galaxies going MAD: the Galaxy-Finder Comparison Project. MNRAS, 428:2039–2052, January 2013.

[101] A. Knebe, H. Yahagi, H. Kase, G. Lewis, and B. K. Gibson. The radial alignment of dark matter subhaloes: from simulations to observations. MNRAS, 388:L34–L38, July 2008.

[102] E. Komatsu, K. M. Smith, J. Dunkley, C. L. Bennett, B. Gold, G. Hinshaw, N. Jarosik, D. Larson, M. R. Nolta, L. Page, D. N. Spergel, M. Halpern, R. S.

Hill, A. Kogut, M. Limon, S. S. Meyer, N. Odegard, G. S. Tucker, J. L. Weiland, E. Wollack, and E. L. Wright. Seven-year Wilkinson Microwave Anisotropy Probe (WMAP) Observations: Cosmological Interpretation. ApJS, 192:18, February 2011.

[103] E. Krause, T. Eifler, and J. Blazek. The impact of intrinsic alignment on current and future cosmic shear surveys. *ArXiv e-prints*, June 2015.

[104] E. Krause, T. Eifler, and J. Blazek. The impact of intrinsic alignment on current and future cosmic shear surveys. MNRAS, 456:207–222, February 2016.

[105] M. Kuhlen, J. Diemand, and P. Madau. The Shapes, Orientation, and Alignment of Galactic Dark Matter Subhalos. ApJ, 671:1135–1146, December 2007.

[106] R. Laureijs, J. Amiaux, S. Arduini, J. . Augueres, J. Brinchmann, R. Cole, M. Cropper, C. Dabin, L. Duvet, A. Ealet, and et al. Euclid Definition Study Report. *ArXiv e-prints*, October 2011.

[107] J. Lee, Y. P. Jing, and Y. Suto. An Analytic Model for the Axis Ratio Distribution of Dark Matter Halos from the Primordial Gaussian Density Field. ApJ, 632:706–712, October 2005.

[108] J. Lee, S. C. Rey, and S. Kim. Alignments of the Galaxies in and around the Virgo Cluster with the Local Velocity Shear. ApJ, 791:15, August 2014.

[109] J. Lee, V. Springel, U.-L. Pen, and G. Lemson. Quantifying the cosmic web - I. The large-scale halo ellipticity-ellipticity and ellipticity-direction correlations. MNRAS, 389:1266–1274, September 2008.

[110] A. Lewis and S. Bridle. Cosmological parameters from CMB and other data: A Monte Carlo approach. Phys.Rev.D, 66(10):103511, November 2002.

[111] C. Li, Y. P. Jing, A. Faltenbacher, and J. Wang. The Detection of the Large-scale Alignment of Massive Galaxies at z ˜ 0.6. ApJ, 770:L12, June 2013.

[112] N. I. Libeskind, S. Cole, C. S. Frenk, T. Okamoto, and A. Jenkins. Satellite systems around galaxies in hydrodynamic simulations. MNRAS, 374:16–28, January 2007.

[113] D. N. Limber. The Analysis of Counts of the Extragalactic Nebulae in Terms of a Fluctuating Density Field. ApJ, 117:134, January 1953.

[114] LSST Science Collaboration, P. A. Abell, J. Allison, S. F. Anderson, J. R. Andrew, J. R. P. Angel, L. Armus, D. Arnett, S. J. Asztalos, T. S. Axelrod, and et al. LSST Science Book, Version 2.0. *ArXiv e-prints*, December 2009.

[115] J. Mackey, M. White, and M. Kamionkowski. Theoretical estimates of intrinsic galaxy alignment. MNRAS, 332:788–798, June 2002.

[116] R. Mandelbaum, C. Blake, S. Bridle, F. B. Abdalla, S. Brough, M. Colless, W. Couch, S. Croom, T. Davis, M. J. Drinkwater, K. Forster, K. Glazebrook, B. Jelliffe, R. J. Jurek, I.-H. Li, B. Madore, C. Martin, K. Pimbblet, G. B. Poole, M. Pracy, R. Sharp, E. Wisnioski, D. Woods, and T. Wyder. The WiggleZ Dark Energy Survey: direct constraints on blue galaxy intrinsic alignments at intermediate redshifts. MNRAS, 410:844–859, January 2011.

[117] R. Mandelbaum, C. M. Hirata, M. Ishak, U. Seljak, and J. Brinkmann. Detection of large-scale intrinsic ellipticity-density correlation from the Sloan Digital Sky Survey and implications for weak lensing surveys. MNRAS, 367:611–626, April 2006.

[118] I. Mohammed and U. Seljak. Analytic model for the matter power spectrum, its covariance matrix and baryonic effects. MNRAS, 445:3382–3400, December 2014.

[119] D. Nelson, A. Pillepich, S. Genel, M. Vogelsberger, V. Springel, P. Torrey, V. Rodriguez-Gomez, D. Sijacki, G. F. Snyder, B. Griffen, F. Marinacci, L. Blecha, L. Sales, D. Xu, and L. Hernquist. The Illustris Simulation: Public Data Release. *ArXiv e-prints*, April 2015.

[120] A. M. Nierenberg, M. W. Auger, T. Treu, P. J. Marshall, C. D. Fassnacht, and M. T. Busha. Luminous Satellites. II. Spatial Distribution, Luminosity Function, and Cosmic Evolution. ApJ, 752:99, June 2012.

[121] T. Okamoto, C. S. Frenk, A. Jenkins, and T. Theuns. The properties of satellite galaxies in simulations of galaxy formation. MNRAS, 406:208–222, July 2010.

[122] T. Okumura, Y. P. Jing, and C. Li. Intrinsic Ellipticity Correlation of SDSS Luminous Red Galaxies and Misalignment with Their Host Dark Matter Halos. ApJ, 694:214–221, March 2009.

[123] B. D. Oppenheimer and R. Davé. Mass, metal, and energy feedback in cosmological simulations. MNRAS, 387:577–600, June 2008.

[124] J. A. Peacock. *Cosmological Physics*. January 1999.

[125] M. J. Pereira, G. L. Bryan, and S. P. D. Gill. Radial Alignment in Simulated Clusters. ApJ, 672:825–833, January 2008.

[126] S. Perlmutter, G. Aldering, G. Goldhaber, R. A. Knop, P. Nugent, P. G. Castro, S. Deustua, S. Fabbro, A. Goobar, D. E. Groom, I. M. Hook, A. G. Kim, M. Y. Kim, J. C. Lee, N. J. Nunes, R. Pain, C. R. Pennypacker, R. Quimby,

C. Lidman, R. S. Ellis, M. Irwin, R. G. McMahon, P. Ruiz-Lapuente, N. Walton, B. Schaefer, B. J. Boyle, A. V. Filippenko, T. Matheson, A. S. Fruchter, N. Panagia, H. J. M. Newberg, W. J. Couch, and T. S. C. Project. Measurements of Ω and Λ from 42 High-Redshift Supernovae. ApJ, 517:565–586, June 1999.

[127] C. Power and A. Knebe. The impact of box size on the properties of dark matter haloes in cosmological simulations. MNRAS, 370:691–701, August 2006.

[128] B. Ratra and P. J. E. Peebles. Cosmological consequences of a rolling homogeneous scalar field. Phys.Rev.D, 37:3406–3427, June 1988.

[129] R. Reyes, R. Mandelbaum, J. E. Gunn, R. Nakajima, U. Seljak, and C. M. Hirata. Optical-to-virial velocity ratios of local disc galaxies from combined kinematics and galaxy-galaxy lensing. MNRAS, 425:2610–2640, October 2012.

[130] A. G. Riess, A. V. Filippenko, P. Challis, A. Clocchiatti, A. Diercks, P. M. Garnavich, R. L. Gilliland, C. J. Hogan, S. Jha, R. P. Kirshner, B. Leibundgut, M. M. Phillips, D. Reiss, B. P. Schmidt, R. A. Schommer, R. C. Smith, J. Spyromilio, C. Stubbs, N. B. Suntzeff, and J. Tonry. Observational Evidence from Supernovae for an Accelerating Universe and a Cosmological Constant. AJ, 116:1009–1038, September 1998.

[131] D. H. Rudd, A. R. Zentner, and A. V. Kravtsov. Effects of Baryons and Dissipation on the Matter Power Spectrum. ApJ, 672:19–32, January 2008.

[132] L. Sales and D. G. Lambas. Anisotropy in the distribution of satellites around primary galaxies in the 2dF Galaxy Redshift Survey: the Holmberg effect. MNRAS, 348:1236–1240, March 2004.

[133] C. Scannapieco, S. D. M. White, V. Springel, and P. B. Tissera. The formation and survival of discs in a ΛCDM universe. MNRAS, 396:696–708, June 2009.

[134] J. Schaye, R. A. Crain, R. G. Bower, M. Furlong, M. Schaller, T. Theuns, C. Dalla Vecchia, C. S. Frenk, I. G. McCarthy, J. C. Helly, A. Jenkins, Y. M. Rosas-Guevara, S. D. M. White, M. Baes, C. M. Booth, P. Camps, J. F. Navarro, Y. Qu, A. Rahmati, T. Sawala, P. A. Thomas, and J. Trayford. The EAGLE project: simulating the evolution and assembly of galaxies and their environments. MNRAS, 446:521–554, January 2015.

[135] F. Schmidt, N. E. Chisari, and C. Dvorkin. Imprint of inflation on galaxy shape correlations. *ArXiv e-prints*, June 2015.

[136] F. Schmidt and D. Jeong. Large-scale structure with gravitational waves. II. Shear. Phys.Rev.D, 86(8):083513, October 2012.

[137] M. D. Schneider and S. Bridle. A halo model for intrinsic alignments of galaxy ellipticities. MNRAS, 402:2127–2139, March 2010.

[138] M. D. Schneider, S. Cole, C. S. Frenk, L. Kelvin, R. Mandelbaum, P. Norberg, J. Bland-Hawthorn, S. Brough, S. Driver, A. Hopkins, J. Liske, J. Loveday, and A. Robotham. Galaxy And Mass Assembly (GAMA): galaxy radial alignments in GAMA groups. MNRAS, 433:2727–2738, August 2013.

[139] M. D. Schneider, C. S. Frenk, and S. Cole. The shapes and alignments of dark matter halos. JCAP, 5:30, May 2012.

[140] S. Sharma and M. Steinmetz. The Angular Momentum Distribution of Gas and Dark Matter in Galactic Halos. ApJ, 628:21–44, July 2005.

[141] C. Sifón, H. Hoekstra, M. Cacciato, M. Viola, F. Köhlinger, R. van der Burg, D. Sand, and M. L. Graham. Constraints on the Alignment of Galaxies in Galaxy Clusters from $\sim$14,000 Spectroscopic Members. *ArXiv e-prints*, June 2014.

[142] S. Singh, R. Mandelbaum, and S. More. Intrinsic alignments of SDSS-III BOSS LOWZ sample galaxies. *ArXiv e-prints*, November 2014.

[143] S. Singh, R. Mandelbaum, and S. More. Intrinsic alignments of SDSS-III BOSS LOWZ sample galaxies. MNRAS, 450:2195–2216, June 2015.

[144] E. Sirko. Initial Conditions to Cosmological N-Body Simulations, or, How to Run an Ensemble of Simulations. ApJ, 634:728–743, November 2005.

[145] D. Spergel, N. Gehrels, C. Baltay, D. Bennett, J. Breckinridge, M. Donahue, A. Dressler, B. S. Gaudi, T. Greene, O. Guyon, C. Hirata, J. Kalirai, N. J. Kasdin, B. Macintosh, W. Moos, S. Perlmutter, M. Postman, B. Rauscher, J. Rhodes, Y. Wang, D. Weinberg, D. Benford, M. Hudson, W.-S. Jeong, Y. Mellier, W. Traub, T. Yamada, P. Capak, J. Colbert, D. Masters, M. Penny, D. Savransky, D. Stern, N. Zimmerman, R. Barry, L. Bartusek, K. Carpenter, E. Cheng, D. Content, F. Dekens, R. Demers, K. Grady, C. Jackson, G. Kuan, J. Kruk, M. Melton, B. Nemati, B. Parvin, I. Poberezhskiy, C. Peddie, J. Ruffa, J. K. Wallace, A. Whipple, E. Wollack, and F. Zhao. Wide-Field InfrarRed Survey Telescope-Astrophysics Focused Telescope Assets WFIRST-AFTA 2015 Report. *ArXiv e-prints*, March 2015.

[146] V. Springel. E pur si muove: Galilean-invariant cosmological hydrodynamical simulations on a moving mesh. MNRAS, 401:791–851, January 2010.

[147] V. Springel, T. Di Matteo, and L. Hernquist. Modelling feedback from stars and black holes in galaxy mergers. MNRAS, 361:776–794, August 2005.

[148] V. Springel, T. Di Matteo, and L. Hernquist. Modelling feedback from stars and black holes in galaxy mergers. MNRAS, 361:776–794, August 2005.

[149] V. Springel and L. Hernquist. Cosmological smoothed particle hydrodynamics simulations: a hybrid multiphase model for star formation. MNRAS, 339:289–311, February 2003.

[150] V. Springel and L. Hernquist. Cosmological smoothed particle hydrodynamics simulations: a hybrid multiphase model for star formation. MNRAS, 339:289–311, February 2003.

[151] V. Springel, S. D. M. White, G. Tormen, and G. Kauffmann. Populating a cluster of galaxies - I. Results at [formmu2]z=0. MNRAS, 328:726–750, December 2001.

[152] M. Takada and M. White. Tomography of Lensing Cross-Power Spectra. ApJ, 601:L1–L4, January 2004.

[153] A. F. Teklu, R.-S. Remus, K. Dolag, A. M. Beck, A. Burkert, A. S. Schmidt, F. Schulze, and L. K. Steinborn. Connecting Angular Momentum and Galactic Dynamics: The complex Interplay between Spin, Mass, and Morphology. *ArXiv e-prints*, March 2015.

[154] A. Tenneti, N. Y. Gnedin, and Y. Feng. Impact of Baryonic Physics on Intrinsic Alignments. *ArXiv e-prints*, July 2016.

[155] A. Tenneti, R. Mandelbaum, and T. Di Matteo. Intrinsic alignments of disk and elliptical galaxies in the MassiveBlack-II and Illustris simulations. *ArXiv e-prints*, October 2015.

[156] A. Tenneti, R. Mandelbaum, T. Di Matteo, Y. Feng, and N. Khandai. Galaxy shapes and intrinsic alignments in the MassiveBlack-II simulation. MNRAS, 441:470–485, June 2014.

[157] A. Tenneti, R. Mandelbaum, T. Di Matteo, A. Kiessling, and N. Khandai. Galaxy shapes and alignments in the MassiveBlack-II hydrodynamic and dark matter-only simulations. MNRAS, 453:469–482, October 2015.

[158] A. Tenneti, S. Singh, R. Mandelbaum, T. D. Matteo, Y. Feng, and N. Khandai. Intrinsic alignments of galaxies in the MassiveBlack-II simulation: analysis of two-point statistics. MNRAS, 448:3522–3544, April 2015.

[159] J. Tinker, A. V. Kravtsov, A. Klypin, K. Abazajian, M. Warren, G. Yepes, S. Gottlöber, and D. E. Holz. Toward a Halo Mass Function for Precision Cosmology: The Limits of Universality. ApJ, 688:709–728, December 2008.

[160] P. Torrey, M. Vogelsberger, D. Sijacki, V. Springel, and L. Hernquist. Moving-mesh cosmology: properties of gas discs. MNRAS, 427:2224–2238, December 2012.

[161] M. A. Troxel and M. Ishak. The intrinsic alignment of galaxies and its impact on weak gravitational lensing in an era of precision cosmology. Phys.Rep., 558:1–59, February 2015.

[162] M. P. van Daalen, J. Schaye, C. M. Booth, and C. Dalla Vecchia. The effects of galaxy formation on the matter power spectrum: a challenge for precision cosmology. MNRAS, 415:3649–3665, August 2011.

[163] F. C. van den Bosch, T. Abel, and L. Hernquist. The angular momentum of gas in protogalaxies - II. The impact of pre-heating. MNRAS, 346:177–185, November 2003.

[164] M. Velliscig, M. Cacciato, J. Schaye, R. A. Crain, R. G. Bower, M. P. van Daalen, C. Dalla Vecchia, C. S. Frenk, M. Furlong, I. G. McCarthy, M. Schaller, and T. Theuns. The alignment and shape of dark matter, stellar, and hot gas distributions in the EAGLE and cosmo-OWLS simulations. MNRAS, 453:721–738, October 2015.

[165] M. Velliscig, M. Cacciato, J. Schaye, R. A. Crain, R. G. Bower, M. P. van Daalen, C. Dalla Vecchia, C. S. Frenk, M. Furlong, I. G. McCarthy, M. Schaller, and T. Theuns. The alignment and shape of dark matter, stellar, and hot gas distributions in the EAGLE and cosmo-OWLS simulations. MNRAS, 453:721–738, October 2015.

[166] M. Velliscig, M. Cacciato, J. Schaye, H. Hoekstra, R. G. Bower, R. A. Crain, M. P. van Daalen, M. Furlong, I. G. McCarthy, M. Schaller, and T. Theuns. Intrinsic alignments of galaxies in the EAGLE and cosmo-OWLS simulations. *ArXiv e-prints*, July 2015.

[167] M. Velliscig, M. P. van Daalen, J. Schaye, I. G. McCarthy, M. Cacciato, A. M. C. Le Brun, and C. D. Vecchia. The impact of galaxy formation on the total mass, mass profile and abundance of haloes. MNRAS, 442:2641–2658, August 2014.

[168] M. Vogelsberger, S. Genel, D. Sijacki, P. Torrey, V. Springel, and L. Hernquist. A model for cosmological simulations of galaxy formation physics. MNRAS, 436:3031–3067, December 2013.

[169] M. Vogelsberger, S. Genel, V. Springel, P. Torrey, D. Sijacki, D. Xu, G. Snyder, S. Bird, D. Nelson, and L. Hernquist. Properties of galaxies reproduced by a hydrodynamic simulation. Nature, 509:177–182, May 2014.

[170] M. Vogelsberger, S. Genel, V. Springel, P. Torrey, D. Sijacki, D. Xu, G. Snyder, D. Nelson, and L. Hernquist. Introducing the Illustris Project: simulating the coevolution of dark and visible matter in the Universe. MNRAS, 444:1518–1547, October 2014.

[171] W. Wang, L. V. Sales, B. M. B. Henriques, and S. D. M. White. Satellite abundances around bright isolated galaxies - II. Radial distribution and environmental effects. MNRAS, 442:1363–1378, August 2014.

[172] Y. Wang, X. Yang, H. J. Mo, C. Li, F. C. van den Bosch, Z. Fan, and X. Chen. Probing the intrinsic shape and alignment of dark matter haloes using SDSS galaxy groups. MNRAS, 385:1511–1522, April 2008.

[173] Y. O. Wang, W. P. Lin, X. Kang, A. Dutton, Y. Yu, and A. V. Macciò. Satellite Alignment. I. Distribution of Substructures and their Dependence on Assembly History from N-body Simulations. ApJ, 786:8, May 2014.

[174] D. H. Weinberg, M. J. Mortonson, D. J. Eisenstein, C. Hirata, A. G. Riess, and E. Rozo. Observational probes of cosmic acceleration. Phys.Rep., 530:87–255, September 2013.

[175] S. Weinberg. *Cosmology*. Cosmology. OUP Oxford, 2008.

[176] X. Yang, F. C. van den Bosch, H. J. Mo, S. Mao, X. Kang, S. M. Weinmann, Y. Guo, and Y. P. Jing. The alignment between the distribution of satellites and the orientation of their central galaxy. MNRAS, 369:1293–1302, July 2006.

[177] A. R. Zentner, E. Semboloni, S. Dodelson, T. Eifler, E. Krause, and A. P. Hearin. Accounting for baryons in cosmological constraints from cosmic shear. Phys.Rev.D, 87(4):043509, February 2013.

[178] P. Zhang. Self-calibration of Gravitational Shear-Galaxy Intrinsic Ellipticity Correlation in Weak Lensing Surveys. ApJ, 720:1090–1101, September 2010.